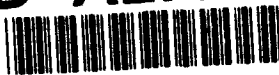


AD-A277 242



15



COLLEGE PARK CAMPUS

**$\eta$ %-SUPERCONVERGENCE IN THE INTERIOR OF LOCALLY REFINED MESHES  
OF QUADRILATERALS: SUPERCONVERGENCE OF THE GRADIENT IN  
FINITE ELEMENT SOLUTIONS OF LAPLACE'S AND POISSON'S EQUATIONS**

by

**DTIC**  
**S** **ELECTE** **D**  
MAR 23 1994  
**F**

**I. Babuška  
T. Strouboulis  
S. K. Gangaraj  
C. S. Upadhyay**

**Technical Note BN-1161**

**and**

**CMC Report No. 93-09  
Texas Engineering Experiment Station  
The Texas A&M University System**

**94-09132**

This document has been approved  
for public release and sale; its  
distribution is unlimited.

**January 1994**



**INSTITUTE FOR PHYSICAL SCIENCE  
AND TECHNOLOGY**

**94 3 22 053**

REPORT DOCUMENTATION PAGE		READ INSTRUCTIONS BEFORE COMPLETING FORM
1. REPORT NUMBER Technical Note BN-1161 & CMC Report No. 93-09	2. GOVT ACCESSION NO.	3. RECIPIENT'S CATALOG NUMBER
4. TITLE (and Subtitle) $\eta$ %-Superconvergence in the Interior of Locally Refined Meshes of Quadrilaterals: Superconvergence of the Gradient in Finite Element Solutions of Laplace's and Poisson's Equations		5. TYPE OF REPORT & PERIOD COVERED Final Life of Contract
7. AUTHOR(s) I. Babuska <sup>1</sup> - T. Strouboulis <sup>2</sup> - S. K. Gangaraj <sup>2</sup> - C. S. Upadhyay <sup>2</sup>		6. PERFORMING ORG. REPORT NUMBER
9. PERFORMING ORGANIZATION NAME AND ADDRESS <sup>1</sup> Institute for Physical Science and Technology University of Maryland College Park, MD 20742-2431		8. CONTRACT OR GRANT NUMBER(s) <sup>1</sup> ONR N00014-90-J-1030 & NSF CCR-88-20279 <sup>2</sup> USARO DAAL03-G-028; NSF MSS- 9025110; TARP-71071
11. CONTROLLING OFFICE NAME AND ADDRESS Department of the Navy Office of Naval Research Arlington, VA 22217		10. PROGRAM ELEMENT, PROJECT, TASK AREA & WORK UNIT NUMBERS
14. MONITORING AGENCY NAME & ADDRESS (if different from Controlling Office)		12. REPORT DATE January 1994
		13. NUMBER OF PAGES 64 + Figures
		15. SECURITY CLASS. (of this report)
		15a. DECLASSIFICATION/DOWNGRADING SCHEDULE
16. DISTRIBUTION STATEMENT (of this Report)  Approved for public release: distribution unlimited		
17. DISTRIBUTION STATEMENT (of the abstract entered in Block 20, if different from Report)		
18. SUPPLEMENTARY NOTES		
19. KEY WORDS (Continue on reverse side if necessary and identify by block number)		
20. ABSTRACT  This paper is the third in a series in which we study the superconvergence of finite element solutions by a computer-based approach. In [1] we studied classical superconvergence and in [2] we introduced the new concept of $\eta$ %-superconvergence and showed that it can be employed to determine regions of least-error for the derivatives of the finite element solution in the interior of any grid of triangular elements. Here we use the same ideas to study the superconvergence of the derivatives of the finite element solution in the interior of complex grids of quadrilaterals of the type used in practical computations.		

# **$\eta$ %-Superconvergence in the Interior of Locally Refined Meshes of Quadrilaterals: Superconvergence of the Gradient in Finite Element Solutions of Laplace's and Poisson's Equations**

**I. Babuška<sup>1</sup>**

**Institute for Physical Science and Technology and Department of Mathematics,  
University of Maryland, College Park, MD 20742, U.S.A.**

**T. Strouboulis<sup>2</sup>, S.K. Gangaraj<sup>2</sup> and C.S. Upadhyay<sup>2</sup>**

**Department of Aerospace Engineering, Texas A&M University,  
College Station, TX 77843, U.S.A.**

**January 1994**

<sup>1</sup>The work of this author was supported by the U.S. Office of Naval Research under Contract N00014-90-J-1030 and by the National Science Foundation under Grant CCR-88-20279.

<sup>2</sup>The work of these authors was supported by the U.S. Army Research Office under Grant DAAL03-G-028, by the National Science Foundation under Grant MSS-9025110 and by the Texas Advanced Research Program under Grant TARP-71071.

Accession For	
NTIS	CRA&I <input checked="" type="checkbox"/>
DTIC	TAB <input type="checkbox"/>
Unannounced <input type="checkbox"/>	
Justification	
By	
Distribution /	
Availability	
Dist	Avail and/or Special
A-1	

## Abstract

This paper is the third in a series in which we study the superconvergence of finite element solutions by a computer-based approach. In [1] we studied classical superconvergence and in [2] we introduced the new concept of  $\eta\%$ -superconvergence and showed that it can be employed to determine regions of least-error for the derivatives of the finite element solution in the interior of any grid of triangular elements. Here we use the same ideas to study the superconvergence of the derivatives of the finite element solution in the interior of complex grids of quadrilaterals of the type used in practical computations.

# 1 Introduction

Classical superconvergence studies the exceptional rates of convergence of values of quantities (derivatives of the displacement, strain, stress etc.) computed from the approximate solution at certain special points in the mesh. These points are called *superconvergence points* for the quantity and the corresponding values are called *superconvergent*. We distinguish two types of superconvergence:

- a) *Direct superconvergence*: The superconvergent values for the quantities are obtained by direct evaluation from the approximate solution at the superconvergence points.
- b) *Superconvergence via post-processing*: The superconvergent values are obtained by some post-processing (local averaging) from the approximate solution.

In this paper we will study only direct superconvergence. A similar study of superconvergence via post-processing is possible and will be the subject of a forthcoming paper.

Classical superconvergence for meshes of quadrilateral elements has been studied by several investigators; see for example [3-9] and the references therein. It should be noted that all the mathematical studies of superconvergence for quadrilaterals elements have addressed the superconvergence in meshes of squares or meshes which can be mapped to a mesh of squares via a sufficiently smooth transformation (see for example [4-5]). However, practical finite element meshes have to conform to complex geometries (boundaries, material-interfaces) and have to be locally refined near reentrant corners, fillets or other critical regions. In [1] we have demonstrated that *the superconvergence points are very sensitive to the geometry of the mesh, the solution-type and the coefficients of the differential operator*. Hence the superconvergence points, in the classical sense, may not exist for the meshes used in engineering computations. Thus classical studies of superconvergence do not result in concrete guidelines on how to sample the various solution quantities in the practical grids.

In [1] we introduced the following new definition of superconvergence: Let  $\{u_h\}$  be a one parameter sequence of finite element solutions of a problem which are computed using a sequence of meshes  $\mathcal{T} = \{T_h\}$  and let  $u$  denote the exact solution. Let us assume that we are interested in the values of the solution or its derivatives or linear combinations of these quantities i.e. in the linear functional  $F(u)(\bar{x})$ . Let us assume that for every element  $\tau$  of the mesh  $T_h$  a special point  $\bar{x}$ , which depends on the geometry (but not the size) of the element, is given. Then denoting

$$(1.1) \quad \Psi(u - u_h) := \max_{\bar{x} \in \tau} |F(u - u_h)(\bar{x})|$$

we are interested in the values of *relative error* in  $F(u)$  at  $\bar{x}$ ,

$$(1.2) \quad \Theta(\bar{x}; F; u, u_h, h, \tau) := \begin{cases} \frac{|F(u - u_h)(\bar{x})|}{\Psi(u - u_h)} & , \text{ if } \Psi(u - u_h) \neq 0 \\ 0 & , \text{ if } \Psi(u - u_h) = 0 \end{cases}$$

If the point  $\bar{x}$  is such that

$$(1.3) \quad \Theta(\bar{x}; F; u, u_h, h, \tau) \leq \frac{\eta}{100} \quad \text{as } h \rightarrow 0$$

then  $\bar{x}$  will be called a  $u$ - $\eta\%$ -superconvergence point relative to the exact solution  $u$  and the family of meshes  $\mathcal{T}$ . Consider now a family of solutions  $\mathcal{U}$ ; the point  $\bar{x}$  will be a  $\mathcal{U}$ - $\eta\%$ -superconvergence point if it is  $u$ - $\eta\%$ -superconvergence point for every  $u \in \mathcal{U}$ . Obviously  $\Theta(\bar{x}; F; u, u_h, h, \tau) \leq 1$  and thus all points in every element  $\tau$  are 100%-superconvergence points. Note that if there exists a point  $\bar{x}$  in the element  $\tau$  for which  $\eta = 0$  in (1.3), i.e.

$$(1.4) \quad \Theta(\bar{x}; F; u, u_h, h, \tau) \rightarrow 0 \quad \text{as } h \rightarrow 0$$

for a particular  $u$  (resp. for every  $u \in \mathcal{U}$ ) then  $\bar{x}$  is a  $u$ -superconvergence (resp.  $\mathcal{U}$ -superconvergence) point in the classical sense.

So far we have assumed that we are interested only in one scalar functional  $F$ . We could also be interested in the points which are superconvergent simultaneously for two (or more) functionals e.g. the derivatives in the  $x_1$  and  $x_2$  directions. We can formalize this by assuming a vector functional; the meaning of the  $\eta\%$ -superconvergence point for the vector functional is obvious. Sometimes we will call it explicitly as simultaneous superconvergence.

Let us note that if  $\eta$  is very small (smaller than a tolerance) we can still *practically* speak about a superconvergence point (with a given tolerance), which is the reason for introducing the notion of the  $\eta\%$ -superconvergence. For example in Section 5.1.1b we report the simultaneous superconvergence for the  $x_1$  and  $x_2$  derivative with tolerance less than 0.001% (for a mesh of biquadratic elements with a mesh-interface).

*Remark 1.1.* In this paper we are interested in the pointwise superconvergence as defined above. Of course the notion of superconvergence can also be understood in different ways. For example we can be interested in the quantity

$$(1.5) \quad \Phi_q(\{\bar{x}_\tau\}; F, u, u_h, h, \{\tau\}) := \frac{\left( \sum_{\tau \in \{\tau\}} \sum_{\bar{x}_\tau \in \{\bar{x}_\tau\}} |F(u - u_h)(\bar{x}_\tau)|^q \right)^{\frac{1}{q}}}{\left( \sum_{\tau \in \{\tau\}} (\Psi(u - u_h))^q \right)^{\frac{1}{q}}}$$

where  $\{\tau\}$  is a set of elements,  $\{\bar{x}_\tau\}$  is a set of points in each element. Then the pointwise superconvergence is related to  $q = \infty$ . Very often for locally refined meshes the area-measure of nonregular mesh-structure is of order  $O(h)$ . If in addition, as it often occurs (see Section 5.4),  $\eta \rightarrow 0$  (at the points  $\{\bar{x}_\tau\}$ ) exponentially with the distance of the element  $\tau$  to the interface we get  $\Phi_q \rightarrow 0$  as  $h \rightarrow 0$  (in fact  $\Phi_q \approx h^{\frac{1}{q}}$ ). Various authors are calling this effect also as superconvergence (see e.g. [4, 5]). Another similar example is to create an "improved" solution (see [10, 11]) and measure the error of this "improved" solution (see [12]). Once more the notion of superconvergence depends on its measure, e.g. if measured in  $L^q$ -norm,  $q < \infty$ , we get superconvergence effects where for  $q = \infty$  there is no superconvergence (see the example of a grid with mesh-interface in Section 5.2 below). Hence *the word superconvergence has to be properly defined.*

The goals of the paper are the following:

1. To show that the  $\eta\%$ -superconvergence points in an element depend on the local neighborhood topology of the mesh.
2. To address in detail the superconvergence for concrete topologies in meshes of square elements with refinements. These results can be practically used for the meshes which have locally this character. (The meshes used in various codes have only a finite number of local topologies.)
3. To show that if we ask only for improved accuracies in an element there are areas where they can be achieved. These areas are robust with respect to the mesh-topologies outside the immediate neighborhood of the element.
4. To demonstrate that the increased accuracy can be achieved only if the meshes are such that the effect of the pollution is under the control.
5. To develop a general procedure to address the superconvergence problem for grids with general topologies.

Following this Introduction we outline the model elliptic problem (Poisson's equation) and we describe the classes of meshes of quadrilaterals for which the study of superconvergence is given. We then describe a computer-based approach which can be employed to find the points of least-error for the derivatives of the solution in any interior element of any mesh. We give examples of application of this approach to study classical and  $\eta\%$ -superconvergence for complex meshes of quadrilaterals with local refinements.

## 2 Preliminaries

### 2.1 The model problem

In this paper we will study the superconvergence of the derivatives of finite element solutions of Poisson's equation. Let  $\Omega \subseteq \mathbb{R}^2$  be a bounded polygonal domain and let its boundary  $\partial\Omega$  be split into two parts  $\Gamma_D$  and  $\Gamma_N$  ( $\Gamma_D$  has positive length). Let  $u$  be the solution of the problem

$$(2.1a) \quad -\Delta u := -\left(\frac{\partial^2 u}{\partial x_1^2} + \frac{\partial^2 u}{\partial x_2^2}\right) = \bar{f}, \quad \text{in } \Omega,$$

$$(2.1b) \quad u = 0, \quad \text{on } \Gamma_D,$$

$$(2.1c) \quad \frac{\partial u}{\partial n} := \sum_{k=1}^2 \frac{\partial u}{\partial x_k} n_k = \bar{g}, \quad \text{on } \Gamma_N.$$

Here  $n_k$ ,  $k = 1, 2$  are the components of the unit outer normal of  $\partial\Omega$ ;  $\bar{f} \in L^2(\Omega)$ ,  $\bar{g} \in L^2(\Gamma_N)$  are given data. If  $\Gamma_D = \emptyset$  it is assumed that the compatibility condition  $\int_{\partial\Omega} \bar{g} = 0$  is satisfied.

Let  $H_{\Gamma_D}^1(\Omega) := \{u \in H^1(\Omega) \mid u = 0 \text{ on } \Gamma_D\}$ . Then the above problem may be put in the variational form: Find  $u \in H_{\Gamma_D}^1(\Omega)$  such that

$$(2.2) \quad B_\Omega(u, v) = L_\Omega(v) \quad \forall v \in H_{\Gamma_D}^1(\Omega)$$

where

$$(2.3) \quad B_\Omega(u, v) := \int_\Omega \nabla u \cdot \nabla v, \quad L_\Omega(v) := \int_\Omega \bar{f}v + \int_{\Gamma_N} \bar{g}v.$$

Let  $\mathcal{T} := \{T_h\}$  be a *regular-family* of meshes of quadrilaterals with straight edges. (It is assumed that for any quadrilaterals  $\tau_i, \tau_j \in T_h$ , the intersection  $\tau_i \cap \tau_j$  is either empty, a vertex or a common edge, and that the regularity conditions (37.40) in [13] hold. For the regularity-conditions for grids of quadrilaterals with refinements see [14].) The meshes  $T_h$  are not assumed to be quasiuniform. We introduce the conforming finite-element spaces



$$(2.4a) \quad S_h^p := \left\{ u \in C^0(\Omega) \mid u|_{\tau_k} \in S_h^p(\tau_k), \quad k = 1, \dots, M(T_h) \right\},$$

$$(2.4b) \quad S_h^p(\tau_k) = \left\{ w \in C^\infty(\tau_k) \mid w \circ F_{\tau_k} \in \hat{S}^{(p,p)}(\hat{\tau}) \right\}$$

where  $\hat{\tau} := (-1, 1)^2$  is the master-element and  $F_{\tau_k}$  is the bilinear mapping of  $\hat{\tau}$  onto  $\tau_k$ ;  $M(T_h)$  is the number of elements in  $T_h$  and

$$(2.5) \quad \hat{S}^{(p,p)}(\hat{\tau}) := \left\{ \hat{P} \mid \hat{P}(\hat{x}_1, \hat{x}_2) = \sum_{\substack{i,j \\ 0 \leq i,j \leq p}} \alpha_{i,j} \hat{x}_1^i \hat{x}_2^j \right\}$$

By our assumption the mapping  $F_{\tau_k}$  is a bilinear map of  $\hat{\tau}$  onto  $\tau_k$ . Hence

$$(2.6) \quad x_1 = \sum_{i,j=0}^1 a_{i,j} \hat{x}_1^i \hat{x}_2^j, \quad x_2 = \sum_{i,j=0}^1 b_{i,j} \hat{x}_1^i \hat{x}_2^j$$

Let  $P(x_1, x_2) = \sum_{0 \leq m+n \leq p} c_{mn} x_1^m x_2^n$  be a polynomial of degree  $p$ ; then

$$(2.7) \quad P(x_1, x_2) = \sum_{0 \leq m+n \leq p} c_{mn} \left( \sum_{i,j=0}^1 a_{i,j} \hat{x}_1^i \hat{x}_2^j \right)^m \left( \sum_{k,l=0}^1 b_{k,l} \hat{x}_1^k \hat{x}_2^l \right)^n = \sum_{\substack{0 \leq i \leq p \\ 0 \leq j \leq p}} d_{ij} \hat{x}_1^i \hat{x}_2^j$$

Hence any polynomial of degree  $p$  belongs to the span of the shape-functions  $S_h^p(\tau_k)$  on every physical element  $\tau_k$ .

Below we will consider meshes which are obtained from a  $h$ -refinement procedure which include elements with irregular connections. We say that an element has  $n$ -irregular connection on one of its sides if it is connected to  $(n+1)$ -neighboring elements on that side. Here we consider only elements with 1-irregular connections and we will refer to the meshes as 1-irregular meshes (see [14]). The precise mathematical development of interpolation spaces for 1-irregular meshes of bilinear elements is given in [14] (see [15] for the biquadratic elements). A systematic approach for the construction of hierarchic variable- $p$  interpolation spaces for 1-irregular meshes is given in [16]. In this paper we will restrict ourselves to bilinear ( $p = 1$ ) and biquadratic ( $p = 2$ ) elements of the Lagrangian family. In meshes of Lagrangian elements with 1-irregular connections there are two types of nodes, the *proper* (or *active*) nodes and the *improper* (or *constrained*) nodes. For bilinear elements a proper node is a vertex for all the elements

which share the node as shown in Fig. 1a (see also [14]). For biquadratic elements a proper node is either a vertex for all the elements which share the node or a midside node for an element and a corner node for other two elements which are connected to the first element through that side as shown in Fig. 1b (see [15]). The details about the implementation of the constrained approximation are discussed in [17]. The constrained nodes can be eliminated by introducing transition (or composite) elements as shown in Fig. 1c and Fig. 1d for the meshes shown in Fig. 1a and Fig. 1b, respectively.

We let  $S_{h,\Gamma_D}^p := S_h^p(\Omega) \cap H_{\Gamma_D}^1(\Omega)$ . The finite element solution  $u_h$  of the model problem satisfies: Find  $u_h \in S_{h,\Gamma_D}^p$  such that

$$(2.8) \quad B_\Omega(u_h, v_h) = L_\Omega(v_h) \quad \forall v_h \in S_{h,\Gamma_D}^p$$

We let  $e_h := u - u_h$  denote the error in the finite element solution.

## 2.2 Definition of $\eta\%$ -superconvergence quantities

Let  $T_h \in \mathcal{T}$  be a finite element grid and  $\tau \in T_h$  be any element. Let  $F(u)$  be the solution-quantity of interest, for example we may have  $F(u) = \frac{\partial u}{\partial x_1}$  or  $\frac{\partial u}{\partial x_2}$  or a linear combination of the derivatives. We now define several geometrical quantities associated with the error in the finite element solution in the element  $\tau$ .

Given  $\eta$ ,  $0 \leq \eta \leq 100$  we define the following:

1.  $\eta\%$ -contour of  $F(u)$  in the element  $\tau \in T_h$  for the exact solution  $u$ :

$$(2.9) \quad C_{F(u)}^{\eta\%}(u; \tau, T_h) := \left\{ \mathbf{x} \in \tau \mid \Theta(\mathbf{x}; F; u, u_h, h, \tau) = \frac{\eta}{100} \right\},$$

Here  $\Theta(\mathbf{x}; F; u, u_h, h, \tau)$  is the relative error as defined in (1.2).

2.  $\eta\%$ -band of  $F(u)$  in the element  $\tau \in T_h$  for the exact solution  $u$ :

$$(2.10) \quad B_{F(u)}^{\eta\%}(u; \tau, T_h) := \left\{ \mathbf{x} \in \tau \mid \Theta(\mathbf{x}; F; u, u_h, h, \tau) < \frac{\eta}{100} \right\}$$

3. Superconvergence points of  $F(u)$  in the element  $\tau \in T_h$  for the class of exact solutions  $\mathcal{U}$ :

$$(2.11) \quad \mathcal{X}_{F(u)}^{\text{sp}}(\mathcal{U}; \tau, T_h) := \bigcap_{u \in \mathcal{U}} C_{F(u)}^{0\%}(u; \tau, T_h)$$

4.  $\eta\%$ -superconvergence regions of  $F(u)$  in the element  $\tau \in T_h$  for the class of exact solutions  $\mathcal{U}$ :

$$(2.12) \quad \mathcal{R}_{F(u)}^{\eta\%}(\mathcal{U}; \tau, T_h) := \bigcap_{u \in \mathcal{U}} B_{F(u)}^{\eta\%}(u; \tau, T_h)$$

Here  $\mathcal{U}$  denotes the set of exact solutions of interest.

*Remark 2.1.* In some cases the sets defined above may be empty.

*Remark 2.2.* The function  $u$  is a solution (resp.  $\mathcal{U}$  is a class of solutions) of (2.1) for a given set of data (resp. for given classes of data). When  $\bar{f} \equiv 0$  the solution  $u$  satisfies Laplace's equation, i.e.  $-\Delta u = 0$  (i.e. the solution is harmonic). The majority of steady-state computations in engineering are done to approximate "harmonic" solutions. (By "harmonic" solutions we mean solutions of the homogeneous differential equation (or system of differential equations) with non-homogeneous boundary-conditions.) Thus it is important to study superconvergence for this class of solutions.

One is interested to know a-priori the  $\eta\%$ -superconvergence regions and the superconvergence points, if they exist, for classes of solutions of interest (In the practical computations in plane elasticity and heat-conduction the class of solutions of interest is the class of "harmonic" solutions with a finite number of algebraic point singularities of the type  $r^\alpha$ ). In general, if  $T_h$  is any grid, it is impossible to predict the locations of the superconvergence regions and points. Here we will make additional assumptions about the approximation which will enable us to determine a-priori the  $\eta\%$ -superconvergence regions and points, if they exist. In particular we will assume that:

1. We are interested in the *asymptotic locations* of the  $\eta\%$ -superconvergence regions as a mesh-parameter  $h$  tends to zero (details about how the limit is taken are given below);
2. The global modes of the error (pollutions) are negligible when compared with the magnitude of the error in the local best-approximation (see Section 3);
3. We are interested in a specific class of solutions. The majority of the results in this paper will be given for the class of harmonic solutions.

In this paper we will determine the asymptotic  $\eta\%$ -superconvergence regions and points for elements in the interior of the mesh and smooth solutions. (The solutions can have point-singularities at the boundaries but they are analytic in the interior of homogeneous domains; all the practical solutions in orthotropic heat-conduction and elasticity are of this type.) The theoretical results are given in [1] for a special class of *locally periodic grids*. Here we will demonstrate through numerical examples that the conclusions of the theoretical study hold, for all practical purposes, for the types of grids of quadrilaterals which are used in practical engineering computations.

### 2.3 The class of locally periodic meshes

We now present the definition of a special class of locally periodic meshes. Let us consider a locally periodic grid defined as follows. Let  $0 < H < H^0$ ,  $\mathbf{x}^0 = (x_1^0, x_2^0) \in \Omega$ ,

$$(2.13) \quad S(\mathbf{x}^0, H) := \left\{ \mathbf{x} = (x_1, x_2) \mid |x_i - x_i^0| < H, \quad i = 1, 2 \right\}$$

and assume that  $H^0$  is sufficiently small such that  $\bar{S}(\mathbf{x}^0, H^0) \subset \Omega$ . Further, let  $\gamma$  be a set of multi-indices  $(i, j)$ ,  $\mathbf{x}^{(i,j)} = (x_1^{(i,j)}, x_2^{(i,j)}) \in \Omega$  and

$$(2.14) \quad c(\mathbf{x}^{(i,j)}, h) := S(\mathbf{x}^{(i,j)}, h) \subset S(\mathbf{x}^0, H), \quad (i, j) \in \gamma$$

be the set of the  $h$ -cells (or cells) which cover exactly  $S(\mathbf{x}^0, H)$  i.e.

$$(2.15a) \quad \bigcup_{(i,j) \in \gamma} \bar{c}(\mathbf{x}^{(i,j)}, h) = \bar{S}(\mathbf{x}^0, H)$$

$$(2.15b) \quad c(\mathbf{x}^{(i_1, j_1)}, h) \cap c(\mathbf{x}^{(i_2, j_2)}, h) = \emptyset \quad \text{for } (i_1, j_1) \neq (i_2, j_2)$$

We will refer to  $S(\mathbf{x}^0, H)$  as the *subdomain of periodicity of the mesh centered at  $\mathbf{x}^0$* . Denoting by

$$(2.16) \quad \bar{c} := S(0, 1) := \left\{ (\bar{x}_1, \bar{x}_2) \mid |\bar{x}_1| < 1, |\bar{x}_2| < 1 \right\}$$

the *unit- (master-) cell  $\bar{c}$* , every  $h$ -cell is an  $h$ -scaled and translated master-cell.

Let  $\tilde{T}$  be a mesh on the master-cell (the master-mesh) and  $\tilde{T}_h^{(i,j)}$  be the mesh on  $c(\mathbf{x}^{(i,j)}, h)$  which is the scaled and translated image of  $\tilde{T}$ . We will consider the family  $\mathcal{T}$  of locally periodic meshes. Let  $T_h \in \mathcal{T}$  and  $T_h(\mathbf{x}^0, H)$  be the restriction of  $T_h$  on  $S(\mathbf{x}^0, H)$  and  $T_h^{(i,j)}$  the restriction of  $T_h(\mathbf{x}^0, H)$  on  $c(\mathbf{x}^{(i,j)}, h)$ . We assume that  $T_h^{(i,j)} = \tilde{T}_h^{(i,j)}$ ,  $(i, j) \in \gamma$  i.e.  $T_h(\mathbf{x}^0, H)$  is made by the periodic repetition of the  $h$ -scaled master mesh.

The type of meshes under consideration is depicted in Fig. 2a, where the subdomains  $S(\mathbf{x}^0, H) \supset S(\mathbf{x}^0, H_1)$  are covered by a periodic array of cells shown in Fig. 2b (where the master-mesh in the master-cell is shown in Fig. 2c). Outside the square  $S(\mathbf{x}^0, H)$  the mesh is arbitrary; it could have curved elements, etc. The values of  $H_1$  depend on  $h$  i.e.  $H_1 = H_1(h)$ . More precisely we will assume that there exist constants  $C_1$  and  $C_2$  independent of  $h$  such that

$$(2.17) \quad C_1 H_1^\alpha \leq h \leq C_2 H_1^\alpha, \quad \alpha > 1$$

### 3 The theoretical setting

Given a function  $u$  and the multi-index  $\alpha := (\alpha_1, \alpha_2)$  we define

$$(3.1a) \quad D^\alpha u := \frac{\partial^{|\alpha|} u}{\partial x_1^{\alpha_1} \partial x_2^{\alpha_2}}, \quad |\alpha| := \alpha_1 + \alpha_2$$

$$(3.1b) \quad (\mathcal{D}^k u)(\mathbf{x}) := \left[ \left( \sum_{|\alpha|=k} |D^\alpha u|^2 \right)(\mathbf{x}) \right]^{\frac{1}{2}}, \quad k \geq 0, \text{ integer}$$

and let us denote

$$(3.2a) \quad \|u\|_{S(\mathbf{x}^0, H_i)} := \|u\|_{L^2(S(\mathbf{x}^0, H_i))}$$

$$(3.2b) \quad |u|_{S(\mathbf{x}^0, H_i)} := \|u\|_{L^\infty(S(\mathbf{x}^0, H_i))}$$

$$(3.2c) \quad \|u\|_{S(\mathbf{x}^0, H_i)} := \sum_{|\alpha|=1} |D^\alpha u|$$

Let  $Q$  be a polynomial of degree  $p+1$  on the master-cell  $\tilde{c}$  and let  $\tilde{T}$  be the master-mesh. Then denote

$$(3.3) \quad \rho := Q - Q_1^{\text{INT}}$$

where  $Q_1^{\text{INT}}$  is the interpolant of degree  $p$  of the function  $Q$  defined over the master-mesh  $\tilde{T}$  (for which  $h = 1$ ). As we mentioned above, any polynomial of degree  $p$  on an element  $\tau_h$  belongs to  $S_1^p(\tau_h)$ . Hence any polynomial of degree  $p$  on  $S(\mathbf{x}^0, H)$  belongs to  $S_1^p(S(\mathbf{x}^0, H))$ . Hence  $\rho$  defined in (3.3) is  $\tilde{c}$ -periodic; this can be shown exactly as in [18]. We have

$$(3.4a) \quad \rho(1, \tilde{x}_2) = \rho(-1, \tilde{x}_2), \quad |\tilde{x}_2| < 1$$

$$(3.4b) \quad \rho(\tilde{x}_1, 1) = \rho(\tilde{x}_1, -1), \quad |\tilde{x}_1| < 1$$

Further let

$$(3.5) \quad H_{\text{PER}}^1(\bar{c}) := \left\{ u \in H^1(\bar{c}) \mid u \text{ satisfies (3.4)} \right\}$$

and

$$(3.6) \quad S_{1,\text{PER}}^p(\bar{c}) := \left\{ u \in H_{\text{PER}}^1(\bar{c}) \mid u|_{\bar{\tau}} \in S_1^p(\bar{\tau}) \quad \forall \bar{\tau} \in \bar{T} \right\}$$

Further let  $\bar{z}^p \in S_{\text{PER}}^1(\bar{c})$  such that

$$(3.7a) \quad B_{\bar{c}}(\bar{z}^p, \bar{v}) = B_{\bar{c}}(\rho, \bar{v}) \quad \forall \bar{v} \in S_{1,\text{PER}}^p(\bar{c})$$

and

$$(3.7b) \quad \int_{\bar{c}} (\rho - \bar{z}^p) = 0$$

Note that the function  $\bar{z}^p$  exists and is uniquely determined (we will compute it numerically in the examples). Let us also define  $\psi \in H^1(\bar{c})$  by

$$(3.8) \quad \psi := \rho - \bar{z}^p = Q - \bar{w} \quad \text{where} \quad \bar{w} := Q_1^{\text{INT}} + \bar{z}^p$$

We will now outline the main theorem of the paper. We will make the following assumptions about the exact solution  $u$ :

*Assumption I*

On  $\bar{S}(\bar{x}^0, H)$

$$(3.9) \quad |D^\alpha u| \leq K < \infty, \quad 0 \leq |\alpha| \leq p+2$$

*Remark 3.1.* Assumption I states that the solution is locally smooth in the subdomain  $\bar{S}(\bar{x}^0, H)$  i.e. the subdomain should be sufficiently far from boundaries, material-interfaces and points where the data are rough.

*Assumption II*

If  $a_\alpha := (D^\alpha u)(\bar{x}^0)$ ,  $\alpha = (\alpha_1, \alpha_2)$ ,  $|\alpha| \leq p+1$  then

$$(3.10) \quad R^2 = \sum_{|\alpha|=p+1} a_\alpha^2 > 0$$

Further, we assume that the mesh  $T(\Omega, h)$  is such that:

*Assumption III*

On  $S(\mathfrak{x}^0, H_1)$ ,  $H_1 < H < H^0$

$$(3.11) \quad \|e_h\|_{S(\mathfrak{x}^0, H_1)} \leq Ch^\beta H_1$$

with  $\beta \geq (p+1) - \epsilon$ , where  $\epsilon$  is specified in the theorem below and where  $C$  is independent of  $T(\Omega, h)$ ,  $H_1$ , but it depends on  $K$ ,  $H$  and  $R$ . We will assume everywhere below that  $H$  is sufficiently small depending on  $K$ ,  $R$  and  $p$ .

*Remark 3.2.* We do not assume that  $u$  is smooth in  $\Omega$  outside of  $S(\mathfrak{x}^0, H)$ . For example,  $\Omega$  can have a boundary with reentrant corners (as in Fig. 2(a)) and hence  $u$  can be unsmooth in the neighborhood of these corners. Nevertheless assumption III makes an implicit requirement on the (refinement of the) mesh in the neighborhood of these corners. If  $u$  is smooth in a convex  $\Omega$  and the mesh is quasi-uniform then

$$(3.12) \quad |e_h|_\Omega \leq Ch^{p+1} |\ln h|^\tau |\mathcal{D}^{p+1}u|_\Omega, \quad \tau \geq 0$$

and hence in assumption III we can take  $\beta < p+1$  arbitrary.

*Remark 3.3.* Assumptions II, III imply that the principal part of the error in  $S(\mathfrak{x}^0, H_1)$  is related to the non-zero  $(p+1)$ -derivatives of the exact solution at  $\mathfrak{x}^0$ .

Let  $\psi_h \in H_{\text{PER}}^1(c(\mathfrak{x}^{(i,j)}, h))$  be the function  $\psi$ , defined above, scaled and translated to the cell  $c(\mathfrak{x}^{(i,j)}, h)$  of the mesh in  $S(\mathfrak{x}^0, H)$  i.e.

$$(3.13) \quad \psi_h(\mathfrak{x}) := h^{p+1} \psi(\tilde{\mathfrak{x}}), \quad \frac{\partial \psi_h}{\partial x_i}(\mathfrak{x}) = h^p \frac{\partial \psi}{\partial \tilde{x}_i}(\tilde{\mathfrak{x}}), \quad i = 1, 2,$$

where  $\mathfrak{x} \in c(\mathfrak{x}^{(i,j)}, h)$  and  $\tilde{\mathfrak{x}} = \frac{1}{h}(\mathfrak{x} - \mathfrak{x}^{(i,j)})$ .

It is easy to see that  $\psi_h$  can be periodically extended over  $S(\mathfrak{x}^0, H_1)$ . In [1] we have proven the following theorem based on the theory of interior estimates (see [19]-[24]):

*Theorem 1.* Let  $H_1 < H < H^0$  and the assumptions I-III and (2.17) hold with

$$(3.14) \quad \alpha = \frac{6p+1}{6p}, \quad \nu = \frac{1}{6(6p+1)}, \quad \beta = p+1 - \epsilon, \quad \epsilon = \nu$$

Then for any  $\mathfrak{x} \in S(\mathfrak{x}^0, H_1)$

$$(3.15) \quad \left| \frac{\partial e_h}{\partial x_i}(\mathfrak{x}) \right| = \left| \frac{\partial \psi_h}{\partial x_i}(\mathfrak{x}) \right| + |\lambda| C h^{p+\nu}$$

with  $|\lambda| \leq 1$  and  $C$  independent of  $h$ .

*Remark 3.4.* Note that  $\psi$  (and thus  $\psi_h$ ) depends on the polynomial  $Q$  which approximates well the solution in  $S(\mathfrak{x}^0, H)$ . Theorem 1 states that for small  $h$  we have on  $S(\mathfrak{x}^0, H_1)$

$$(3.16) \quad \frac{\partial e_h}{\partial x_i}(\mathfrak{x}) \approx \frac{\partial \psi_h}{\partial x_i}(\mathfrak{x})$$

or more precisely

$$(3.17) \quad \left| \frac{\partial e_h}{\partial x_i}(\mathfrak{x}) \right| = \left| h^p \frac{\partial \psi}{\partial \tilde{x}_i}(\tilde{\mathfrak{x}}) \right| + |\lambda| C h^{p+\nu}.$$

On the other hand it is easy to see that

$$(3.18) \quad \max \left( \left| \frac{\partial e_h}{\partial x_1} \right|_{c(\mathfrak{x}^{(i,j)}, h)}, \left| \frac{\partial e_h}{\partial x_2} \right|_{c(\mathfrak{x}^{(i,j)}, h)} \right) \geq C h^p$$

where  $C$  depends on the constant  $R$  defined in (3.10). Nevertheless this does not mean that

$$(3.19) \quad \left| \frac{\partial e_h}{\partial x_i} \right|_{\tau} \geq C h^p, \quad i = 1, 2$$

The case that

$$(3.20) \quad \left| \frac{\partial e_h}{\partial x_i} \right|_{\tau} \leq C h^{p+\sigma_0}, \quad \sigma_0 > 0, \quad \text{for either } i = 1 \text{ or } 2,$$

is very exceptional. Hence we will assume that (3.20) does not happen i.e. we will assume that there exists a constant  $\bar{c} > 0$  independent of  $h$  such that

$$(3.21) \quad \left| \frac{\partial e_h}{\partial x_i} \right|_{\tau} \geq \bar{c} \|e_h\|_{\tau}$$



This assumption could formally be improved by imposing additional assumptions on the  $a_\alpha$ 's (defined in assumption II). Note also that (3.21) is always assumed to hold in the classical superconvergence theories.

*Remark 3.5.* Under assumption (3.21) Theorem 1 states that: A point  $\tilde{\mathbf{x}}$  in the element  $\tilde{\tau}$  is asymptotically  $\eta\%$ -superconvergence point for  $F(u) = \frac{\partial u}{\partial x_i}$ ,  $i = 1, 2$ , if and only if

$$(3.22a) \quad \tilde{\Theta}(\tilde{\mathbf{x}}; F; Q, \tilde{w}, 1, \tilde{\tau}) \leq \frac{\eta}{100}$$

where

$$(3.22b) \quad \tilde{\Theta}(\tilde{\mathbf{x}}; F; Q, \tilde{w}, 1, \tilde{\tau}) := \frac{|\tilde{F}(\psi)(\tilde{\mathbf{x}})|}{\tilde{\Psi}(\psi)}, \quad \text{if } \tilde{\Psi}(\psi) := |\psi|_{\tilde{\tau}} \neq 0$$

and zero otherwise (see also (1.2)).

*Remark 3.6.* Theorem 1 states that at a superconvergence point the accuracy is by a factor  $h^\nu$  (with  $\nu$  given in (3.14)) better than in the other points. The value of the factor  $\nu$  in (3.14) is a theoretical one and practically we usually see  $\nu = 1$ , or higher, but the theoretical determination of the largest  $\nu$  is out of scope of this paper. For some examples of observed values of  $\nu$  in numerical experiments see Section 5.2. The case  $\nu > 0$  is of course sufficient for the analysis of the existence of the superconvergence points and  $\eta\%$ -superconvergence regions.

## 4 The methodology for determining the $\eta\%$ -superconvergence regions

### 4.1 The method of freezing the periodicity

In this paper superconvergence is treated as local behavior and is based on the local behavior of the solution in the interior of the domain. We will consider the class of solutions which are locally smooth in  $S(\mathbf{x}^0, H)$ , namely,

$$(4.1) \quad \mathcal{U}^G := \left\{ u \in H^1(\Omega) \mid |D^\alpha u|_{S(\mathbf{x}^0, H)} < K, \quad 0 \leq |\alpha| \leq p+2 \right\}$$

where  $S(\mathbf{x}^0, H)$  denotes an interior subdomain of interest in which the mesh is locally periodic as described above (the subdomain must be a finite distance away from the boundary and points of roughness of the source term; see Fig. 2a). In many instances we are only interested in the subclass of solutions in  $\mathcal{U}^G$  which are harmonic, namely,

$$(4.2) \quad \mathcal{U}^H := \left\{ u \in \mathcal{U}^G \mid \Delta u = 0 \text{ in } \Omega \right\}$$

We may also assume that the functions are harmonic in a subdomain which is slightly bigger than  $S(\mathfrak{x}^0, H)$  and which includes  $S(\mathfrak{x}^0, H)$  in its interior.

a. *The classes of  $(p+1)$ -degree monomial solutions.*

Let us assume that for a given locally periodic grid with corresponding periodic master-mesh  $\tilde{T}$ , given material orthotropy and given class of smooth solutions  $\mathcal{U}$  we consider

$$(4.3) \quad \mathcal{Q} := \left\{ Q \mid Q(x_1, x_2) = \sum_{k=1}^{nd} \alpha_k Q_k(x_1, x_2), \quad Q_k(x_1, x_2) = \sum_{\ell=0}^{p+1} \beta_\ell x_1^\ell x_2^{p+1-\ell} \right\}$$

the class of  $(p+1)$ -degree monomials which occur in all  $(p+1)$ -degree Taylor-series expansions of functions from  $\mathcal{U}$ . Here  $Q_k$ ,  $k = 1, \dots, nd$  denotes a set of linearly independent monomials which form a basis for  $\mathcal{Q}$ . For example, let us assume that  $\mathcal{U}$  is the class of smooth solutions  $\mathcal{U}^G$  given in (4.1); in this case we may choose

$$(4.4) \quad Q_k(x_1, x_2) := x_1^{p+2-k} x_2^{k-1}, \quad 1 \leq k \leq nd = p+2$$

and we obtain the class of all  $(p+1)$ -degree monomials  $\mathcal{Q}^G$ .

In the case that we are interested only in the class of harmonic solutions  $\mathcal{U}^H$  given in (4.2) we will take  $\mathcal{Q}$  as the two-dimensional linear space of harmonic monomials of degree  $(p+1)$  denoted by  $\mathcal{Q}^H$ , namely,

$$(4.5a) \quad \mathcal{Q}^H := \left\{ Q^H \mid Q^H(x_1, x_2) = \sum_{k=1}^2 \alpha_k Q_k^H(x_1, x_2) \right\},$$

$$(4.5b) \quad Q_1^H(x_1, x_2) = \operatorname{Re}(z^{p+1}), \quad Q_2^H(x_1, x_2) = \operatorname{Im}(z^{p+1}), \quad z = x_1 + ix_2.$$

In the previous Section we outlined Theorem 1 which states that we can obtain the asymptotic values of the error for any smooth solution  $u$  in the interior of a periodic mesh-subdomain by solving the periodic boundary-value problem (3.7), using the master-mesh  $\tilde{T}$  over the master-cell  $\tilde{c}$ , with data obtained from the local  $(p+1)$ -degree Taylor-series expansion  $Q$  of the exact solution. Based on this result we will construct a

numerical procedure to determine the  $\eta\%$ -superconvergence quantities for a given class of smooth solutions by employing the corresponding class of  $(p+1)$ -degree monomials.

In order to apply the results of the theoretical study to the practical meshes, for which the mesh is not locally periodic (like for example the mesh shown in Fig. 3a), the following technique of *freezing the periodicity* will be employed:

1. Let  $\omega_0^h$  be an interior patch of elements of interest (shown shaded gray in Fig. 3a) in which we study the  $\eta\%$ -superconvergence. Define the  $s$ -layered patch of elements  $\omega_s^h$ ,  $s \geq 1$ , surrounding the patch  $\omega_0^h$  by

$$(4.6) \quad \omega_s^h := \bigcup_{\substack{X \in N(\tau') \\ \tau' \subseteq \omega_{s-1}^h}} \omega_X, \quad \omega_X := \bigcup_{X \in N(\tau')} \tau'$$

where  $N(\tau')$  denotes the set of the vertices of element  $\tau'$ ,  $\omega_X$  is the patch of the elements connected to vertex  $X$ . The patch  $\omega_s^h$  is shown with thick black perigram in Fig. 3b.

2. Complete the patch  $\omega_s^h$  to a periodic-grid over a slightly larger square periodic-cell which encloses the patch as shown in Fig. 3c. The periodic-cell is then scaled and translated to the unit master-cell  $\tilde{c}$ .
3. Assume that the mesh in the neighborhood of element  $\tau$  is made from the periodic repetition of  $h$ -cells obtained from the master-cell (by  $h$ -scaling and translation) and let  $h$  tend to zero. Then the theoretical-setting of the previous Section applies and the asymptotic error-function in the mesh-cell  $\omega_0^h$  can be obtained by solving the periodic boundary-value problem over the master-cell  $\tilde{c}$ . Based on the results of the theoretical study, outlined in Section 3, the asymptotic locations of the  $\eta\%$ -superconvergence quantities in any element  $\tau \subseteq \omega_0^h$  for a solution  $u$  (resp. class of solutions  $\mathcal{U}$ ) can be obtained from the corresponding quantities (defined on the master-cell  $\tilde{c}$ ) for the local  $(p+1)$ -degree Taylor-series expansion  $Q$  of  $u$  (resp. the class  $\mathcal{Q}$  of the local  $(p+1)$ -degree Taylor-series expansions of functions  $u \in \mathcal{U}$ ), namely:

$$(4.7) \quad \lim_{h \rightarrow 0} C_{F(u)}^{\eta\%}(u; \tau, T_h) = \tilde{C}_{F(u)}^{\eta\%}(Q; \tilde{\tau}, \tilde{T})$$

$$(4.8) \quad \lim_{h \rightarrow 0} B_{F(u)}^{\eta\%}(u; \tau, T_h) = \tilde{B}_{F(u)}^{\eta\%}(Q; \tilde{\tau}, \tilde{T})$$

$$(4.9) \quad \lim_{h \rightarrow 0} \mathcal{X}_{F(u)}^{\text{sup}}(\mathcal{U}; \tau, T_h) = \tilde{\mathcal{X}}_{F(u)}^{\text{sup}}(Q; \tilde{\tau}, \tilde{T})$$

$$(4.10) \quad \lim_{h \rightarrow 0} \mathcal{R}_{F(u)}^{\eta\%}(\mathcal{U}; \tau, T_h) = \tilde{\mathcal{R}}_{F(u)}^{\eta\%}(Q; \tilde{\tau}, \tilde{T})$$

**Remark 4.1.** The above limits hold for the locally periodic meshes under the assumptions of the theoretical analysis outlined in Section 3 (see [1] for the details). Hence for the general grids the limit should be understood for the mesh which is constructed by freezing the periodicity (as is, for example, shown in Fig. 3c).

In the numerical examples it will be demonstrated that the results of  $\eta\%$ -superconvergence obtained from the above methodology hold, for all practical purposes, for the complex grids used in engineering computations (provided that the pollution-error is controlled, the approximation is in the asymptotic range and that sufficient number of mesh-layers are included in the patch  $\omega_i^h$ ).

**Remark 4.2.** Above we assumed that  $\omega_0^h = \omega_X$ ; of course we can use any other patch as  $\omega_0^h$ , for example consisting of one element only.

## 4.2 Determination of the $\eta\%$ -superconvergence quantities

The asymptotic  $\eta\%$ -contours for a given solution  $u$  can be obtained by contouring the function  $\psi$ , defined in (3.8), corresponding to the local Taylor-series expansion  $Q$  of the solution  $u$ . The superconvergence points  $\tilde{\mathbf{x}}$  for a given class of solutions  $\mathcal{U}$  satisfy

$$(4.11) \quad F(\psi_i)(\tilde{\mathbf{x}}) = 0, \quad 1 \leq i \leq nd$$

i.e. when there is a superconvergence point then the zero-contours of  $F(\psi_i)$  intersect at  $\tilde{\mathbf{x}}$  for  $1 \leq i \leq nd$ . Here  $\psi_i := \rho_i - z^{\rho_i}$  which is obtained from (3.7) for  $\rho_i = Q_i - (Q_i)_1^{\text{INT}}$  where  $Q_i$  is the  $i$ -th basis monomial of the  $nd$ -dimensional monomial space  $Q$  corresponding to the class  $\mathcal{U}$ , as discussed in Section 4.1. We also let  $\tilde{w}_i := (Q_i)_1^{\text{INT}} + z^{\rho_i}$ .

The asymptotic  $\eta\%$ -superconvergence bands for a solution  $u$  can be determined from the function  $F(\psi)$  by using piecewise linear interpolation of  $F(\psi)$  on a sufficiently refined uniform mesh obtained by subdividing the quadrilateral of interest.

The asymptotic  $\eta\%$ -superconvergence regions for a class of solutions  $\mathcal{U}$  can be determined by using numerical optimization. In particular, consider the uniform subdivision of the element  $\tau$  into subtriangles with vertices at the set of points  $\Xi := \{\xi_k\}_{k=1}^{\text{np}}$ . Define the relative-error function at the point  $\xi_k$

$$(4.12) \quad \tilde{\Theta}_{F(u)}^{\Xi}(\xi_k; F; Q, \{\tilde{w}_i\}_{i=1}^{nd}, 1, \tilde{\tau}) := \max_{\alpha_i} \frac{\left| \sum_{i=1}^{nd} \alpha_i F(\psi_i)(\xi_k) \right|}{\max_{j=1, \dots, np} \left| \sum_{i=1}^{nd} \alpha_i F(\psi_i)(\xi_j) \right|} \cdot 100,$$

Then the function  $\tilde{\Theta}_{F(u)}^{\Xi}(\tilde{x}; F; Q, \{\tilde{w}_i\}_{i=1}^{nd}, 1, \tilde{\tau})$  can be defined for any point  $\tilde{x} \in \tilde{\tau}$  by using linear interpolation in the subtriangles. The asymptotic  $\eta\%$ -superconvergence regions in the element  $\tau$  can be approximated using the level-sets of the functions  $\tilde{\Theta}_{F(u)}^{\Xi}(\tilde{x}; F; Q, \{\tilde{w}_i\}_{i=1}^{nd}, 1, \tilde{\tau})$  i.e.

$$(4.13) \quad \tilde{\mathcal{R}}_{F(u)}^{\eta\%}(Q; \tilde{\tau}, \tilde{T}) \approx \left\{ \tilde{x} \in \tilde{\tau} \mid \tilde{\Theta}_{F(u)}^{\Xi}(\tilde{x}; F; Q, \{\tilde{w}_i\}_{i=1}^{nd}, 1, \tilde{\tau}) < \eta\% \right\}$$

We will call the above approach the *direct approach*. It is also possible to use a *simplified approach* which avoids the use of numerical optimization at every point. First observe that

$$(4.14) \quad \max_{\alpha_i} \left( \frac{\left| \sum_{i=1}^{nd} \alpha_i F(\psi_i)(\tilde{x}) \right|}{\max_{j=1, \dots, np} \left| \sum_{i=1}^{nd} \alpha_i F(\psi_i)(\xi_j) \right|} \right) \leq \left[ \min_{\alpha_i} \left( \frac{\max_{j=1, \dots, np} \left| \sum_{i=1}^{nd} \alpha_i F(\psi_i)(\xi_j) \right|}{\left( \sum_{i=1}^{nd} \alpha_i^2 \right)^{\frac{1}{2}}} \right) \right]^{-1} \sqrt{\sum_{i=1}^{nd} (F(\psi_i)(\tilde{x}))^2}$$

Hence we can define the function

$$(4.15) \quad \hat{\tilde{\Theta}}_{F(u)}^{\Xi}(\tilde{x}; F; Q, \{\tilde{w}_i\}_{i=1}^{nd}, 1, \tilde{\tau}) := \frac{1}{Z_{\Xi}} \sqrt{\sum_{i=1}^{nd} (F(\psi_i)(\tilde{x}))^2},$$

where

$$(4.16) \quad Z_{\Xi} := \min_{\alpha_i} \left( \frac{\max_{j=1, \dots, np} \left| \sum_{i=1}^{nd} \alpha_i F(\psi_i)(\xi_j) \right|}{\left( \sum_{i=1}^{nd} \alpha_i^2 \right)^{\frac{1}{2}}} \right)$$

The quantity  $Z_{\Xi}$  can be computed using numerical optimization. Let

$$(4.17) \quad \widehat{\mathcal{R}}_{F(u)}^{\eta\%}(Q; \tau, \tilde{T}) := \left\{ \tilde{u} \in \tau \mid \widehat{\Theta}_{F(u)}^{\Xi}(\tilde{u}; F; Q, \{\tilde{w}_i\}_{i=1}^{nd}, 1, \tilde{\tau}) < \frac{\eta}{100} \right\}$$

denote the approximate regions of  $\eta\%$ -superconvergence for the class of solutions  $Q$  obtained by the simplified approach.

The common  $\eta\%$ -superconvergence region in an element  $\tau$  for a given class of meshes and materials can be determined by using either the direct or the simplified approach.

*Remark 4.3.* Note that we have

$$(4.18) \quad \widehat{\mathcal{R}}_{F(u)}^{\eta\%}(Q; \tilde{\tau}, \tilde{T}) \subseteq \mathcal{R}_{F(u)}^{\eta\%}(Q; \tilde{\tau}, \tilde{T}).$$

Therefore the simplified approach results to a conservative estimate for the  $\eta\%$ -superconvergence regions. For the class of harmonic functions  $\mathcal{U}^H$  we observed that the regions obtained by the two approaches are very similar.

*Remark 4.4.* The functions defined in (4.12), (4.15) depend on the set of points  $\Xi$ . To ensure good accuracy in the approximation of the  $\eta\%$ -superconvergence regions a sufficient number of points must be employed. In the examples below the set of points  $\Xi$  was obtained by subdividing the quadrilateral into two triangles and by refining these triangles uniformly several times. The points in  $\Xi$  are the vertices of this triangulation.

## 5 Numerical studies of superconvergence

We will now give examples of numerical studies of classical superconvergence and  $\eta\%$ -superconvergence for complex grids of quadrilaterals. In this Section we will address the following questions:

1. Given any periodic mesh of quadrilaterals (with complex geometry and/or local refinements etc.), where are the superconvergence points for the derivatives, for the class of harmonic and general solutions?
2. Given an element in the interior of a complex grid of quadrilaterals, where are the points of least-error for the derivatives for the class of harmonic and general solutions?
3. Can we put some reasonable restrictions on the grid (which can be controlled in the computation) such that  $\eta\%$ -superconvergence for the derivatives is assured for any solution (including solutions with algebraic point-singularities i.e. all the solutions which are of interest in the practical computations) in the interior of any practical grid?

## 5.1 Determination of the superconvergence points for the periodic meshes

In [1] we demonstrated that the classical superconvergence points for the derivatives in periodic meshes of triangles or squares can be determined numerically. Here we use the same methodology to find the superconvergence points for periodic meshes of square elements with refinements (or meshes obtained from these meshes via a smooth transformation). We studied in detail the superconvergence in the periodic meshes shown in Fig. 4 and we give the results below.

### 5.1.1 Grid with mesh-interface with constrained nodes

In order to study the superconvergence in the elements near a mesh-interface with constrained nodes we considered the periodic-cell shown in Fig. 4a. Note that although the theoretical setting was outlined for a square periodic unit-cell  $\tilde{c}$ , it is also valid for the rectangular unit-cell employed in this example. Here  $\tilde{c} = (-0.5h, 0.5h) \times (0, 1)$  and  $h = 0.05$ . We are interested in determining the superconvergence points for the  $x_1$ - and  $x_2$ -derivatives for the class of harmonic and the class of general solutions for bilinear and biquadratic elements.

#### (a) Bilinear elements

For bilinear elements, the only quadratic harmonic monomial which gives non-zero error is  $Q_1^H(x_1, x_2) = x_1^2 - x_2^2$ . Therefore we have superconvergence of the  $x_1$ - and  $x_2$ -derivatives along the zero-lines of  $\frac{\partial \psi_1^H}{\partial x_1}$ ,  $\frac{\partial \psi_1^H}{\partial x_2}$ , respectively (where  $\psi_1^H$  is the periodic error-function which corresponds to  $Q_1^H$ ) which are shown in Fig. 5a. The points of intersection of these lines are superconvergence points for the  $x_1$ - and  $x_2$ -derivatives, simultaneously; these points are given in Table 1.

Further we note that for the class of general solutions there are two general quadratic monomials which give non-zero error, namely  $Q_1^G(x_1, x_2) = x_1^2$ ,  $Q_2^G(x_1, x_2) = x_2^2$ . Let us denote the error-functions in the periodic mesh-cell, corresponding to these monomials, by  $\psi_1^G$  and  $\psi_2^G$ , respectively and analyze their structure. First consider the function  $\psi_2^G$  and let us denote by  $\rho_2$  the interpolation-error function introduced in (3.3) which is associated to  $Q_2^G$ . We can easily see that  $Q_2^G$  and  $(Q_2^G)_1^{\text{INT}}$  are independent of  $x_1$  and that  $\rho_2 = 0$  on every boundary line of the elements parallel to the mesh-interface. In addition for every fixed  $x_1$ ,  $(Q_2^G)_1^{\text{INT}}$  is a linear interpolant of  $Q_2^G$ . From this we see that in (3.7a) we have

$$(5.1) \quad B_{\tilde{c}}(\rho_2, \tilde{v}) = 0 \quad \forall \tilde{v} \in S_{1, \text{PER}}^1(\tilde{c})$$

and hence  $\rho_2$  is a constant function. Therefore

$$(5.2) \quad \frac{\partial \psi_2^G}{\partial x_i} = \frac{\partial \rho_2}{\partial x_i}, \quad i = 1, 2$$

and (as special case)  $\frac{\partial \psi_2^G}{\partial x_1}$  vanishes identically.

Let us now analyze  $\psi_1^G$ . Because  $\rho_1$  is symmetric with respect to  $x_1$ , so is  $z^{\rho_1}$ . Hence in every element of size  $h$ ,  $z^{\rho_1}$  is constant for fixed  $x_2$ . In addition it is easy to write difference equations for the values of  $z^{\rho_1}$  at the nodal points (of elements of size  $h$ ). From this we conclude that the function  $z^{\rho_1}$  has to be linear in the subdomain occupied by elements of size  $h$  and using the periodicity we conclude that  $z^{\rho_1}$  has to be constant in this subdomain. From the difference equations it is easy to see that the function  $z^{\rho_1}$  is not constant in the subdomain occupied by elements of size  $\frac{h}{2}$ . A more detailed analysis shows that the derivatives of the function  $z^{\rho_1}$  decay exponentially with the distance from the mesh-interface.

Because  $z^{\rho_1}$  is constant and  $\frac{\partial \psi_2^G}{\partial x_1}$  vanishes identically as discussed above, there are superconvergence lines for the  $x_1$ -derivatives; these lines are the same as the superconvergence lines for the  $x_1$ -derivatives for the harmonic solutions (shown by thick line in Fig. 5a). For the  $x_2$ -derivative there is one superconvergence point in each element at the intersections of the zero-lines of  $\frac{\partial \psi_1^G}{\partial x_2}$ ,  $\frac{\partial \psi_2^G}{\partial x_2}$ , as shown in Fig. 5b.

Since  $z^{\rho_i}$ ,  $i = 1, 2$ , is constant in the elements of size  $h$  the simultaneous superconvergence points for both derivatives are located at the centers of these elements. We note that in the elements of size  $\frac{h}{2}$  the simultaneous superconvergence points are not at the center of the element (for harmonic solutions) or they do not exist at all (for general solutions). Nevertheless in the element of size  $\frac{h}{2}$  not at the interface the  $\eta\%$ -value at the centers of the elements is very small and these points are simultaneous superconvergence points for very small tolerance. This follows from the exponential decay of the derivatives of the function  $z^{\rho_i}$  with the distance from the interface.

#### (b) Biquadratic elements

For the biquadratic elements we note that the harmonic and general monomials of degree 3 (namely  $Q_1^H(x_1, x_2) = x_1^3 - 3x_1x_2^2$ ,  $Q_2^H(x_1, x_2) = x_2^3 - 3x_1^2x_2$ , and  $Q_1^G(x_1, x_2) = x_1^3$ ,  $Q_2^G(x_1, x_2) = x_2^3$ ) result in identical error-functions  $\psi_1^G$ ,  $\psi_2^G$  in all the elements.

Let us analyze the functions  $\psi_i^G$ ,  $i = 1, 2$ , analogously as in the case of bilinear elements. First, let us address the case  $i = 2$ . As in the case of bilinear elements  $Q_2^G$  and  $(Q_2^G)_1^{\text{INT}}$  are independent of  $x_1$  and  $\rho_2$  is identically zero on the element-boundaries and the center-lines parallel to the mesh-interface. Moreover  $(Q_2^G)_1^{\text{INT}}$  is a quadratic interpolant of  $Q_2^G$  for every fixed  $x_1$ . Taking into account that  $Q_2^G(x_1, x_2) = x_2^3$ , analogously as before, we conclude that



$$(5.3) \quad B_z(\rho_2, \tilde{v}) = 0 \quad \forall \tilde{v} \in S_{1,PER}^2(\bar{c})$$

and hence  $z^{\rho_2}$  is constant. Therefore

$$(5.4) \quad \frac{\partial \psi_2^G}{\partial x_i} = \frac{\partial \rho_2}{\partial x_i}, \quad i = 1, 2$$

and  $\frac{\partial \psi_2^G}{\partial x_1}$  vanishes identically and hence we have superconvergence lines for the  $x_1$ -derivative which are the zero-lines of  $\frac{\partial \psi_1^G}{\partial x_1}$  (these lines are the thick lines shown in Fig. 5c). Further the zero-lines of  $\frac{\partial \psi_2^G}{\partial x_2}$  are the Gauss-lines parallel to the mesh-interface.

Let us now consider the case  $i = 1$ . First we observe that  $z^{\rho_1}$  is antisymmetric with respect to  $x_1$  and hence  $z^{\rho_1}(0, x_2) = 0$ . In the elements of size  $h$  the antisymmetry of  $z^{\rho_1}$  implies that  $z^{\rho_1}$  has to be linear in  $x_1$ . From the periodicity of  $z^{\rho_1}$  it follows that  $z^{\rho_1}$  is identically zero. Therefore, in the elements of size  $h$ ,  $\frac{\partial \psi_1^G}{\partial x_2}$  is identically zero and the superconvergence-lines for the  $x_2$ -derivative in the elements of size  $h$  are the Gauss-lines parallel to the mesh-interface (the zero-lines of  $\frac{\partial \psi_2^G}{\partial x_2}$ ). The superconvergence lines for the  $x_1$ -derivative in the elements of size  $h$  are the Gauss-lines perpendicular to the mesh-interface (the zero-lines of  $\frac{\partial \psi_1^G}{\partial x_1}$ ).

For the elements of size  $\frac{h}{2}$  the situation is more complicated because  $z^{\rho_1}$  is non-zero although its derivatives decay exponentially with the distance from the mesh-interface. Hence the superconvergence lines for the  $x_1$ -derivative in the elements of size  $\frac{h}{2}$  (the zero-lines of  $\frac{\partial \psi_1^G}{\partial x_1}$ ) are curved as shown in Fig. 5c. For elements which are far from the mesh-interface the superconvergence-lines are practically the Gauss-lines perpendicular to the mesh-interface. Further  $\frac{\partial \psi_1^G}{\partial x_2} \neq 0$ , in the elements of size  $\frac{h}{2}$ , and the values of  $\eta\%$  at the Gauss-lines parallel to the mesh-interface (the zero-lines of  $\frac{\partial \psi_2^G}{\partial x_2}$ ) do not exceed 0.001%. Therefore the Gauss-lines parallel to the mesh-interface are  $\eta\%$ -superconvergence lines for the  $x_2$ -derivative with tolerance less than 0.001%.

From what we said above we see that there exist "almost" simultaneous superconvergence points (with tolerance less than 0.001%) and hence for all practical purposes we can use them as superconvergence points (these points are listed in Table 1). This was also mentioned in Remark 1.1.

### 5.1.2 Grid with mesh-interface with transition elements

We also studied the superconvergence in the elements near a mesh-interface with transition elements by employing the rectangular periodic mesh-cell shown in Fig. 4b.

#### (a) Linear elements

In order to find the superconvergence points for the class of harmonic solutions we considered the periodic error functions  $\psi_1^H, \psi_2^H$  which correspond to the quadratic harmonic basis monomials,  $Q_1^H(x_1, x_2) = x_1^2 - x_2^2$ ,  $Q_2^H(x_1, x_2) = x_1 x_2$ . The function  $z^{\rho_2}$  is antisymmetric with respect to the axis  $x_1 = 0$  (note that the mesh is symmetric about this axis). Using the periodicity condition we see that  $z^{\rho_2} = 0$ . Hence  $\psi_2^H$  is identically equal to zero at the nodes and thus in the bilinear elements there exist lines of superconvergence for the  $x_1$ - and  $x_2$ -derivatives at the zero-lines of  $\frac{\partial \psi_1^H}{\partial x_1}, \frac{\partial \psi_1^H}{\partial x_2}$ , respectively. In the triangular elements there exist superconvergence points for the  $x_1$ - (resp.  $x_2$ -) derivative at the intersection of zero-lines of  $\frac{\partial \psi_1^H}{\partial x_1}, \frac{\partial \psi_2^H}{\partial x_1}$  (resp.  $\frac{\partial \psi_1^H}{\partial x_2}, \frac{\partial \psi_2^H}{\partial x_2}$ ); these points are given in Table 2a. For the class of general solutions there are three basis monomials of quadratic degree,  $Q_1^G(x_1, x_2) = x_1^2$ ,  $Q_2^G(x_1, x_2) = x_2^2$ ,  $Q_3^G(x_1, x_2) = x_1 x_2$ . We determined the superconvergence points in the bilinear square-elements for the  $x_1$ - (resp.  $x_2$ -) derivative at the intersection of the zero-lines of  $\frac{\partial \psi_1^G}{\partial x_1}, \frac{\partial \psi_2^G}{\partial x_1}$  (resp.  $\frac{\partial \psi_1^G}{\partial x_2}, \frac{\partial \psi_2^G}{\partial x_2}$ ); these points are given in Table 2a. We note that  $\psi_3^G = \rho_3 = 0$  in the square elements; in the triangular elements we utilized also the function  $\psi_3^G$ . In this Table we also indicate which ones of the superconvergence points for the class of harmonic solutions in the triangular elements are also valid for the class of general solutions.

#### (b) Quadratic elements

We computed the superconvergence points for the  $x_1$ - (resp.  $x_2$ -) derivative in the elements for the class of harmonic solutions by considering the intersections of the zero-lines of the  $x_1$ - (resp.  $x_2$ -) derivatives for the error-functions corresponding to the two cubic harmonic basis monomials; the points are given in Table 2b. Note that for the class of general solutions there are no superconvergence points in any element of this mesh.

### 5.1.3 A periodic-mesh with several refinements

We also studied the superconvergence for the periodic mesh of bilinear elements shown in Fig. 4c. For this mesh we determined the points of simultaneous superconvergence for the  $x_1$ - and  $x_2$ -derivatives for the class of harmonic solutions; these points are given in Table 3. Note that for some elements with constrained nodes the superconvergence points for the derivatives coincide with a vertex of the element.

## 5.2 Rate of convergence at the superconvergence points

We performed model computations on finite-element meshes with mesh-interface (with constrained nodes or with transition elements) and we checked the rate of convergence of the derivatives at the superconvergence points which are given in Tables 1, 2 for these meshes. We found that the rate of convergence at the superconvergence points (given in Tables 1, 2) is of order  $(p + 1)$ . We also checked the rate of convergence at the  $p \times p$  Gauss-Legendre points (for  $p = 1, 2$ ) in the square elements near the mesh-interface and found that these points are not superconvergence points, in general.

In the computations we considered the Dirichlet boundary-value problem for the Laplacian in the domain  $\Omega = (0, 1)^2$  with Dirichlet-data obtained from the harmonic exact solution  $u(x_1, x_2) = \sin(\pi x_1) \sinh(\pi x_2)$ . The domain  $\Omega$  was meshed with the periodic grids with cell-size  $h$  as shown in Figs. 6 and 7. For these meshes we computed the maximum values of  $|\frac{\partial e_h}{\partial x_1}|, |\frac{\partial e_h}{\partial x_2}|$  (the maximum was computed over the superconvergence points or the Gauss-Legendre points) in the square-elements of size  $\frac{h}{2}$  at the mesh-interface and one-layer away from it.

The results of the convergence study for the mesh-interface with constrained nodes are given in Tables 4a, 4b, 5a, 5b. In Table 4a (resp. Table 5a) we give the values of  $|\frac{\partial e_h}{\partial x_1}|$  (resp.  $|\frac{\partial e_h}{\partial x_2}|$ ) at the superconvergence point and the Gauss-Legendre point in the elements of size  $\frac{h}{2}$  at the interface and one-layer away from the interface for bilinear approximation ( $p = 1$ ). In Table 4b (resp. Table 5b) we give the maximum values of  $|\frac{\partial e_h}{\partial x_1}|$  (resp.  $|\frac{\partial e_h}{\partial x_2}|$ ) (computed over the superconvergence points or the Gauss-Legendre points) in the same elements for biquadratic approximation ( $p = 2$ ). We observed that:

- (i) When the superconvergence points are employed we have

$$(5.5a) \quad \left| \frac{\partial e_h}{\partial x_i} \right|_{\text{sup}} := \max_{\mathbf{x}^{\text{sup}} \in \tau} \left| \frac{\partial e_h}{\partial x_i}(\mathbf{x}^{\text{sup}}) \right| \approx Ch^{p+1}, \quad i = 1, 2$$

where  $\mathbf{x}^{\text{sup}}$  denotes a superconvergence point.

- (ii) When the Gauss-Legendre points are employed we have

$$(5.5b) \quad \left| \frac{\partial e_h}{\partial x_1} \right|_{G-L} := \max_{\mathbf{x}^{G-L} \in \tau} \left| \frac{\partial e_h}{\partial x_1}(\mathbf{x}^{G-L}) \right| \approx \bar{C}h^p$$

$$(5.5c) \quad \left| \frac{\partial e_h}{\partial x_2} \right|_{G-L} := \max_{\mathbf{x}^{G-L} \in \tau} \left| \frac{\partial e_h}{\partial x_2}(\mathbf{x}^{G-L}) \right| \approx \bar{C} h^{p+1}$$

where  $\mathbf{x}^{G-L}$  denotes a Gauss-Legendre point.

We note that the values of  $\left| \frac{\partial e_h}{\partial x_2} \right|$  appear to be superconvergent at the Gauss-Legendre points. (More precisely they are not superconvergent but it cannot be seen in the computations because the points are  $\eta\%$ -superconvergence with very small tolerance, as explained in Section 5.1.1.) We also note that the values of the constant  $\bar{C}$  at the elements one-layer away from the mesh-interface are much smaller than the values of  $\bar{C}$  in the element at the mesh-interface.

The results of the convergence study for the mesh-interface with transition elements are given in Tables 6a, 6b, 7. In Table 6a (resp. 6b) we give the maximum values of  $\left| \frac{\partial e_h}{\partial x_1} \right|$  (the maximum is computed either over the superconvergence points or the Gauss-Legendre points in each element) for linear (resp. quadratic) elements of size  $\frac{h}{2}$  at the mesh-interface or one-layer away from it. We observed that when the superconvergence points from Tables 2a, 2b (resp. the Gauss-Legendre points) are employed the rate of convergence is of order  $(p+1)$  (resp.  $p$ ). In Table 7 we give the values of  $\left| \frac{\partial e_h}{\partial x_1} \right|$  computed at the superconvergence points (given in Table 2a) and at the center of the element for the triangular elements  $\tau_1, \tau_2$  (shown in Fig. 4b). We observe that the rate of convergence of the  $x_1$ -derivative is  $(p+1)$  (resp.  $p$ ) at the superconvergence point (resp. at the center of the element).

In theoretical studies of superconvergence [4, 5] the superconvergence is analyzed for discrete mean-square norms evaluated over subdomains (by employing the set of all superconvergence points in a subdomain). A simple generalization of the discrete-norm used in [4, 5] and elsewhere is

$$(5.6) \quad E_q = \left[ \frac{1}{N} \sum_{i=1}^N \left( \left| \frac{\partial e_h}{\partial x_1}(\bar{\mathbf{x}}_i) \right|^q + \left| \frac{\partial e_h}{\partial x_2}(\bar{\mathbf{x}}_i) \right|^q \right) \right]^{\frac{1}{q}}$$

where  $N$  denotes the number of points  $\{\bar{\mathbf{x}}_i\}_{i=1}^N$  (used in the definition of  $E_q$ ) in the subdomain for which the discrete-norm is evaluated (for  $q = 2$  the norm of [4, 5] is obtained). For the Dirichlet problem with exact solution  $u(x_1, x_2) = \sin(\pi x_1) \sinh(\pi x_2)$  in the domain  $\Omega = (0, 1)^2$  and with mesh-interface along the line  $x_2 = \frac{1}{2}$  (as shown in Fig. 6a) we computed the discrete-norm  $E_q$  using the Gauss-Legendre points in the elements in the subdomain  $\Omega_0 = (0.25, 0.75) \times (0.50, 0.75)$  for meshes of bilinear

and biquadratic elements and several values of  $q \in [1, \infty]$ . The values of the discrete-norm and its convergence rates are given in Tables 8a (resp. 8b) for bilinear (resp. biquadratic) elements. We observe that

$$(5.7) \quad E_q \approx Ch^{p+\frac{1}{q}}$$

(See also Remark 1.1.)

*Remark 5.1.* As noted in Remark 3.3, by employing the theory (which is given in detail in [1]) we cannot show that the gain of the convergence rate is  $h^\nu$  with  $\nu = 1$ , as has been observed in the computations.

### 5.3 Relative error at the superconvergence points for meshes which are not locally periodic.

The classical superconvergence points are obtained assuming that the grid is locally periodic. However, the meshes which are used in practical computations are not expected to satisfy this assumption. In such meshes we can still use the points from a periodic pattern (for example the points for the mesh-interface given above) to sample the solution, if that pattern appears in the interior of the grid. We now show that by using such points we obtain more accurate values of the derivatives than if we employ the  $p \times p$  Gauss-Legendre points in each element (as is customarily done).

We considered the domain  $\Omega = (0, 1)^2$  with Neumann boundary conditions  $\bar{g}$  on  $\partial\Omega$  and source-function  $\bar{f}$  corresponding to the exact solution,  $u(x_1, x_2) = e^{-k[(x_1-a)^2+(x_2-b)^2]}$ . Here we let  $k = 10$  and  $(a, b) = (0, 0)$ . A mesh of bilinear elements was generated using an adaptive algorithm as shown in Fig. 8a. We will focus on the elements in Patch I (shown in Fig. 8a and Fig. 8b) and Patch II (shown in Fig. 8c and Fig. 8d). In the elements shown in each patch we computed the relative error  $\Theta(\bar{x}; \frac{\partial u}{\partial x_i}; u, u_h, h, \tau)$ ,  $i = 1, 2$ , in the  $x_1$ - and  $x_2$ -derivatives of  $u_h$  at the center of the element (the Gauss-Legendre point) or at the superconvergence point which was obtained by assuming that the element belongs to the periodic mesh-interface pattern (shown in Fig. 4a). In Table 9a (resp. Table 9b) we give the values of the relative error in the derivatives at the superconvergence points and the Gauss-Legendre points for the elements in Patch I (resp. Patch II). We observe that in the elements with constrained nodes in Patch I (elements 1-16) the relative error at the superconvergence points is substantially smaller than the relative error at the Gauss-Legendre points. In particular the relative errors in the  $x_1$ -derivative at the Gauss-Legendre points are around 25% whereas at the superconvergence points they are around 2%. In the case of the elements with constrained nodes in Patch II (elements 1-4) the relative error in the  $x_2$ -derivative at the superconvergence points is much smaller than the relative error in the  $x_2$ -derivative at the Gauss-Legendre points. Hence we can conclude that the superconvergence points

from a periodic mesh-pattern should be used instead of the Gauss-Legendre points to sample the derivatives of the solution in the interior of any general grid which (may not be locally periodic but) includes that pattern in its interior.

#### 5.4 $\eta\%$ -superconvergence in periodic meshes with local refinements

We shall now describe numerical examples to illustrate the methodology described in Section 4 to determine regions of  $\eta\%$ -superconvergence. We shall first use the methodology to find  $\eta\%$ -superconvergence regions  $\mathcal{R}_{\frac{\partial}{\partial x_i}}^{\eta\%}(Q; \tau, \tilde{T})$ ,  $i = 1, 2$ , for the derivatives in the element  $\tau$  in the periodic mesh  $\tilde{T}$  for the class  $Q$  of (harmonic or general) polynomial solutions of degree  $(p + 1)$ . We will then demonstrate that the methodology can also be used to find  $\eta\%$ -superconvergence regions in elements in the interior of any locally refined mesh or a mesh with distorted elements.

We considered the periodic meshes shown in Figs. 4a-4c. In Figs. 9a-9d we give the  $\eta\%$ -superconvergence regions for the elements in the mesh shown in Fig. 4a. Figs. 9a and 9b show  $\mathcal{R}_{\frac{\partial}{\partial x_1}}^{\eta\%}(Q^H; \tau, \tilde{T})$ , for  $\eta\% = 5\%, 10\%, 25\%$ , for  $p = 1$  and  $p = 2$ , respectively.

In Figs. 9c and 9d the regions  $\mathcal{R}_{\frac{\partial}{\partial x_2}}^{\eta\%}(Q^H; \tau, \tilde{T})$ , for  $\eta\% = 5\%, 10\%, 25\%$ , are given for  $p = 1$  and  $p = 2$ , respectively. It can be observed that the  $\eta\%$ -superconvergence regions for the  $x_1$ -derivative in the elements with constrained nodes are very different from the  $\eta\%$ -superconvergence regions for the  $x_1$ -derivative in the elements away from the interface. However, the  $\eta\%$ -superconvergence regions for the  $x_2$ -derivative in the elements with constrained nodes are very similar to the  $\eta\%$ -superconvergence regions for the  $x_2$ -derivative in the elements away from the mesh-interface.

The  $\eta\%$ -superconvergence regions for the elements in the mesh shown in Fig. 4b are given in Figs. 10a-10c, for the class of harmonic solutions. It can be observed that the effect of transition elements in the elements of size  $\frac{h}{2}$  decays after one layer of elements. In Figs. 11a-11d we give  $\eta\%$ -superconvergence regions for the class of general solutions. Note that in the triangular elements, there are no regions for either derivative for  $\eta\% \leq 25\%$  and that the effect of the transition elements is significant up to 4 layers of elements in the refined mesh.

We also studied the  $\eta\%$ -superconvergence regions in the elements in the periodic mesh-pattern of Fig. 4c. In Figs. 12a-12d we show the  $\eta\%$  superconvergence regions for  $p = 1$  and  $p = 2$  for the class of harmonic solutions. Figs. 12a and 12b show the regions  $\mathcal{R}_{\frac{\partial}{\partial x_1}}^{\eta\%}(Q^H; \tau, \tilde{T}_h)$ , for  $\eta\% = 5\%, 10\%, 25\%$  for  $p = 1$  and  $p = 2$ , respectively. In Figs. 12c and 12d we show the regions  $\mathcal{R}_{\frac{\partial}{\partial x_2}}^{\eta\%}(Q^H; \tau, \tilde{T}_h)$ , for  $\eta\% = 5\%, 10\%, 25\%$  for  $p = 1$  and  $p = 2$ , respectively. It can be seen from Figs. 12a and 12c that the values of the  $\eta\%$  function for the  $x_1$  and  $x_2$  derivatives at the center of the elements which have constrained nodes is greater than 25%.

To demonstrate the decay of the effect of mesh-interface on the superconvergence we computed the values of maximum relative error for the class of harmonic solutions at the Gauss-Legendre points. In Table 10a (resp. 10b) we give the values of

$$(5.8) \quad \eta\%^{G-L} := \max_{Q \in Q^H} \Theta(\tilde{x}^{G-L}; \frac{\partial u}{\partial x_1}; Q, \tilde{w}, 1, \tilde{\tau})$$

for the elements  $\tilde{\tau}$  of size  $\frac{h}{2}$ , which are separated by 0, 1, 2 and 3 layers from the mesh-interface for bilinear (resp. biquadratic) approximation for the mesh-interface with constrained nodes. In Tables 10c (resp. 10d) we give the values of  $\eta\%^{G-L}$  for linear (resp. quadratic) elements for the mesh-interface with transition elements. In both cases we computed the values only for the square elements of size  $\frac{h}{2}$ . We observed that the value of  $\eta\%^{G-L}$  decays rapidly as we consider elements away from the interface. Hence the Gauss-Legendre points in the elements of size  $\frac{h}{2}$  which are separated by several mesh-layers from the mesh-interface are  $\eta\%$ -superconvergence points for very small tolerance.

### 5.5 $\eta\%$ superconvergence for general meshes with local refinements

Here we demonstrate that, for all practical purposes, the  $\eta\%$ -superconvergence regions can be determined for any element in the interior of any grid with local refinements. Let us consider the locally-refined mesh shown in Fig. 13a and let us assume that we are interested to determine the  $\eta\%$ -superconvergence regions for the derivatives in the elements shown shaded gray in the interior of the patch of interest (which is shown with thick perigram in Fig. 13a). In order to find the  $\eta\%$ -superconvergence regions, the patch, which is shown in 13b, was extracted from the mesh and completed into a periodic mesh  $\tilde{T}$  in the square-cell  $\tilde{c}$ , as shown in Fig. 13c. In Fig. 14a we show the regions of  $\eta\%$ -superconvergence,  $\mathcal{R}_{\frac{\partial u}{\partial x_1}}^{\eta\%}(Q^H; \tau_i, \tilde{T})$  for  $\eta\% = 5\%, 10\%, 25\%$ .

In Fig. 14b we show the bands of  $\eta\%$  relative error  $B_{\frac{\partial u}{\partial x_1}}^{\eta\%}(u; \tau, T_h)$  which were obtained by solving the Neumann problem in the mesh shown in Fig. 13a with data consistent with the harmonic solution  $u(x_1, x_2) = \sin(\pi x_1) \sinh(\pi x_2)$ . It can be observed that the regions of  $\eta\%$ -superconvergence are practically the same as the bands of  $\eta\%$  relative error. (Here we observe that there is only one monomial of degree  $(p+1)$  with non-zero relative error in the  $x_1$ -derivative in the elements of interest).

We also repeated the above computations with the exact solution (Gaussian hill function)  $u(x_1, x_2) = e^{-k[(x_1-a)^2+(x_2-b)^2]}$  with  $k = 10$  (note that this solution is not harmonic). The center of the Gaussian hill  $(a, b)$  is allowed to take values of  $(0.5,$

0.5), (-0.65, -0.3) and (0.25, 0.35). In Figs. 15a, 16a and 17a we show the bands of  $\eta\%$ -relative error  $B_{\frac{\partial u}{\partial x_1}}^{\eta\%}(u; \tau, T_h)$  obtained by solving the Neumann boundary-value problem in the mesh  $T_h$  shown in Fig. 13a. In Figs. 15b, 16b and 17b we give the bands of  $\eta\%$ -relative error  $B_{\frac{\partial u}{\partial x_1}}^{\eta\%}(Q; \tau, \tilde{T})$  obtained by solving the periodic boundary-value problem over the periodic mesh  $\tilde{T}$  shown in Fig. 13c with data consistent with the Taylor series expansion  $Q$  of the Gaussian hill function. It can be observed that the  $\eta\%$ -relative error bands obtained from the actual finite element solution are, for all practical purposes, identical to those obtained from the periodic boundary-value problem using the Taylor series expansion. In Fig. 18 we show the  $\eta\%$ -superconvergence regions  $\mathcal{R}_{\frac{\partial u}{\partial x_1}}^{\eta\%}(Q^G; \tau, \tilde{T})$  for  $\eta\% = 10\%, 30\%, 50\%$ . In the element with constrained nodes the  $\eta\%$ -superconvergence regions for the class of general solutions and  $\eta\% \leq 50\%$ , do not include the center of the element which is the Gauss-Legendre point for  $p = 1$ .

## 5.6 $\eta\%$ -superconvergence regions for a complex grid of skewed quadrilaterals generated by a mesh generator

We will now give an example of finding the  $\eta\%$ -superconvergence regions in the interior of a complex grid generated by commercial-like mesh-generator. We considered the mesh of skewed quadrilaterals shown in Fig. 19a. We were interested to find the  $\eta\%$ -superconvergence regions in the elements which are shown shaded in Figs. 19a, 20a. In each case we considered the mesh-patches which include three mesh-layers around the elements of interest as shown in Figs. 19b, 20b. These mesh-patches were scaled and translated into the square-cell  $\tilde{c} := (-0.5, 0.5) \times (-0.5, 0.5)$  and each mesh-patch was completed into a periodic mesh  $\tilde{T}_1$  (resp.  $\tilde{T}_2$ ) as shown in Fig. 19c (resp. Fig. 20c).

In order to demonstrate that the results for the  $\eta\%$ -superconvergence regions obtained from the methodology are also, for all practical purposes, valid in the actual mesh we performed the following computations. We computed the  $\eta\%$ -relative error regions with the error obtained by solving the following problems:

- P1: Neumann boundary-value problem (with data consistent with the exact solution  $u$ ) solved using the domain and the mesh (actual grid) shown in Fig. 19a.
- P2: Neumann boundary-value problem (with data consistent with the Taylor series expansion  $Q$  of the exact solution  $u$  about the center of the mesh-patch of interest) solved using the domain and the mesh (actual grid) shown in Fig. 19a.
- P3: Periodic boundary-value problem (with data consistent with the Taylor series expansion  $Q$  of the exact solution  $u$  about the center of the mesh-patch of interest) solved using the periodic domain and mesh (periodic grid obtained by freezing the periodicity) shown in Figs. 19c and 20c.



We computed the  $\eta\%$ -relative error regions for the following solutions:

$$(5.5a) \quad u(x_1, x_2) = \operatorname{Re}(w^{(k)}(z)), \quad k = 1, \dots, 4$$

$$(5.5b) \quad w^{(k)}(z) = \frac{1}{a^2 - (z + z_0^{(k)})^2} + \frac{1}{a^2 + (z + z_0^{(k)})^2} - \left( \frac{1}{a^2 - 1} + \frac{1}{a^2 + 1} \right)$$

where  $z = x_1 + ix_2$  and we let  $a = 2$  and  $z_0^{(1)} = \frac{1}{2}(1 + i)$ ,  $z_0^{(2)} = \frac{1}{2}(-1 + i)$ ,  $z_0^{(3)} = \frac{1}{2}(-1 - i)$ ,  $z_0^{(4)} = \frac{1}{2}(1 - i)$ . The exact solutions given above are analytic in the domain and are typical solutions of elliptic boundary-value problems in two dimensions (see also [25]). We computed the regions of 25% relative error in the shaded elements shown in Figs. 19b, 20b and determined the 25%-relative error region which is common to all four solutions  $\mathcal{R}_{\frac{\partial u}{\partial x_i}}^{25\%}(\{w^{(k)}\}_{k=1}^4; \tau, T_h)$ ,  $i = 1, 2$ . In Figs. 21a, 21b, 21c (resp. 21d, 21e, 21f) we show the 25%-common regions  $\mathcal{R}_{\frac{\partial u}{\partial x_1}}^{25\%}(\{w^{(k)}\}_{k=1}^4; \tau, T_h)$  (resp.  $\mathcal{R}_{\frac{\partial u}{\partial x_2}}^{25\%}(\{w^{(k)}\}_{k=1}^4; \tau, T_h)$ ) in the elements shown in Fig. 19a, computed by solving the problems P1, P2, P3, respectively. It can be observed that the 25%-common regions, computed from the three problems, are identical, for all practical purposes. In Fig. 21g (resp. 21h) we show the  $\eta\%$ -superconvergence regions  $\mathcal{R}_{\frac{\partial u}{\partial x_1}}^{25\%}(Q^H; \tau, \tilde{T}_1)$  (resp.  $\mathcal{R}_{\frac{\partial u}{\partial x_2}}^{25\%}(Q^H; \tau, \tilde{T}_1)$ ). Note that the 25%-superconvergence regions lie entirely within the 25%-common regions.

Similarly in Figs. 22a, 22b, 22c (resp. 22d, 22e, 22f) we show the 25%-common regions  $\mathcal{R}_{\frac{\partial u}{\partial x_1}}^{25\%}(\{w^{(k)}\}_{k=1}^4; \tau, T_h)$  (resp.  $\mathcal{R}_{\frac{\partial u}{\partial x_2}}^{25\%}(\{w^{(k)}\}_{k=1}^4; \tau, T_h)$ ), in the elements shown in Fig. 20a, computed by solving the problems P1, P2, P3, respectively. In Fig. 22g (resp. Fig. 22h) we show the  $\eta\%$ -superconvergence regions  $\mathcal{R}_{\frac{\partial u}{\partial x_1}}^{25\%}(Q^H; \tau, \tilde{T}_2)$  (resp.  $\mathcal{R}_{\frac{\partial u}{\partial x_2}}^{25\%}(Q^H; \tau, \tilde{T}_2)$ ). Again we note that the 25%-superconvergence regions are well within the corresponding 25%-common regions.

From the results in Sections 5.5 and 5.6 we make the following observations:

- (i) The  $\eta\%$ -relative error regions computed from the exact solution and the actual or its Taylor series expansion using the periodic grid are, for all practical purposes, identical.
- (ii) Since we have studied  $\eta\%$ -superconvergence for smooth solutions the mesh was allowed to be quite arbitrary.
- (iii) The locations of the  $\eta\%$ -superconvergence regions, for small  $\eta$ , in the elements cannot be predicted based on intuition. In many instances they are quite far from the Gauss-Legendre points and hence the Gauss-Legendre points may not be suitable sampling points.

## 5.7 The pollution effect and $\eta\%$ -superconvergence for singular solutions

In this Section we give examples which show the effect of the pollution on the superconvergence of finite element solutions. In particular we demonstrate that:

1. In finite element approximations of singular solutions with quasiuniform meshes the *pollution error* may be significant (depending on the strength of the singularity, the polynomial degree of the elements and the region of interest) and the  $\eta\%$ -superconvergence regions may not exist, asymptotically.
2. For meshes which are nearly equilibrated in the energy-norm the pollution-effect is insignificant and, for all practical purposes, we can have  $\eta\%$ -superconvergence of the derivatives (as predicted by the methodology of Section 4) in any interior element of the mesh.

To show the pollution effect for meshes of bilinear elements we considered the  $L$ -shaped domain shown in Fig. 23 with boundary conditions compatible with the exact solution  $u(r, \theta) = r^\alpha \sin(\alpha\theta)$ . For  $\alpha = \frac{2}{3}$  (resp.  $\alpha = \frac{1}{3}$ ) homogeneous Dirichlet boundary-conditions (resp. homogeneous mixed boundary-conditions) were applied on the edges of the reentrant corner; in the remaining edges of the boundary Neumann boundary-conditions compatible with the exact solution were imposed. Note that the theoretical analysis shows (see [24], [26] and the references therein) that for quasiuniform meshes of bilinear elements ( $p = 1$ ) the pollution effect is significant (asymptotically) for  $\alpha < \frac{1}{2}$ . Thus as the mesh is refined uniformly we expect to see the following:

- (i) For  $\alpha = \frac{2}{3}$  the  $\eta\%$ -superconvergence regions exist asymptotically, as predicted by the methodology.
- (ii) For  $\alpha = \frac{1}{3}$  there are no  $\eta\%$ -superconvergence regions, asymptotically, due to the pollution effect.

We now proceed to the description of the numerical results.

We meshed the  $L$ -shaped domain with uniform-mesh of bilinear elements and considered the mesh-patches in the subdomains shown in Fig. 24a (subdomain A) and Fig. 24b (subdomain B). In Figs. 25a, 25b and 25c (resp. Fig. 25d, 25e and 25f) we show the bands  $B_{\frac{\partial u}{\partial x_1}}^{\eta\%}(u; \tau, T_h)$  in subdomain A (resp. subdomain B) for the uniform meshes with element-size  $h$ ,  $\frac{h}{2}$  and  $\frac{h}{4}$ , respectively, for  $\alpha = \frac{2}{3}$ . It can be observed that

the  $\eta\%$ -bands for  $\frac{\partial u}{\partial x_1}$  exist asymptotically and coincide with the bands predicted by the methodology of Section 4. In Figs. 26a, 26b and 26c (resp. Figs. 26d, 26e and 26f) we show the bands  $B_{\frac{\partial u}{\partial x_1}}^{\eta\%}(u; \tau, T_h)$  for  $\alpha = \frac{1}{3}$ ; it can be observed that the  $\eta\%$ -bands disappear as the mesh-size  $h$  tends to zero. *The reason for the disappearance of the bands is that the error is uniformly large in the entire element (see also [26]).*

We now consider the class of grids which are nearly equilibrated in the energy-norm which are obtained by refining adaptively a coarse mesh of squares. In Fig. 27a (resp. Fig. 28a) we show a nearly equilibrated grid for the exact solution  $u(\tau, \theta) = \tau^{\frac{2}{3}} \sin(\frac{2}{3}\theta)$  and mark the elements of interest in Patch P (resp. Patch Q). The periodic meshes obtained by completing these patches are shown in Fig. 27b and Fig. 28b for patches P and Q, respectively. In Fig. 29a and (resp. Fig. 30a) we show the bands  $B_{\frac{\partial u}{\partial x_1}}^{\eta\%}(u; \tau, T_h)$  obtained from the solution of the finite element problem on the actual mesh and in Fig. 29b (resp. Fig. 30b) we show the corresponding  $\eta\%$ -bands obtained from the periodic boundary-value problem using Taylor series expansion on the mesh shown in Fig. 27b (resp. Fig. 28b), respectively.

We also considered the nearly equilibrated grid for the exact solution  $u(\tau, \theta) = \tau^{\frac{1}{3}} \sin(\frac{1}{3}\theta)$  with appropriate boundary conditions, as discussed earlier. The mesh and the elements of interest are shown in Fig. 31a and Fig. 32a. The corresponding periodic meshes for these patches are shown in Fig. 31b and Fig. 32b. We computed the bands  $B_{\frac{\partial u}{\partial x_1}}^{\eta\%}(u; \tau, T_h)$  using the finite element solution in the actual mesh shown in Fig. 31a (or Fig. 32a) and the bands  $B_{\frac{\partial u}{\partial x_1}}^{\eta\%}(Q; \tau, \tilde{T})$  from the finite-element solution of the periodic boundary-value problem using the mesh shown in Fig. 31b (or Fig. 32b). These are shown in Fig. 33a and Fig. 33b (resp. Fig. 34a and Fig. 34b) for the patch shown in Fig. 31a (resp. Fig. 32a). It can be seen that the corresponding bands are identical.

Hence we conclude that when the mesh is adaptive (nearly equilibrated in the energy norm) the  $\eta\%$ -superconvergence regions, which are determined using the methodology of Section 4, are valid for any interior-patch of the mesh.

## 6 Summary of conclusions

We presented the new concept of  $\eta\%$ -superconvergence which enables us to determine the points of least error for the derivatives in elements in the interior of general meshes of quadrilaterals. We conducted a numerical study to determine the applicability of the new concept in practical grids and we arrived at the following conclusions:

1. The regions of  $\eta\%$ -superconvergence in any mesh can be determined by using a computer-based approach. This approach takes directly into account the topol-

ogy of the mesh, the degree  $p$  of the elements and the nature of the solution (harmonic or general).

2. The classical superconvergence points (i.e. the 0%-superconvergence points) in an element are very sensitive to the local geometry of the mesh and in some cases they may not exist.
3. The  $\eta$ %-superconvergence regions for the derivatives in an interior element are robust with respect to the topology of the mesh outside the immediate neighborhood of the element and can always be determined for any class of smooth solutions using the method of freezing the periodicity.
4. For singular solutions computed using quasi-uniform meshes, the pollution error may be significant and  $\eta$ %-superconvergence regions may not exist asymptotically for these meshes. However, for meshes which are nearly equilibrated in the energy norm, the pollution error in the derivatives is negligible and  $\eta$ %-superconvergence regions for the derivatives can be determined in any interior element of the mesh.
5. The position of the superconvergence points for the typical local topologies, as reported here, can be used if the mesh generator creates meshes with a small number of local mesh-topologies as for example in the codes using constrained square meshes with refinements (or mapped meshes).

The methodology presented in this paper can be also employed to study the  $\eta$ %-superconvergence of flux-quantities in finite element approximations of elliptic systems ( $\eta$ %-superconvergence of the gradient of the displacement, strain, stress in elasticity etc.).

## References

1. I. BABUŠKA, T. STROUBOULIS, C.S. UPADHYAY AND S.K. GANGARAJ, *Study of superconvergence by a computer-based approach. Superconvergence of the gradient in the finite element solutions of Laplace's and Poisson's equations*, Technical Note BN-1155, Institute for Physical Science and Technology, University of Maryland, College Park, Maryland, November 1993.
2. I. BABUŠKA, T. STROUBOULIS, AND C.S. UPADHYAY,  $\eta$ %-superconvergence of finite element approximations in the interior of general meshes of triangles, Technical Note BN-1160, Institute for Physical Science and Technology, University of Maryland, College Park, Maryland, December 1993.
3. J. DOUGLAS, JR., T. DUPONT AND M.F. WHEELER, *An  $L^\infty$  estimate and a superconvergence result for a Galerkin method for elliptic equations based on tensor products of piecewise polynomials*, RAIRO Anal. Numér., 8 (1974), pp. 61-66.
4. M. ZLÁMAL, *Superconvergence and reduced integration in the finite element method*, Math. Comp., 32 (1978), pp. 663-685.
5. P. LESANT AND M. ZLÁMAL, *Superconvergence of the gradient of finite element solutions*, RAIRO Anal. Numér., 13 (1979), pp. 139-166.
6. R.Z. DAUTOV, A.V. LAPIN AND A.D. LYASHKO, *Some mesh schemes for quasi-linear elliptic equations*, U.S.S.R. Comput. Math. Math. Phys., 20 (1980), pp. 62-78.
7. M.T. NAKAO, *Superconvergence of the gradient of Galerkin approximations for elliptic problems*, RAIRO Math. Model. Numer. Anal., 21 (1987), pp. 679-695.
8. M. KRÍŽEK AND P. NEITTAANMÄKI, *On superconvergence techniques*, Acta Applic. Math., 9 (1987), pp. 175-198.
9. R. DURÁN, M.A. MUSCHIETTI AND R. RODRÍGUEZ, *Asymptotically exact error estimators for rectangular finite elements*, SIAM J. Numer. Anal., 29 (1992), pp. 78-88.
10. O.C. ZIENKIEWICZ AND J.Z. ZHU, *The superconvergent patch recovery and a posteriori error estimates. Part 1: The recovery technique*, Internat. J. Numer. Methods Engrg., 33 (1992), pp. 1331-1364.
11. O.C. ZIENKIEWICZ AND J.Z. ZHU, *The superconvergence patch recovery (SPR) and adaptive finite element refinement*, Comput. Methods Appl. Mech. Engrg., 101 (1992), pp. 207-224.

12. R.E. EWING AND J. WANG, *Analysis of mixed finite element methods on locally refined grids*, Numer. Math., 63 (1992), pp. 183-194.
13. P.G. CIARLET, *Basic error estimates for elliptic problems*, in: P.G. Ciarlet and J.L. Lions, eds., Handbook of Numerical Analysis, Vol. II, North-Holland, Amsterdam (1991), pp. 17-351.
14. I. BABUŠKA AND A. MILLER, *A feedback finite element method with a-posteriori error estimation: Part I. The finite element method and some basic properties of the a-posteriori error estimator*, Comput. Methods Appl. Mech. Engrg., 61 (1987), pp. 1-40.
15. I. BABUŠKA AND D. YU, *Asymptotically exact a posteriori error estimator for biquadratic elements*, Finite Elements in Analysis and Design, 3 (1987), pp. 341-354.
16. L. DEMKOWICZ, J.T. ODEN, W. RACHOWICZ AND O. HARDY, *Toward a universal adaptive  $h - p$  strategy; Part I, constrained approximation and data structure*, Comput. Methods in Appl. Mech. Engrg., 77 (1987), pp. 79-112.
17. T. STROUBOULIS AND K.A. HAQUE, *Recent experiences with error estimation and adaptivity, Part II: Error estimation for  $h$ -adaptive approximation on grids of triangles and quadrilaterals*, Comput. Methods Appl. Engrg., 100 (1992), pp. 359-430.
18. I. BABUŠKA, T. STROUBOULIS AND C.S. UPADHYAY, *A model study of the quality of a-posteriori estimators for linear elliptic problems: Error estimation in the interior of patchwise uniform grids of triangles*, Comput. Methods Appl. Mech. Engrg. (1994), in press.
19. J.A. NITSCHKE AND A.H. SCHATZ, *Interior estimates for Ritz-Galerkin methods*, Math. Comp. 28 (1974), pp. 937-958.
20. J.H. BRAMBLE, J.A. NITSCHKE AND A.H. SCHATZ, *Maximum-norm estimates for Ritz-Galerkin methods*, Math. Comp. 29 (1975), pp. 677-688.
21. A.H. SCHATZ AND L.B. WAHLBIN, *Interior maximum norm estimates for finite element methods*, Math. Comp. 31 (1977), pp. 414-442.
22. A.H. SCHATZ AND L.B. WAHLBIN, *Maximum norm estimates in the finite element method on plane polygonal domains. Part 1*, Math. Comp. 32 (1978), pp. 73-109.
23. A.H. SCHATZ AND L.B. WAHLBIN, *Maximum norm estimates in the finite element method on plane polygonal domains. Part 2, refinements*, Math. Comp. 33 (1979), pp. 465-492.

24. L.B. WAHLBIN, *Local behavior in finite element methods*, in: P.G. Ciarlet and J.L. Lions, eds., *Handbook of Numerical Analysis*, Vol. II (North-Holland, Amsterdam, 1991), pp. 357-522.
25. I. BABUŠKA AND H.C. ELMAN, *Performance of the h-p versions of the finite element method with various elements*, *Internat. J. Numer. Methods Engrg.* (1993), pp. 2503-2523.
26. I. BABUŠKA, T. STROUBOULIS, A. MATHUR AND C.S. UPADHYAY, *Pollution error in the h-version of the finite-element method and the local quality of a-posteriori error estimators*, in preparation, (1993).

## List of Figures

**Fig. 1.** *h*-refinement for bilinear and biquadratic quadrilaterals: 1-irregular rule. The active nodes are shown with a solid circle and the constrained nodes are indicated by a circle. (a) A mesh-patch of bilinear elements showing the locations of active and constrained nodes; (b) A mesh-patch of biquadratic elements showing the location of active and constrained nodes; (c) The mesh-patch of bilinear quadrilaterals shown in (a) with transition elements; (d) The mesh-patch of biquadratic elements shown in (b) with transition elements.

**Fig. 2.** Locally periodic grid: (a) An *L*-shaped domain with a periodic-mesh subdomain  $S(\mathbf{x}^0, H)$  covered exactly by a periodic array of *h*-cells. The perimeter of the periodic-mesh subdomain  $S(\mathbf{x}^0, H)$  is shown with a thick line; (b) The master-mesh  $\bar{T}$  in the periodic-mesh subdomain  $S(\mathbf{x}^0, H^0)$ .

**Fig. 3.** Method of freezing the periodicity: (a) A finite element mesh of skewed quadrilaterals with the interior mesh-patch  $\omega_0^h$  shown shaded gray and the mesh-patch  $\omega_3^h$  (which includes  $\omega_0^h$  in its interior) shown with thick-black perigram; (b) Extraction of the mesh-patch  $\omega_3^h$  and completion to a periodic mesh in a square-cell; (c) The finite element mesh assumed by the method of freezing the periodicity.

**Fig. 4.** Typical mesh topologies in locally refined meshes: (a) Mesh-interface with constrained nodes; (b) Mesh-interface with transition elements; (c) A periodic mesh with two levels of refinement.

**Fig. 5.** Mesh-interface with constrained nodes: Superconvergence points. (a) Bilinear elements: Zero-lines of  $\frac{\partial \psi_1^H}{\partial x_1}$  (thick-lines) and  $\frac{\partial \psi_1^H}{\partial x_2}$  (thin-lines) intersecting at the points of simultaneous superconvergence for the  $x_1$ - and  $x_2$ -derivatives for the class of harmonic solutions; (b) Bilinear elements: Zero-lines of  $\frac{\partial \psi_1^G}{\partial x_2}$  (thick-lines) and  $\frac{\partial \psi_2^G}{\partial x_2}$  (thin-lines) intersecting at the points of superconvergence for the  $x_2$ -derivative for the class of general solutions; (c) Biquadratic elements: Zero-lines of  $\frac{\partial \psi_1^G}{\partial x_1}$  (thick-lines) and  $\frac{\partial \psi_2^G}{\partial x_2}$  (thin-lines) and their intersections. Note that  $\frac{\partial \psi_1^G}{\partial x_2}$  does not vanish (in the elements of size  $\frac{h}{2}$  but is very small) at these points which are 0.001% superconvergence points.

**Fig. 6.** Rate of convergence at the superconvergence points: Sequence of meshes with a mesh-interface. Meshes with constrained nodes along the interface. The cell-size in the meshes is (a)  $h = 0.25$ ; (b)  $h = 0.125$ ; (c)  $h = 0.0625$ ; (d)  $h = 0.03125$ .

**Fig. 7.** Rate of convergence at the superconvergence points: Sequence of meshes with a mesh-interface. Meshes with transition-elements along the interface. The cell size in the meshes is (a)  $h = 0.25$ ; (b)  $h = 0.125$ ; (c)  $h = 0.0625$ ; (d)  $h = 0.03125$ .



**Fig. 8.** Relative error at the superconvergence points: An adaptive mesh of bilinear elements generated for the exact solution  $u(x_1, x_2) = e^{-k[(x_1-a)^2+(x_2-b)^2]}$  used for the study. (a) An interior patch of elements with a mesh-interface (Patch I) in the finite element mesh; (b) The mesh-patch I with the elements of interest enumerated; (c) An interior patch of elements with a small region with a mesh-interface (Patch II); (d) The mesh-patch II with the elements of interest enumerated.

**Fig. 9.**  $\eta\%$ -superconvergence in periodic meshes with local refinements: Contours of 0%-error and  $\eta\%$ -superconvergence regions for the harmonic monomials of degree  $(p+1)$ . The elements shown shaded gray in the mesh (to the right) are considered. (a)  $C_{\frac{\partial u}{\partial x_1}}^{0\%}(Q^H; \tau, \tilde{T})$  and  $\mathcal{R}_{\frac{\partial u}{\partial x_1}}^{\eta\%}(Q^H; \tau, \tilde{T})$  for  $p = 1$ ; (b)  $C_{\frac{\partial u}{\partial x_1}}^{0\%}(Q^H; \tau, \tilde{T})$  and  $\mathcal{R}_{\frac{\partial u}{\partial x_1}}^{\eta\%}(Q^H; \tau, \tilde{T})$  for  $p = 2$ ; (c)  $C_{\frac{\partial u}{\partial x_2}}^{0\%}(Q^H; \tau, \tilde{T})$  and  $\mathcal{R}_{\frac{\partial u}{\partial x_2}}^{\eta\%}(Q^H; \tau, \tilde{T})$  for  $p = 1$ ; (d)  $C_{\frac{\partial u}{\partial x_2}}^{0\%}(Q^H; \tau, \tilde{T})$  and  $\mathcal{R}_{\frac{\partial u}{\partial x_2}}^{\eta\%}(Q^H; \tau, \tilde{T})$  for  $p = 2$ .

**Fig. 10.**  $\eta\%$ -superconvergence in periodic meshes with local refinements: Mesh with transition elements at the mesh interface. Contours of 0%-error and  $\eta\%$ -superconvergence for the class of harmonic monomials of degree  $(p+1)$ . (a)  $C_{\frac{\partial u}{\partial x_1}}^{0\%}(Q^H; \tau, \tilde{T})$  and  $\mathcal{R}_{\frac{\partial u}{\partial x_1}}^{\eta\%}(Q^H; \tau, \tilde{T})$  for  $p = 1$ ; (b)  $C_{\frac{\partial u}{\partial x_2}}^{0\%}(Q^H; \tau, \tilde{T})$  and  $\mathcal{R}_{\frac{\partial u}{\partial x_2}}^{\eta\%}(Q^H; \tau, \tilde{T})$  for  $p = 1$ ; (c)  $C_{\frac{\partial u}{\partial x_1}}^{0\%}(Q^H; \tau, \tilde{T})$  and  $\mathcal{R}_{\frac{\partial u}{\partial x_1}}^{\eta\%}(Q^H; \tau, \tilde{T})$  for  $p = 2$ ; The thin line is the 0%-error contour for the monomial  $Q_1^H$  and the thick line is the 0%-error contour for the monomial  $Q_2^H$ . Note that in the triangular subelements we have superconvergence points and in the square elements we have bands of superconvergence.

**Fig. 11.**  $\eta\%$ -superconvergence in periodic meshes with local refinements: Mesh with transition elements at the mesh interface. Contours of 0% error and  $\eta\%$ -superconvergence regions for the class of general monomials of degree  $(p+1)$ .

- (a)  $C_{\frac{\partial u}{\partial x_1}}^{0\%}(Q^H; \tau, \tilde{T})$  and  $\mathcal{R}_{\frac{\partial u}{\partial x_1}}^{\eta\%}(Q^H; \tau, \tilde{T})$  for  $p = 1$ ;
- (b)  $C_{\frac{\partial u}{\partial x_2}}^{0\%}(Q^H; \tau, \tilde{T})$  and  $\mathcal{R}_{\frac{\partial u}{\partial x_2}}^{\eta\%}(Q^H; \tau, \tilde{T})$  for  $p = 1$ ;
- (c)  $C_{\frac{\partial u}{\partial x_1}}^{0\%}(Q^H; \tau, \tilde{T})$  and  $\mathcal{R}_{\frac{\partial u}{\partial x_1}}^{\eta\%}(Q^H; \tau, \tilde{T})$  for  $p = 2$ ;
- (d)  $C_{\frac{\partial u}{\partial x_2}}^{0\%}(Q^H; \tau, \tilde{T})$  and  $\mathcal{R}_{\frac{\partial u}{\partial x_2}}^{\eta\%}(Q^H; \tau, \tilde{T})$  for  $p = 2$ .

Note that for  $p = 2$ , there are no regions of  $\eta\%$ -superconvergence for  $\eta\% \leq 5\%$ .

**Fig. 12.**  $\eta\%$ -superconvergence in periodic meshes with local refinements as shown in Fig. 4c. Contours of 0% error and  $\eta\%$ -superconvergence regions for the class of harmonic monomials of degree  $(p+1)$ . (a)  $C_{\frac{\partial u}{\partial x_1}}^{0\%}(Q^H; \tau, \tilde{T})$  and  $\mathcal{R}_{\frac{\partial u}{\partial x_1}}^{\eta\%}(Q^H; \tau, \tilde{T})$  for  $p = 1$ ; (b)  $C_{\frac{\partial u}{\partial x_2}}^{0\%}(Q^H; \tau, \tilde{T})$  and  $\mathcal{R}_{\frac{\partial u}{\partial x_2}}^{\eta\%}(Q^H; \tau, \tilde{T})$  for  $p = 2$ ; (c)  $C_{\frac{\partial u}{\partial x_1}}^{0\%}(Q^H; \tau, \tilde{T})$  and  $\mathcal{R}_{\frac{\partial u}{\partial x_1}}^{\eta\%}(Q^H; \tau, \tilde{T})$  for  $p = 1$ ; (d)  $C_{\frac{\partial u}{\partial x_2}}^{0\%}(Q^H; \tau, \tilde{T})$  and  $\mathcal{R}_{\frac{\partial u}{\partial x_2}}^{\eta\%}(Q^H; \tau, \tilde{T})$  for  $p = 2$ . The thin line corresponds to the 0%-error contour for the monomial  $Q_1^H$  and the thick line corresponds to the

0%-contour for the monomial  $Q_2^H$ . Note that in some elements, the  $\eta\%$  at the Gauss-Legendre point is more than 25%.

**Fig. 13.**  $\eta\%$ -superconvergence for general meshes with local refinements: Adaptive mesh of bilinear square elements generated using the exact solution  $u(x_1, x_2) = e^{-k[(x_1-a)^2+(x_2-b)^2]}$ ,  $k = 10$ . (a) The finite element mesh  $T_h$  in the domain  $\Omega$ . The interior mesh-patch of interest is shown with a thick perigram; (b) The interior mesh-patch of interest (shown in (a)) is shown with the elements in which superconvergence is studied (shown with gray shading); (c) The periodic mesh  $\tilde{T}$  obtained by completing the patch of interest. The patch of elements in which superconvergence is studied are shown with gray shading.

**Fig. 14.**  $\eta\%$ -superconvergence for general meshes with local refinements: Adaptive mesh of bilinear square elements shown in Fig. 13a. (a)  $\eta\%$ -superconvergence regions  $\mathcal{R}_{\frac{\partial u}{\partial x_1}}^{\eta\%}(Q^H; \tau_i, \tilde{T})$  for the harmonic solutions in the elements marked gray in the periodic mesh  $\tilde{T}$  shown in Fig. 13c; (b) Bands of  $\eta\%$ -relative error for the exact solution  $u(x_1, x_2) = \sin(\pi x_1) \sinh(\pi x_2)$  in the elements marked gray in the finite element mesh  $T_h$  as shown in Fig. 13b. Note that the  $\eta\%$ -superconvergence regions shown in (a) are very similar to the bands of  $\eta\%$ -relative error shown in (b).

**Fig. 15.**  $\eta\%$ -superconvergence for general meshes with local refinements: Adaptive mesh of bilinear elements shown in Fig. 13a. (a) Bands of  $\eta\%$ -relative error  $\mathcal{B}_{\frac{\partial u}{\partial x_1}}^{\eta\%}(u; \tau, T_h)$  for the exact solution  $u(x_1, x_2) = e^{-k[(x_1-a)^2+(x_2-b)^2]}$  where  $k = 10$  and  $(a, b) = (0.5, 0.5)$  computed by solving the Neumann problem in the mesh shown in Fig. 13a. The bands of  $\eta\%$ -relative error shown for the elements marked gray in Fig. 13b; (b) Bands of  $\eta\%$ -relative error  $\mathcal{B}_{\frac{\partial u}{\partial x_1}}^{\eta\%}(Q; \tau, \tilde{T})$  for the Taylor series expansion of  $u$  computed by solving the periodic boundary-value problem in the periodic mesh  $\tilde{T}$  shown in Fig. 13c. The bands of  $\eta\%$ -relative error shown for the elements marked gray in Fig. 13c. Note that the bands of  $\eta\%$ -relative error computed from the finite element solution are very similar to the bands of  $\eta\%$ -relative error computed from the periodic boundary-value problem.

**Fig. 16.**  $\eta\%$ -superconvergence for general meshes with local refinements: Adaptive mesh of bilinear square elements shown in Fig. 13a: (a) Bands of  $\eta\%$ -relative error  $\mathcal{B}_{\frac{\partial u}{\partial x_1}}^{\eta\%}(u; \tau, T_h)$  for the exact solution  $u(x_1, x_2) = e^{-k[(x_1-a)^2+(x_2-b)^2]}$  where  $k = 10$  and  $(a, b) = (-0.65, -0.30)$  computed by solving the Neumann problem in the mesh shown in Fig. 13a. The bands of  $\eta\%$ -relative error shown for the elements marked gray in Fig. 13b; (b) Bands of  $\eta\%$ -relative error  $\mathcal{B}_{\frac{\partial u}{\partial x_1}}^{\eta\%}(Q; \tau, \tilde{T})$  for the Taylor series expansion of  $u$  computed by solving the periodic boundary-value problem in the periodic mesh  $\tilde{T}$  shown in Fig. 13c. Note that the bands obtained from the above figures are very similar.

Fig. 17.  $\eta\%$ -superconvergence for general meshes with local refinements: Adaptive mesh of bilinear square elements shown in Fig. 13a: (a) Bands of  $\eta\%$ -relative error  $B_{\frac{\partial u}{\partial x_1}}^{\eta\%}(u; \tau, T_h)$  for the exact solution  $u(x_1, x_2) = e^{-k[(x_1-a)^2 + (x_2-b)^2]}$  where  $k = 10$  and  $(a, b) = (0.25, 0.35)$  computed by solving the Neumann problem in the mesh shown in Fig. 13a. The bands of  $\eta\%$ -relative error shown for the elements marked gray in Fig. 13b; (b) Bands of  $\eta\%$ -relative error  $B_{\frac{\partial u}{\partial x_1}}^{\eta\%}(Q; \tau, \tilde{T})$  for the Taylor series expansion of  $u$  computed by solving the periodic boundary-value problem in the periodic mesh  $\tilde{T}$  shown in Fig. 13c. Note that the bands of  $\eta\%$ -relative error given in the above two figures are very similar.

Fig. 18.  $\eta\%$ -superconvergence for general meshes with local refinements: Adaptive mesh of bilinear square elements shown in Fig. 13b. Regions of  $\eta\%$ -superconvergence  $\mathcal{R}_{\frac{\partial u}{\partial x_1}}^{\eta\%}(Q^G; \tau, \tilde{T})$  for the general solutions in the elements marked gray in the periodic mesh  $\tilde{T}$  (shown in Fig. 13c). Note that regions are shown for  $\eta\% = 10\%, 30\%, 50\%$  and that in some elements the regions do not exist for  $\eta\% \leq 25\%$ .

Fig. 19.  $\eta\%$ -superconvergence for a grid generated by a mesh generator: Mesh of skewed quadrilaterals generated by converting a mesh of triangles. (a) The finite element mesh in the domain. The patch of elements in which superconvergence is studied are marked with gray shading. The patch surrounding these elements is shown with a thick perigram. (b) The patch of elements shown in (a); (c) The periodic mesh  $\tilde{T}$  generated by completing the patch shown in (b).

Fig. 20.  $\eta\%$ -superconvergence for a grid generated by a mesh generator: Mesh of skewed quadrilaterals generated by converting a mesh of triangles. (a) The finite element mesh in the domain. The patch of elements in which superconvergence is studied are shown with gray shading. The mesh patch surrounding these elements is shown with a thick perigram; (b) The patch of elements marked in (a); (c) The periodic mesh  $\tilde{T}$  generated by completing the patch shown in (b).

Fig. 21.  $\eta\%$ -superconvergence for a grid of skewed quadrilaterals generated by a mesh generator: Elements shown with gray shading in Fig. 19a. Contours of 25%-relative error for the four solutions given in Section 5.6. The regions of 25%-relative error which are common to the four solutions are shaded gray. Bilinear elements ( $p = 1$ ). (a) Contours of 25%-relative error and 25%-common regions for the  $x_1$ -derivative computed by solving the problem P1 (Neumann problem with data consistent with the exact solution); (b) Contours of 25%-relative error and 25%-common regions for the  $x_1$ -derivative computed by solving the problem P2 (Neumann problem with data consistent with Taylor series expansion); (c) Contours of 25%-relative error and 25%-common regions for the  $x_1$ -derivative computed by solving the problem P3 (Periodic boundary-value problem with Taylor series expansion); (d) Contours of 25%-relative error and 25%-common regions for the  $x_2$ -derivative computed by solving problem P1 (Neumann problem over the entire domain); (e) Contours of 25%-relative error

and 25%-common regions for the  $x_2$ -derivative computed by solving the problem P2 (Neumann problem with data consistent with Taylor series expansion); (f) Contours of 25%-relative error and 25%-common regions for the  $x_2$ -derivative computed by solving the problem P3 (Periodic boundary-value problem with Taylor series expansion); (g)  $\eta\%$ -superconvergence regions  $\mathcal{R}_{\frac{\partial u}{\partial x_1}}^{\eta\%}(Q^H; \tau, \tilde{T})$  for the  $x_1$ -derivative for the harmonic solutions of degree 2. (h)  $\eta\%$ -superconvergence regions  $\mathcal{R}_{\frac{\partial u}{\partial x_2}}^{\eta\%}(Q^H; \tau, \tilde{T})$  for the  $x_2$ -derivative of the error for the harmonic solutions of degree 2. Note that Figures (a), (b) and (c) (resp. Figures (d), (e) and (f)) are, for all practical purposes, identical.

**Fig. 22.**  $\eta\%$ -superconvergence for a grid of skewed quadrialterals generated by a mesh generator: Elements shown with gray shading in Fig. 20a. Contours of 25%-relative error for the four solutions given in Section 5.6. The regions of 25%-relative error which are common to the four solutions are shaded gray. Bilinear elements ( $p = 1$ ). (a) Contours of 25%-relative error and 25%-common regions for the  $x_1$ -derivative computed by solving the problem P1 (Neumann problem with data consistent with the exact solution); (b) Contours of 25%-relative error and 25%-common regions for the  $x_1$ -derivative computed by solving the problem P2 (Neumann problem with data consistent with Taylor series expansion); (c) Contours of 25%-relative error and 25%-common regions for the  $x_1$ -derivative computed by solving the problem P3 (Periodic boundary-value problem with Taylor series expansion); (d) Contours of 25%-relative error and 25%-common regions for the  $x_2$ -derivative computed by solving problem P1 (Neumann problem over the entire domain); (e) Contours of 25%-relative error and 25%-common regions for the  $x_2$ -derivative computed by solving the problem P2 (Neumann problem with data consistent with Taylor series expansion); (f) Contours of 25%-relative error and 25%-common regions for the  $x_2$ -derivative computed by solving the problem P3 (Periodic boundary-value problem with Taylor series expansion); (g)  $\eta\%$ -superconvergence regions  $\mathcal{R}_{\frac{\partial u}{\partial x_1}}^{\eta\%}(Q^H; \tau, \tilde{T})$  for the  $x_1$ -derivative for the harmonic solutions of degree 2. (h)  $\eta\%$ -superconvergence regions  $\mathcal{R}_{\frac{\partial u}{\partial x_2}}^{\eta\%}(Q^H; \tau, \tilde{T})$  for the  $x_2$ -derivative of the error for the harmonic solutions of degree 2. Note that Figures (a), (b) and (c) (resp. Figures (d), (e) and (f)) are, for all practical purposes, identical.

**Fig. 23.** Pollution effect and  $\eta\%$ -superconvergence for singular solutions:  $L$ -shaped domain.

**Fig. 24.** Pollution effect and  $\eta\%$ -superconvergence for singular solutions:  $L$ -shaped domain meshed with a uniform mesh of square elements. (a) Subdomain A; (b) Subdomain B.

**Fig. 25.** Pollution effect and  $\eta\%$ -superconvergence for singular solutions:  $L$ -shaped domain meshed with a uniform mesh of squares; exact solution  $u(r, \theta) = r^{\frac{2}{3}} \sin \frac{2}{3} \theta$ ; bilinear elements ( $p = 1$ ). Bands of  $\eta\%$ -relative error for the  $x_1$ -derivative  $B_{\frac{\partial u}{\partial x_1}}^{\eta\%}(u; \tau, T_h)$

for the elements in: (a) Subdomain A with element size  $h$ ; (b) Subdomain A with element size  $\frac{h}{2}$ ; (c) Subdomain A with element size  $\frac{h}{4}$ ; (d) Subdomain B with element size  $h$ ; (e) Subdomain B with element size  $\frac{h}{2}$ ; (f) Subdomain B with element size  $\frac{h}{4}$ . Note that as the element size is decreased the bands converge to the bands predicted by the methodology of Section 4.

**Fig. 26.** Pollution effect and  $\eta\%$ -superconvergence for singular solutions:  $L$ -shaped domain meshed with a uniform mesh of squares. Exact solution  $u(r, \theta) = r^{\frac{1}{3}} \sin \frac{1}{3}\theta$ ,  $p = 1$ . Bands of  $\eta\%$ -relative error for the  $x_1$ -derivative  $B_{\frac{\partial u}{\partial x_1}}^{\eta\%}(u; \tau, T_h)$  for the elements in: (a) Subdomain A with element size  $h$ ; (b) Subdomain A with element size  $\frac{h}{2}$ ; (c) Subdomain A with element size  $\frac{h}{4}$ ; (d) Subdomain B with element size  $h$ ; (e) Subdomain B with element size  $\frac{h}{2}$ ; (f) Subdomain B with element size  $\frac{h}{4}$ . Note that as the element size is decreased the bands of 25%-relative error disappear.

**Fig. 27.** Pollution effect and  $\eta\%$ -superconvergence for singular solutions:  $L$ -shaped domain; exact solution  $u(r, \theta) = r^{\frac{2}{3}} \sin \frac{2}{3}\theta$ ; bilinear elements ( $p = 1$ ). (a) Adaptive mesh of square elements (nearly equilibrated in the energy norm). The patch of elements in which superconvergence is studied are shown with gray shading. The patch surrounding these elements is marked with a thick perigram (Patch P); (b) Periodic mesh  $\tilde{T}$  obtained by completing the interior patch shown in (a).

**Fig. 28.** Pollution effect and  $\eta\%$ -superconvergence for singular solutions:  $L$ -shaped domain; exact solution  $u(r, \theta) = r^{\frac{2}{3}} \sin \frac{2}{3}\theta$ ; bilinear elements ( $p = 1$ ). (a) Adaptive mesh of square elements (nearly equilibrated in the energy norm). The patch of elements in which superconvergence is studied are shown with gray shading. The patch surrounding these elements is marked with a thick perigram (Patch Q); (b) Periodic mesh  $\tilde{T}$  obtained by completing the interior patch shown in (a).

**Fig. 29.** Pollution effect and  $\eta\%$ -superconvergence for singular solutions:  $L$ -shaped domain; exact solution  $u(r, \theta) = r^{\frac{2}{3}} \sin \frac{2}{3}\theta$ ; bilinear elements ( $p = 1$ ). The patch of elements shown with gray shading in Fig. 27a (Patch P). (a) Bands of  $\eta\%$ -relative error for the  $x_1$ -derivative  $B_{\frac{\partial u}{\partial x_1}}^{\eta\%}(u; \tau, T_h)$  computed by solving the finite element problem for elements in Patch P; (b) Bands of  $\eta\%$ -relative error for the  $x_1$ -derivative  $B_{\frac{\partial u}{\partial x_1}}^{\eta\%}(Q; \tau, \tilde{T})$  computed by solving the periodic boundary-value problem with data consistent with the Taylor series expansion of  $u$ .

**Fig. 30.** Pollution effect and  $\eta\%$ -superconvergence for singular solutions:  $L$ -shaped domain; exact solution  $u(r, \theta) = r^{\frac{1}{3}} \sin \frac{2}{3}\theta$ ; bilinear elements ( $p = 1$ ). The patch of elements shown with gray shading in Fig. 28a (Patch Q). (a) Bands of  $\eta\%$ -relative error for the  $x_1$ -derivative  $B_{\frac{\partial u}{\partial x_1}}^{\eta\%}(u; \tau, T_h)$  computed by solving the finite element problem for elements in Patch Q; (b) Bands of  $\eta\%$ -relative error for the  $x_1$ -derivative  $B_{\frac{\partial u}{\partial x_1}}^{\eta\%}(Q; \tau, \tilde{T})$  computed by solving the periodic boundary-value problem with data consistent with the Taylor series expansion of  $u$ .

**Fig. 31.** Pollution effect and  $\eta\%$ -superconvergence for singular solutions:  $L$ -shaped domain; exact solution  $u(r, \theta) = r^{\frac{1}{3}} \sin \frac{1}{3}\theta$ ; bilinear elements ( $p = 1$ ). (a) Adaptive mesh of square elements (nearly equilibrated in the energy norm). The patch of elements in which superconvergence is studied are shown with gray shading. The patch surrounding these elements is marked with a thick perigram. (b) Periodic mesh  $\tilde{T}$  obtained by completing the interior patch shown in (a).

**Fig. 32.** Pollution effect and  $\eta\%$ -superconvergence for singular solutions:  $L$ -shaped domain. Exact solution  $u(r, \theta) = r^{\frac{1}{3}} \sin \frac{1}{3}\theta$ .  $p = 1$ . (a) Adaptive mesh of square elements (nearly equilibrated in the energy norm). The elements in which superconvergence is studied are shown with gray shading. The patch surrounding these elements is marked with a thick perigram. (b) Periodic mesh  $\tilde{T}$  obtained by completing the interior patch shown in (a).

**Fig. 33.** Pollution effect and  $\eta\%$ -superconvergence for singular solutions:  $L$ -shaped domain; exact solution  $u(r, \theta) = r^{\frac{1}{3}} \sin \frac{1}{3}\theta$ ; bilinear elements ( $p = 1$ ). The patch of elements shown with gray shading in Fig. 31a. (a) Bands of  $\eta\%$ -relative error for the  $x_1$ -derivative  $B_{\frac{\partial u}{\partial x_1}}^{\eta\%}(u; \tau, T_h)$  computed by solving the finite element problem; (b) Bands of  $\eta\%$ -relative error for the  $x_1$ -derivative  $B_{\frac{\partial u}{\partial x_1}}^{\eta\%}(u; \tau, \tilde{T})$  computed by solving the periodic boundary-value problem with data consistent with Taylor series expansion of  $r^{\frac{1}{3}} \sin \frac{1}{3}\theta$ .

**Fig. 34.** Pollution effect and  $\eta\%$ -superconvergence for singular solutions:  $L$ -shaped domain; exact solution  $u(r, \theta) = r^{\frac{1}{3}} \sin \frac{1}{3}\theta$ ; bilinear elements ( $p = 1$ ). Elements shown with gray shading in Fig. 32a. (a) Bands of  $\eta\%$ -relative error for the  $x_1$ -derivative  $B_{\frac{\partial u}{\partial x_1}}^{\eta\%}(u; \tau, T_h)$  computed by solving the finite element problem; (b) Bands of  $\eta\%$ -relative error for the  $x_1$ -derivative  $B_{\frac{\partial u}{\partial x_1}}^{\eta\%}(u; \tau, \tilde{T})$  computed by solving the periodic boundary-value problem with data consistent with Taylor series expansion of  $r^{\frac{1}{3}} \sin \frac{1}{3}\theta$ .

Simultaneous superconvergence points for the $x_1$ - and $x_2$ -derivatives in the elements near the mesh-interface of Fig. 4a		
Element	$p = 1$	$p = 2$
$\tau_1$	( 0.3449514150, 0.189895754)	(-.2378069181, -.5773502692) (-.5421972529, .5773502692) (.6071187677, .5773502692)
$\tau_2$	(-0.3449514150, 0.189895754)	(.2378069181, -.5773502692) (-.6071187677, -.5773502692) (.5421972529, .5773502692)
$\tau_3$	( 0.0000001171, 0.000000000)	(-.6111972936, -.5773502692) (.5449056851, -.5773502692) (.5773502692, .5773502692) (-.5773502692, .5773502692)
$\tau_4$	(-0.0000001171, 0.000000000)	(.6111972936, -.5773502692) (-.5449056851, -.5773502692) (.5773502692, .5773502692) (-.5773502692, .5773502692)

**Table 1.** Superconvergence points in the elements near the mesh-interface with constrained nodes: Master element coordinates of the points for the elements shown in Fig. 4a. The points of simultaneous superconvergence for the  $x_1$ - and  $x_2$ -derivatives are given. Note that for  $p = 1$ , the superconvergence points in  $\tau_1$  and  $\tau_2$  are not close to the center of the element and that for  $p = 2$ , there are only three superconvergence points in the elements  $\tau_1$  and  $\tau_2$ . The points for  $p = 2$  are  $\eta\%$ -superconvergence points with  $\eta\% \leq 0.001\%$ .

Superconvergence points for the $x_1$ -, $x_2$ -derivative in the elements near the mesh-interface of Fig. 4b; linear elements				
Element	$\chi_{\frac{\partial}{\partial x_1}}^{\text{sup}}(Q^H; \tau_i, \tilde{T})$	$\chi_{\frac{\partial}{\partial x_1}}^{\text{sup}}(Q^G; \tau_i, \tilde{T})$	$\chi_{\frac{\partial}{\partial x_2}}^{\text{sup}}(Q^H; \tau_i, \tilde{T})$	$\chi_{\frac{\partial}{\partial x_2}}^{\text{sup}}(Q^G; \tau_i, \tilde{T})$
$\tau_1$	(0.5000000000, 0.5000000000)	YES	(0.2219334168, 0.2291334168)	NO
$\tau_2$	(0.0000000000, 0.6500546310)	NO	(0.7743219764, 0.0000000000)	NO
$\tau_3$	(0.6500546310, 0.0000000000)	NO	(0.0000000000, 0.7743219764)	NO
$\tau_4$	(0.0000000000, 0.9038367177)	YES	(-0.4759591794, 0.0000004630)	YES
$\tau_5$	(0.0000000000, 0.9038367177)	YES	(0.4759591794, 0.0000004630)	YES
$\tau_6$	(0.0000000000, 0.8164965809)	YES	(0.0000000100, 0.0000000000)	YES
$\tau_7$	(0.0000000000, 0.8164965809)	YES	(-0.0000000100, 0.0000000000)	YES

**Table 2a.** Superconvergence points in the elements near the mesh-interface with transition elements: Master element coordinates of the points for the elements shown in Fig. 4b; linear elements. The superconvergence points for the triangular sub-elements are given in the master-element coordinates of each triangle. The points which are also superconvergence points for the general solutions are indicated by "yes".



Superconvergence points for the $x_1$ -, $x_2$ -derivative in the elements near the mesh-interface of Fig. 4b; quadratic elements				
Element	$\chi_{\frac{\partial}{\partial x_1}}^{\text{sup}}(Q^H; \tau_i, \tilde{T})$	$\chi_{\frac{\partial}{\partial x_1}}^{\text{sup}}(Q^G; \tau_i, \tilde{T})$	$\chi_{\frac{\partial}{\partial x_2}}^{\text{sup}}(Q^H; \tau_i, \tilde{T})$	$\chi_{\frac{\partial}{\partial x_2}}^{\text{sup}}(Q^G; \tau_i, \tilde{T})$
$\tau_1$	(0.6346980477, 0.2686462265);	NO	(0.3376461192, 0.3623896091);	NO
	(0.2686462265, 0.6346980477);	NO	(0.0555703987, 0.0555703987);	NO
	(0.3978751334, 0.3978751334);	NO		
	(0.2960013625, 0.2960013625);	NO		
$\tau_2$	(0.2728756106, 0.2305710433);	NO	(0.0000000000, 0.1358925622);	NO
	(0.6495869087, 0.3168545738);	NO	(0.0000000000, 0.7973549868);	NO
			(0.2899495590, 0.4545768446);	NO
			(0.4561334539, 0.2890038707);	NO
$\tau_3$	(0.2305710433, 0.2728756106);	NO	(0.1358925622, 0.0000000000);	NO
	(0.3168545738, 0.6495869087);	NO	(0.7973549868, 0.0000000000);	NO
			(0.4545768446, 0.2899495590);	NO
			(0.2890038707, 0.4561334539);	NO
$\tau_4$	(0.5779800281, -0.1233185871);	NO	(1.0000000000, -0.7250525375);	NO
	(-0.5783530068, 0.0846847343);	NO	(1.0000000000, 0.5795077940);	NO
	(-0.5775012409, 0.9724859376);	NO	(-1.0000000000, 0.5546779289);	NO
			(-1.0000000000, 0.4051347137)	NO

Table 2b. Superconvergence points for the elements near the mesh-interface with transition elements: Master element coordinates of the points for the elements shown in Fig. 4b; quadratic elements. The superconvergence points for the triangular sub-elements are given in the master-element coordinates of each triangle. The points which are also superconvergence points for the general solutions are indicated by "yes". Note that there are no superconvergence points for the class of general solutions.

Simultaneous superconvergence points for the $x_1$ - and $x_2$ -derivatives for the mesh of Fig. 4c	
Bilinear elements	
Element	$\chi_{\frac{\partial^2}{\partial x_2^2}}^{\text{sup}}(Q^G; \tau_i, \tilde{T}) \cap \chi_{\frac{\partial^2}{\partial x_1^2}}^{\text{sup}}(Q^G; \tau_i, \tilde{T})$
$\tau_5$	( 1.0000000000, 1.0000000000)
$\tau_8$	( 0.6000010117, 0.2000010310)
$\tau_9$	( 0.2000001110, 0.6000000313)
$\tau_{10}$	(-1.0000000000, 1.0000000000)
$\tau_{11}$	(-0.6000010117, -0.1999987998)
$\tau_{12}$	( 0.6000010117, -0.1999987998)
$\tau_{13}$	( 1.0000000000, 1.0000000000)
$\tau_{14}$	(-0.2000001110, -0.6000000313)
$\tau_{15}$	(-1.0000000000, -1.0000000000)
$\tau_{16}$	(-1.0000000000, 1.0000000000)
$\tau_{17}$	(-1.0000000000, -1.0000000000)
$\tau_{18}$	( 0.2000001110, -0.6000000313)
$\tau_{19}$	(-1.0000000000, 1.0000000000)
$\tau_{20}$	(-1.0000000000, -1.0000000000)
$\tau_{21}$	( 1.0000000000, -1.0000000000)

**Table 3.** Superconvergence points for a periodic mesh with several refinements: Master element coordinates of the points in the elements of the mesh shown in Fig. 4c; bilinear elements. The points of simultaneous superconvergence for the  $x_1$ - and  $x_2$ -derivatives are given. Here we report the coordinates of the superconvergence points which are distinct from the Gauss-Legendre points. Note that for some elements the superconvergence points are at the vertex of the element.

Grid with mesh-interface with constrained nodes				
Bilinear elements				
Cell-size $h$	Gauss-Legendre Points		Superconvergence points from Table 1	
	$\left  \frac{\partial e_h}{\partial x_1} \right _{G-L}$	$\left  \frac{\partial e_h}{\partial x_1} \right _{G-L} h^{-1}$	$\left  \frac{\partial e_h}{\partial x_1} \right _{\text{sup}}$	$\left  \frac{\partial e_h}{\partial x_1} \right _{\text{sup}} h^{-2}$
Element of size $\frac{h}{2}$ at the mesh-interface				
0.25000	.57517440E+00	2.30	.17657086E+00	2.83
0.12500	.31086194E+00	2.49	.38090653E-01	2.44
0.06250	.15849922E+00	2.54	.86690122E-02	2.22
0.03125	.79755480E-01	2.55	.21457579E-02	2.20
Element of size $\frac{h}{2}$ one layer away from the mesh-interface				
0.25000	.77153390E-01	0.31	.77003693E-01	1.23
0.12500	.34914069E-01	0.28	.19916182E-01	1.28
0.06250	.16510365E-01	0.27	.52710414E-02	1.35
0.03125	.77883456E-02	0.25	.13379941E-02	1.37

**Table 4a.** Rate of convergence at the superconvergence points: Grids with mesh-interface with constrained nodes shown in Figs. 6a-6d, exact solution  $u(x_1, x_2) = \sin(\pi x_1) \sinh(\pi x_2)$ , bilinear elements ( $p = 1$ ). The values of  $\left| \frac{\partial e_h}{\partial x_1} \right|$  at the Gauss-Legendre points and the superconvergence points (from Table 1) are given in the square elements of size  $\frac{h}{2}$  at the mesh-interface and one layer away from the mesh-interface are given.

Grid with mesh-interface with constrained nodes				
Biquadratic elements				
Cell-size $h$	Gauss-Legendre Points		Superconvergence points from Table 1	
	$\left  \frac{\partial e_h}{\partial x_1} \right _{G-L}$	$\left  \frac{\partial e_h}{\partial x_1} \right _{G-L} h^{-2}$	$\left  \frac{\partial e_h}{\partial x_1} \right _{sup}$	$\left  \frac{\partial e_h}{\partial x_1} \right _{sup} h^{-3}$
Element of size $\frac{h}{2}$ at the mesh-interface				
0.25000	.35616628E-01	0.57	.34981651E-01	2.24
0.12500	.45941576E-02	0.29	.33414467E-02	1.71
0.06250	.10988098E-02	0.28	.41561324E-03	1.70
0.03125	.26815619E-03	0.28	.51379346E-04	1.69
Element of size $\frac{h}{2}$ one layer away from the mesh-interface				
0.25000	.76959609E-02	0.12	.76081781E-02	0.49
0.12500	.72206159E-03	0.05	.66641794E-03	0.34
0.06250	.16100891E-03	0.04	.68416871E-04	0.28
0.03125	.40986412E-04	0.04	.80145619E-05	0.26

**Table 4b.** Rate of convergence at the superconvergence points: Grids with mesh-interface with constrained nodes shown in Figs. 6a-6d, exact solution  $u(x_1, x_2) = \sin(\pi x_1) \sinh(\pi x_2)$ , biquadratic elements ( $p = 2$ ). The maximum values of  $\left| \frac{\partial e_h}{\partial x_1} \right|$  at the Gauss-Legendre points and the superconvergence points (from Table 1) are given in the square elements of size  $\frac{h}{2}$  at the mesh-interface and one layer away from the mesh-interface are given.

Grid with mesh-interface with constrained nodes				
Bilinear elements				
Cell-size $h$	Gauss-Legendre Points		Superconvergence points from Table 1	
	$\left  \frac{\partial e_h}{\partial x_2} \right _{G-L}$	$\left  \frac{\partial e_h}{\partial x_2} \right _{G-L} h^{-2}$	$\left  \frac{\partial e_h}{\partial x_2} \right _{sup}$	$\left  \frac{\partial e_h}{\partial x_2} \right _{sup} h^{-2}$
Element of size $\frac{h}{2}$ at the mesh-interface				
0.25000	.95499223E-01	1.52	.14953978E+00	2.39
0.12500	.20029031E-01	1.28	.32446341E-01	2.08
0.06250	.44797614E-02	1.15	.74421844E-02	1.91
0.03125	.11031333E-02	1.13	.18400167E-02	1.88
Element of size $\frac{h}{2}$ one layer away from the mesh-interface				
0.25000	.99972051E-01	1.60	.99972059E-01	1.60
0.12500	.21907125E-01	1.40	.20028986E-01	1.28
0.06250	.47790173E-02	1.22	.45774021E-02	1.17
0.03125	.11739024E-02	1.20	.11421790E-02	1.17

**Table 5a.** Rate of convergence at the superconvergence points: Grids with mesh-interface with constrained nodes shown in Figs. 6a-6d, exact solution  $u(x_1, x_2) = \sin(\pi x_1) \sinh(\pi x_2)$ , bilinear elements ( $p = 1$ ). The values of  $\left| \frac{\partial e_h}{\partial x_2} \right|$  at the Gauss-Legendre points and the superconvergence points (from Table 1) are given in the square elements of size  $\frac{h}{2}$  at the mesh-interface and one layer away from the mesh-interface are given.

Grid with mesh-interface with constrained nodes				
Biquadratic elements				
Cell-size $h$	Gauss-Legendre Points		Superconvergence points from Table 1	
	$\left  \frac{\partial e_h}{\partial x_2} \right _{G-L}$	$\left  \frac{\partial e_h}{\partial x_2} \right _{G-L} h^{-3}$	$\left  \frac{\partial e_h}{\partial x_2} \right _{sup}$	$\left  \frac{\partial e_h}{\partial x_2} \right _{sup} h^{-3}$
Element of size $\frac{h}{2}$ at the mesh-interface				
0.25000	.29600593E-01	1.72	.23262232E-01	1.49
0.12500	.36423052E-02	1.87	.29870942E-02	1.53
0.06250	.44509815E-03	1.82	.37367439E-03	1.53
0.03125	.55001651E-04	1.80	.46708914E-04	1.53
Element of size $\frac{h}{2}$ one layer away from the mesh-interface				
0.25000	.52147491E-02	0.33	.52147491E-02	0.33
0.12500	.38514170E-03	0.20	.38514162E-03	0.20
0.06250	.35773791E-04	0.15	.35773789E-04	0.15
0.03125	.46018761E-05	0.15	.46049812E-05	0.15

**Table 5b.** Rate of convergence at the superconvergence points: Grids with mesh-interface with constrained nodes shown in Figs. 6a-6d, exact solution  $u(x_1, x_2) = \sin(\pi x_1) \sinh(\pi x_2)$ , biquadratic elements ( $p = 2$ ). The maximum values of  $\left| \frac{\partial e_h}{\partial x_2} \right|$  at the Gauss-Legendre points and the superconvergence points (from Table 1) are given in the square elements of size  $\frac{h}{2}$  at the mesh-interface and one layer away from the mesh-interface are given.

Grid with mesh-interface with transition elements				
Linear elements				
Cell-size $h$	Gauss-Legendre Points		Superconvergence points from Table 1	
	$\left  \frac{\partial e_h}{\partial x_1} \right _{G-L}$	$\left  \frac{\partial e_h}{\partial x_1} \right _{G-L} h^{-1}$	$\left  \frac{\partial e_h}{\partial x_1} \right _{sup}$	$\left  \frac{\partial e_h}{\partial x_1} \right _{sup} h^{-2}$
Element of size $\frac{h}{2}$ at the mesh-interface				
0.25000	.26294012E-01	0.11	.71260207E-01	1.14
0.12500	.10959010E-01	0.09	.10239329E-01	0.66
0.06250	.98340266E-02	0.16	.20809826E-02	0.53
0.03125	.60270808E-02	0.19	.53221772E-03	0.54
Element of size $\frac{h}{2}$ one layer away from the mesh-interface				
0.25000	.24196256E-01	0.10	.53080555E-01	0.85
0.12500	.60704882E-02	0.05	.74038127E-02	0.47
0.06250	.16056918E-02	0.03	.88662264E-03	0.23
0.03125	.10302041E-02	0.03	.23838655E-03	0.24

**Table 6a.** Rate of convergence at the superconvergence points: Grids with mesh-interface with transition elements shown in Figs. 7a-7d, exact solution  $u(x_1, x_2) = \sin(\pi x_1) \sinh(\pi x_2)$ , linear elements ( $p = 1$ ). The values of  $\left| \frac{\partial e_h}{\partial x_1} \right|$  at the Gauss-Legendre points and the superconvergence points (from Tables 2a, 2b) are given in the square elements of size  $\frac{h}{2}$  at the mesh-interface and one layer away from the mesh-interface are given.

Grid with mesh-interface with transition elements				
Quadratic elements				
Cell-size $h$	Gauss-Legendre Points		Superconvergence points from Table 1	
	$\left  \frac{\partial e_h}{\partial x_1} \right _{G-L}$	$\left  \frac{\partial e_h}{\partial x_1} \right _{G-L} h^{-2}$	$\left  \frac{\partial e_h}{\partial x_1} \right _{\text{sup}}$	$\left  \frac{\partial e_h}{\partial x_1} \right _{\text{sup}} h^{-3}$
Element of size $\frac{h}{2}$ at the mesh-interface				
0.25000	.40118091E-01	0.64	.44601274E-01	2.86
0.12500	.11331178E-01	0.73	.11754109E-01	6.01
0.06250	.30112286E-02	0.77	.10030098E-02	4.11
0.03125	.74461581E-03	0.77	.12576887E-03	4.12
Element of size $\frac{h}{2}$ one layer away from the mesh-interface				
0.25000	.64905047E-02	0.10	.71044126E-02	0.45
0.12500	.10139819E-02	0.07	.11000841E-02	0.56
0.06250	.24176022E-03	0.06	.17214310E-03	0.71
0.03125	.53840918E-04	0.06	.21691406E-04	0.71

**Table 6b.** Rate of convergence at the superconvergence points: Grids with mesh-interface with transition elements shown in Figs. 7a-7d, exact solution  $u(x_1, x_2) = \sin(\pi x_1) \sinh(\pi x_2)$ , quadratic elements ( $p = 2$ ). The maximum values of  $\left| \frac{\partial e_h}{\partial x_1} \right|$  at the Gauss-Legendre points and the superconvergence points (from Tables 2a, 2b) are given in the square elements of size  $\frac{h}{2}$  at the mesh-interface and one layer away from the mesh-interface are given.



Grid with mesh-interface with transition elements				
Linear elements				
Cell-size $h$	Center of the element		Superconvergence points from Table 1	
	$\left  \frac{\partial e_h}{\partial x_1} \right $	$\left  \frac{\partial e_h}{\partial x_1} \right  h^{-1}$	$\left  \frac{\partial e_h}{\partial x_1} \right $	$\left  \frac{\partial e_h}{\partial x_1} \right  h^{-2}$
Triangular element $\tau_1$ at the mesh-interface				
0.25000	.64847413E-01	0.26	.71810910E-01	1.15
0.12500	.23381462E-01	0.19	.20457913E-01	1.31
0.06250	.90781904E-02	0.15	.72098413E-02	1.85
0.03125	.43145871E-02	0.14	.18104208E-02	1.85
Triangular element $\tau_3$ at the mesh-interface				
0.25000	.55608910E-01	0.22	.64651209E-01	1.03
0.12500	.24097771E-01	0.19	.27108881E-01	1.73
0.06250	.90104544E-02	0.14	.10000891E-01	2.56
0.03125	.45067131E-02	0.14	.25104930E-02	2.57

**Table 7.** Rate of convergence at the superconvergence points: Grids with mesh-interface with transition elements shown in Figs. 7a-7d, exact solution  $u(x_1, x_2) = \sin(\pi x_1) \sinh(\pi x_2)$ , linear elements ( $p = 1$ ). The values of  $\left| \frac{\partial e_h}{\partial x_1} \right|$  are given at the center of the triangular elements  $\tau_2$  and  $\tau_1$  (see Fig. 4b) and at the superconvergence points (from Table 2a).

Rate of convergence of $E_q$		
Grids with mesh-interface		
Bilinear elements		
$h$	$E_1$	$E_1 h^{-2}$
0.25000	.38189339E+00	6.11
0.12500	.94191674E-01	6.02
0.06250	.24140167E-01	6.18
0.03125	.60765580E-02	6.22
$h$	$E_2$	$E_2 h^{-\frac{3}{2}}$
0.25000	.42966792E+00	3.44
0.12500	.14797583E+00	3.35
0.06250	.51739635E-01	3.31
0.03125	.18205665E-01	3.30
$h$	$E_3$	$E_3 h^{-\frac{4}{3}}$
0.25000	.47927923E+00	3.04
0.12500	.18460718E+00	2.95
0.06250	.72701566E-01	2.93
0.03125	.28800505E-01	2.93
$h$	$E_4$	$E_4 h^{-\frac{5}{4}}$
0.25000	.50758796E+00	2.87
0.12500	.20781247E+00	2.80
0.06250	.86769758E-01	2.78
0.03125	.36422194E-01	2.78
$h$	$E_{10}$	$E_{10} h^{-\frac{11}{10}}$
0.25000	.56625513E+00	2.60
0.12500	.26052825E+00	2.57
0.06250	.12086784E+00	2.55
0.03125	.56320092E-01	2.55
$h$	$E_\infty$	$E_\infty h^{-1}$
0.25000	.62835301E+00	2.51
0.12500	.31841522E+00	2.51
0.06250	.15947373E+00	2.55
0.03125	.79755480E-01	2.55

**Table 8a.** Rate of convergence of the discrete-norm  $E_q$ . Meshes shown in Fig. 6a-6d, exact solution  $u(x_1, x_2) = \sin(\pi x_1) \sinh(\pi x_2)$ , bilinear elements ( $p = 1$ ). The discrete-norm  $E_q$  was computed using the Gauss-Legendre points in the elements in the subdomain  $\Omega_0 = (0.25, 0.75) \times (0.5, 0.75) \subseteq \Omega = (0, 1)^2$ . The mesh-interface is located along the line  $x_2 = 0.50$ .

Rate of convergence of $E_q$		
Grids with mesh-interface		
Biquadratic elements		
$h$	$E_1$	$E_1 h^{-3}$
0.25000	.21415864E-01	1.37
0.12500	.27893542E-02	1.43
0.06250	.35907094E-03	1.47
0.03125	.45166015E-04	1.48
$h$	$E_2$	$E_2 h^{-\frac{5}{2}}$
0.25000	.24765556E-01	0.79
0.12500	.46104445E-02	0.83
0.06250	.82232958E-03	0.84
0.03125	.14526387E-03	0.84
$h$	$E_3$	$E_3 h^{-\frac{7}{3}}$
0.25000	.27360051E-01	0.70
0.12500	.61654349E-02	0.79
0.06250	.12477526E-02	0.80
0.03125	.24915430E-03	0.81
$h$	$E_4$	$E_4 h^{-\frac{8}{3}}$
0.25000	.29631698E-01	0.67
0.12500	.72911007E-02	0.79
0.06250	.15701595E-02	0.80
0.03125	.32847516E-03	0.80
$h$	$E_{10}$	$E_{10} h^{-\frac{21}{10}}$
0.25000	.35949866E-01	0.66
0.12500	.10195347E-01	0.80
0.06250	.25087484E-02	0.85
0.03125	.58695587E-03	0.85
$h$	$E_\infty$	$E_\infty h^{-2}$
0.25000	.44992746E-01	0.72
0.12500	.13862436E-01	0.89
0.06250	.34181964E-02	0.88
0.03125	.86914062E-03	0.89

Table 8b. Rate of convergence of the discrete-norm  $E_q$ . Meshes shown in Fig. 6a-6d, exact solution  $u(x_1, x_2) = \sin(\pi x_1) \sinh(\pi x_2)$ , biquadratic elements ( $p = 2$ ). The discrete-norm  $E_q$  was computed using the Gauss-Legendre points in the elements in the subdomain  $\Omega_0 = (0.25, 0.75) \times (0.5, 0.75) \subseteq \Omega = (0, 1)^2$ . The mesh-interface is located along the line  $x_2 = 0.50$ .

Relative error at the superconvergence points and Gauss points in the elements in the mesh-patch shown in Fig. 8a, $p = 1$				
Element number $i$	$\Theta(\bar{x}; \frac{\partial u}{\partial x_1}; u, u_h, h, \tau_i)$		$\Theta(\bar{x}; \frac{\partial u}{\partial x_2}; u, u_h, h, \tau_i)$	
	Gauss point	Point from Table 1a	Gauss point	Point from Table 1a
Elements at the mesh-interface				
1	0.244	0.011	0.079	0.054
2	0.254	0.020	0.079	0.056
3	0.246	0.013	0.084	0.044
4	0.253	0.019	0.084	0.046
5	0.248	0.014	0.088	0.039
6	0.251	0.017	0.089	0.040
7	0.249	0.015	0.089	0.036
8	0.250	0.016	0.089	0.036
9	0.250	0.016	0.089	0.036
10	0.249	0.015	0.089	0.036
11	0.251	0.017	0.088	0.040
12	0.248	0.014	0.088	0.039
13	0.253	0.019	0.084	0.046
14	0.246	0.013	0.084	0.044
15	0.254	0.020	0.079	0.056
16	0.244	0.011	0.079	0.054
Elements one layer away from the mesh-interface				
17	0.061	0.060	0.044	0.044
18	0.066	0.062	0.044	0.044
19	0.060	0.060	0.043	0.043
20	0.064	0.060	0.043	0.043
21	0.059	0.058	0.042	0.042
22	0.063	0.060	0.040	0.040
23	0.058	0.058	0.040	0.040
24	0.061	0.060	0.039	0.039
25	0.059	0.057	0.039	0.039
26	0.059	0.057	0.040	0.040
27	0.059	0.057	0.040	0.040
28	0.059	0.057	0.042	0.042
29	0.064	0.060	0.043	0.043
30	0.060	0.060	0.043	0.043
31	0.066	0.062	0.044	0.044
32	0.061	0.060	0.044	0.044

**Table 9a.** Relative error at the superconvergence points for meshes which are not locally periodic: Mesh shown in Fig. 8a, bilinear elements ( $p = 1$ ) exact solution  $u(x_1, x_2) = e^{-k[(x_1-a)^2+(x_2-b)^2]}$ ,  $k = 10$ ,  $(a, b) = (0,0)$ . The relative errors in the  $x_1$ - and  $x_2$ -derivatives at the Gauss-Legendre point and the superconvergence points (given in Table 1) are given for the various elements in Patch I shown in Fig. 8a and enumerated as shown in Fig. 8b. Note that the relative error of  $x_1$ -derivative at the superconvergence points for elements 1-16 is around 0.02, but the relative error at the Gauss-Legendre point is around 0.25.

Relative error at the superconvergence points and Gauss points in the elements in the mesh-patch shown in Fig. 8c, $p = 1$				
Element number $i$	$\Theta(\bar{x}; \frac{\partial u}{\partial x_1}; u, u_h, h, \tau_i)$		$\Theta(\bar{x}; \frac{\partial u}{\partial x_2}; u, u_h, h, \tau_i)$	
	Gauss point	Point from Table 1a	Gauss point	Point from Table 1a
Elements at the mesh-interface				
1	0.091	0.084	0.378	0.102
2	0.111	0.097	0.381	0.106
3	0.118	0.101	0.424	0.191
4	0.131	0.118	0.447	0.197
Elements one layer away from the mesh-interface				
5	0.067	0.064	0.081	0.080
6	0.067	0.064	0.087	0.084
7	0.069	0.064	0.099	0.093
8	0.069	0.064	0.101	0.099

**Table 9b.** Relative error at the superconvergence points for meshes which are not locally periodic: Mesh shown in Fig. 8c, bilinear elements ( $p = 1$ ) exact solution  $u(x_1, x_2) = e^{-k[(x_1-a)^2+(x_2-b)^2]}$ ,  $k = 10$ ,  $(a, b) = (0, 0)$ . The relative errors in the  $x_1$ - and  $x_2$ -derivatives at the Gauss-Legendre point and the superconvergence points (given in Table 1) are given for the various elements in Patch II shown in Fig. 8c and numbered as shown in Fig. 8d. Note that the relative error of  $x_2$ -derivative at the superconvergence points is smaller than the relative error at the Gauss-Legendre point.

Grid with mesh-interface of Fig. 4a		
Bilinear elements		
Layer	$\frac{d}{h}$	$\eta\%^{G-L} = \max_{Q \in Q^H} \Theta(\tilde{x}^{G-L}; \frac{\partial u}{\partial x_1}, Q, \tilde{w}, 1, \tilde{\tau})$
0	0.25	26.713
1	0.75	4.124
2	1.25	0.454
3	1.75	0.042

**Table 10a.**  $\eta\%$ -superconvergence in periodic meshes with local refinements. Grid with mesh-interface shown in Fig. 4a; bilinear elements; Harmonic solutions,  $x_1$ -derivative of the error.  $\eta\%$  values at the  $(1 \times 1)$  Gauss-Legendre points in the elements of size  $(\frac{h}{2})$  in different layers away from the interface. The distance between the Gauss-Legendre point considered and the interface is denoted by  $d$ .

Grid with mesh-interface of Fig. 4a			
Biquadratic elements			
Layer	Point	$\frac{d}{h}$	$\eta\%^{G-L} = \max_{Q \in Q^H} \Theta(\tilde{x}^{G-L}; \frac{\partial u}{\partial x_1}, Q, \tilde{w}, 1, \tilde{\tau})$
0	1	.1056624327	25.137
	2	.1056624327	25.137
	3	.3943375673	1.566
	4	.3943375673	1.566
1	1	.6056624327	4.910
	2	.6056624327	4.910
	3	.8943375673	0.306
	4	.8943375673	0.306
2	1	1.1056624327	0.325
	2	1.1056624327	0.325
	3	1.3943375673	0.020
	4	1.3943375673	0.020
3	1	1.6056624327	0.019
	2	1.6056624327	0.019
	3	1.8943375673	0.002
	4	1.8943375673	0.002

**Table 10b.**  $\eta\%$ -superconvergence in periodic meshes with local refinements. Grid with mesh-interface with constrained nodes shown in Fig. 4a; biquadratic elements; Harmonic solutions,  $x_1$ -derivative of the error.  $\eta\%$  values at the  $(2 \times 2)$  Gauss-Legendre points in the elements of size  $(\frac{h}{2})$  in different layers away from the interface. (The master element coordinates of the points in the element are: Point 1 =  $(\frac{-1}{\sqrt{3}}, \frac{-1}{\sqrt{3}})$ ; Point 2 =  $(\frac{1}{\sqrt{3}}, \frac{-1}{\sqrt{3}})$ ; Point 3 =  $(\frac{-1}{\sqrt{3}}, \frac{1}{\sqrt{3}})$ ; Point 4 =  $(\frac{1}{\sqrt{3}}, \frac{1}{\sqrt{3}})$ ). The distance between the Gauss-Legendre point considered and the interface is denoted by  $d$ .



Grid with mesh-interface of Fig. 4b		
Linear elements		
Layer	$\frac{d}{h}$	$\eta\%^{G-L} = \max_{Q \in Q^H} \Theta(\tilde{x}^{G-L}; \frac{\partial u}{\partial x_1}, Q, \tilde{w}, 1, \tilde{\tau})$
0	0.25	4.389
1	0.75	0.230
2	1.25	0.023
3	1.75	0.002

**Table 10c.**  $\eta\%$ -superconvergence in periodic meshes with local refinements. Grid with mesh-interface with transition elements shown in Fig. 4b; linear elements; Harmonic solutions,  $x_1$ -derivative of the error.  $\eta\%$  values at the  $(1 \times 1)$  Gauss-Legendre points in the elements of size  $(\frac{h}{2})$  in different layers away from the interface. The distance between the Gauss-Legendre point considered and the interface is denoted by  $d$ .

Grid with mesh-interface of Fig. 4b			
Quadratic elements			
Layer	Point	$\frac{d}{h}$	$\eta\%^{G-L} = \max_{Q \in Q^H} \Theta(\bar{x}^{G-L}; \frac{\partial u}{\partial x_1}, Q, \bar{w}, 1, \bar{\tau})$
0	1	.1056624327	36.202
	2	.1056624327	16.369
	3	.3943375673	6.812
	4	.3943375673	7.243
1	1	.6056624327	25.589
	2	.6056624327	12.789
	3	.8943375673	0.813
	4	.8943375673	1.544
2	1	1.1056624327	15.290
	2	1.1056624327	5.707
	3	1.3943375673	0.546
	4	1.3943375673	0.003
3	1	1.6056624327	3.001
	2	1.6056624327	0.004
	3	1.8943375673	0.000
	4	1.8943375673	0.000

**Table 10d.**  $\eta\%$ -superconvergence in periodic meshes with local refinements. Grid with mesh-interface with transition elements shown in Fig. 4b; quadratic elements; Harmonic solutions,  $x_1$ -derivative of the error.  $\eta\%$  values at the  $(2 \times 2)$  Gauss-Legendre points in the elements of size  $(\frac{h}{2})$  in different layers away from the interface. (The master element coordinates of the points in the element are: Point 1 =  $(\frac{-1}{\sqrt{3}}, \frac{-1}{\sqrt{3}})$ ; Point 2 =  $(\frac{1}{\sqrt{3}}, \frac{-1}{\sqrt{3}})$ ; Point 3 =  $(\frac{-1}{\sqrt{3}}, \frac{1}{\sqrt{3}})$ ; Point 4 =  $(\frac{1}{\sqrt{3}}, \frac{1}{\sqrt{3}})$ ). The distance between the Gauss-Legendre point considered and the interface is denoted by  $d$ .

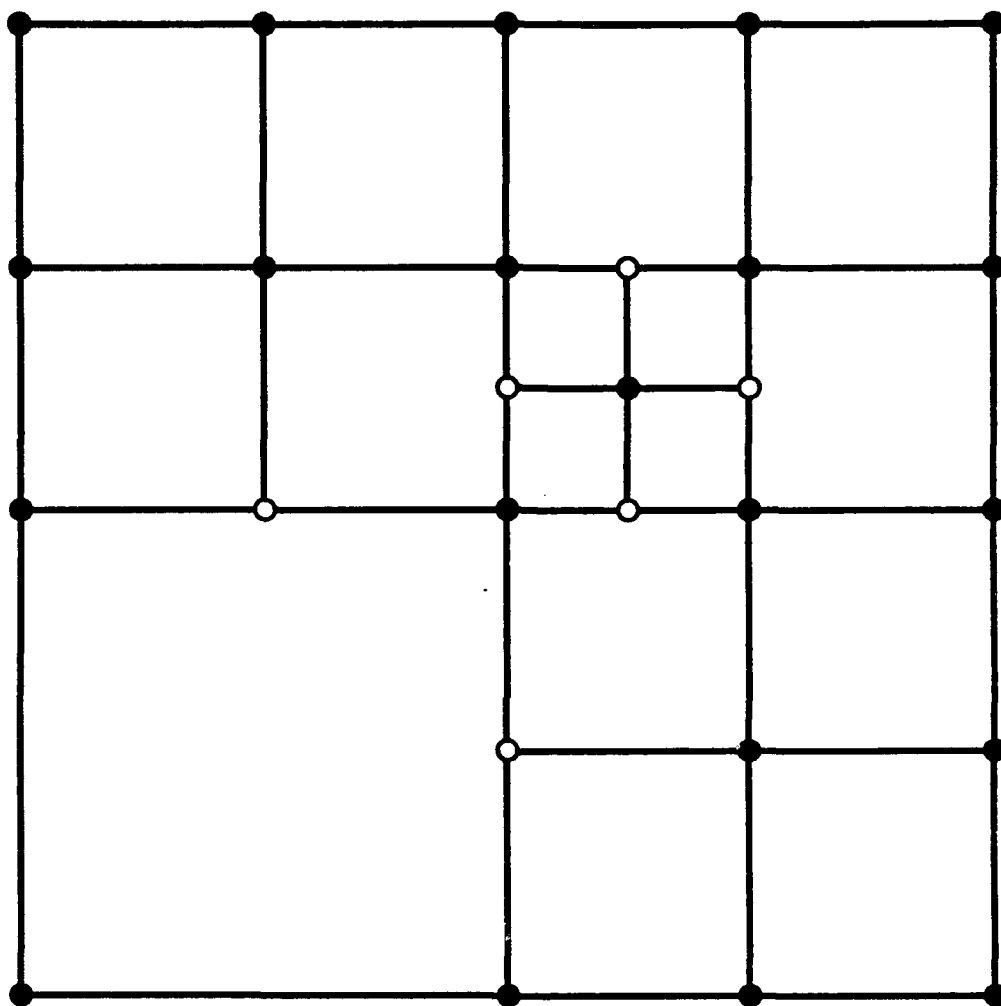


**Fig. 1a**

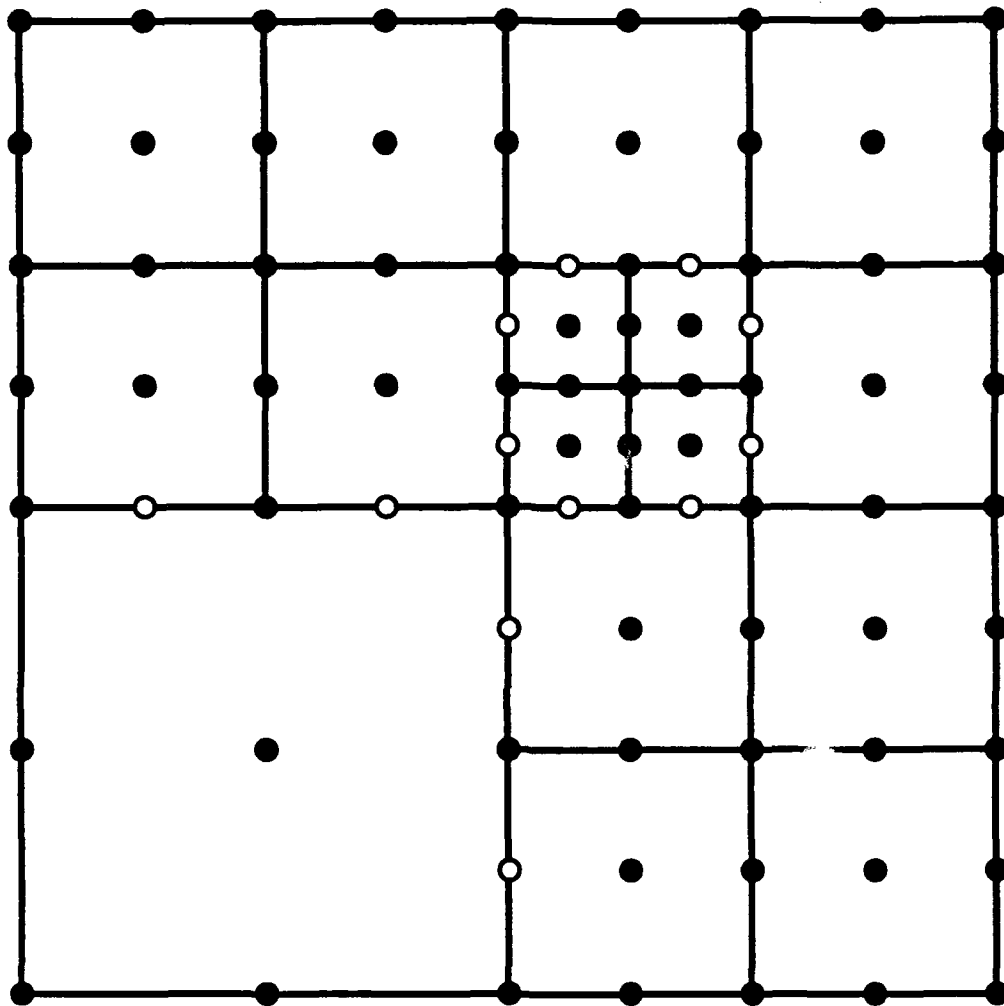


**Fig. 1b**





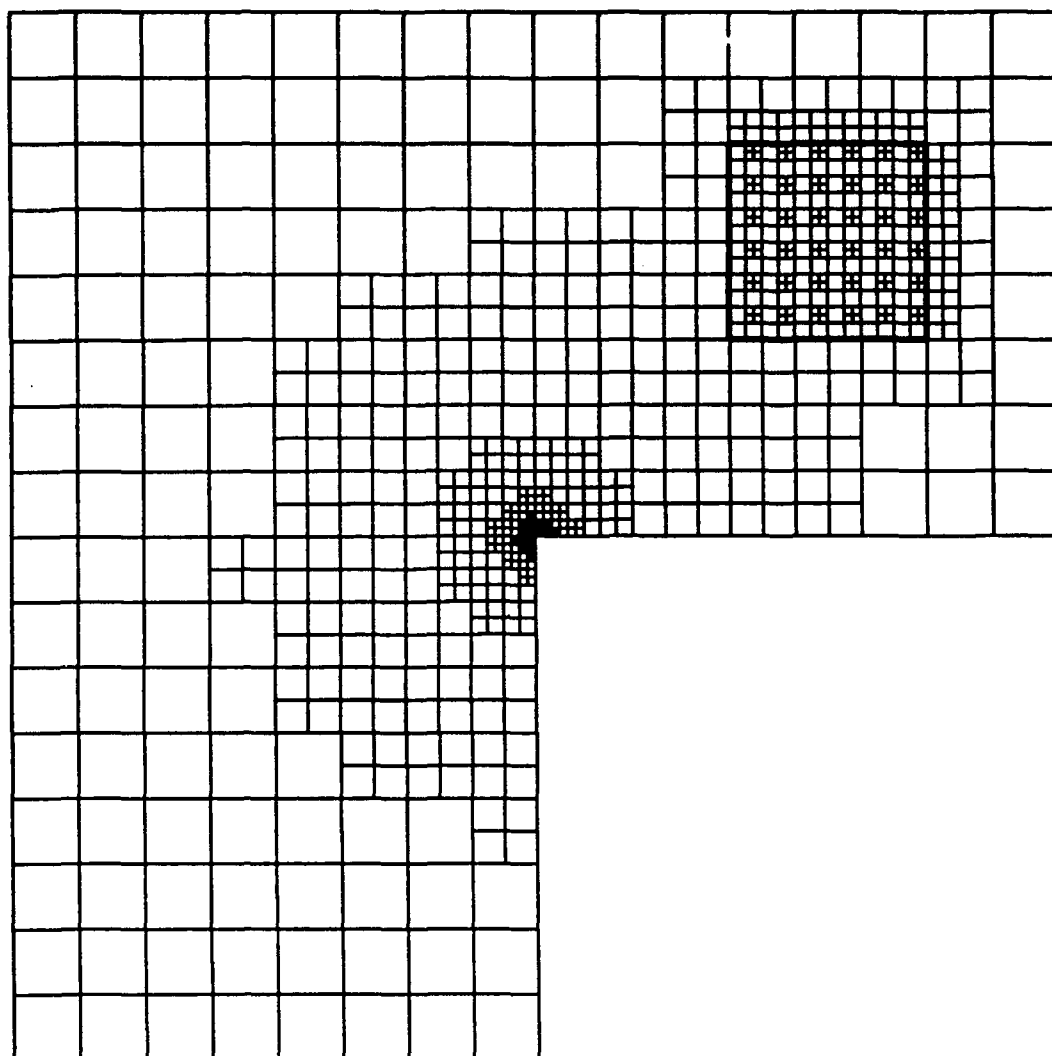


**Fig. 2a**

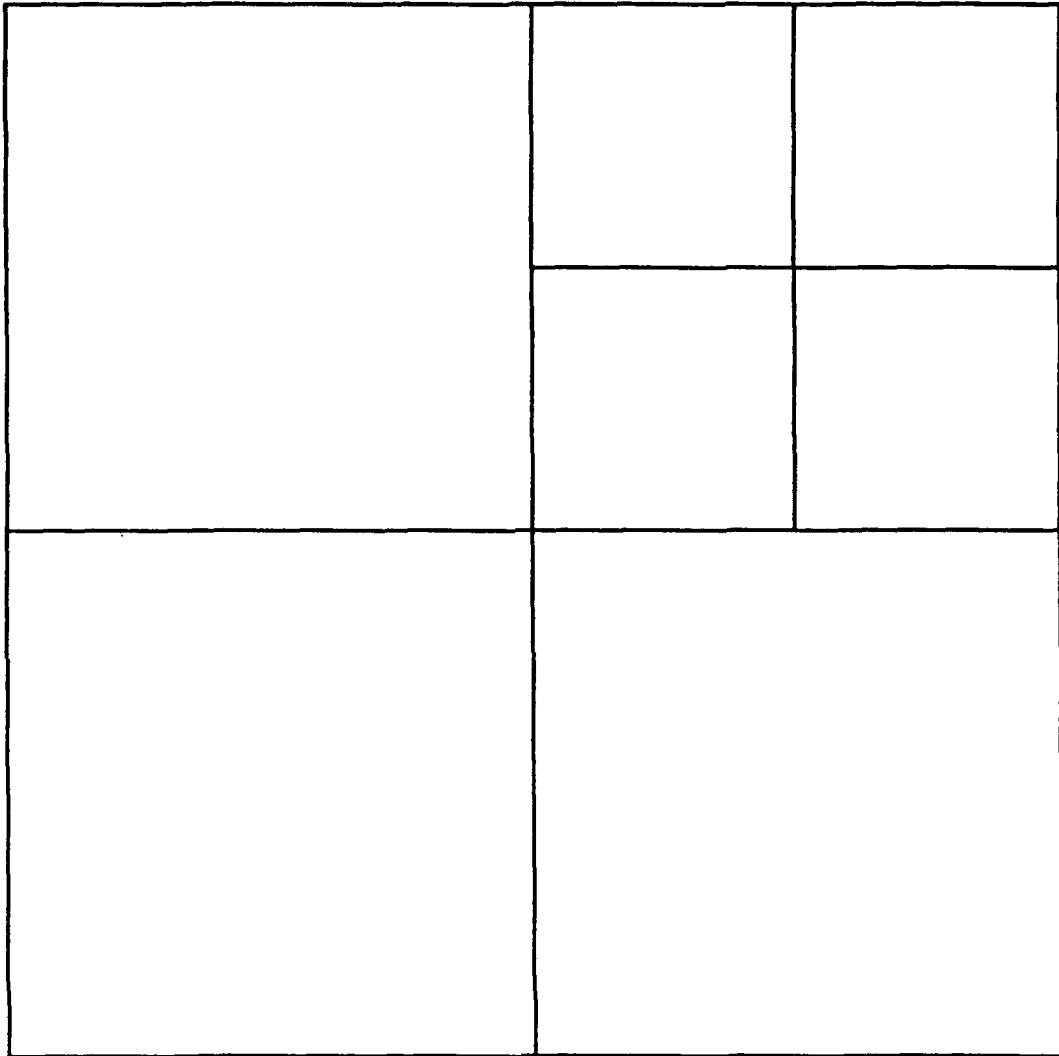


**Fig. 2b**



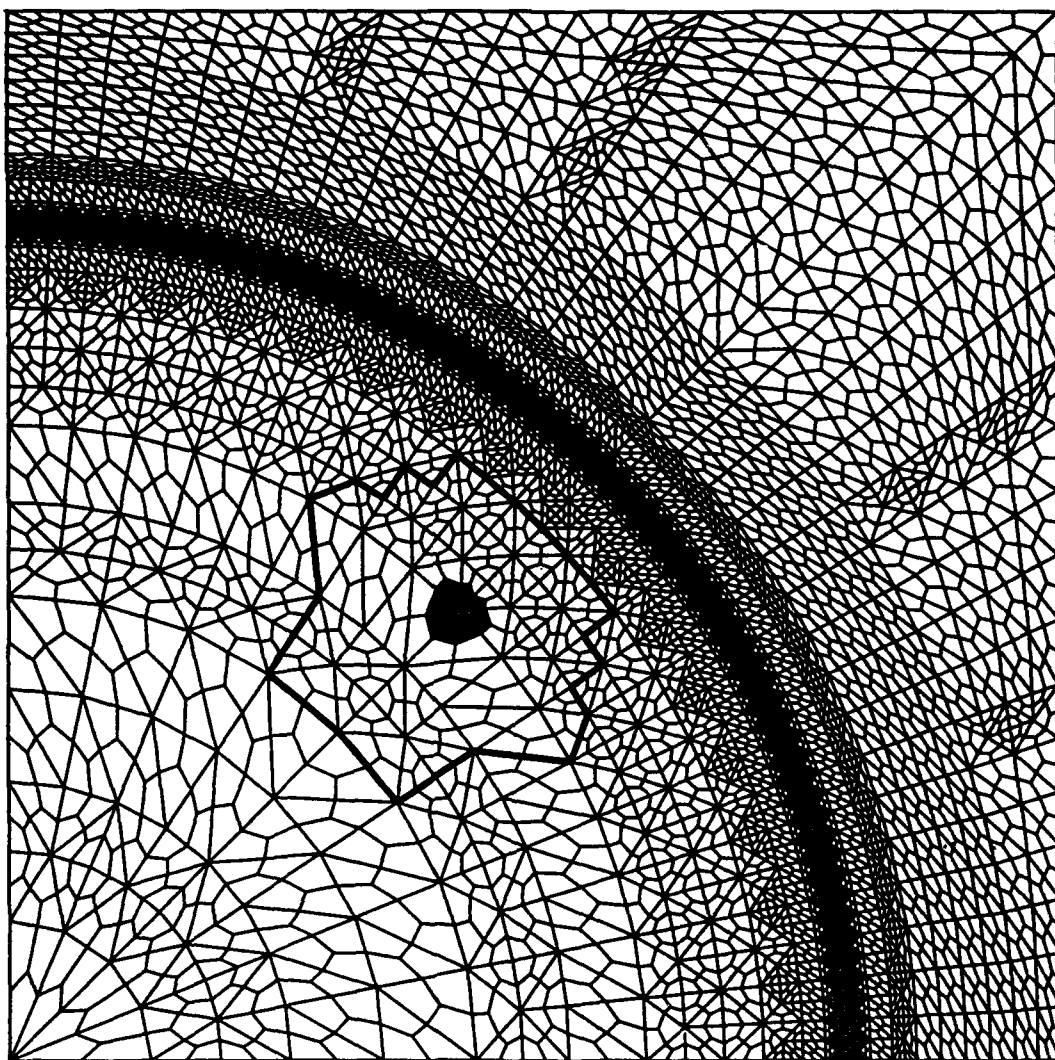


**Fig. 3a**

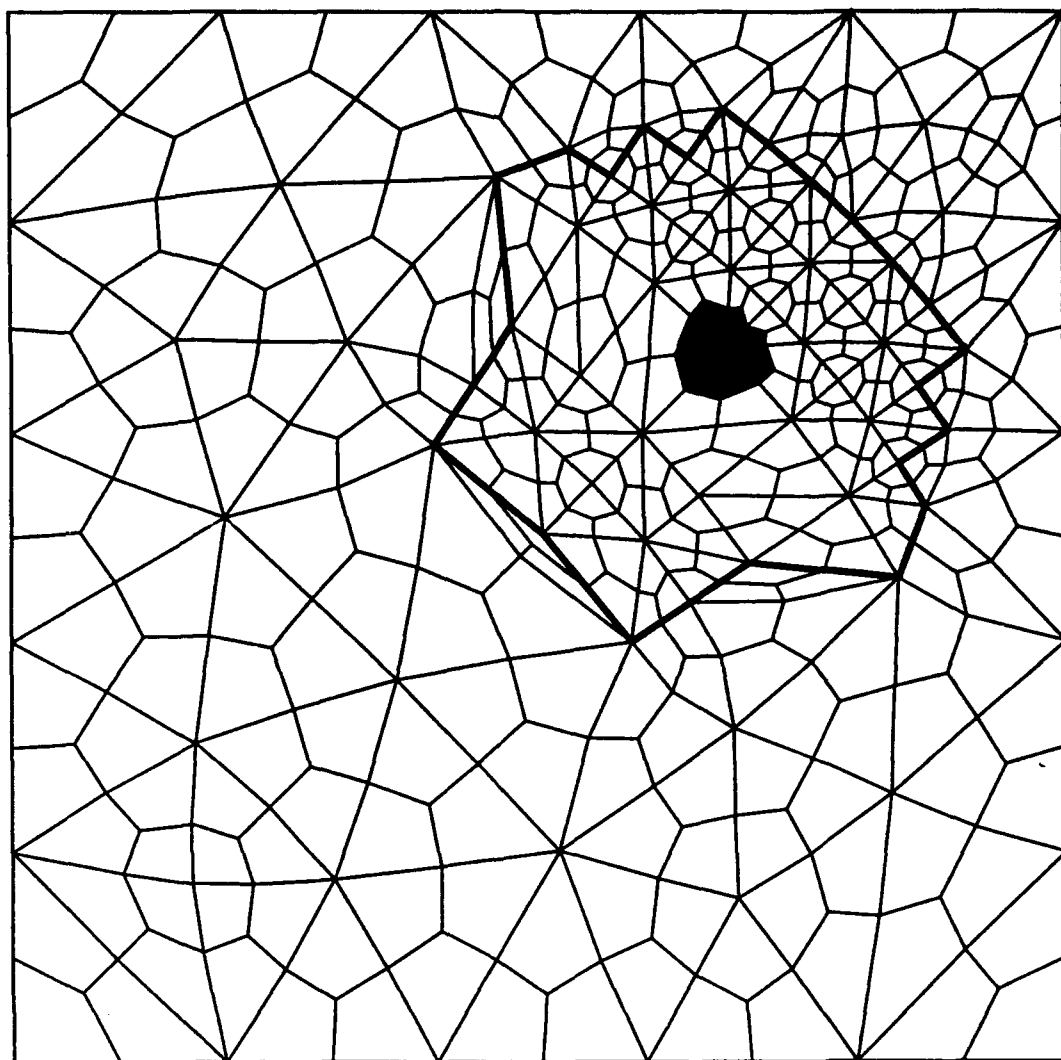


**Fig. 3b**

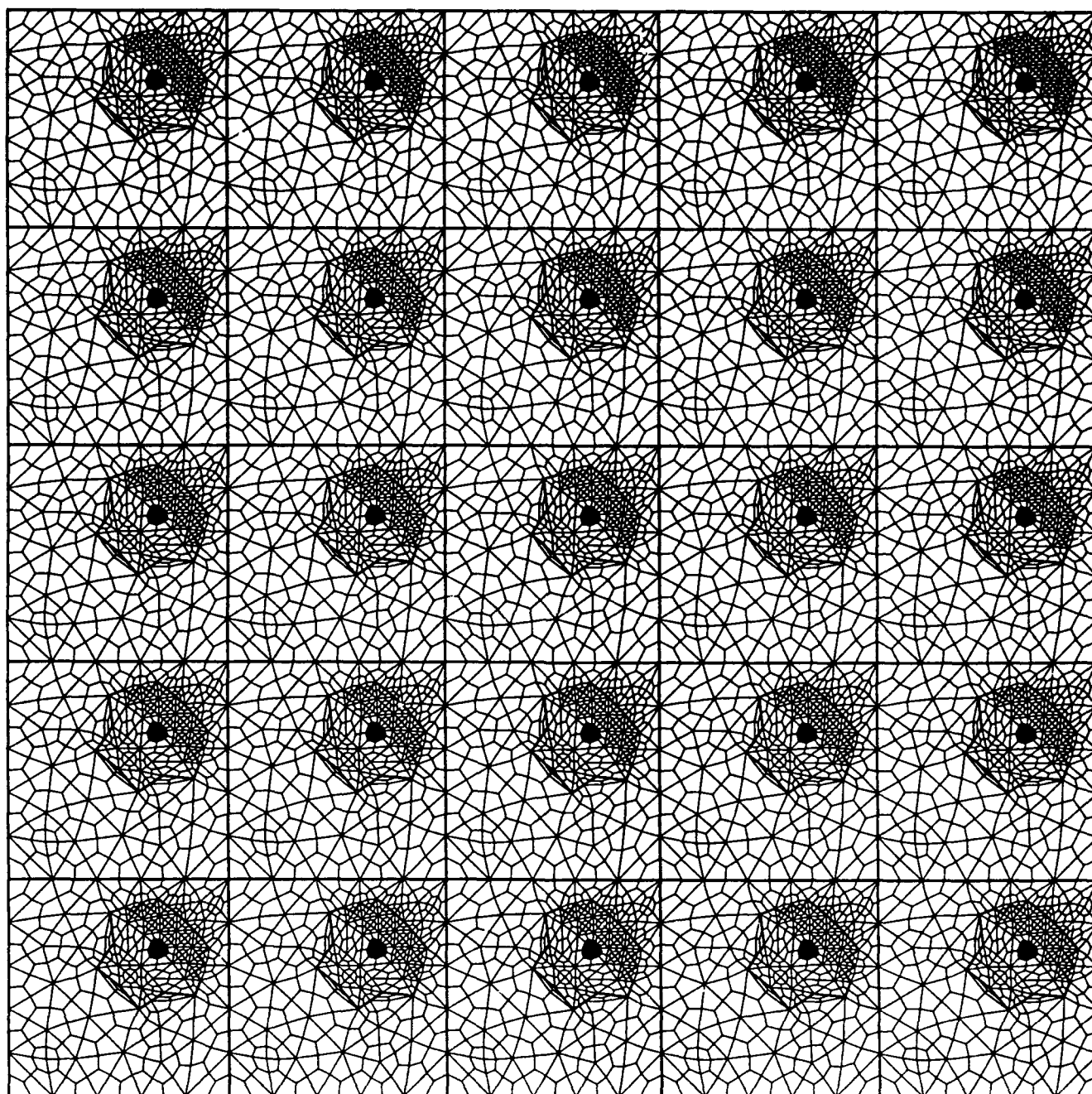


**Fig. 3c**

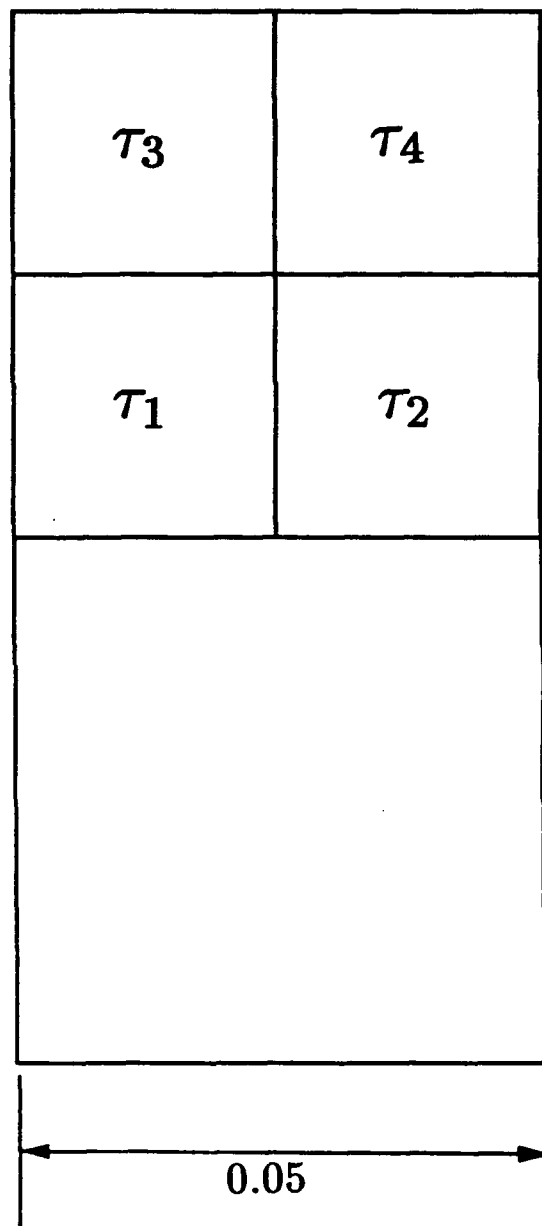
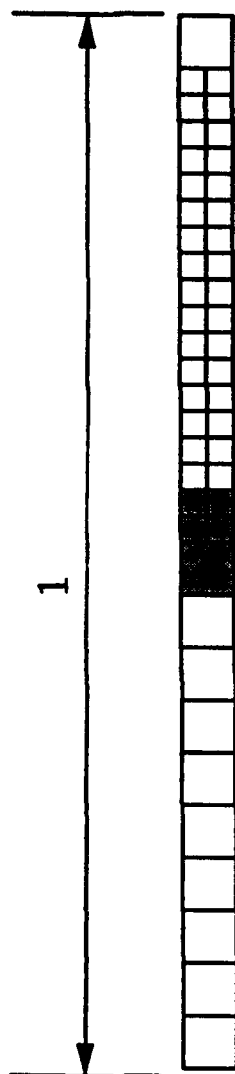


**Fig. 4a**

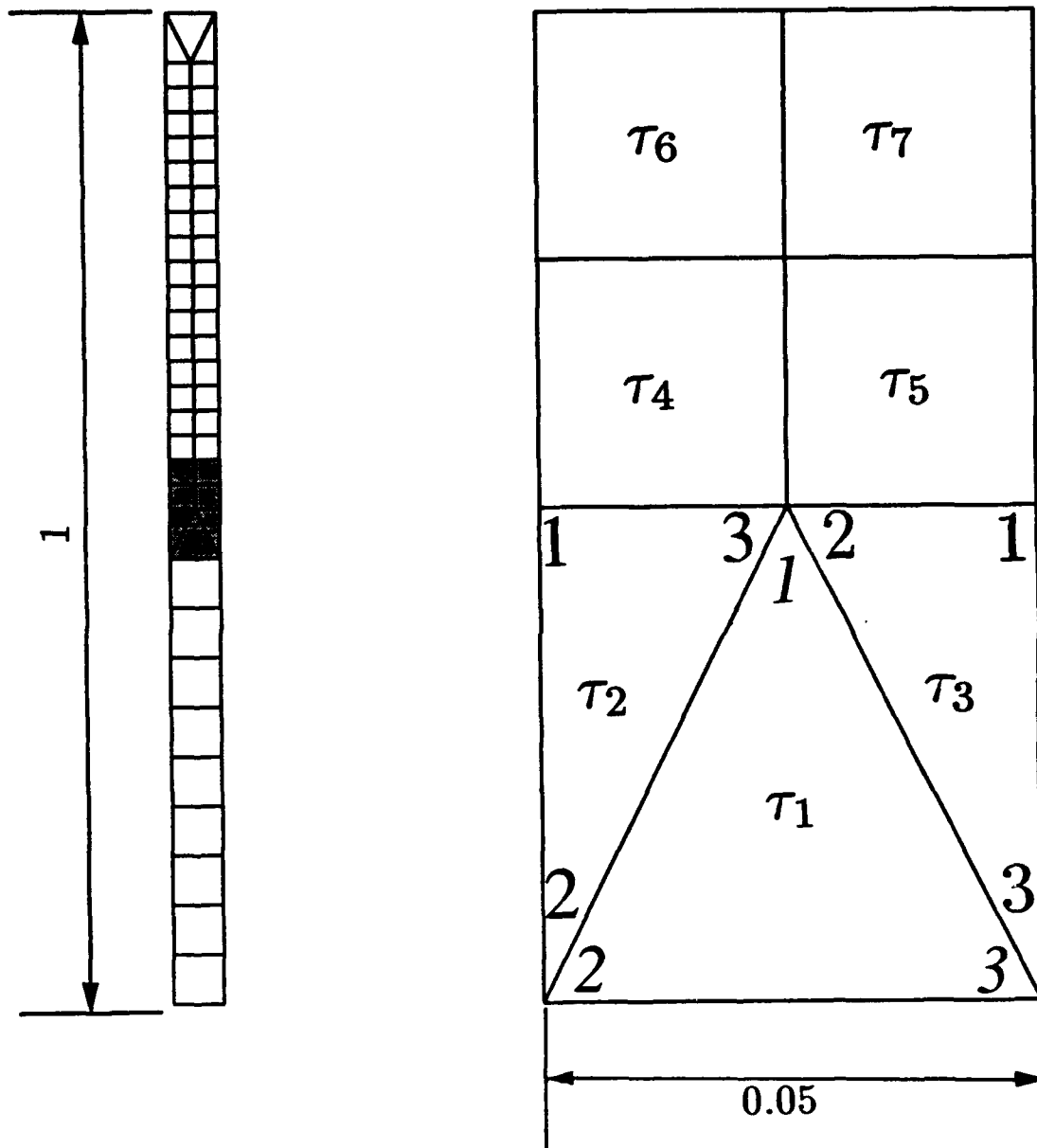


**Fig. 4b**

$\tau_7$	$\tau_{15}$	$\tau_{14}$		$\tau_{18}$	$\tau_{17}$
	$\tau_8$	$\tau_{21}$	$\tau_{20}$	$\tau_9$	$\tau_{16}$
		$\tau_{13}$	$\tau_{19}$		
$\tau_4$	$\tau_{12}$	$\tau_{11}$		$\tau_6$	
	$\tau_5$	$\tau_{10}$			
$\tau_1$	$\tau_2$			$\tau_3$	

**Fig. 4c**

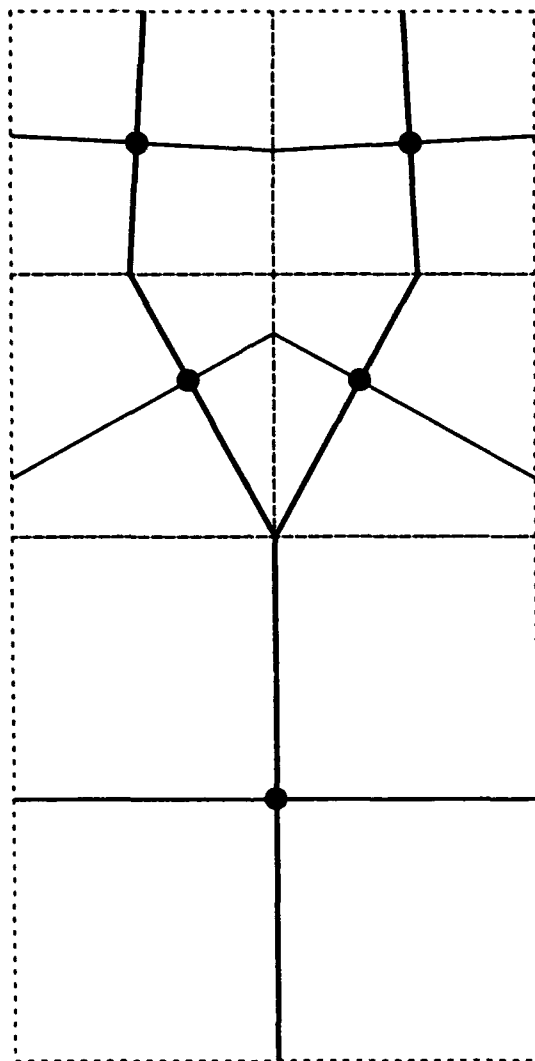


**Fig. 5a**

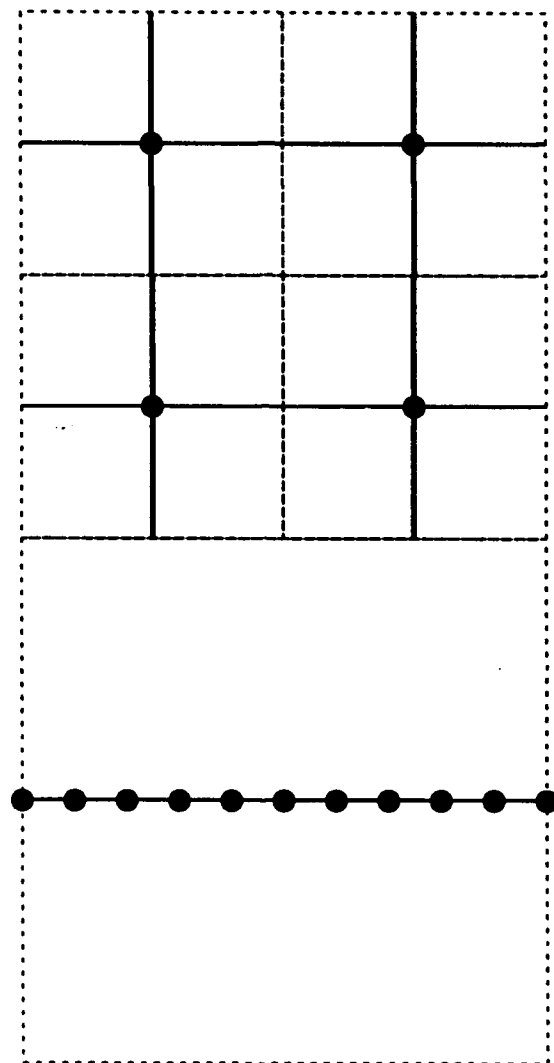


**Fig. 5b**



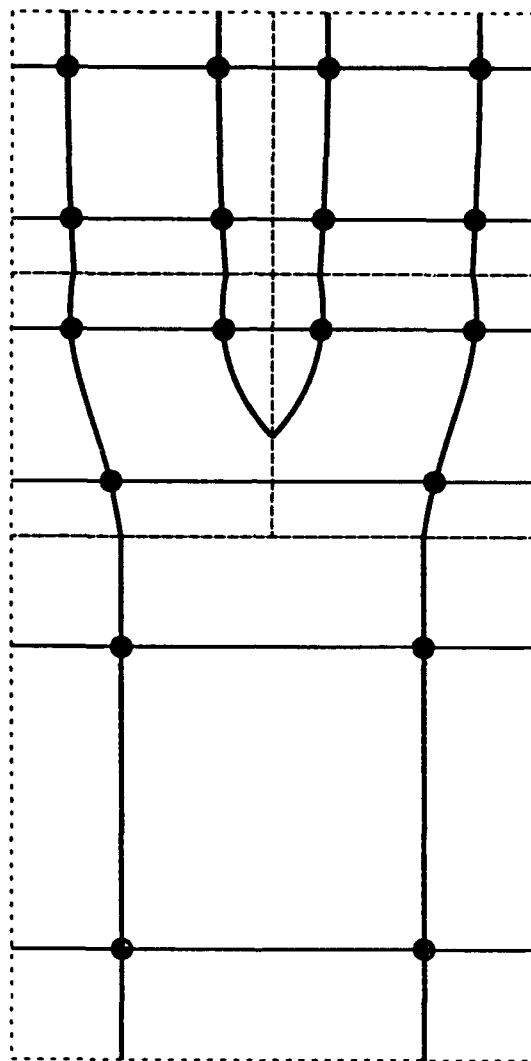


**Fig. 5c**


**Fig. 6a**

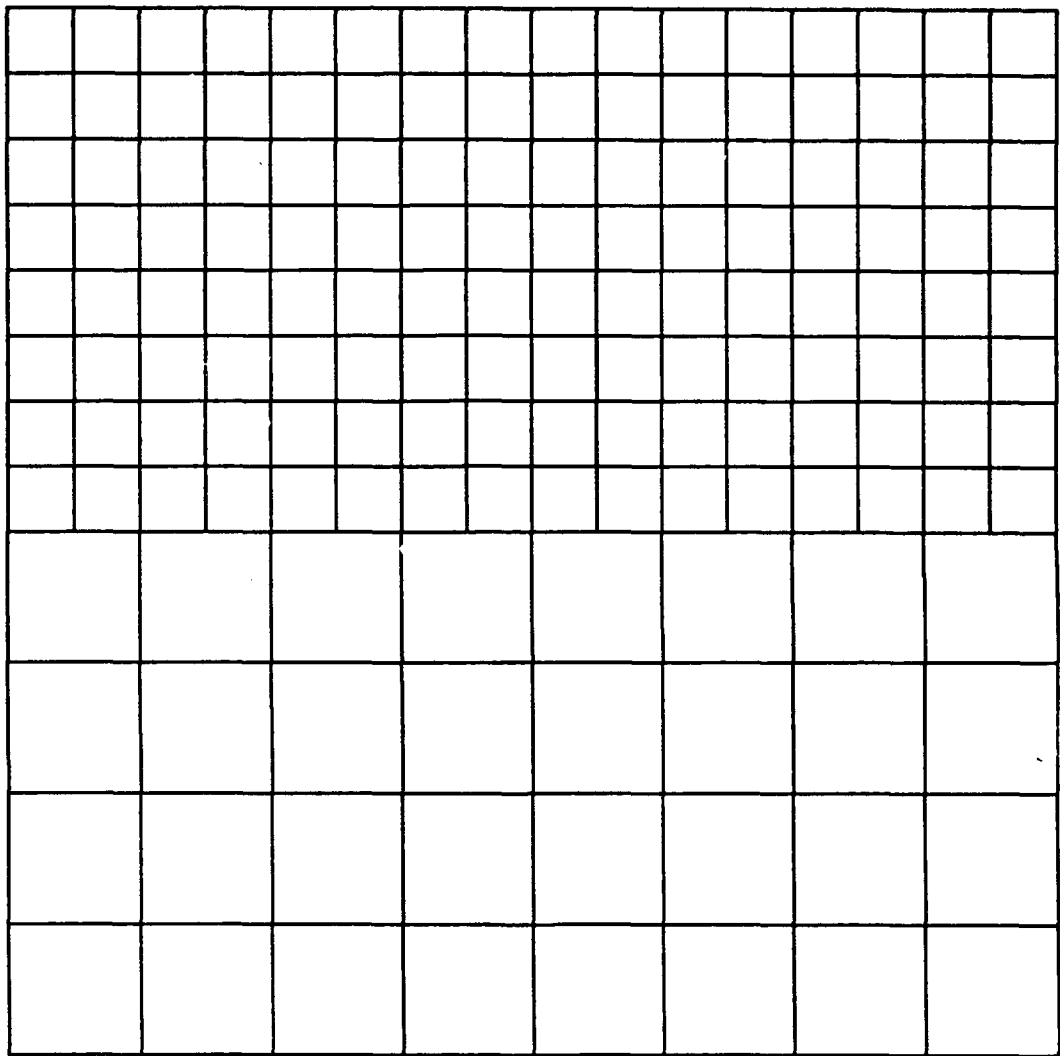


**Fig. 6b**

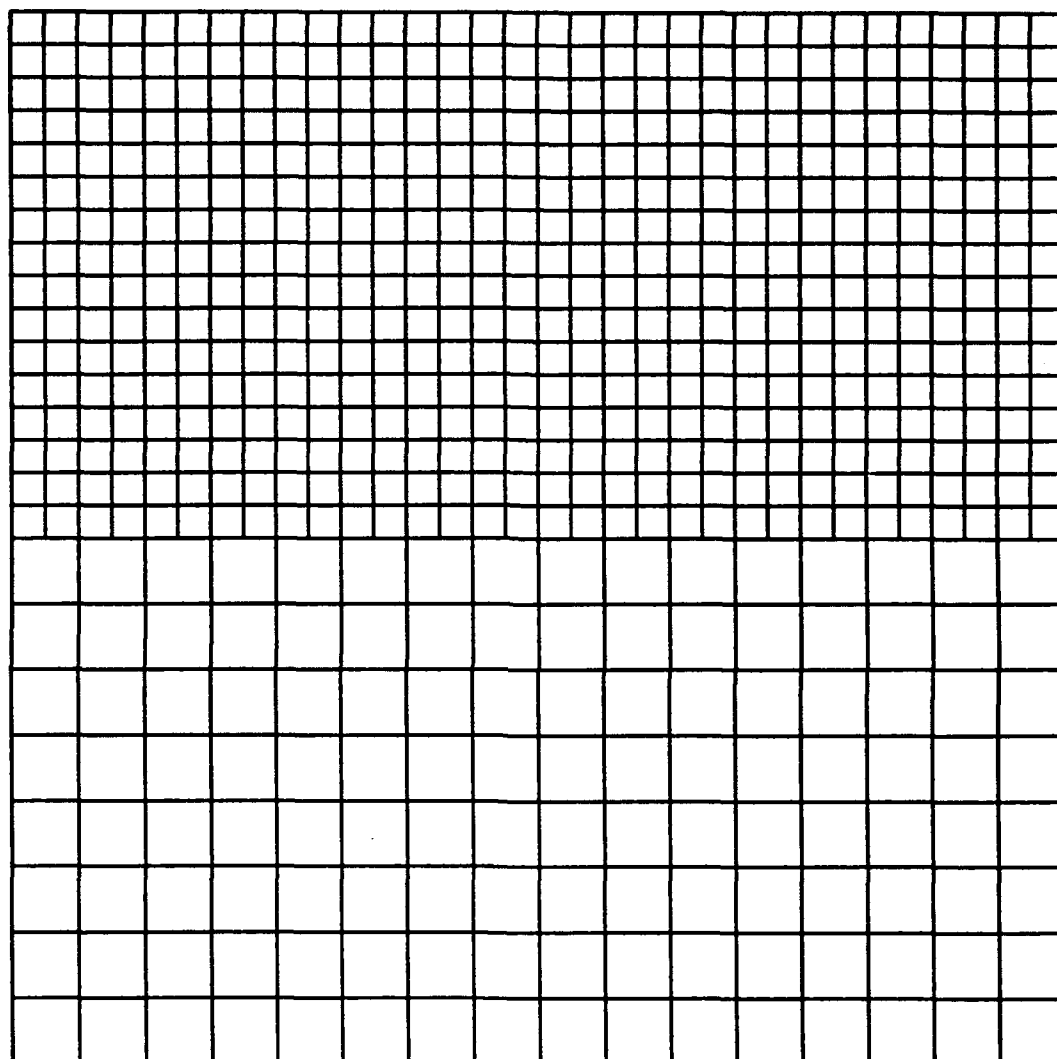


**Fig. 6c**

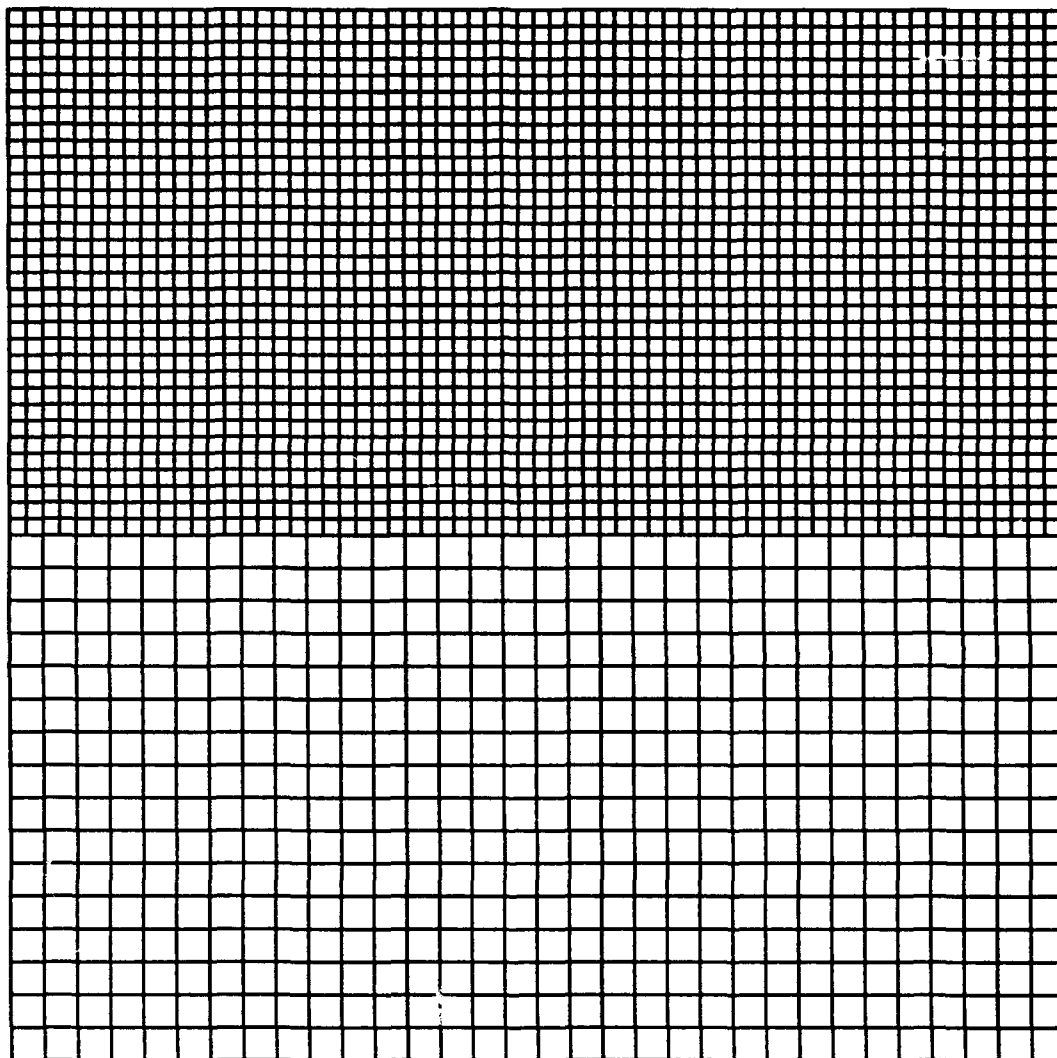


**Fig. 6d**

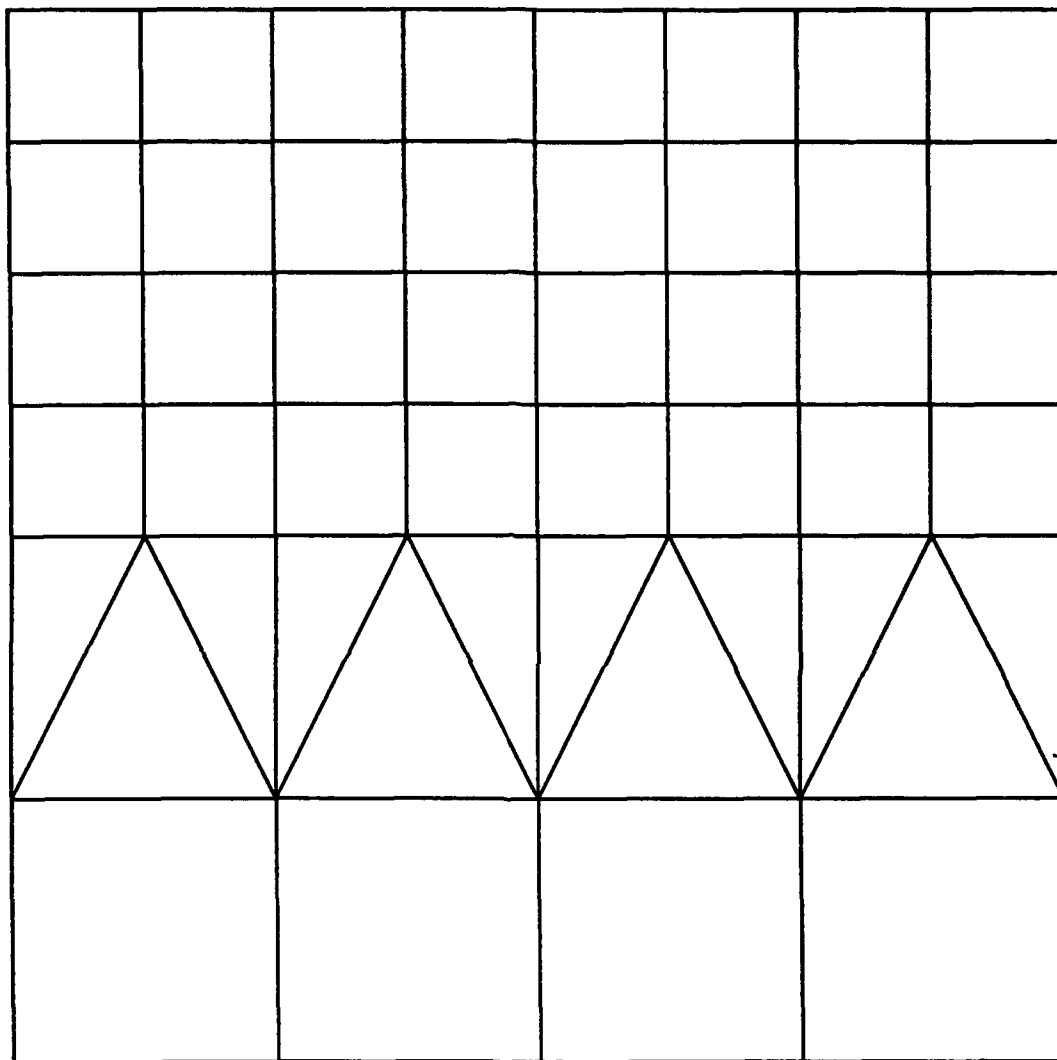


**Fig. 7a**

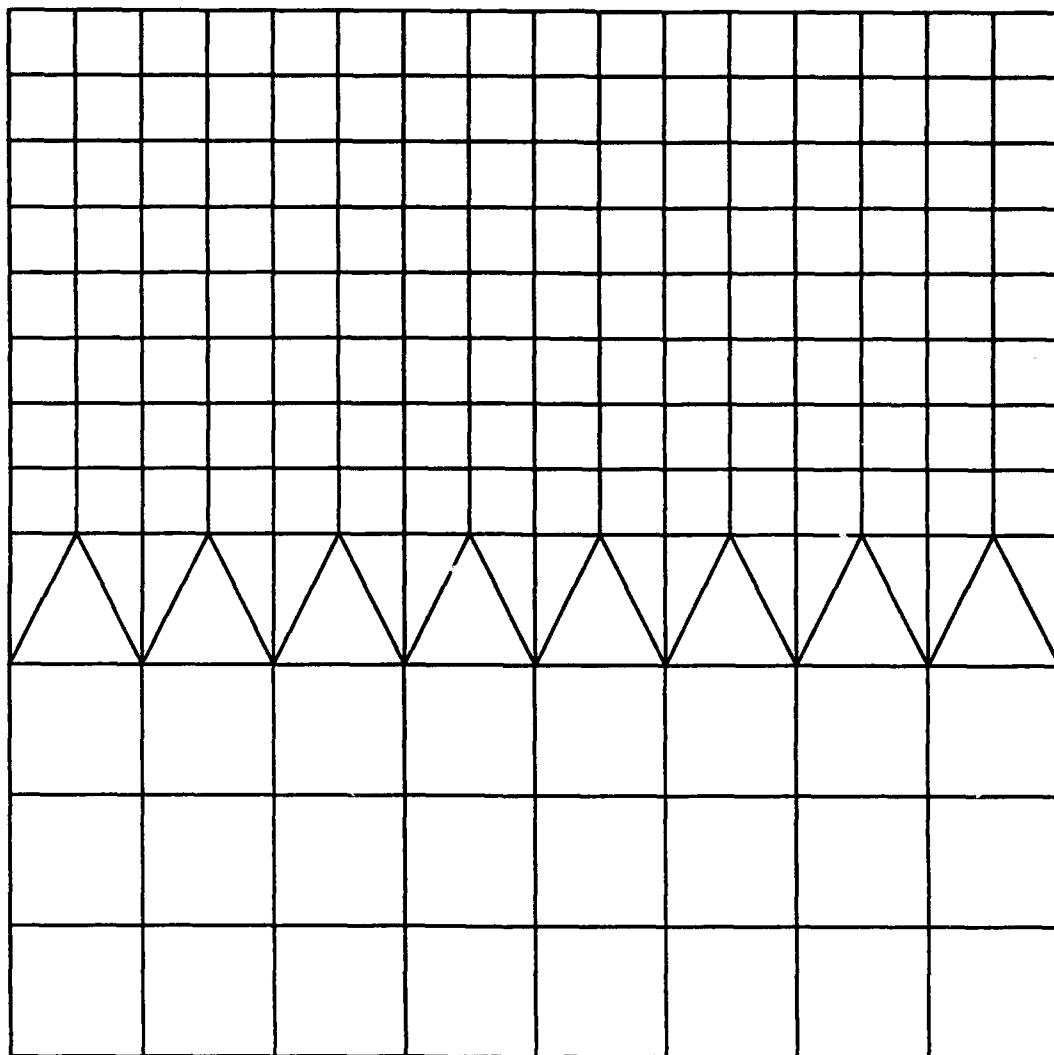


**Fig. 7b**

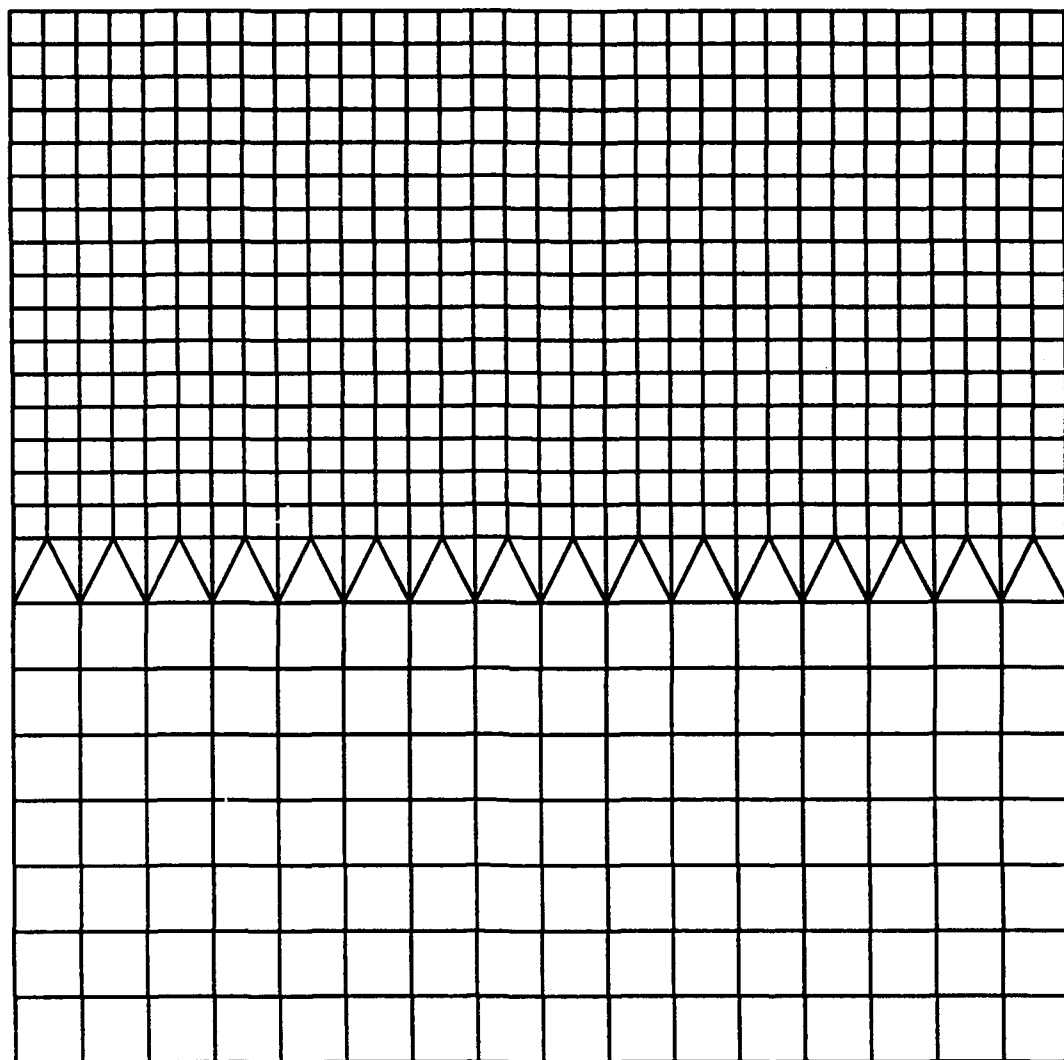


**Fig. 7c**



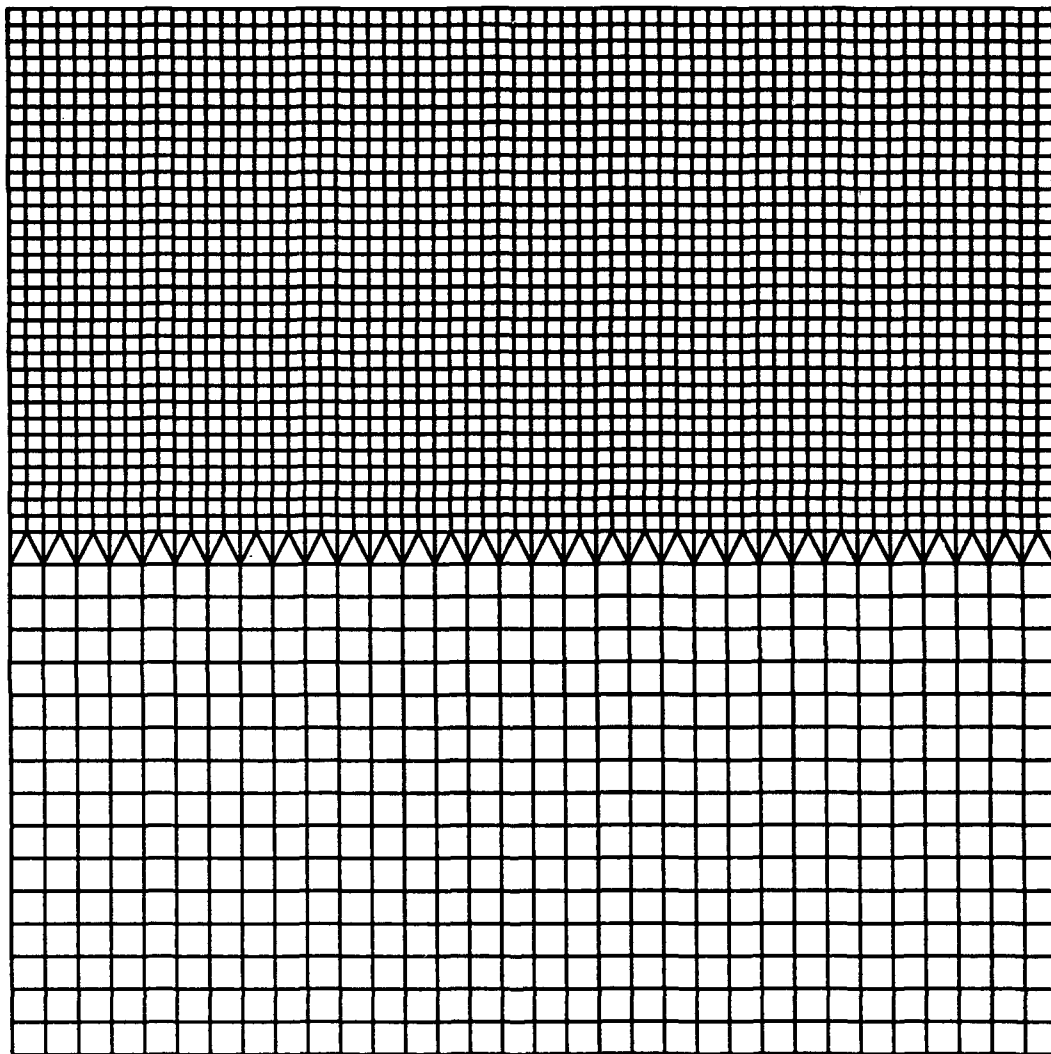


**Fig. 7d**

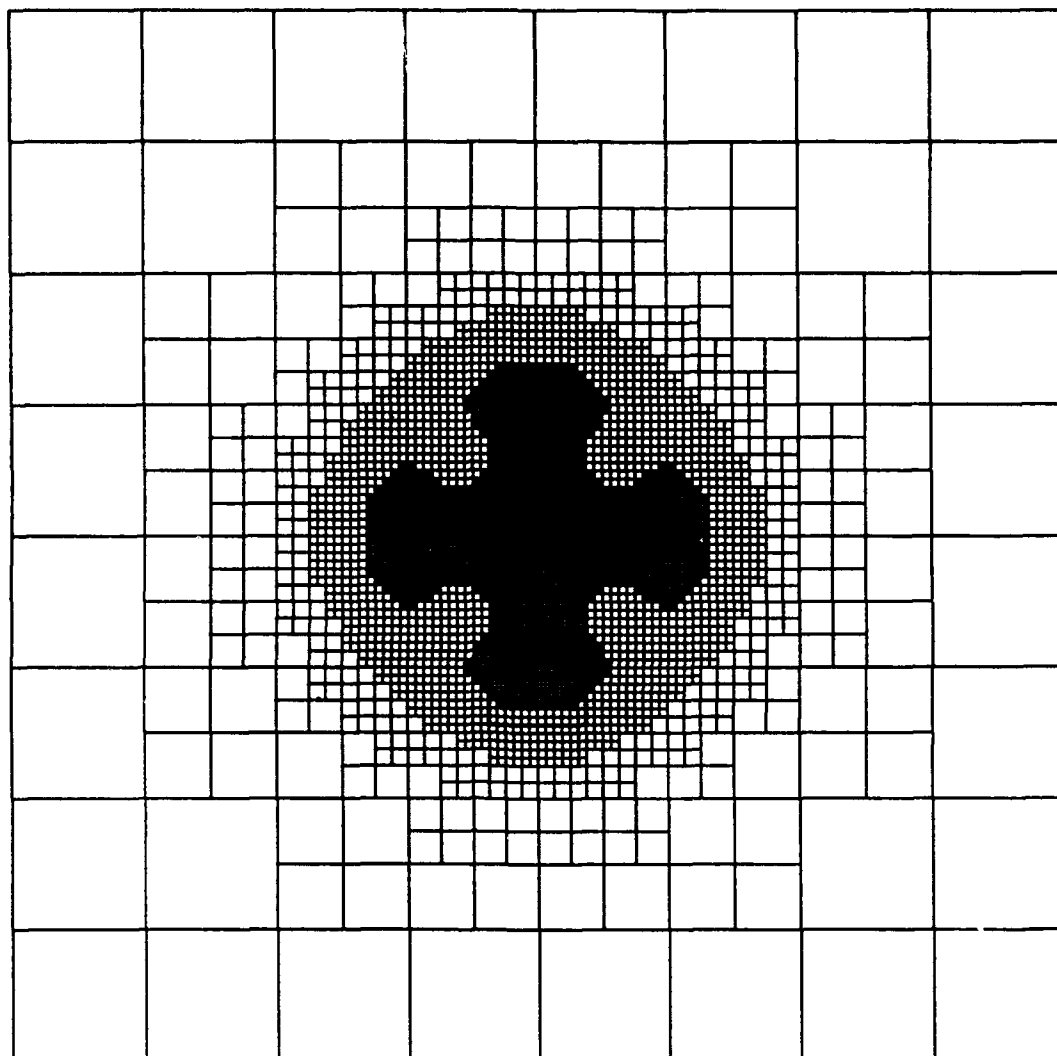


**Fig. 8a**



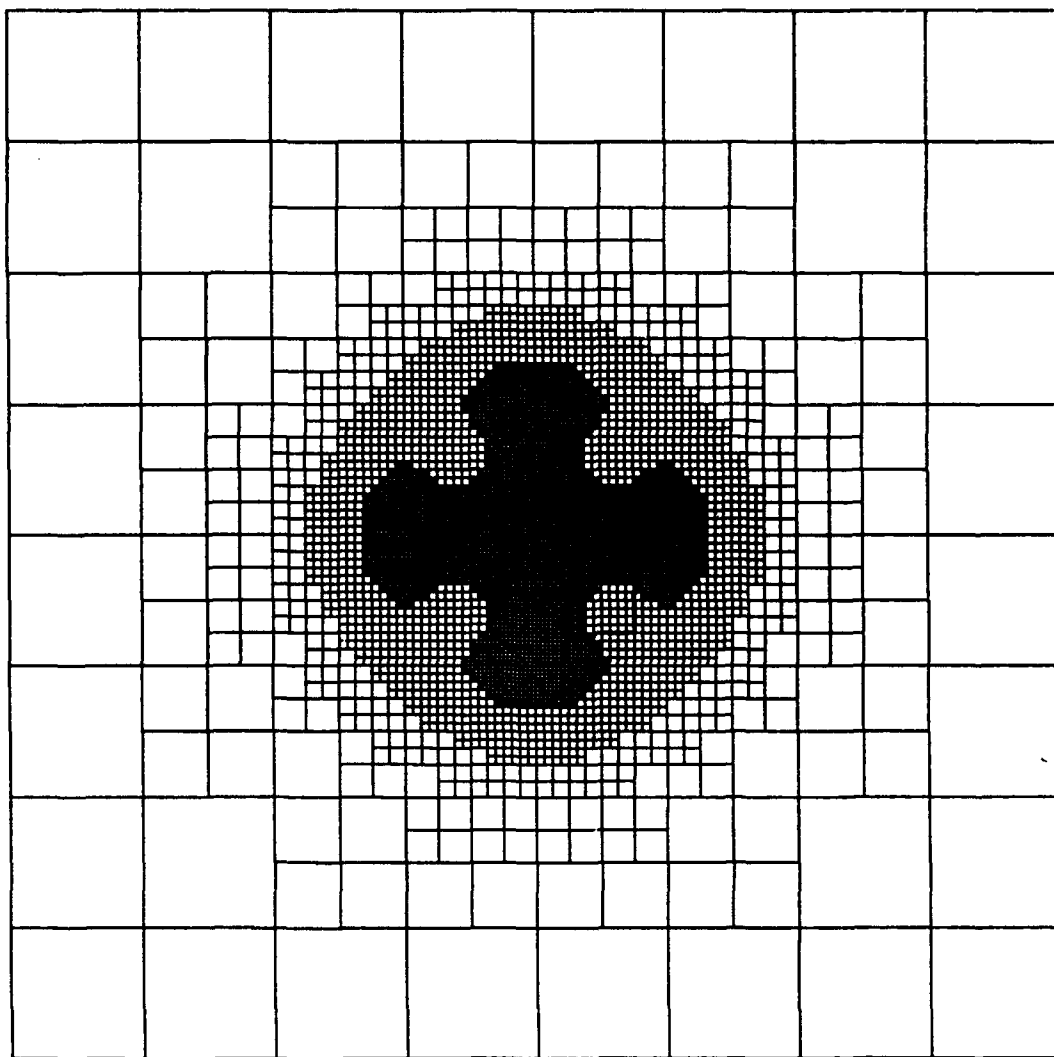


**Fig. 8c**



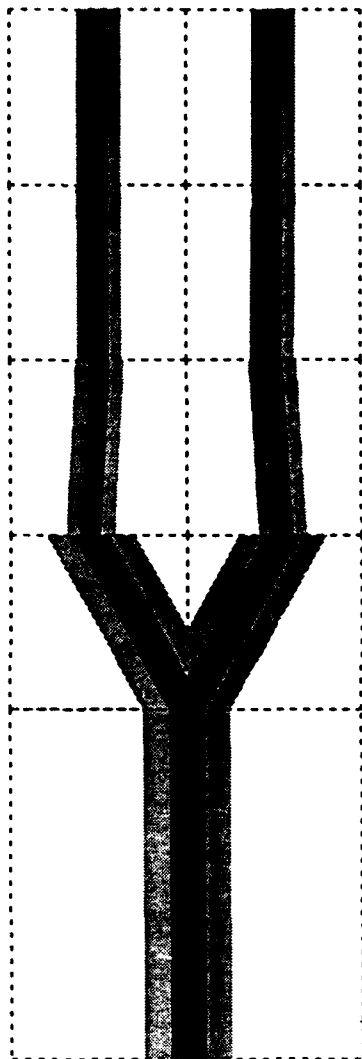


**Fig. 9a**

Simplified approach with L-2 norm  
Contours of  $dux - duhx = \eta$   
 $p = 1$



—  $F\{Q1\} = 0\%$   
—  $F\{Q2\} = 0\%$

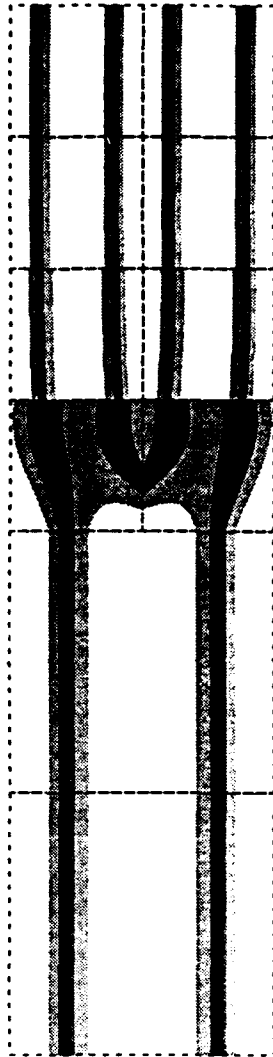
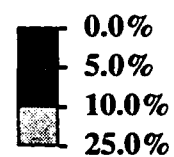


**Fig. 9b**

Simplified approach with L-2 norm  
Contours of  $d_{ux} - d_{uhx} = \eta$   
 $p = 2$



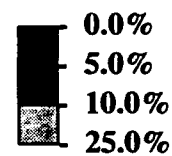
—  $F\{Q1\} = 0\%$   
—  $F\{Q2\} = 0\%$



**[REDACTED]**

\_\_\_\_\_ F{Q1} = 0%

\_\_\_\_\_ F{Q2} = 0%





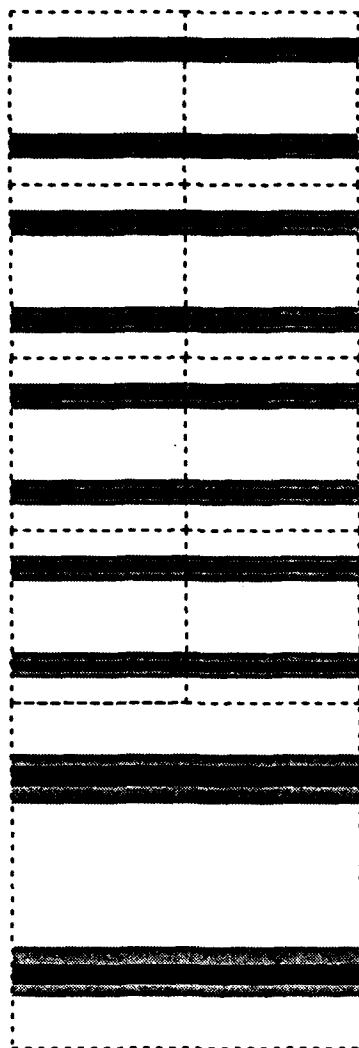


**Fig. 9d**

Simplified approach with L-2 norm  
 Contours of  $duy - duhy \approx \eta$   
 $p = 2$



—  $F\{Q1\} = 0\%$   
 —  $F\{Q2\} = 0\%$

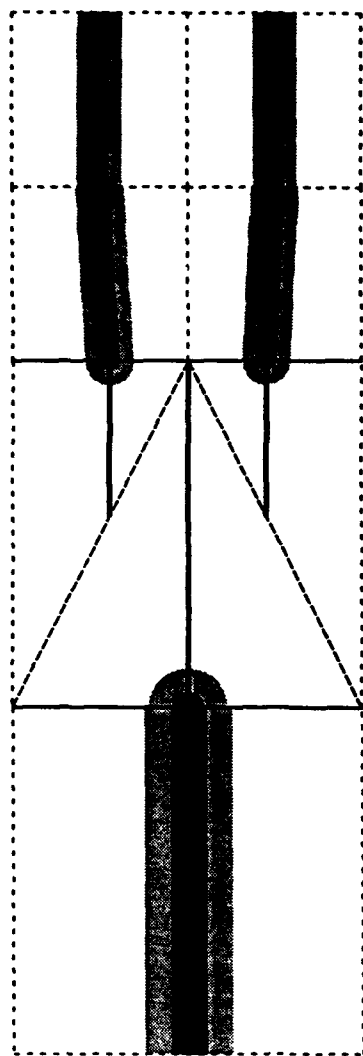
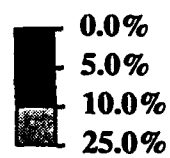


**Fig. 10a**

Simplified approach with L-2 norm  
Contours of  $\text{dux} - \text{duhx} = \text{eta}$   
 $p = 1$



—  $F\{Q1\} = 0\%$   
—  $F\{Q2\} = 0\%$

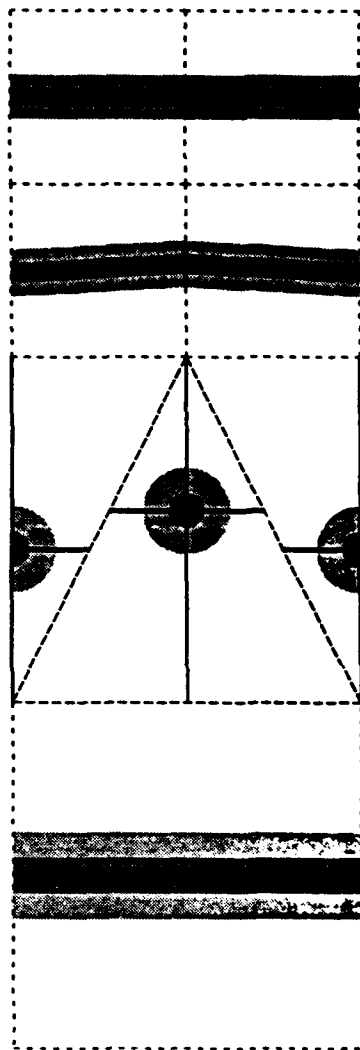
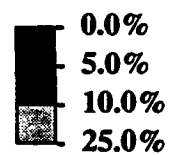


**Fig. 10b**

Simplified approach with L-2 norm  
Contours of duy - duhy = eta  
 $p = 1$



—  $F\{Q1\} = 0\%$   
—  $F\{Q2\} = 0\%$

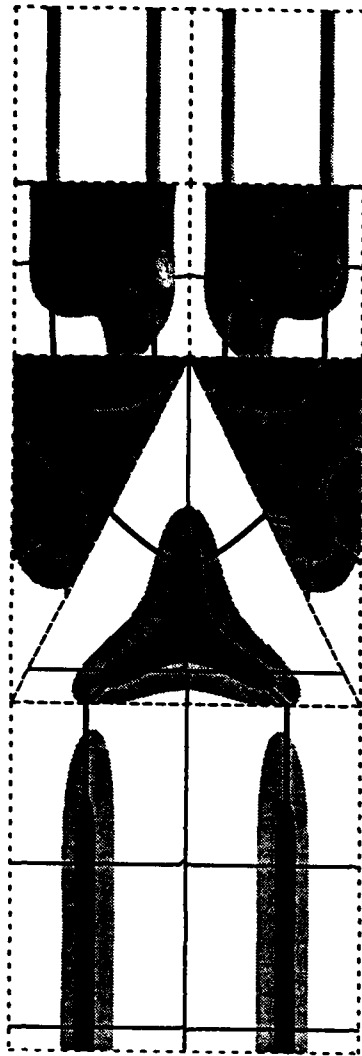


**Fig. 10c**

Simplified approach with L-2 norm  
Contours of  $du_x - du_{hx} = \eta$   
 $p = 2$



—  $F\{Q1\} = 0\%$   
—  $F\{Q2\} = 0\%$

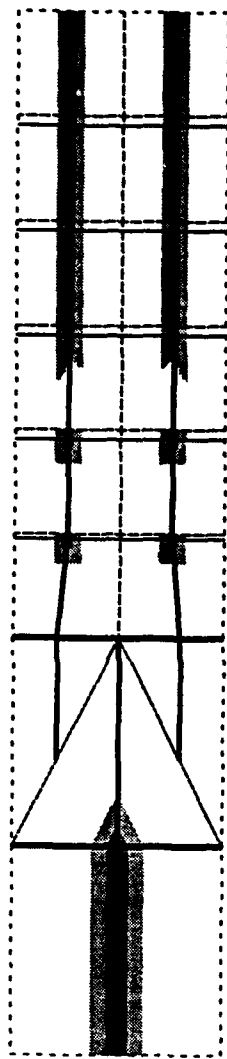
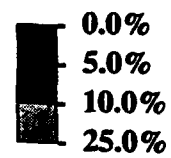


**Fig. 11a**

Direct approach  
Contours of  $du_x - du_{hx} = \epsilon$   
 $p = 1$



—  $F\{Q1\} = 0\%$   
—  $F\{Q2\} = 0\%$

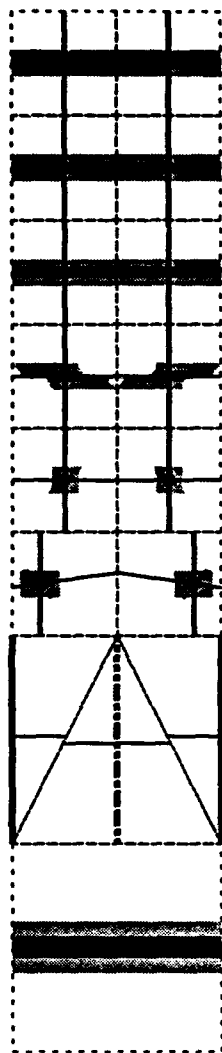
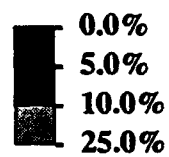


**Fig. 11b**

Direct approach  
Contours of duy - duhy = eta  
 $p = 1$



—  $F\{Q1\} = 0\%$   
—  $F\{Q2\} = 0\%$

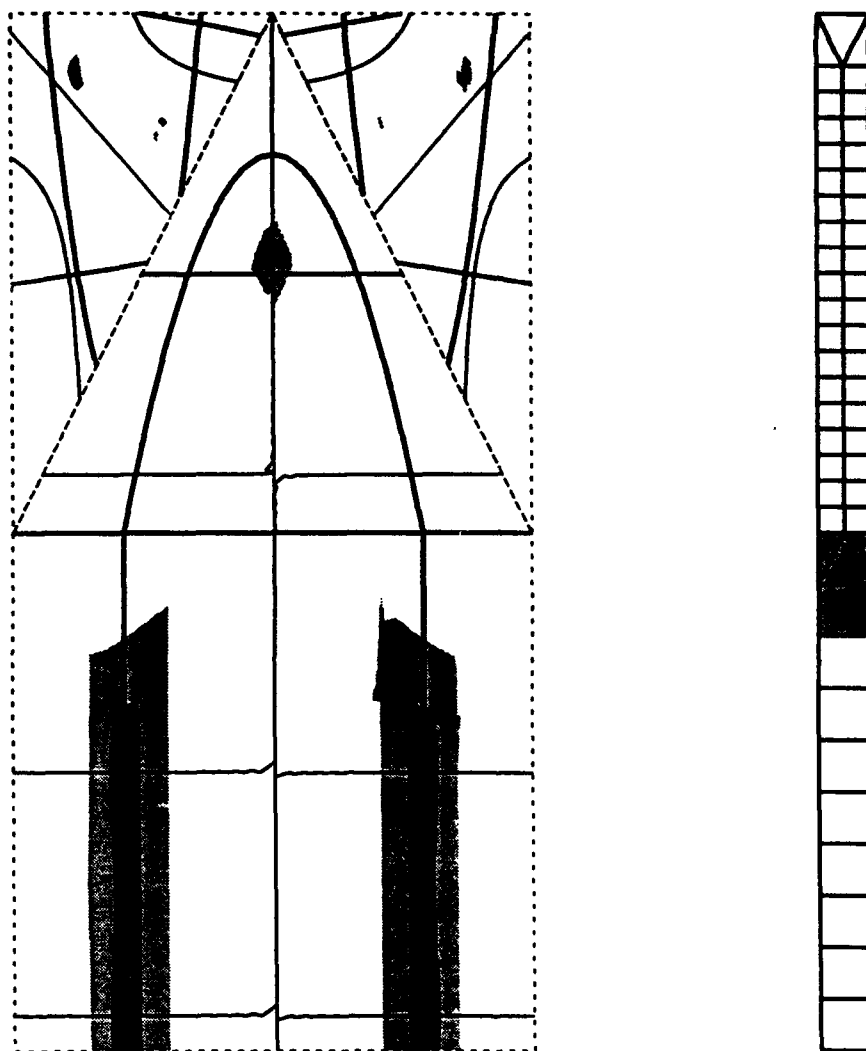
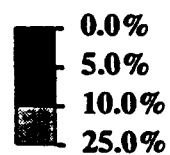


**Fig. 11c**

**Direct approach**  
**Contours of  $dux - duhx = \eta$**   
 $p = 2$



**$F\{Q1\} = 0\%$**   
 **$F\{Q2\} = 0\%$**

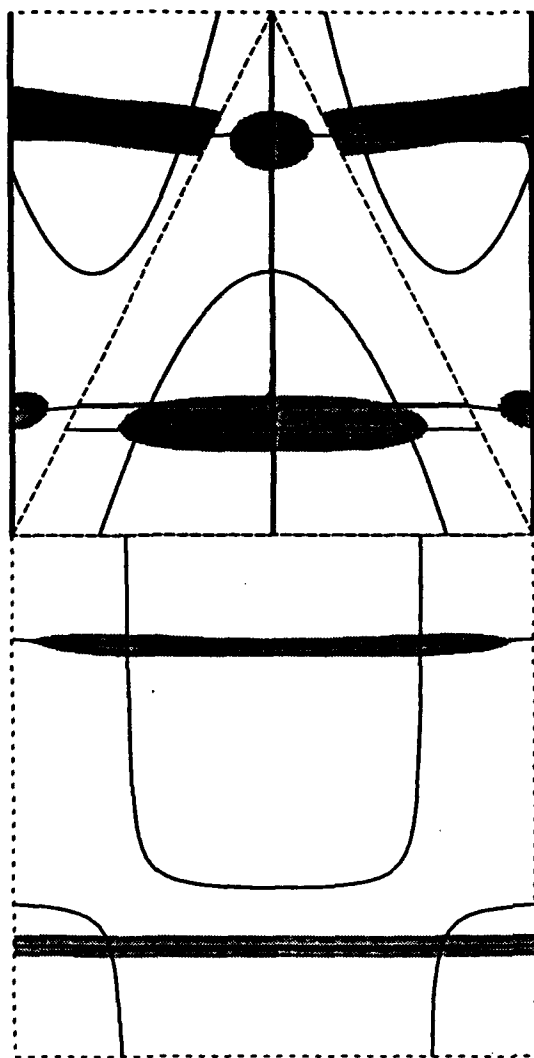


**Fig. 11d**

Direct approach  
Contours of  $\text{duy} - \text{duhy} = \text{eta}$   
 $p = 2$



—  $F\{Q1\} = 0\%$   
—  $F\{Q2\} = 0\%$



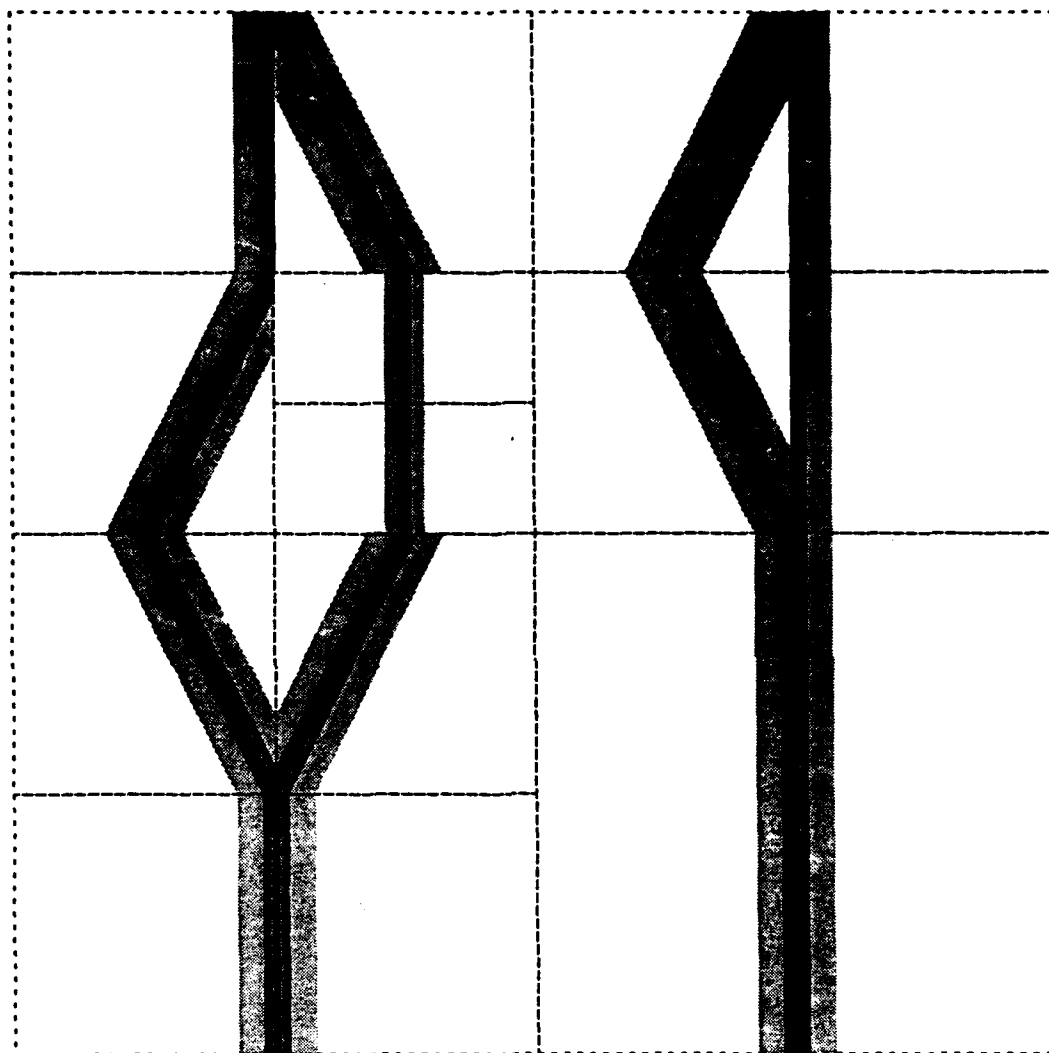
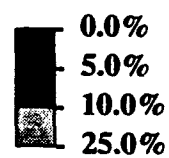


**Fig. 12a**

Simplified approach with L-2 norm  
 Contours of  $\text{dux} - \text{duhx} = \text{eta}$   
 $p = 1$



—  $F\{Q1\} = 0\%$   
 —  $F\{Q2\} = 0\%$

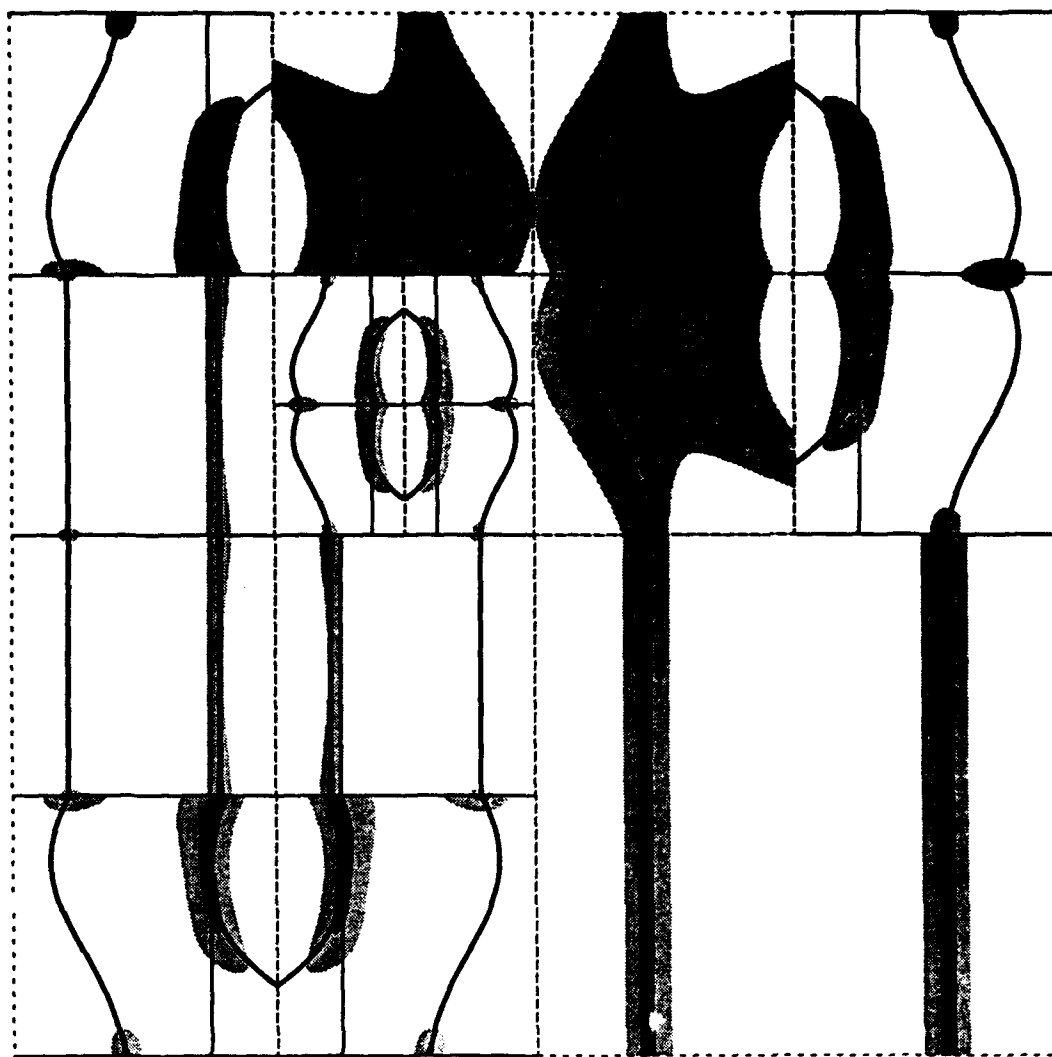
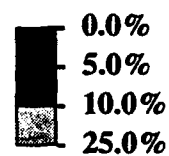


**Fig. 12b**

Simplified approach with L-2 norm  
 Contours of  $\text{dux} - \text{duhx} = \text{eta}$   
 $p = 2$



—  $F\{Q1\} = 0\%$   
 —  $F\{Q2\} = 0\%$

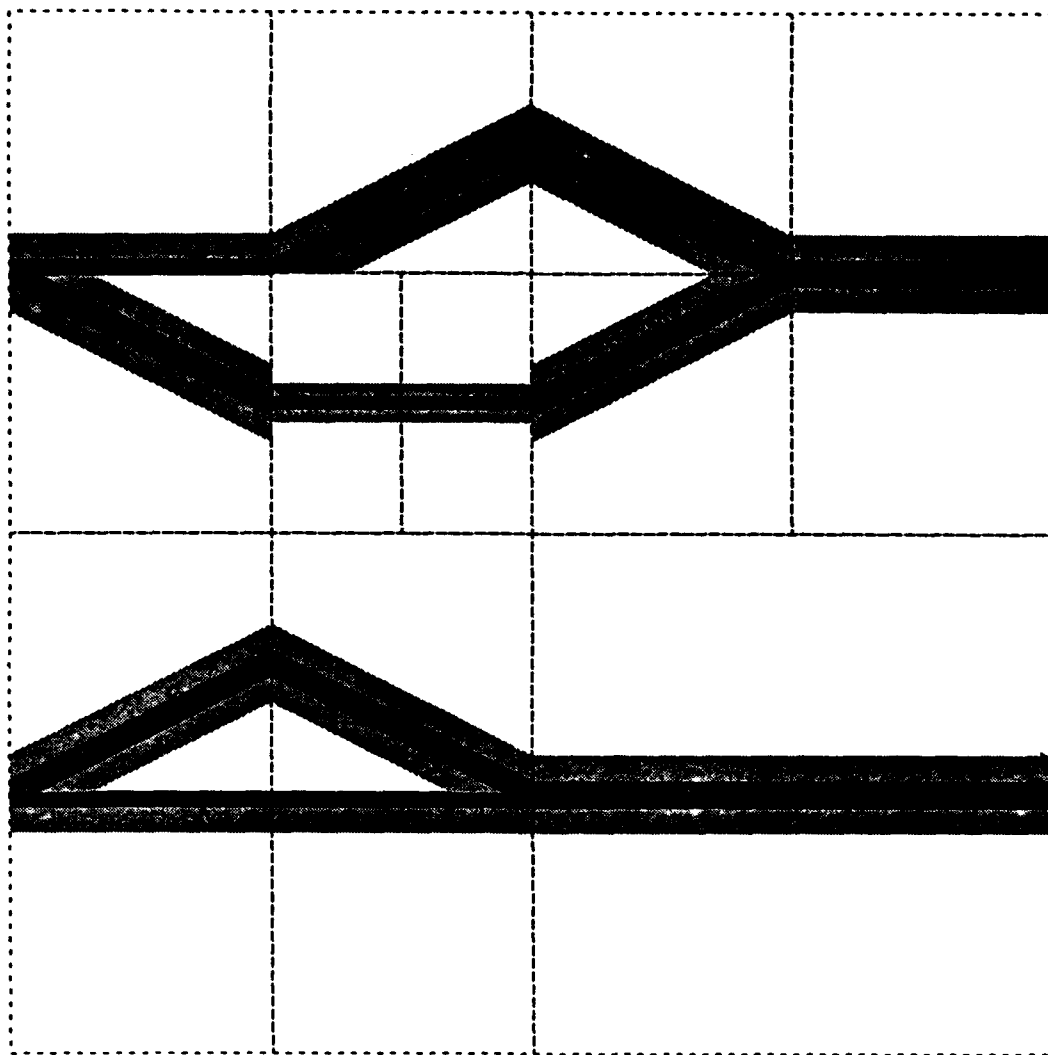
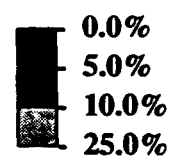


**Fig. 12c**

**Simplified approach with L-2 norm**  
**Contours of duy - duhy = eta**  
 $p = 1$



—  $F\{Q1\} = 0\%$   
 —  $F\{Q2\} = 0\%$

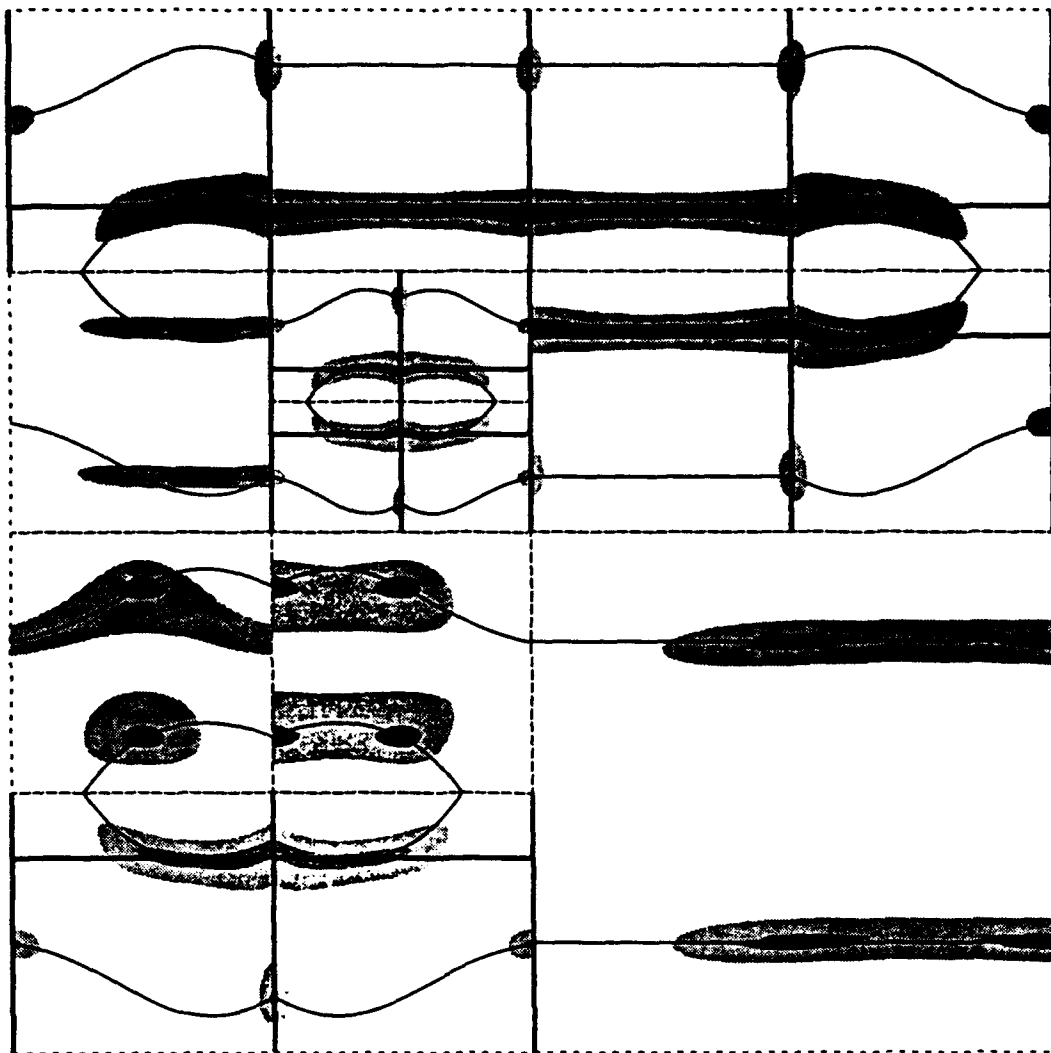


**Fig. 12d**

Simplified approach with L-2 norm  
 Contours of  $du_y - du_{hy} = \eta$   
 $p = 2$



—  $F\{Q1\} = 0\%$   
 —  $F\{Q2\} = 0\%$

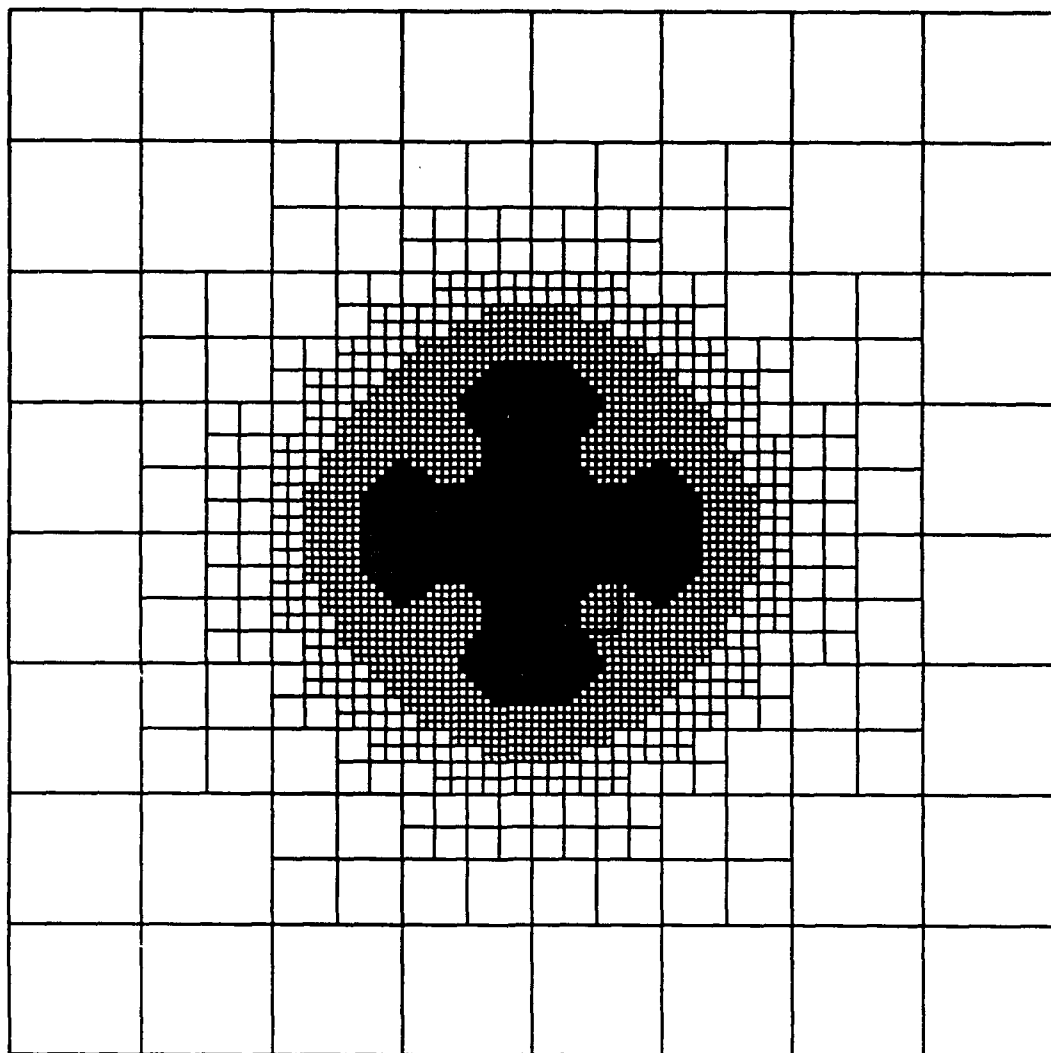


**Fig. 13a**

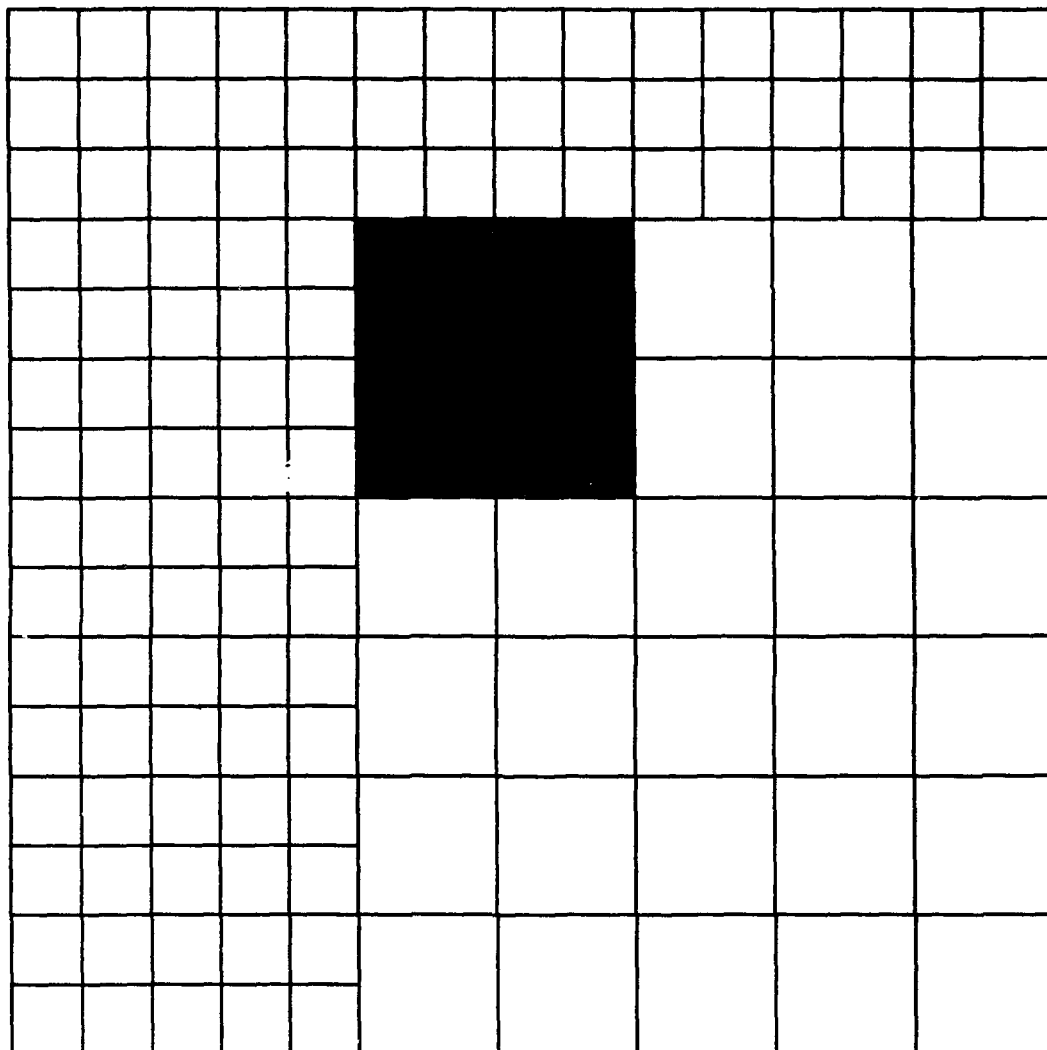


**Fig. 13b**

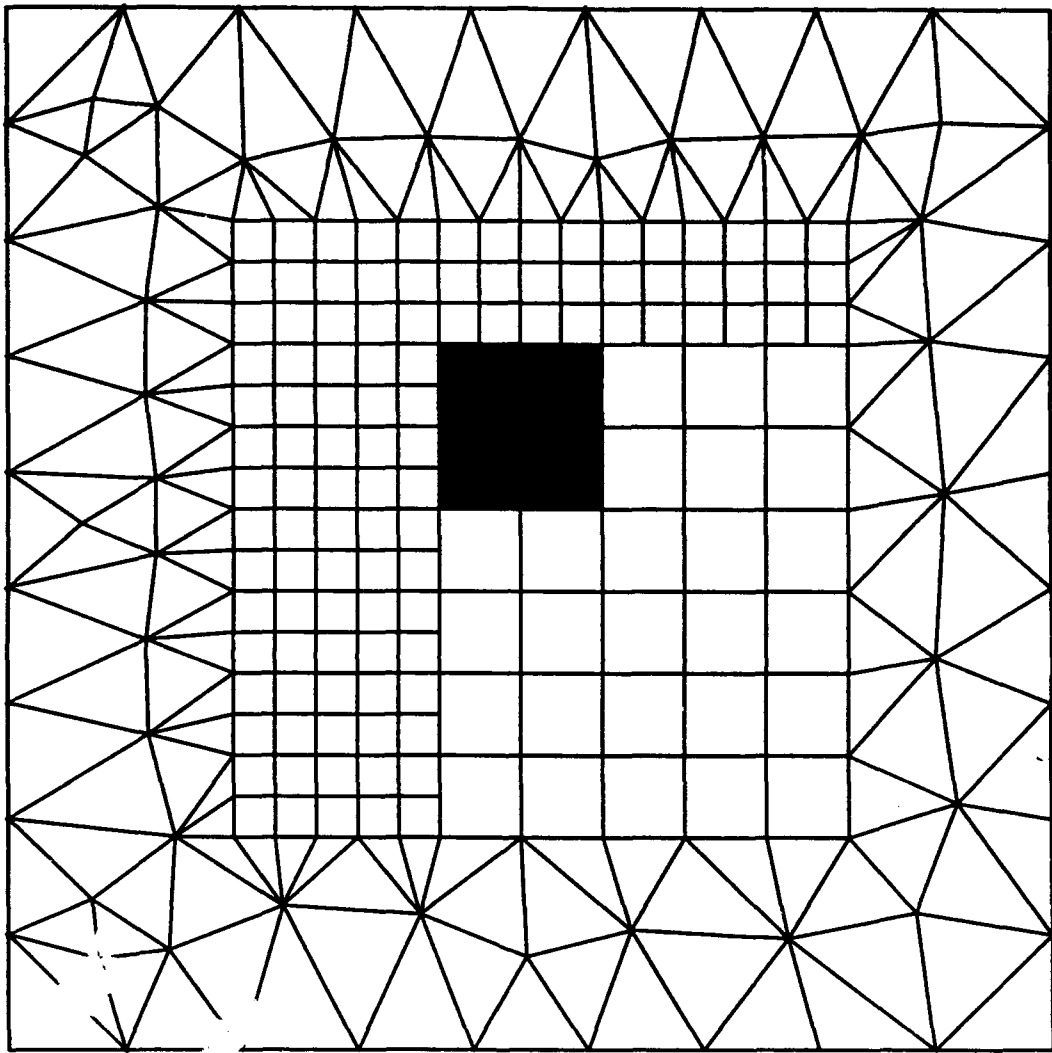


**Fig. 13c**

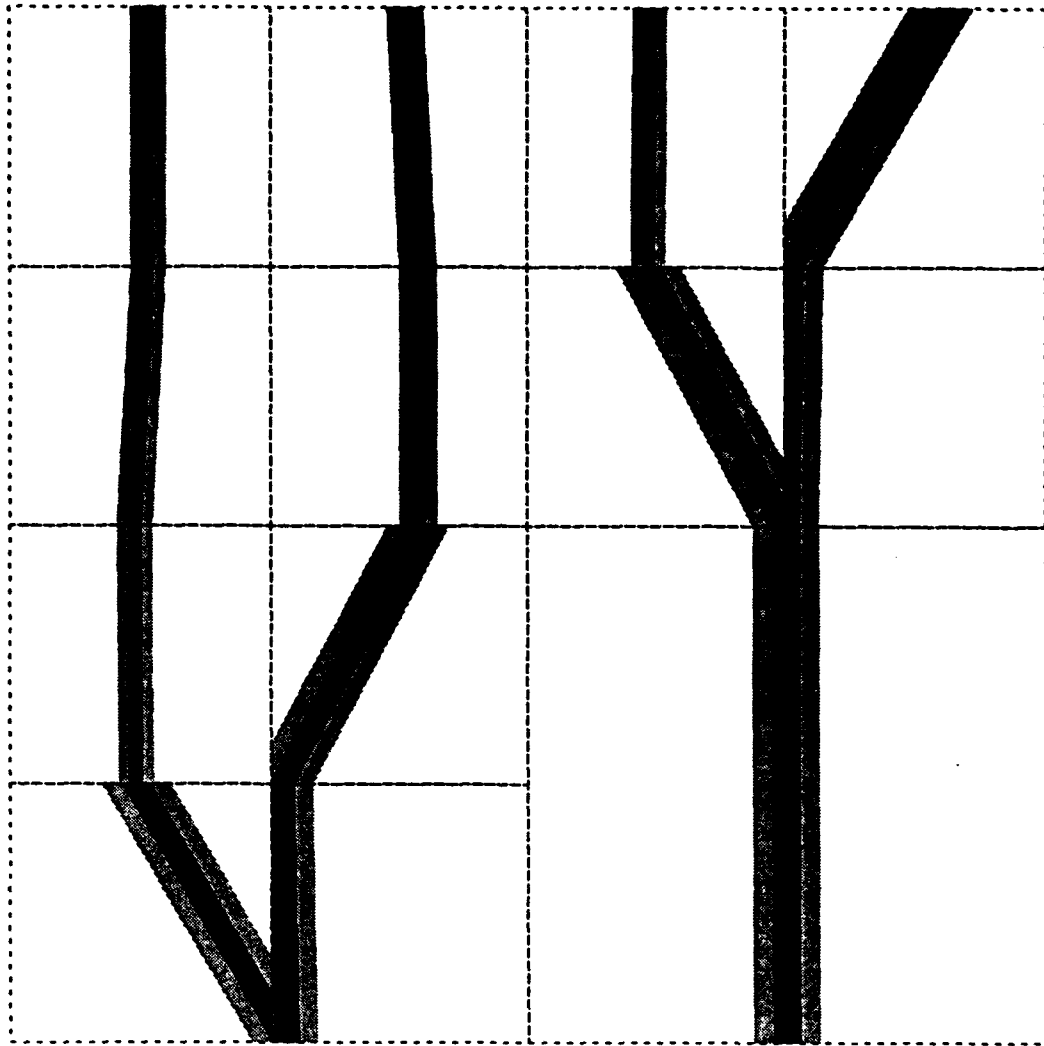
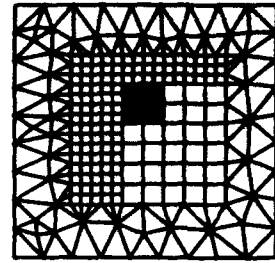
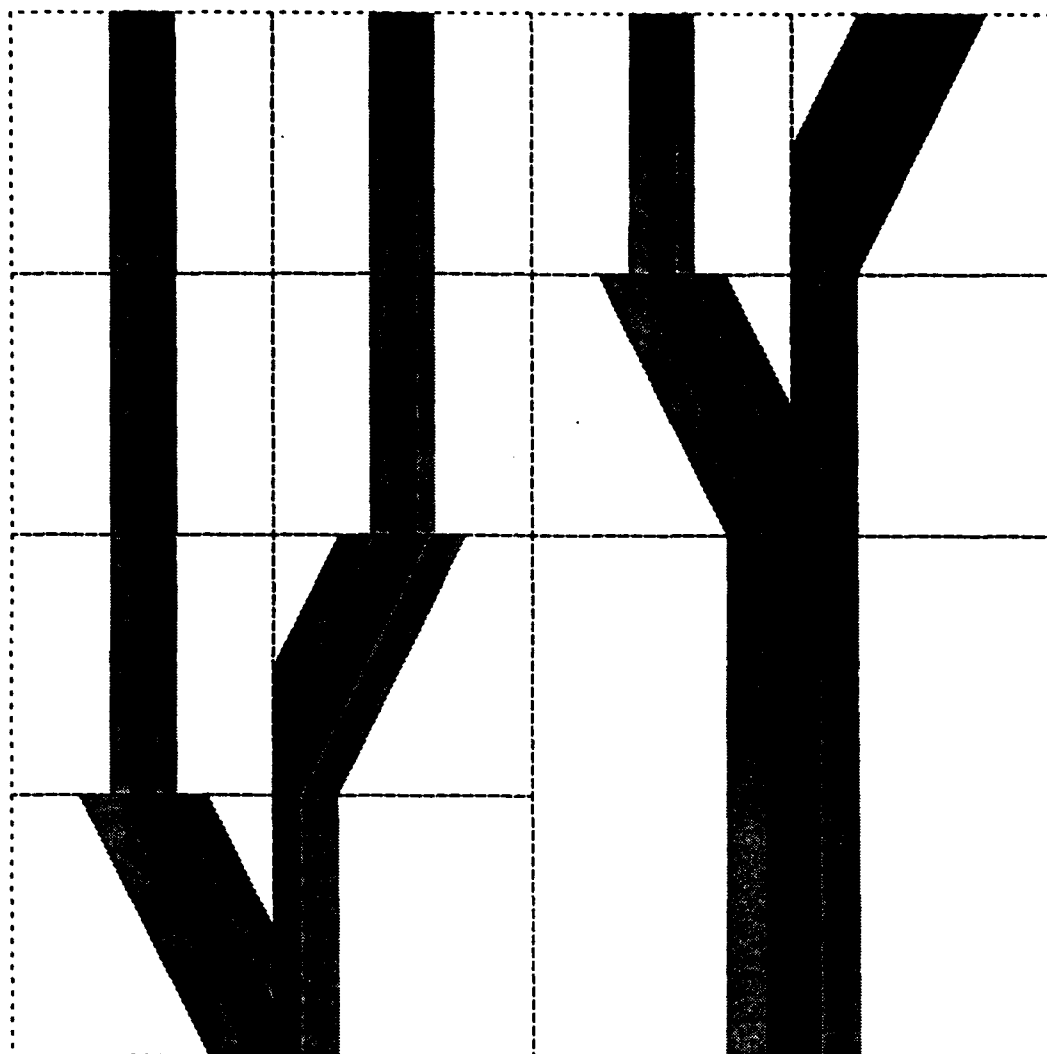


**Fig. 14a**

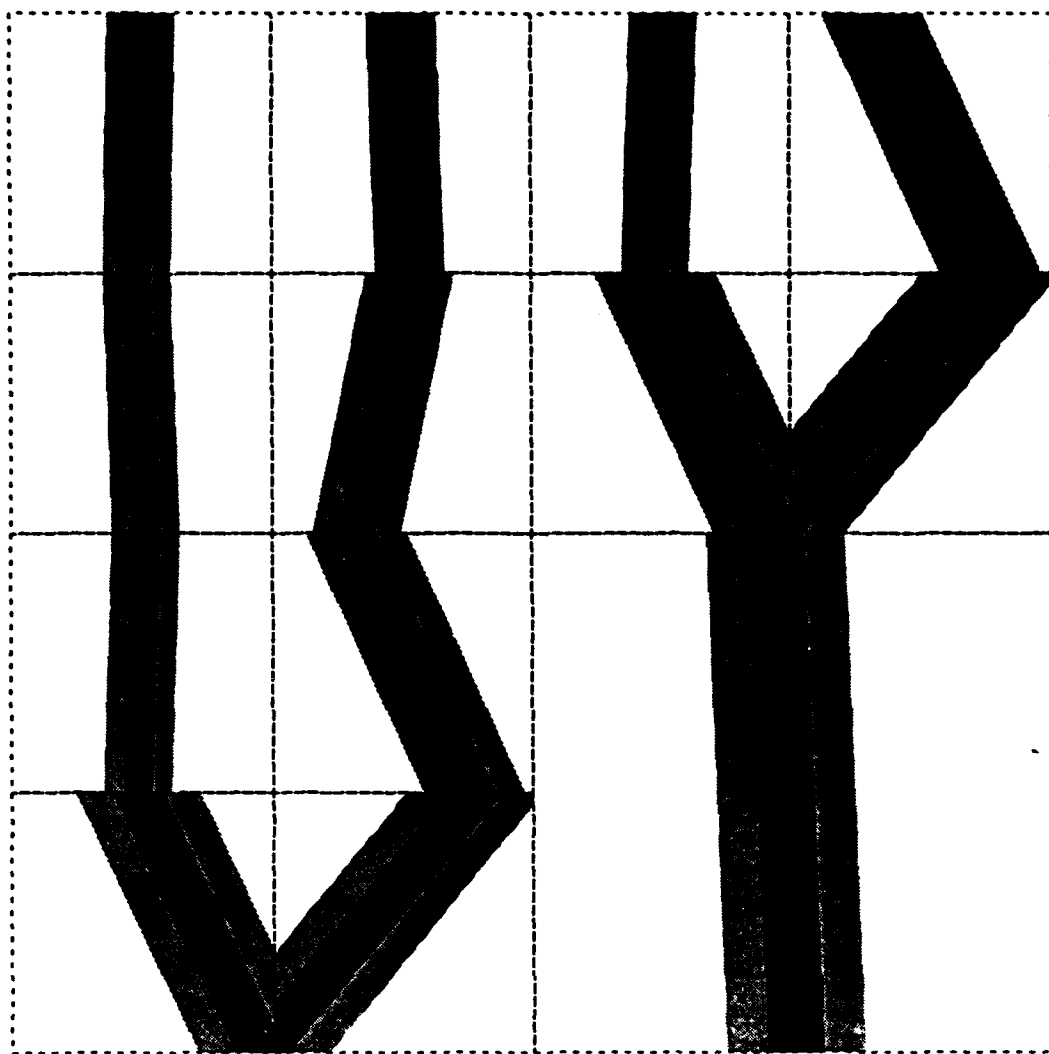
**Simplified approach with L-2 norm**



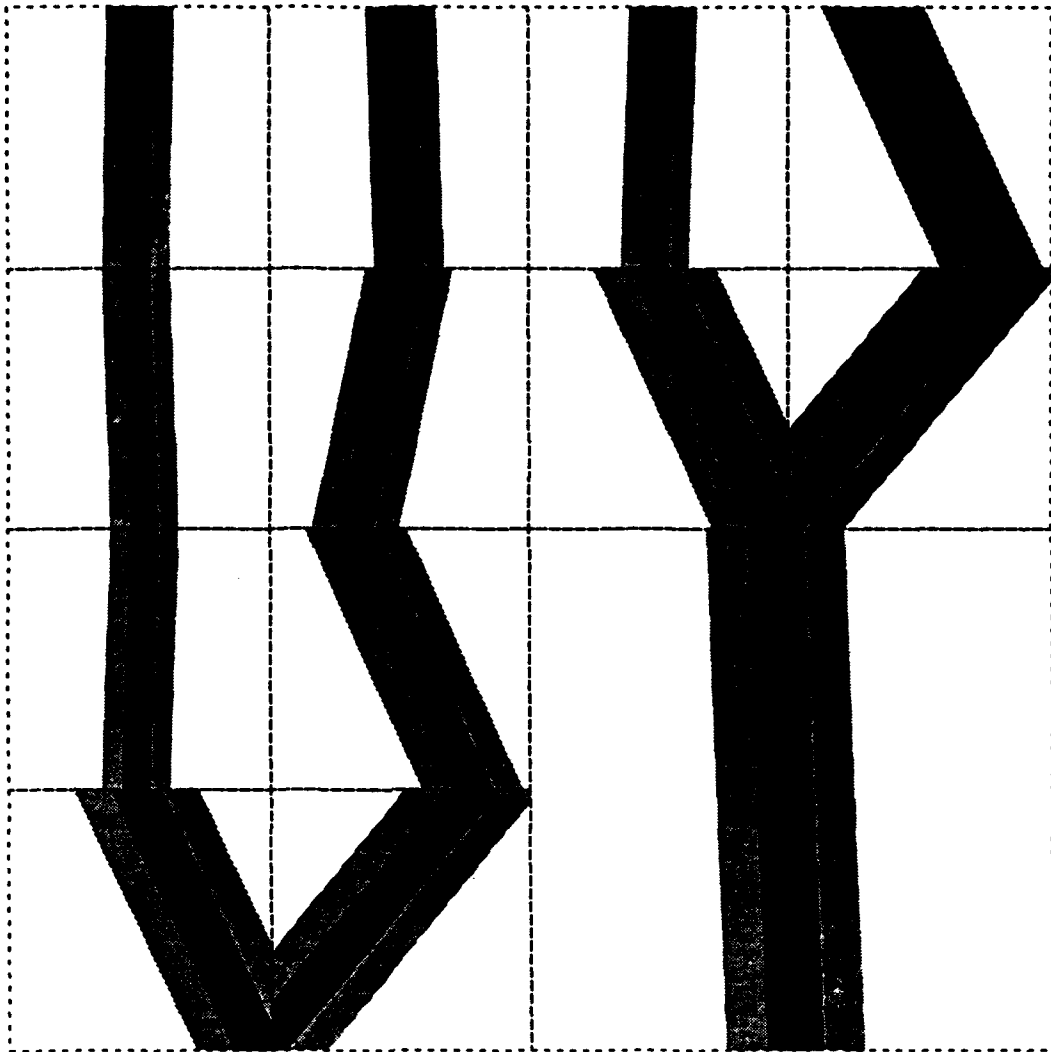
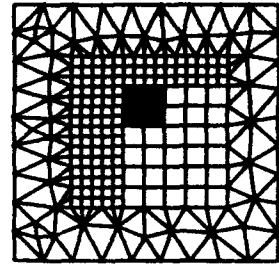




**Fig. 14b**



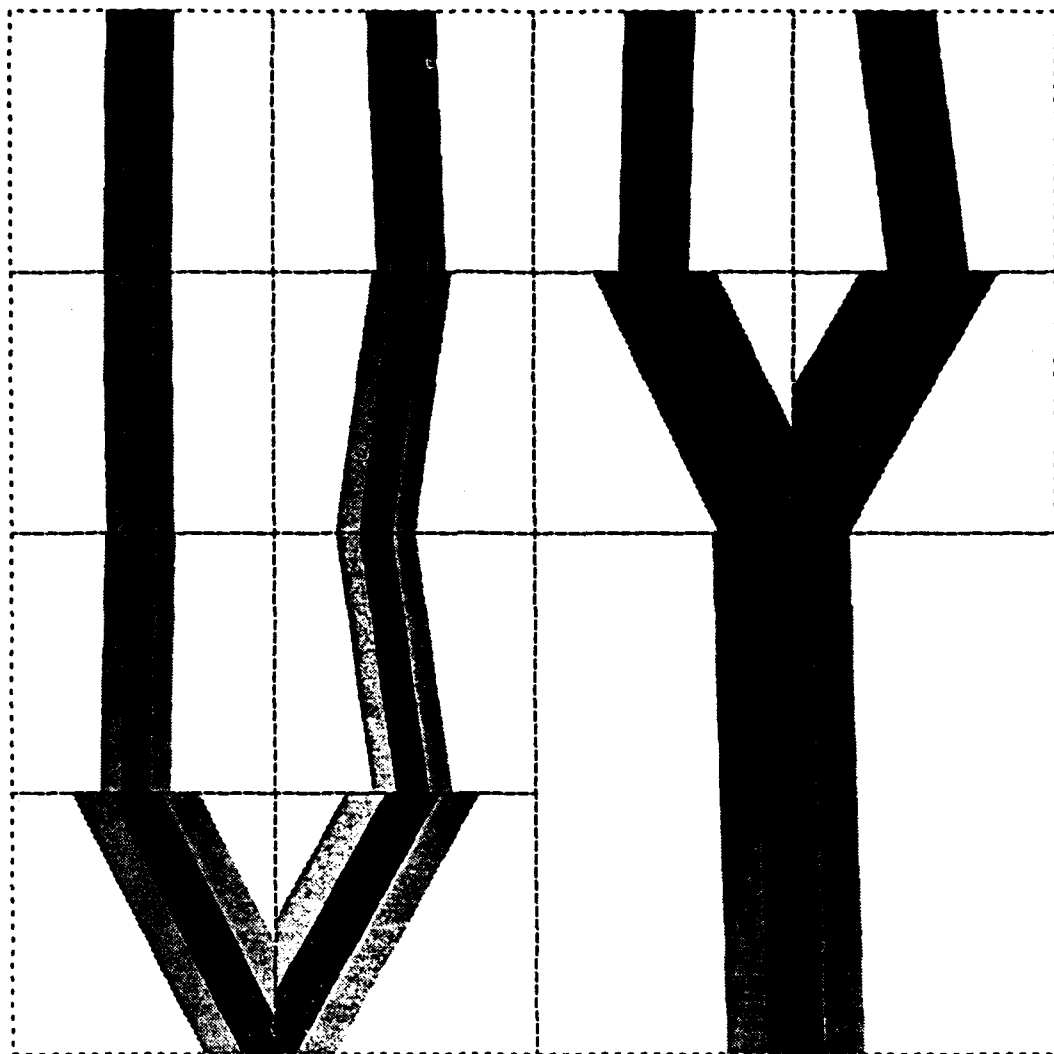
**Fig. 15a**



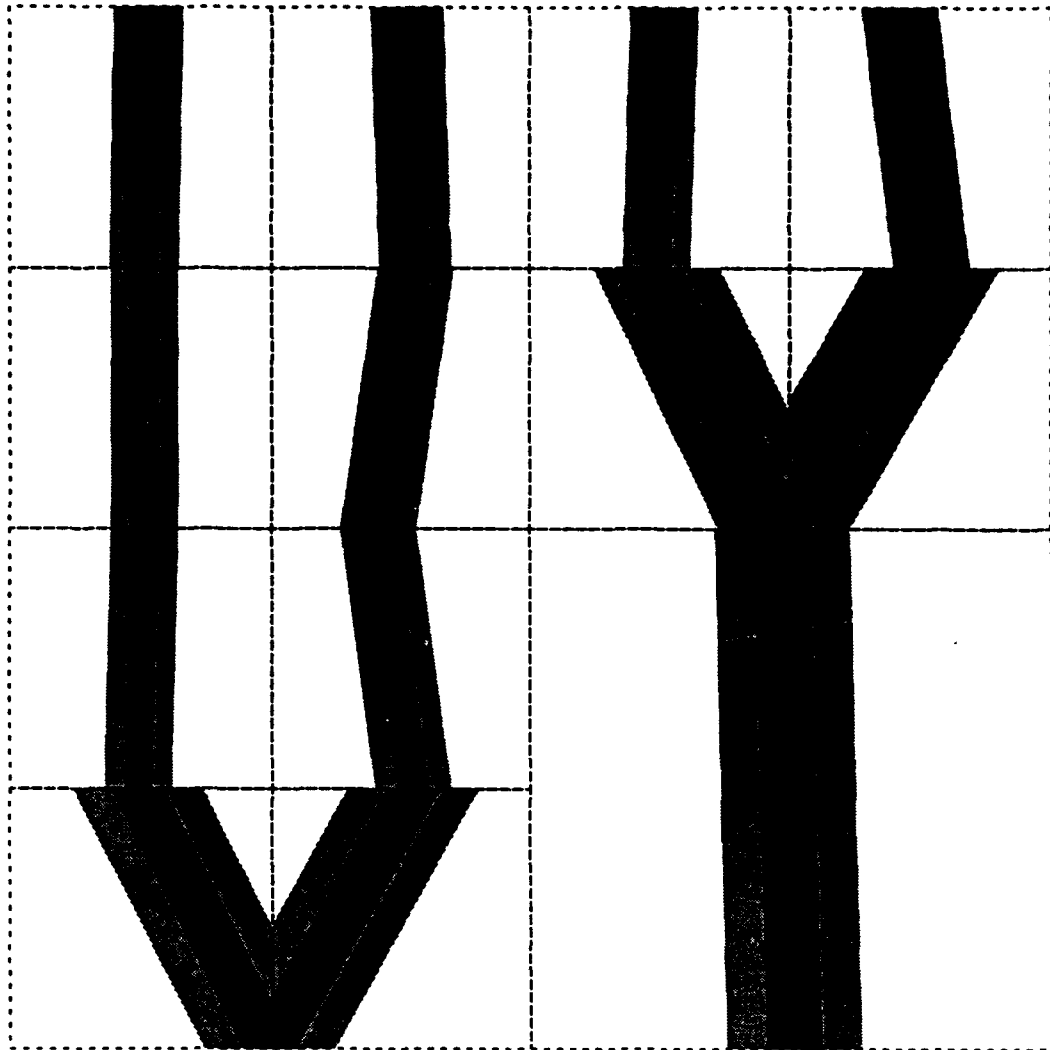
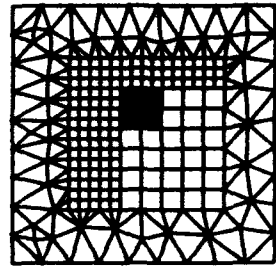
**Fig.15b**

**Simplified approach with L-2 norm**



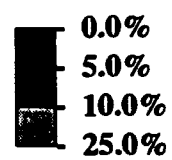


**Fig. 16a**



**Fig. 16b**

**Simplified approach with L-2 norm**



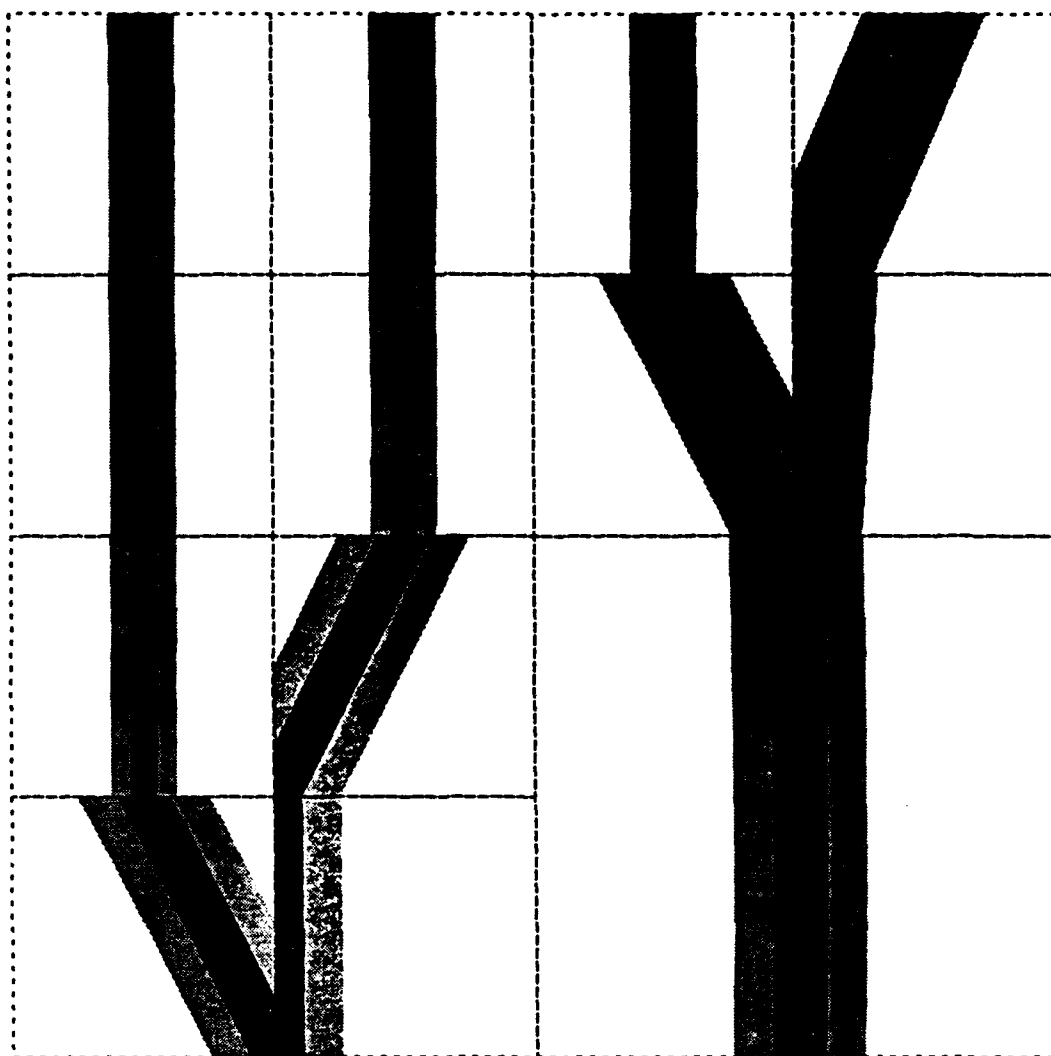


**Fig. 17a**

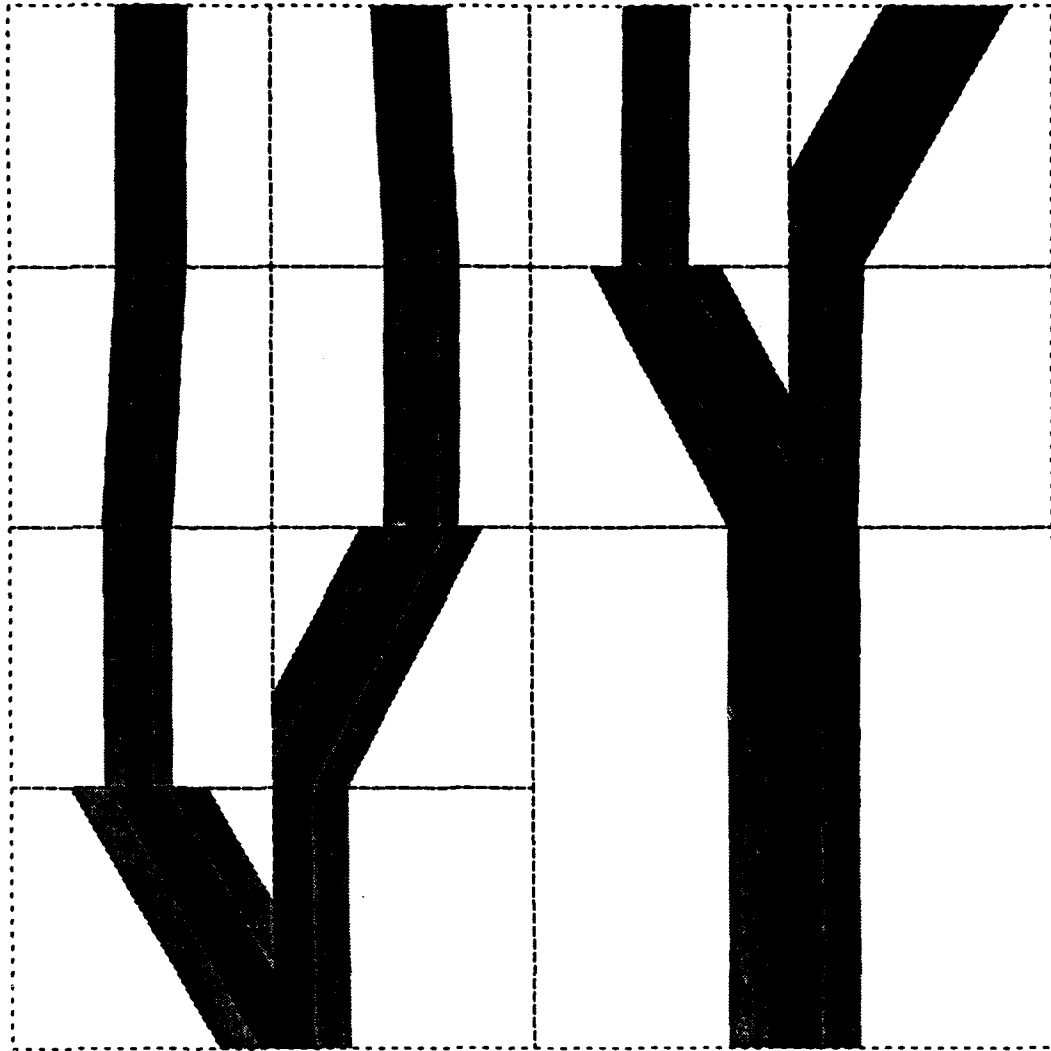
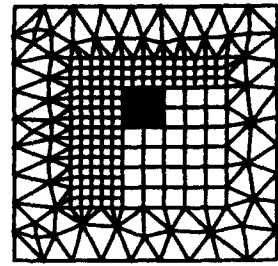


**Fig. 17b**

**Simplified approach with L-2 norm**



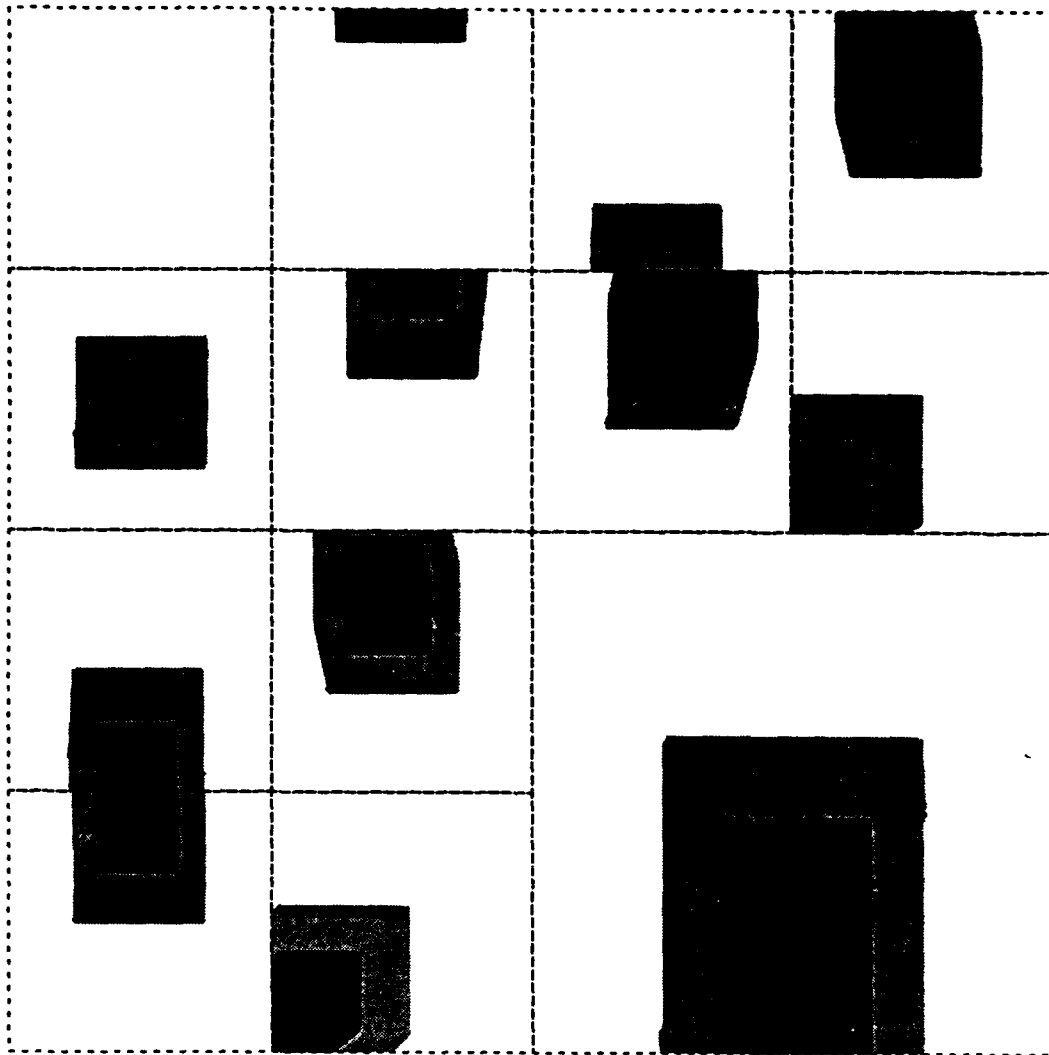
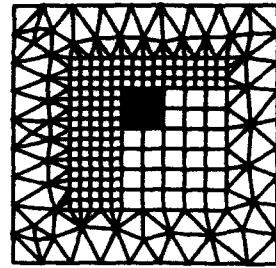
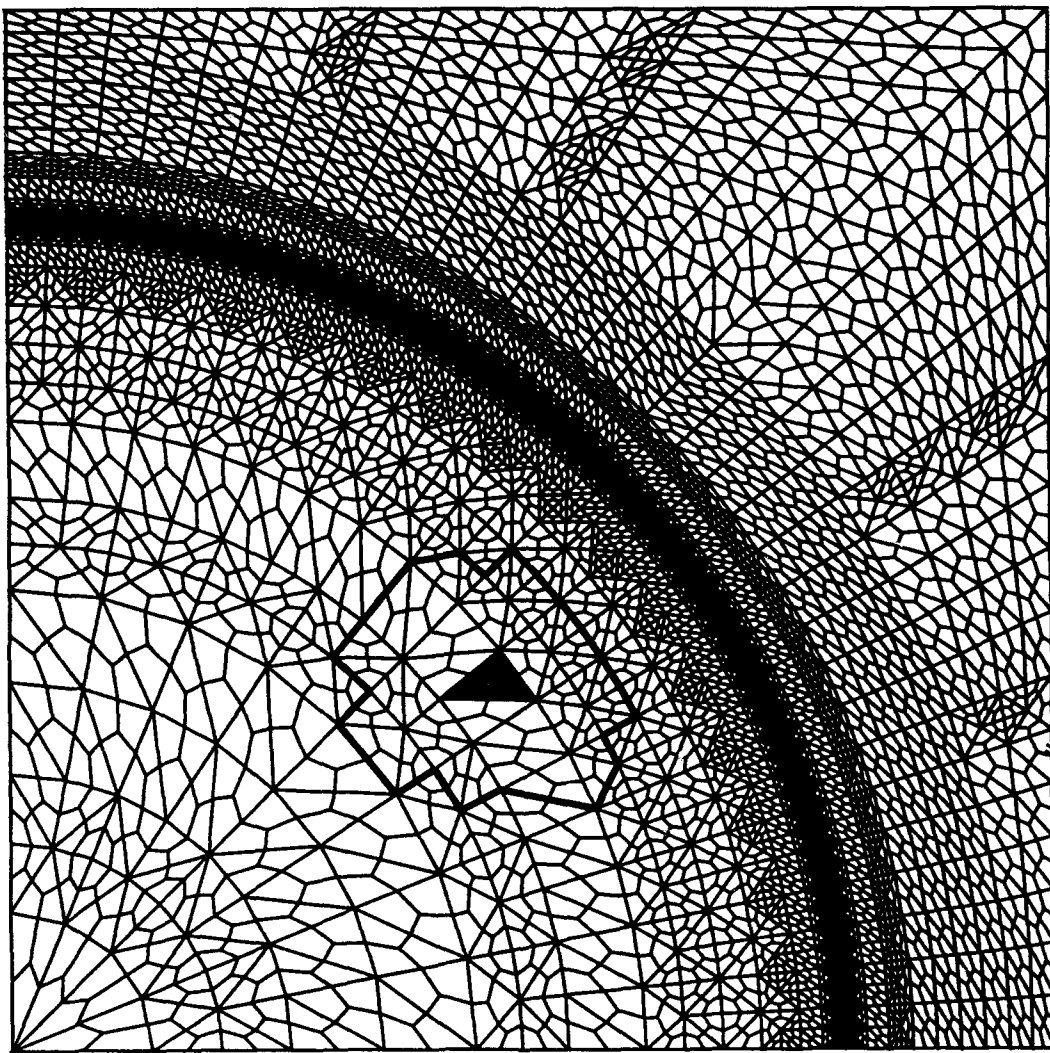


**Fig. 18**

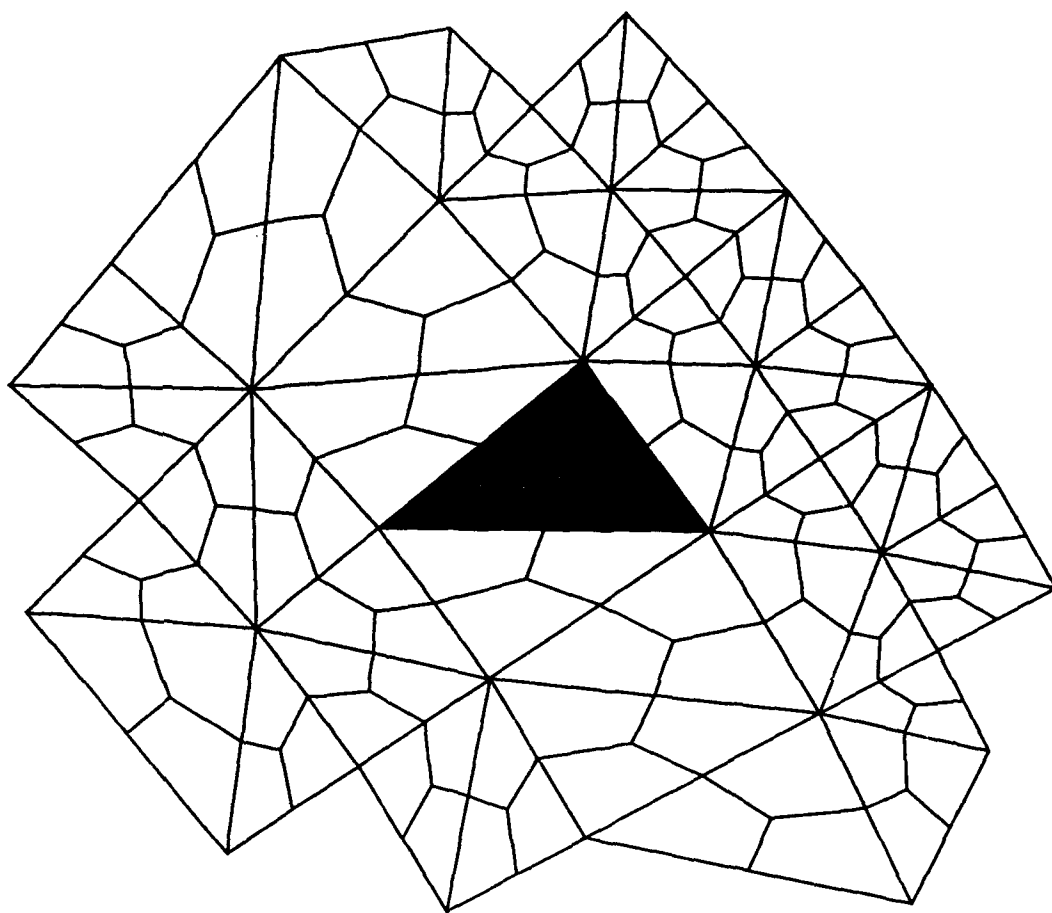
**Direct approach**



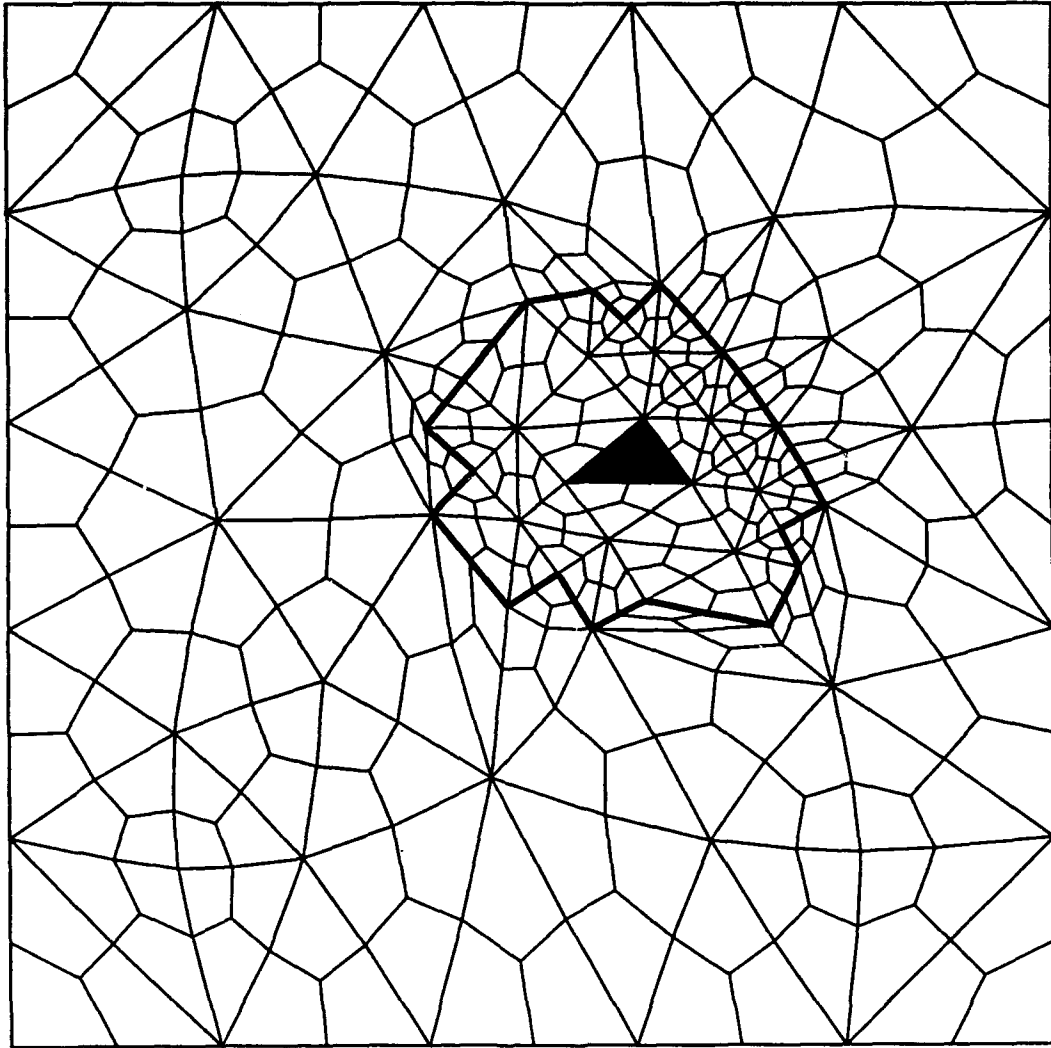




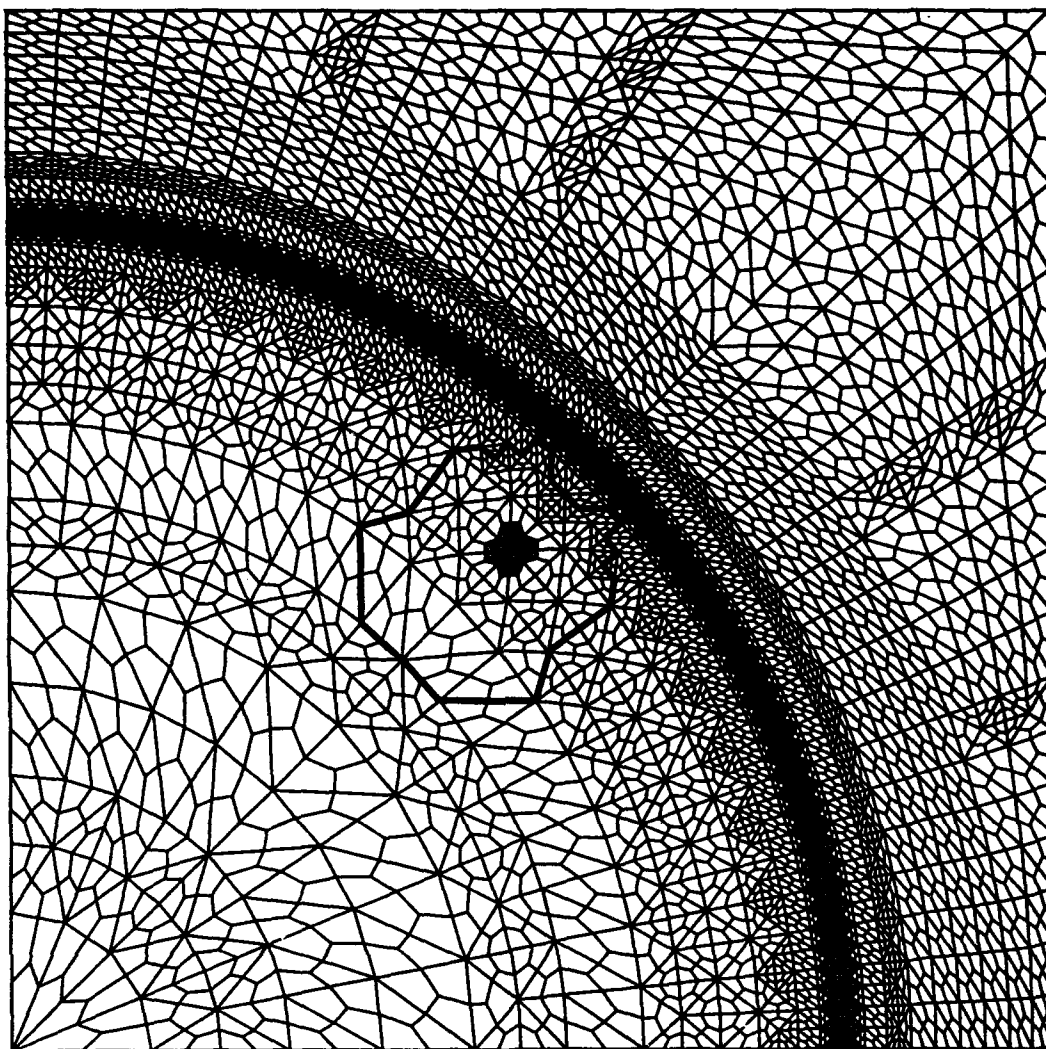
**Fig. 19a**



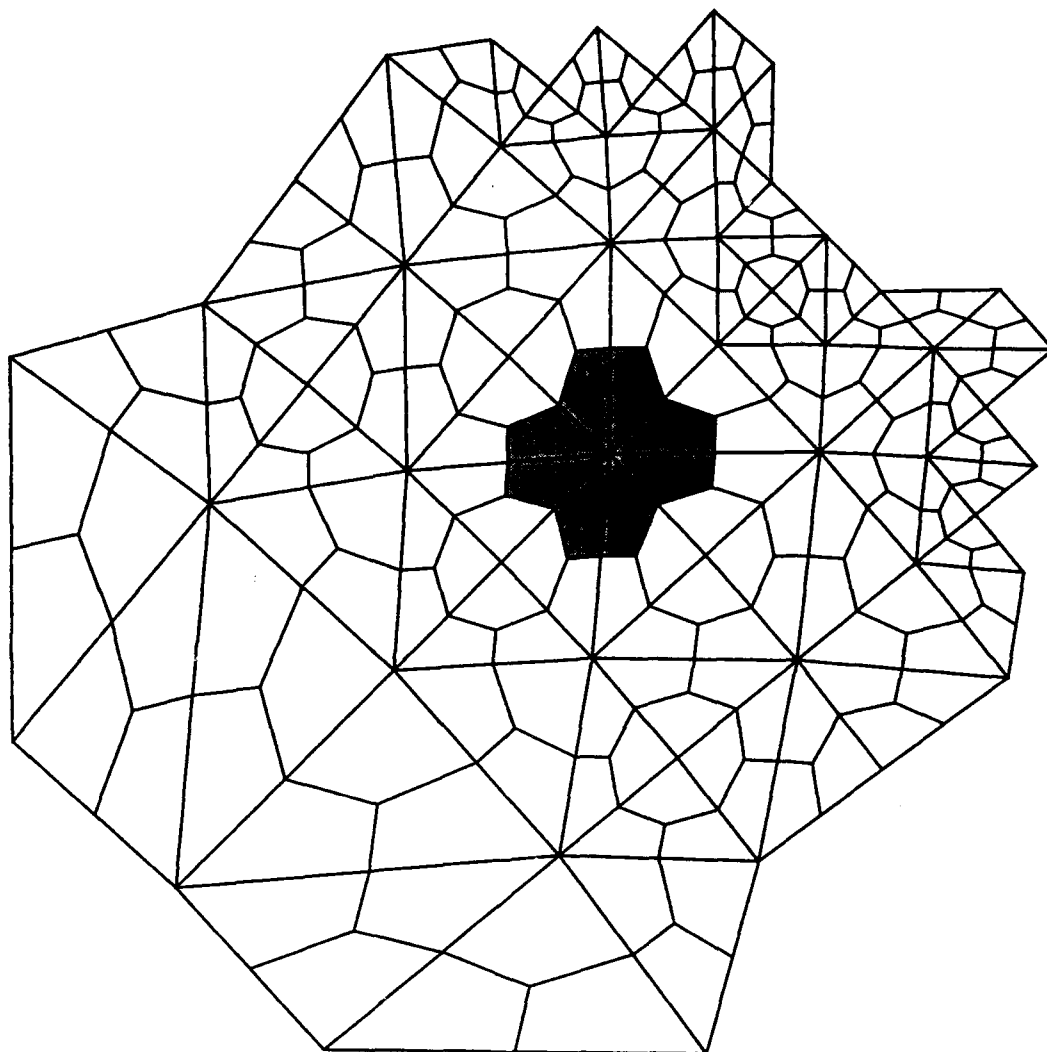
**Fig. 19b**



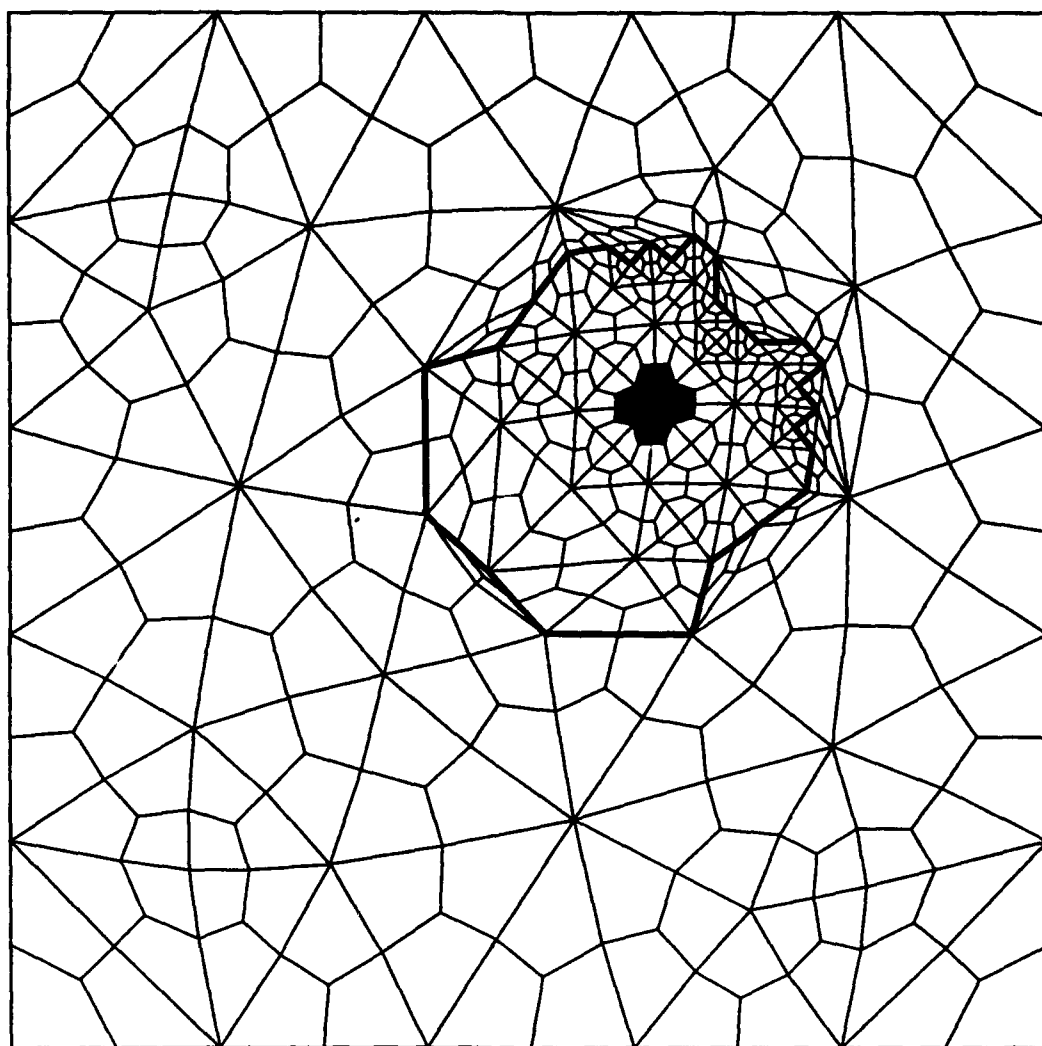
**Fig. 19c**



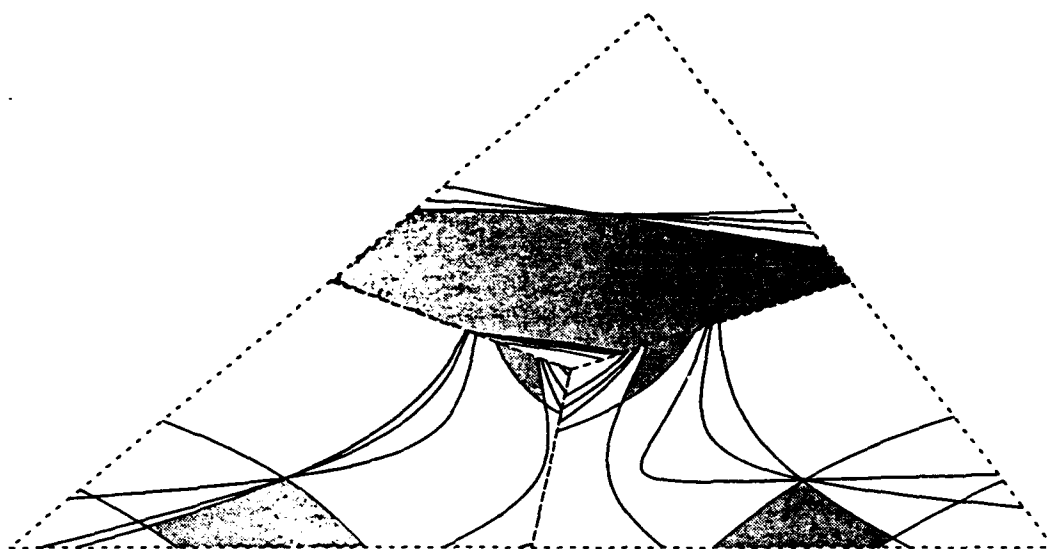
**Fig. 20a**



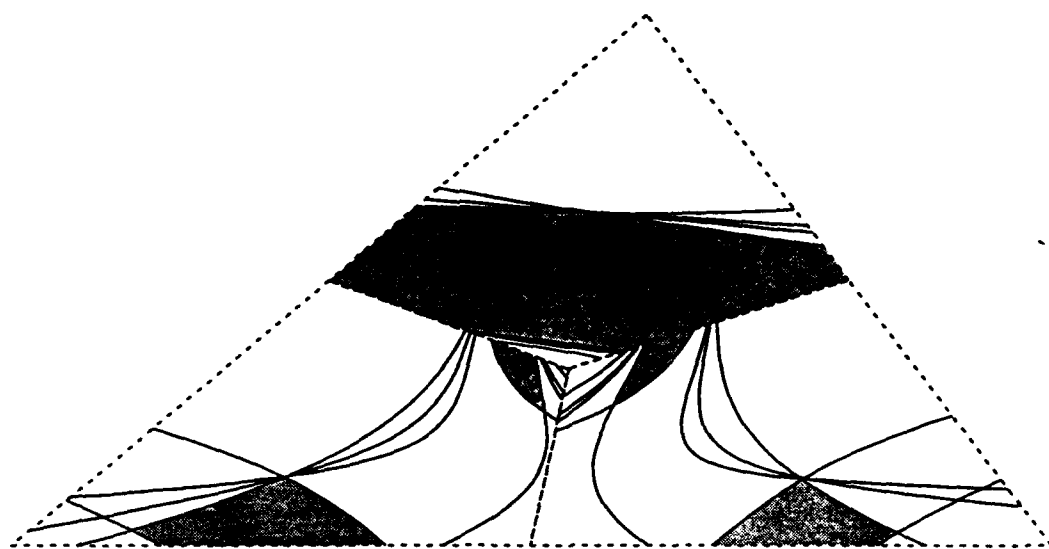
**Fig. 20b**



**Fig. 20c**

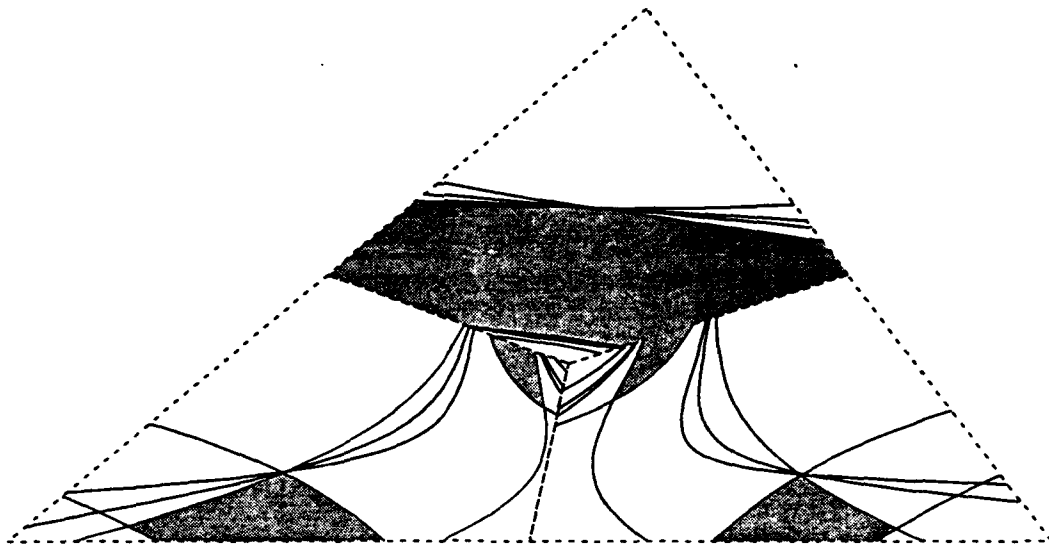
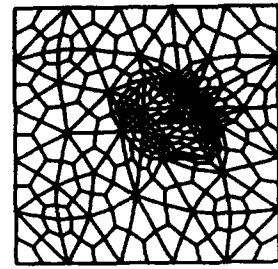


**Fig. 21a**

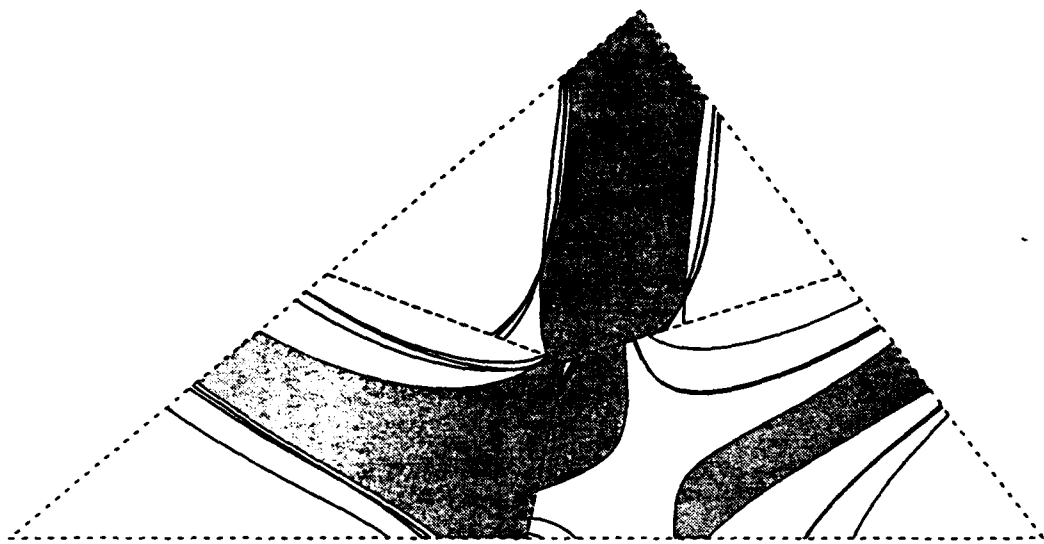


**Fig. 21b**

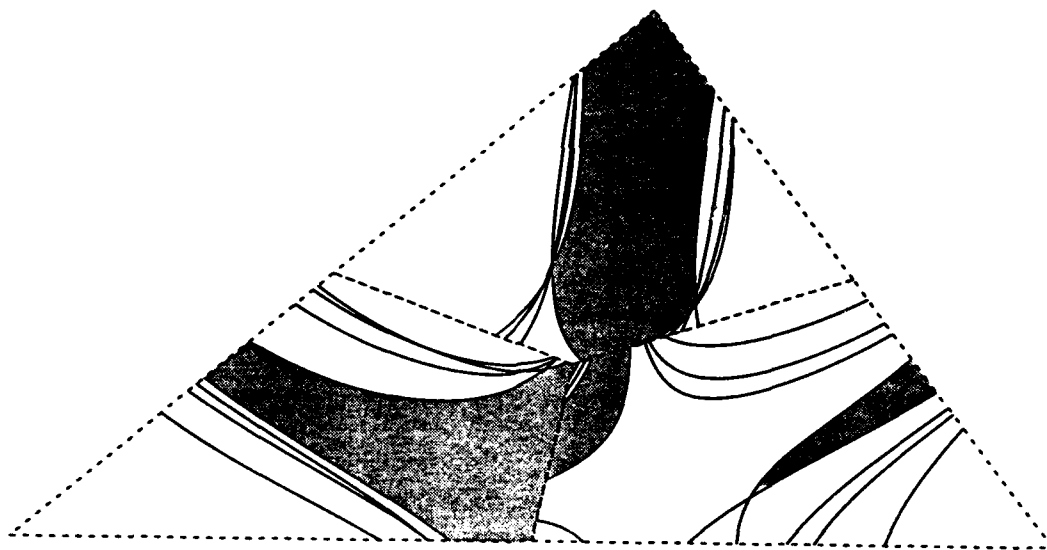




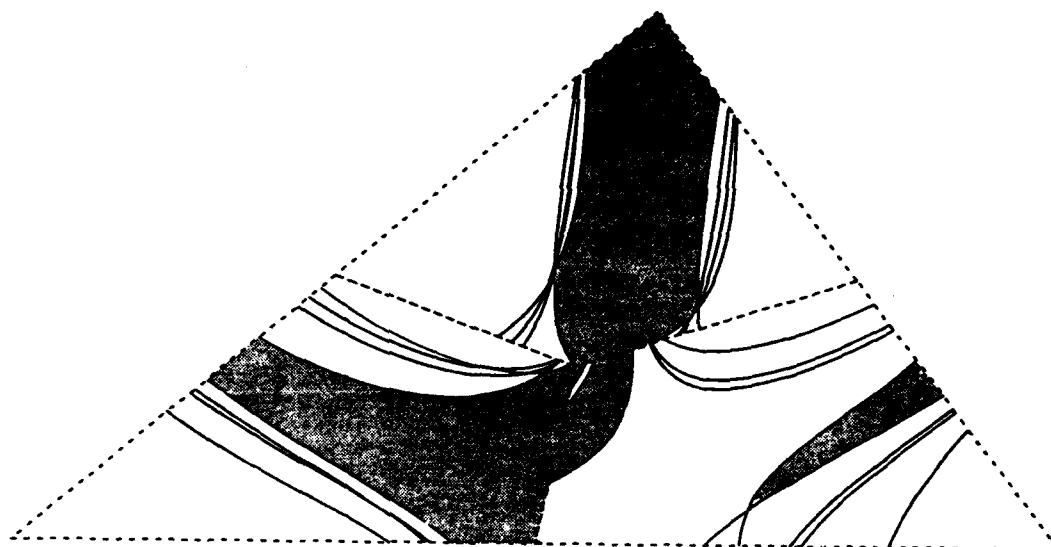
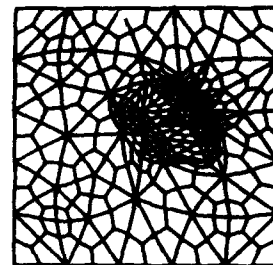
**Fig. 21c**



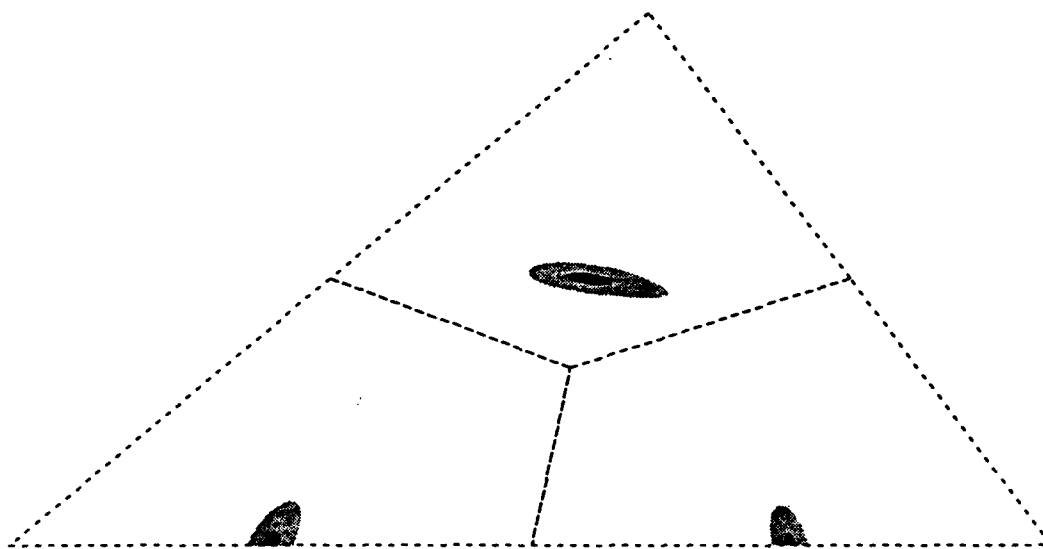
**Fig. 21d**



**Fig. 21e**

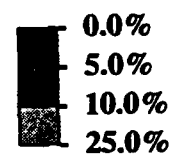


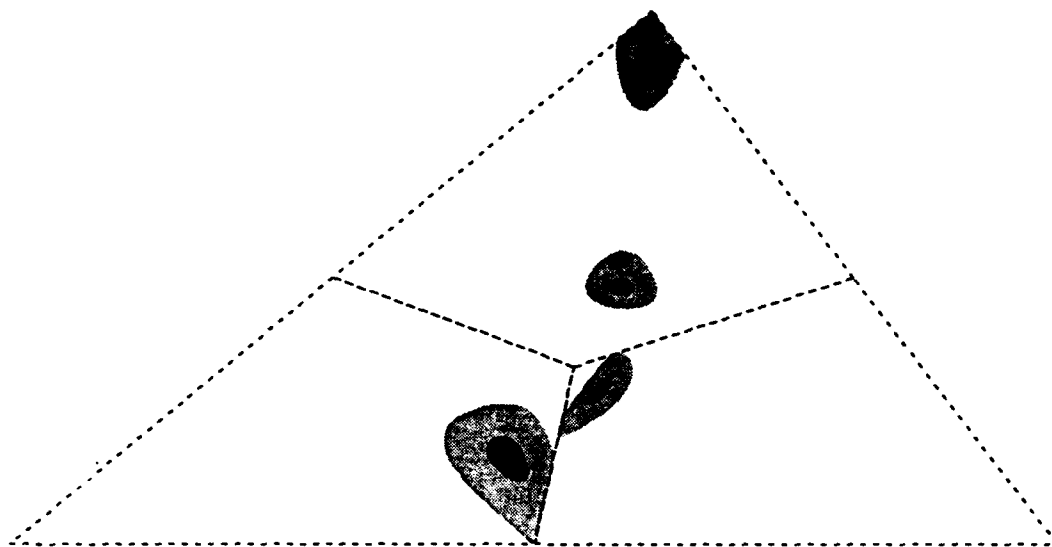
**Fig. 21f**



**Fig. 21g**

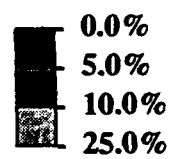
**Simplified approach with L-2 norm**

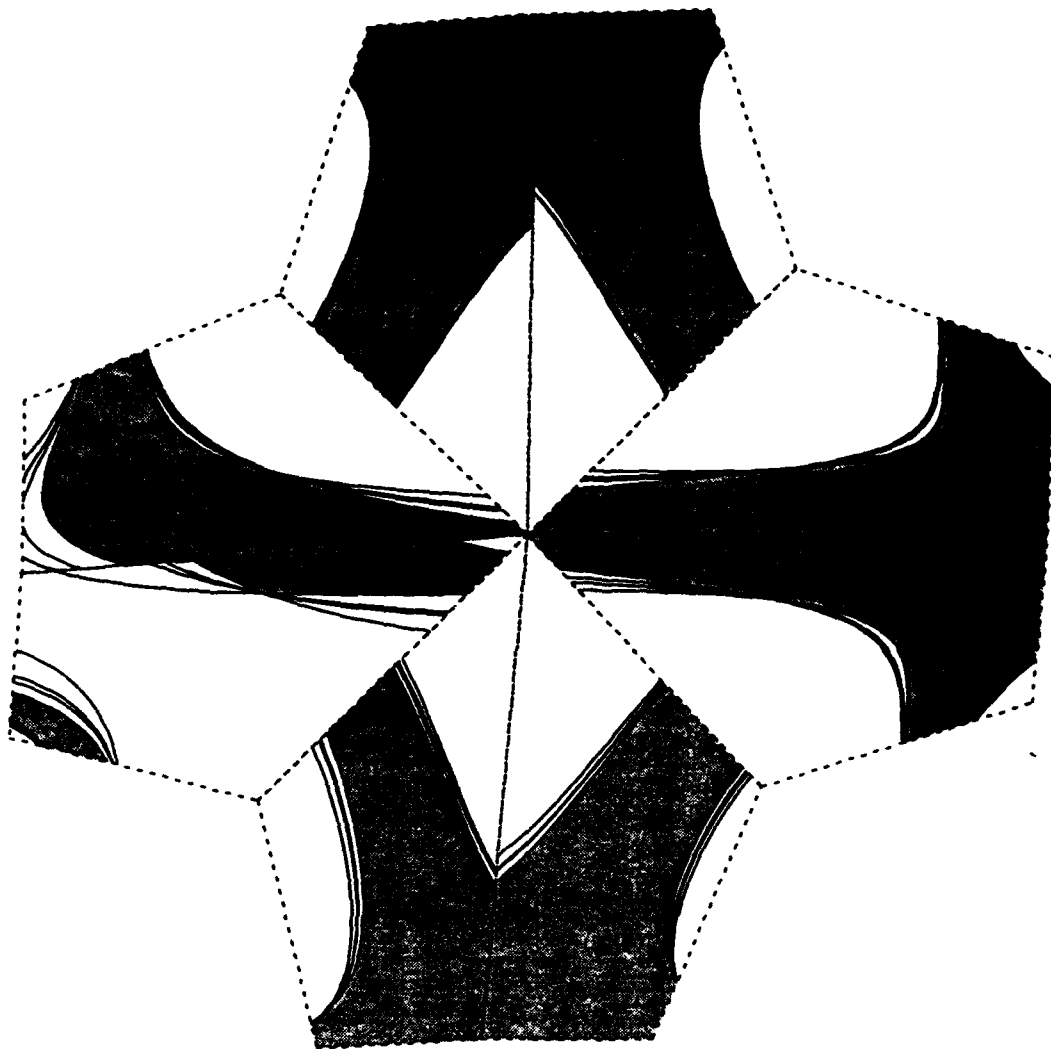




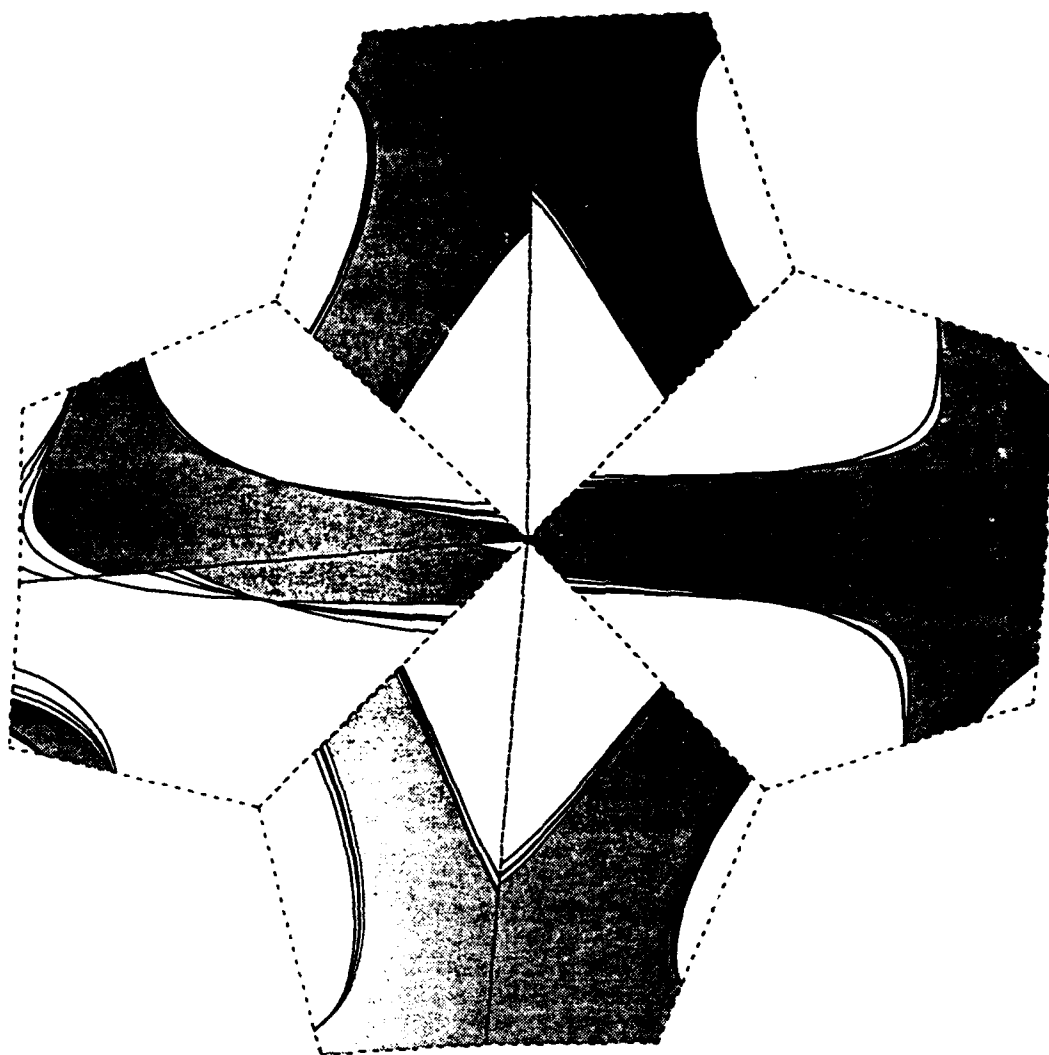
**Fig. 21h**

**Simplified approach with L-2 norm**



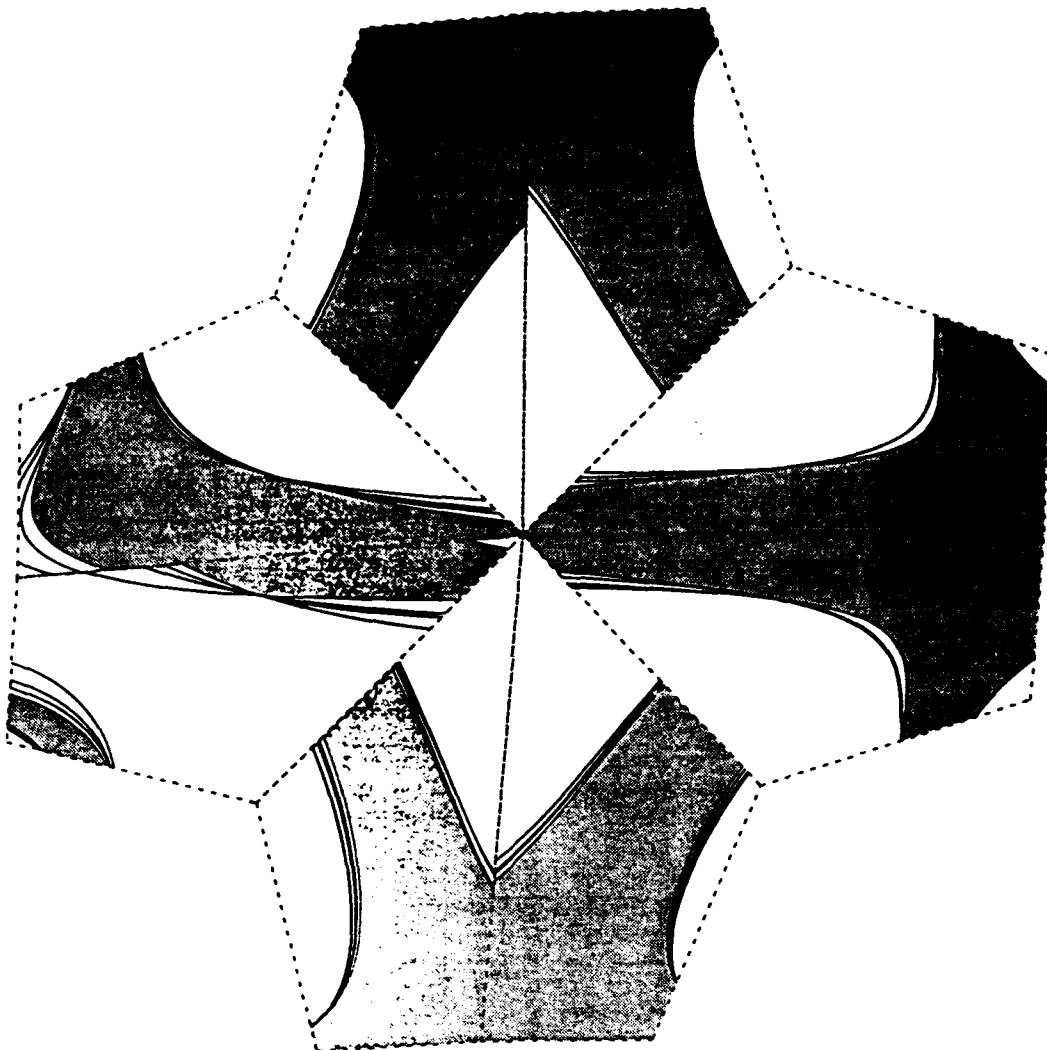
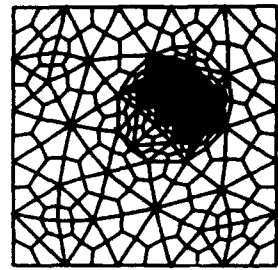


**Fig. 22a**

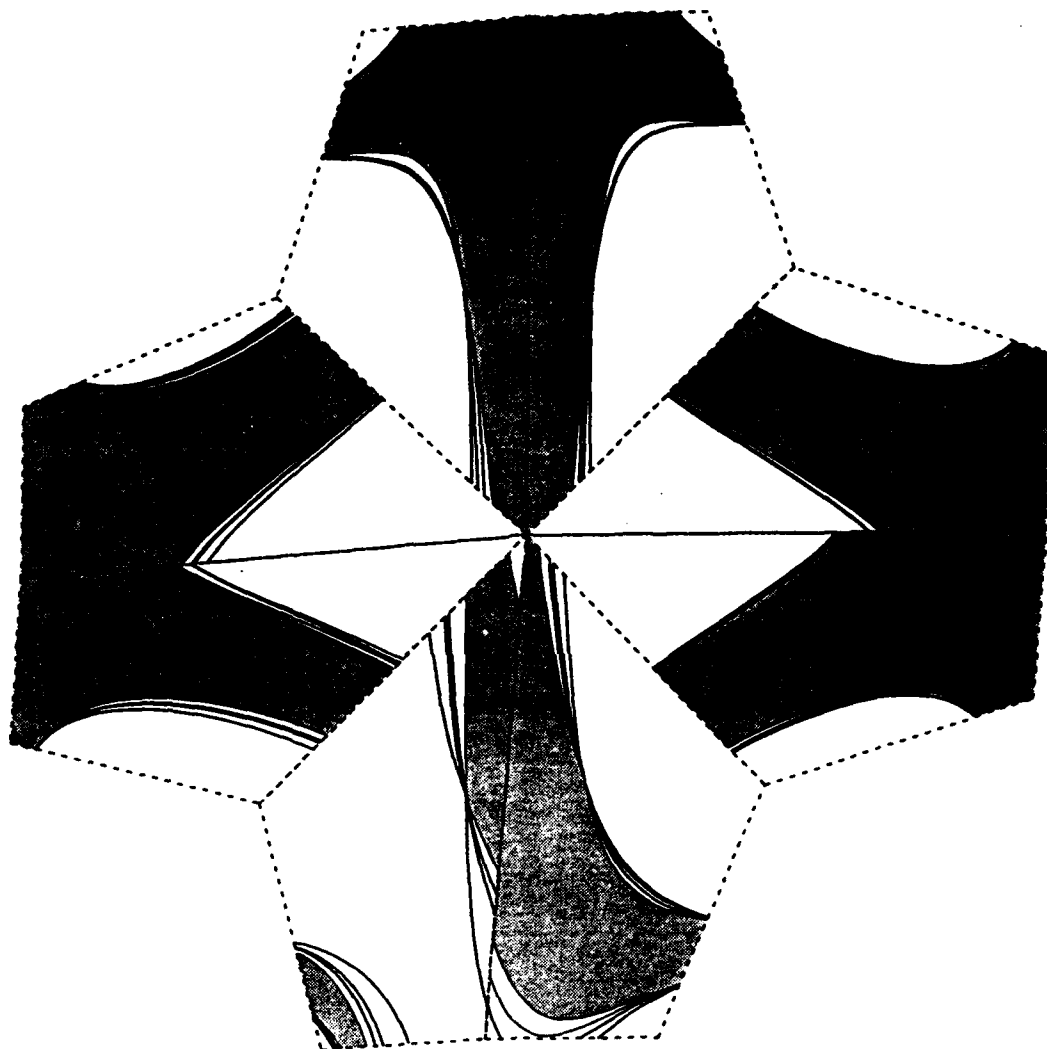


**Fig. 22b**

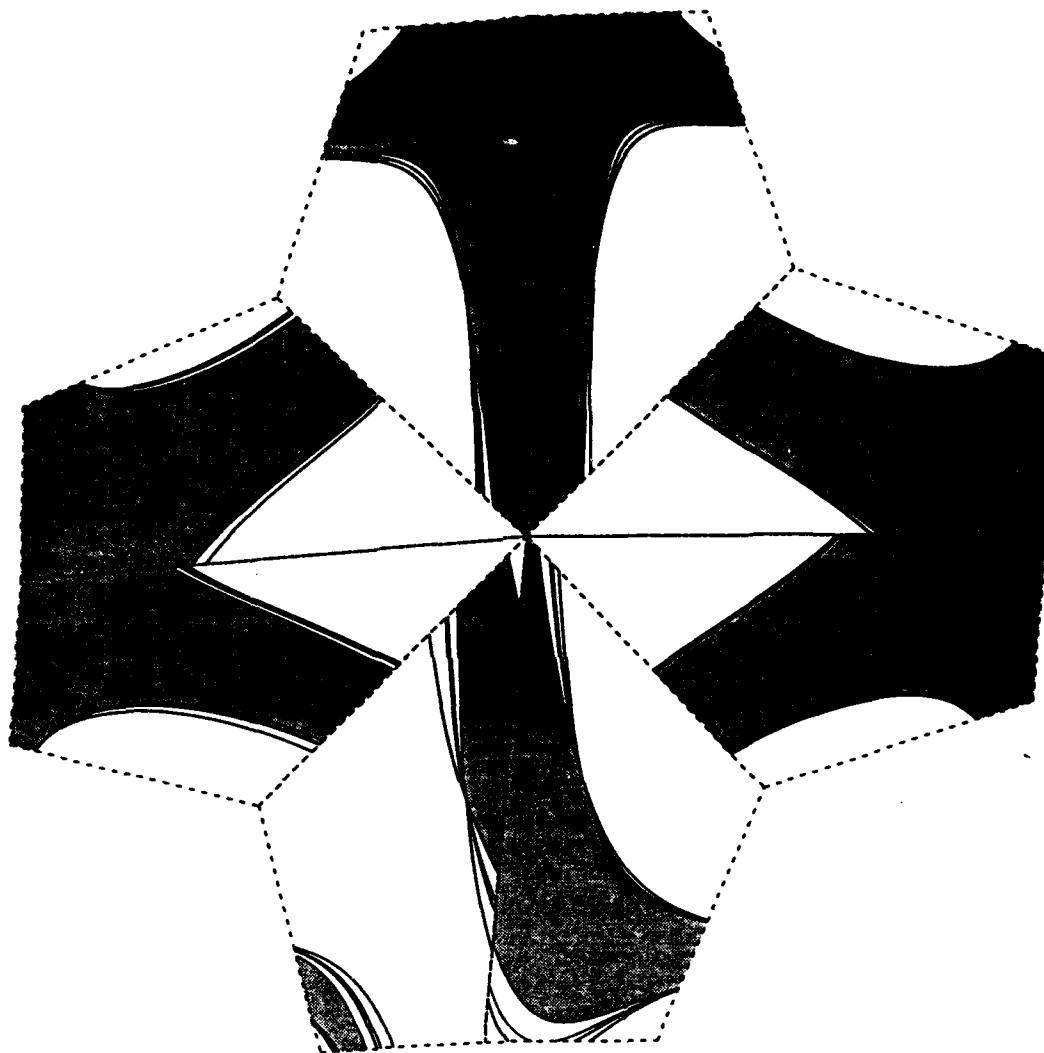




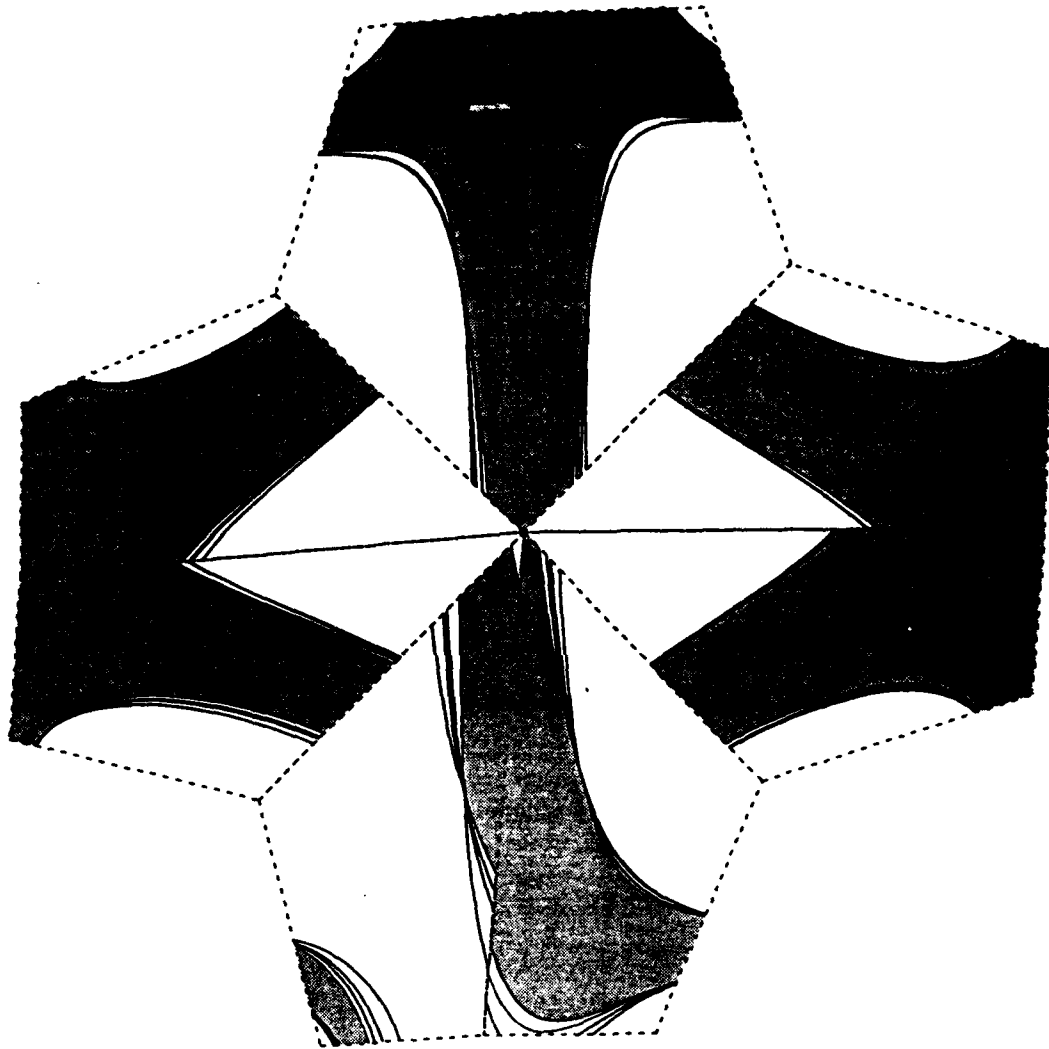
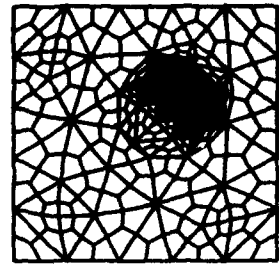
**Fig. 22c**



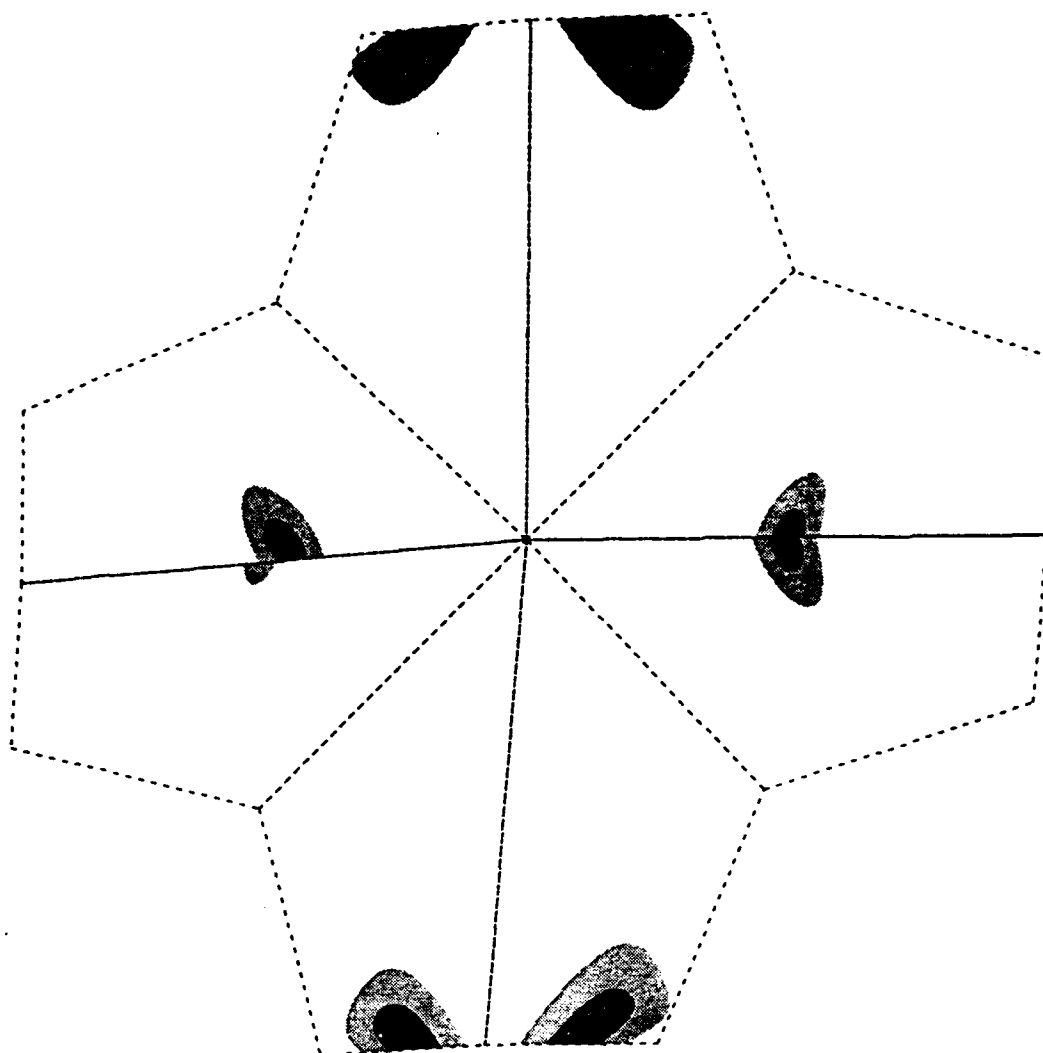
**Fig. 22d**



**Fig. 22e**

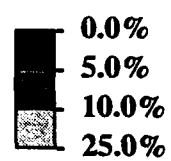


**Fig. 22f**



**Fig. 22g**

**Simplified approach with L-2 norm**



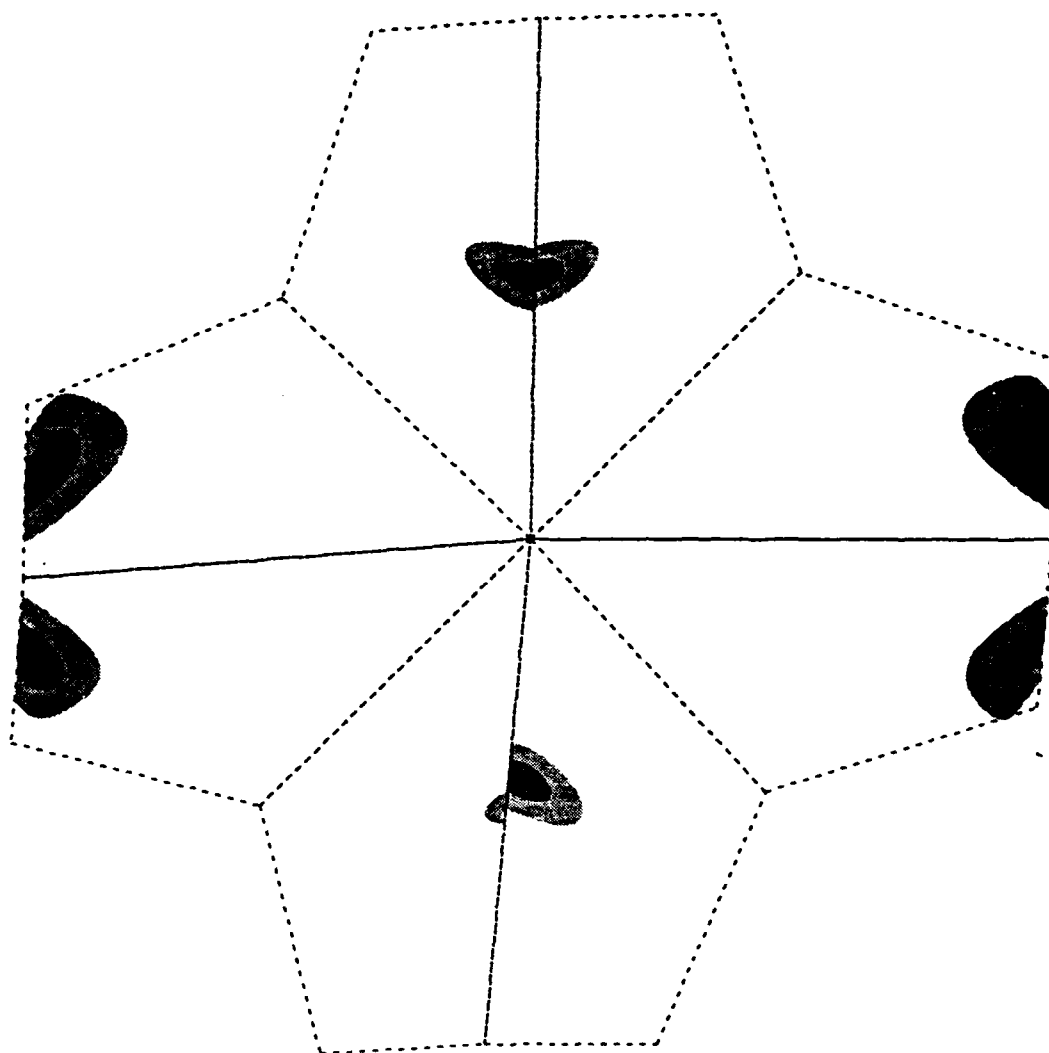


**Fig. 22h**

**Simplified approach with L-2 norm**



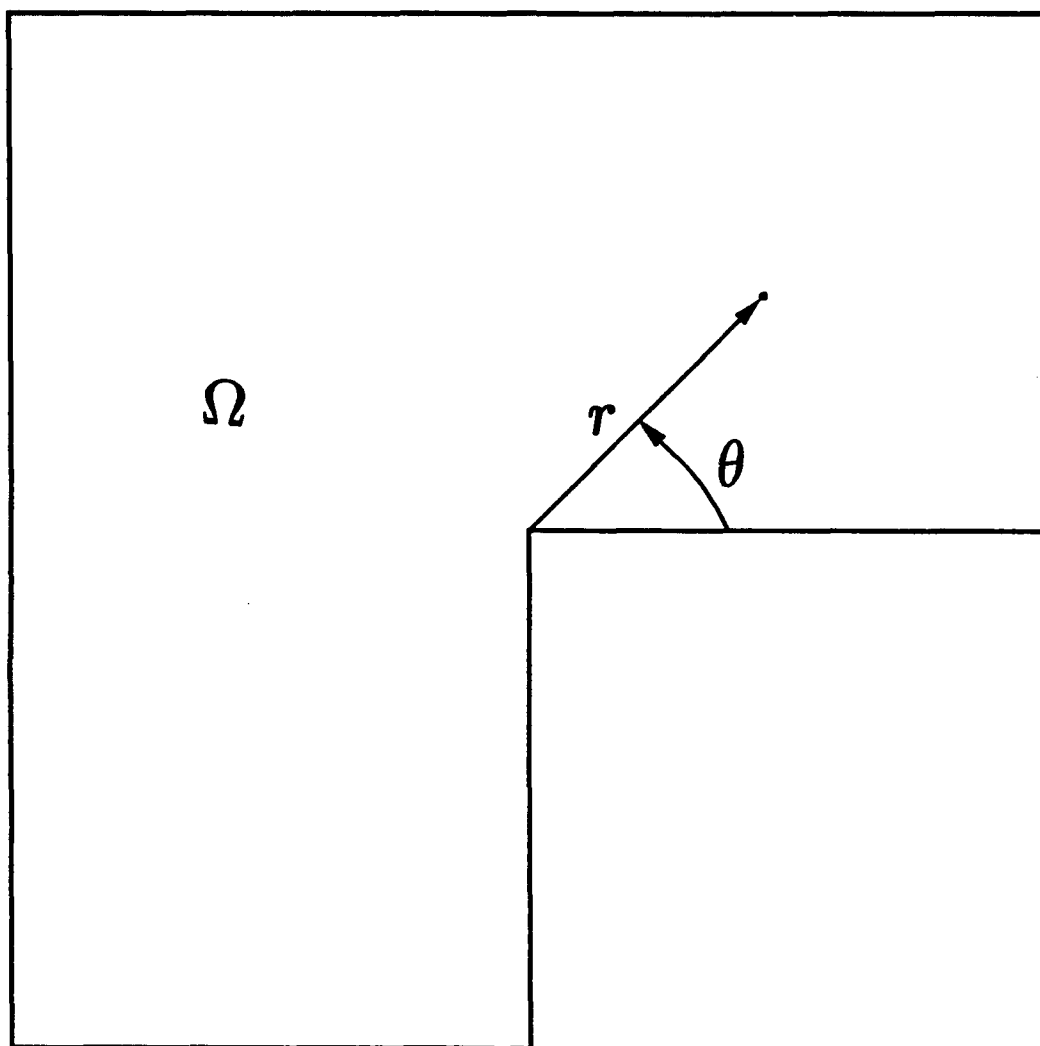


**Fig. 23**

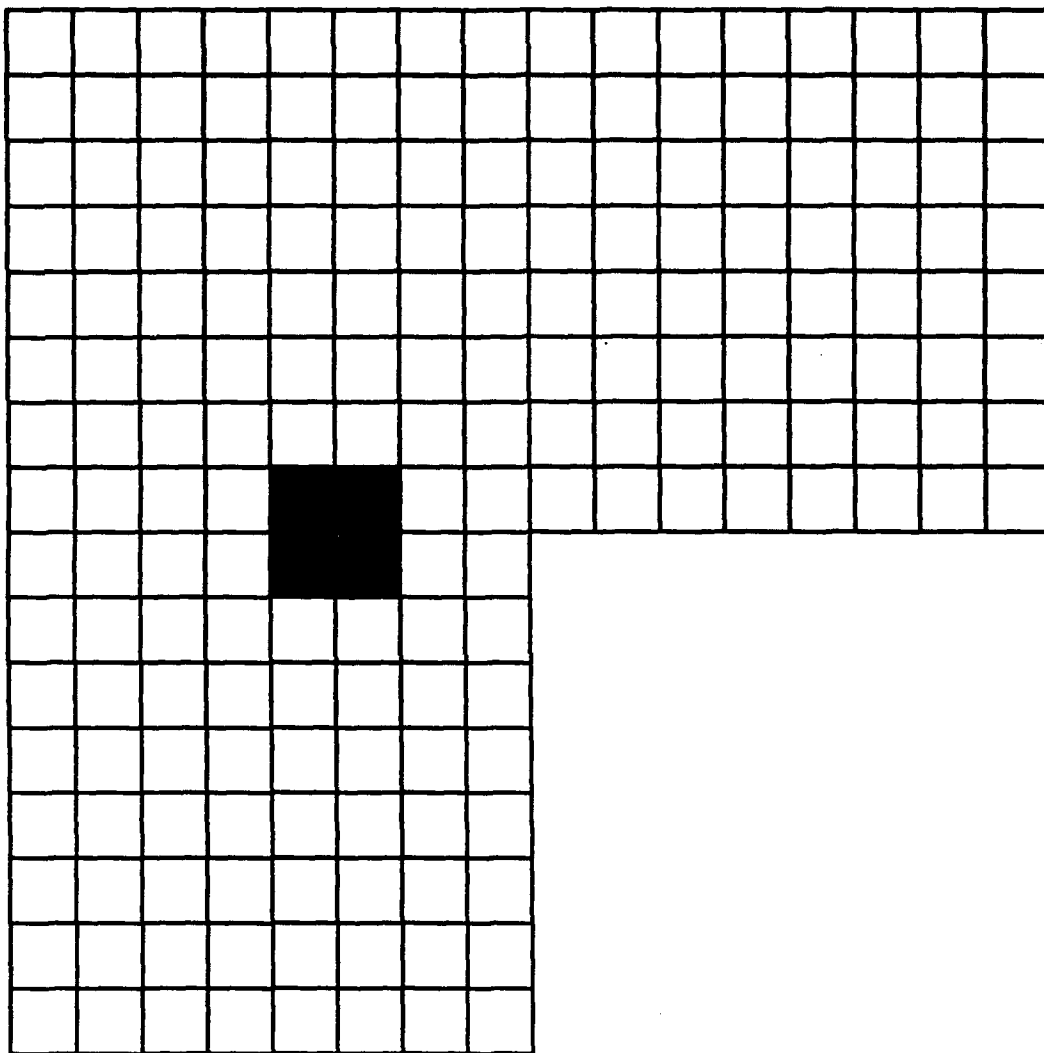


**Fig. 24a**



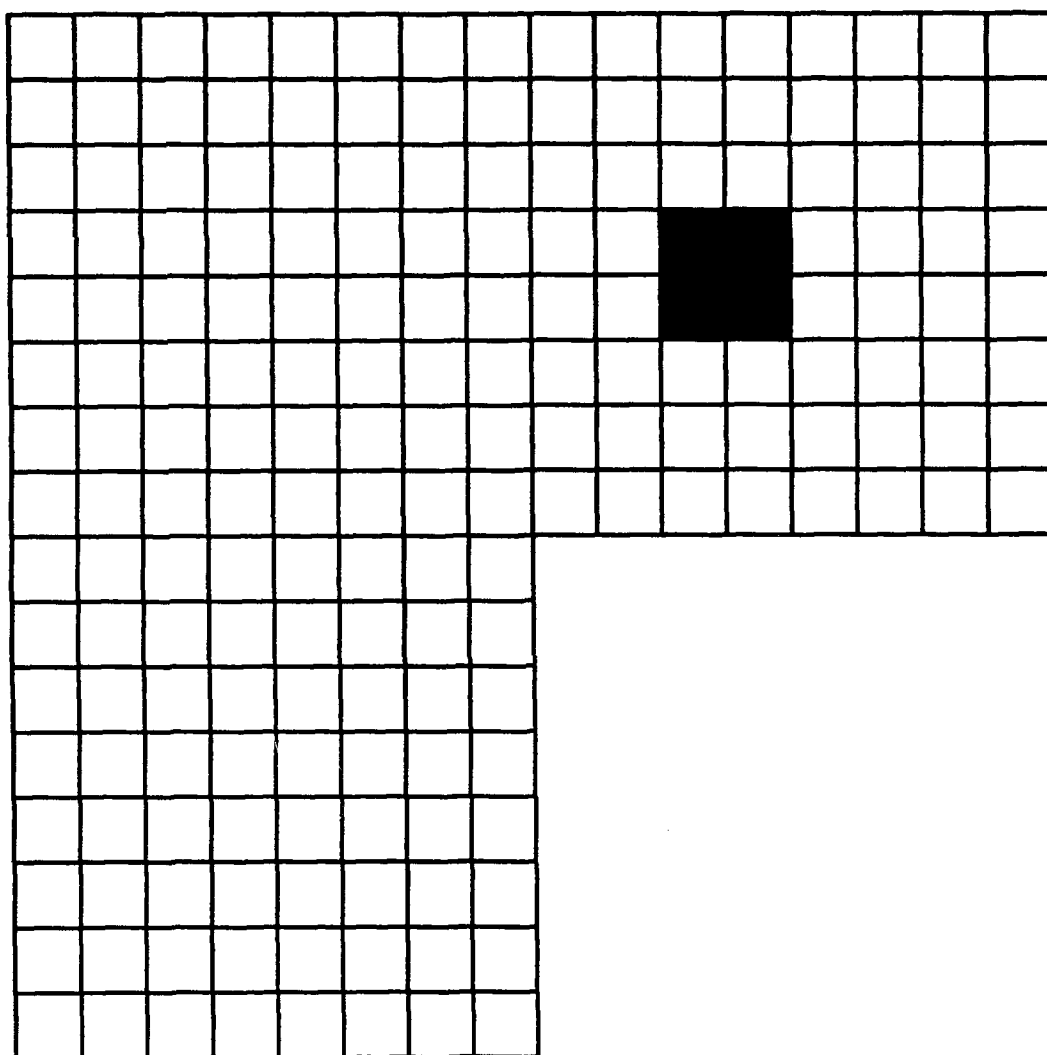


**Fig. 24b**

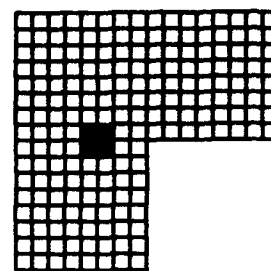
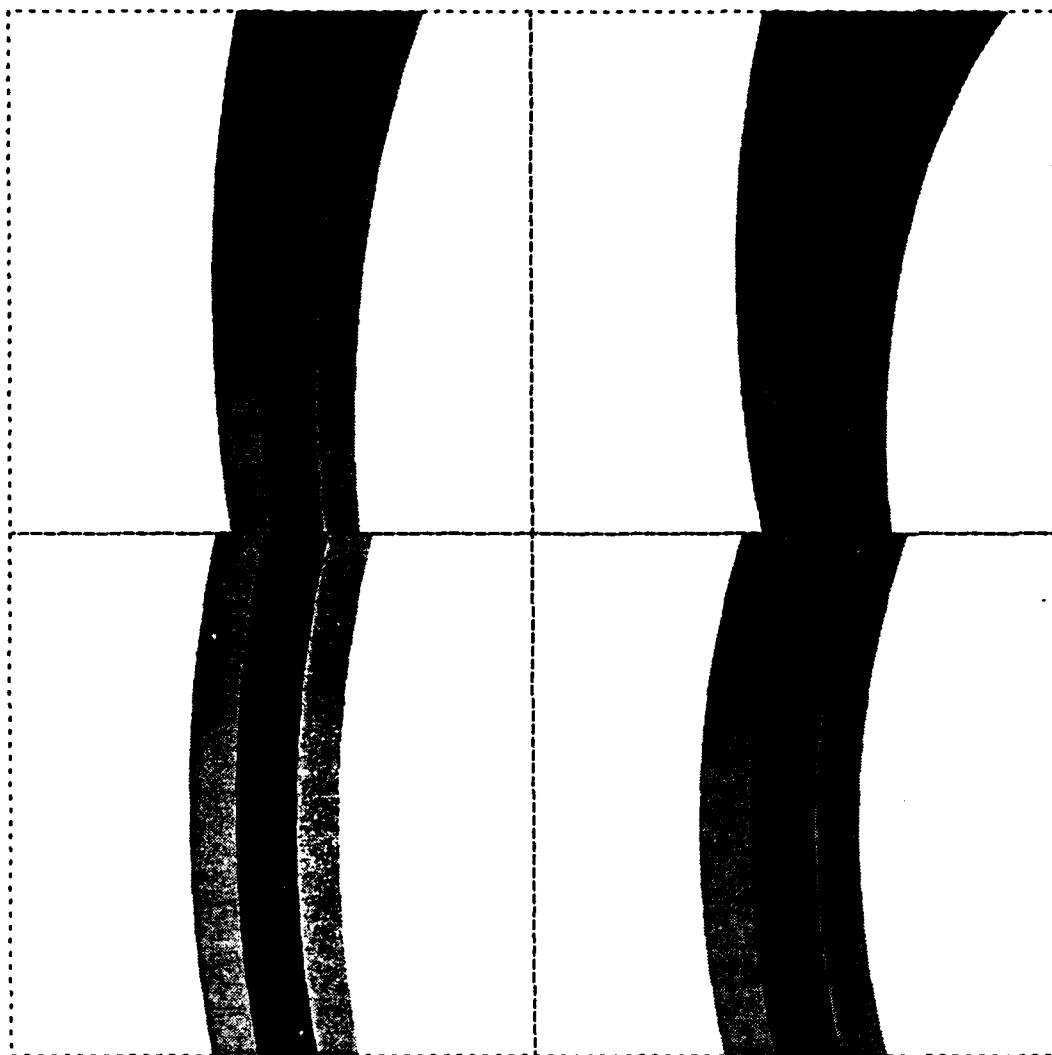


**Fig. 25a**

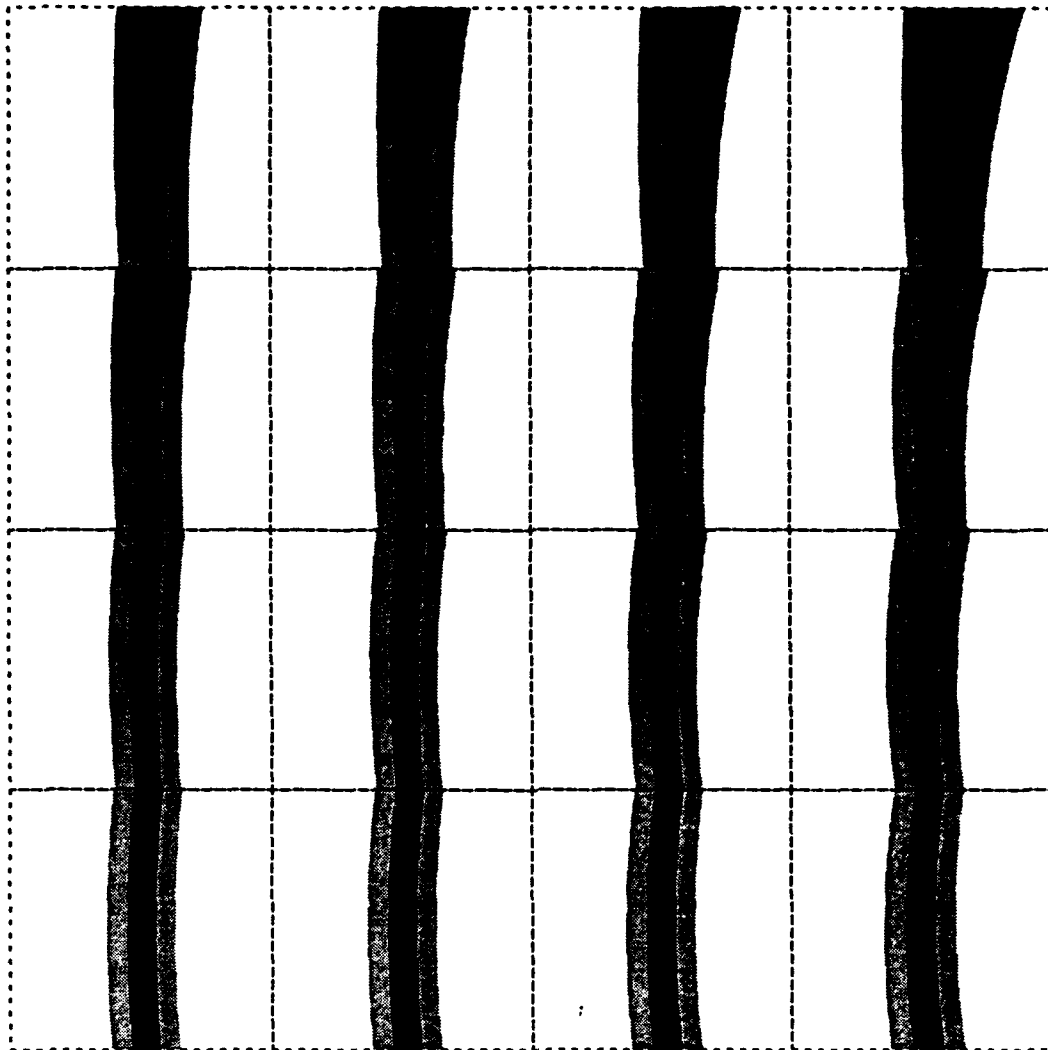
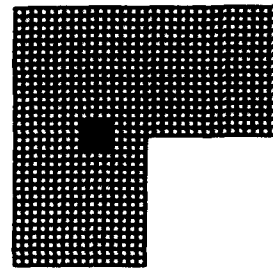


**Fig. 25b**

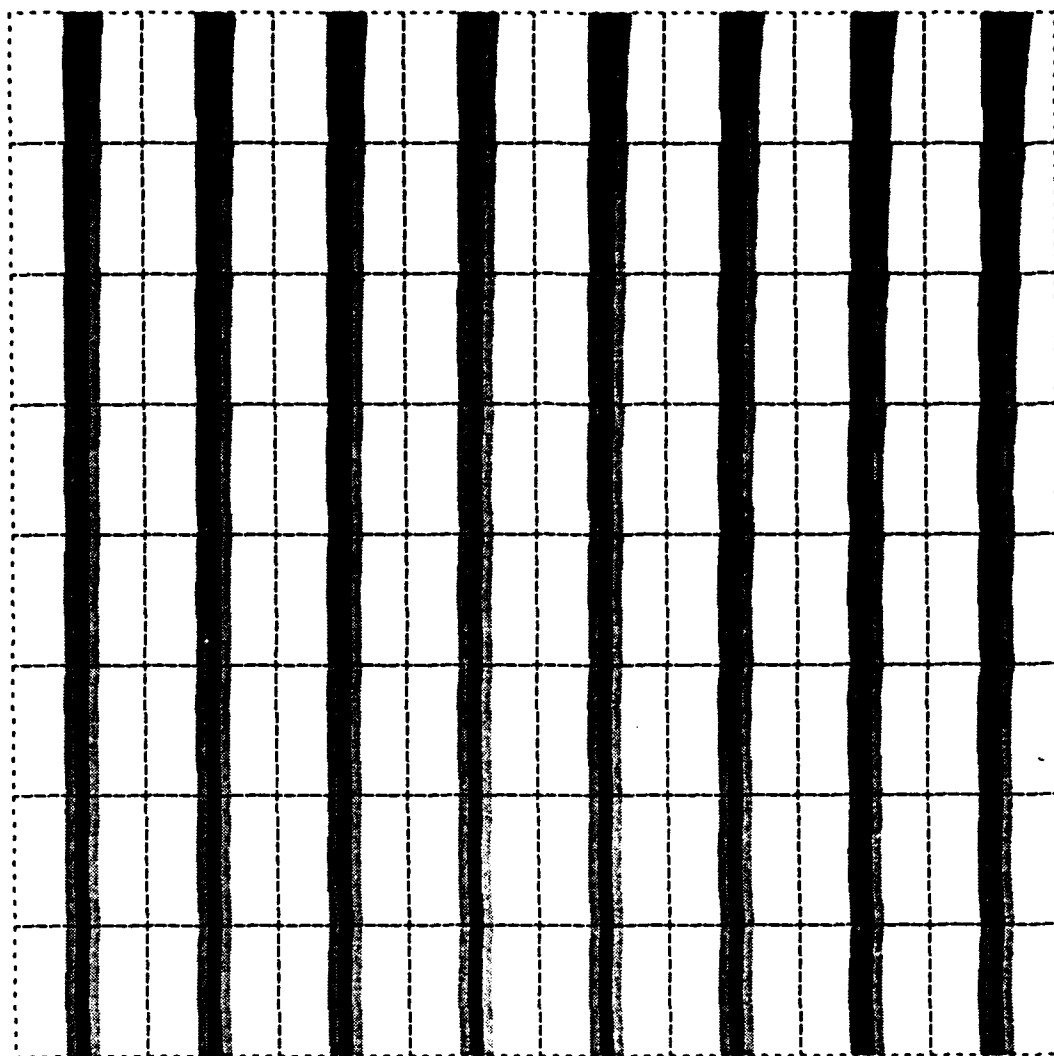
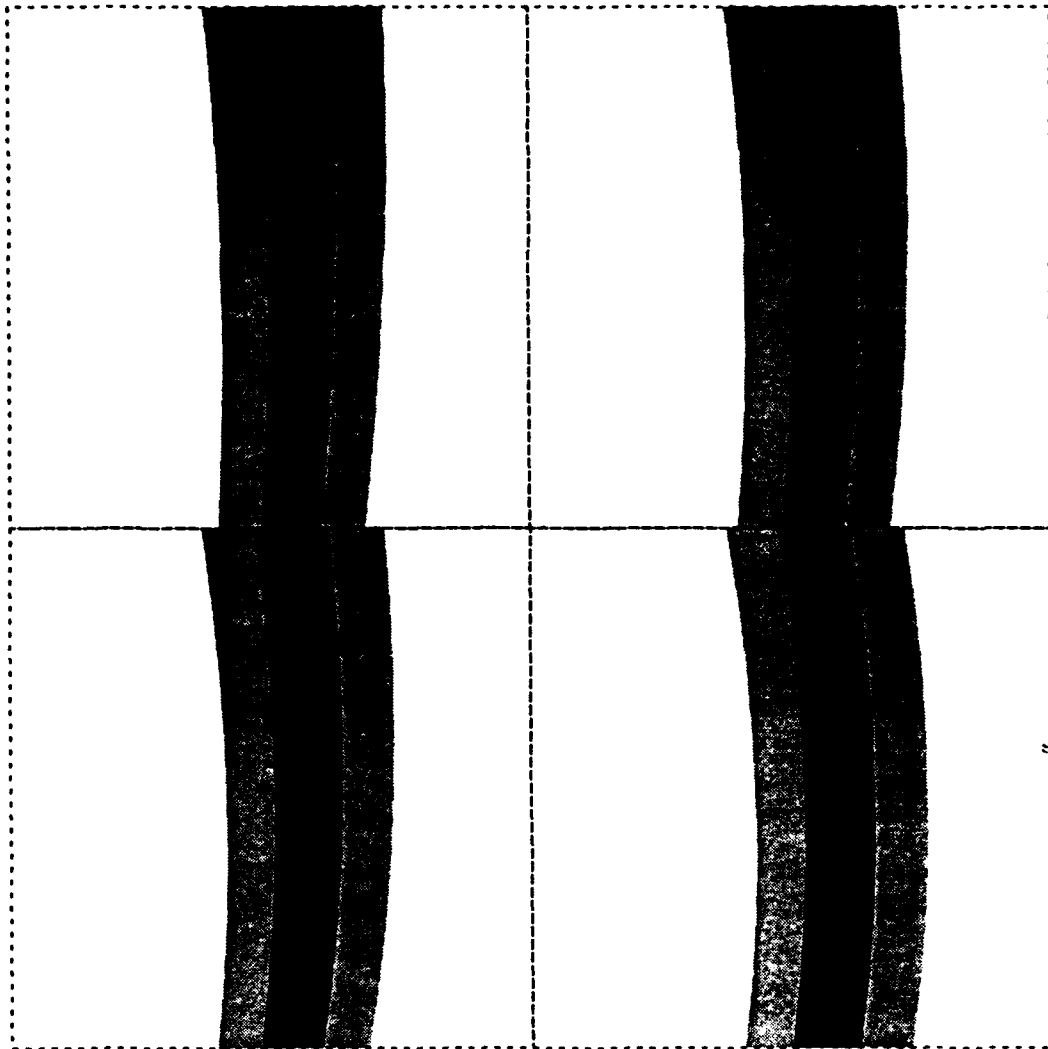
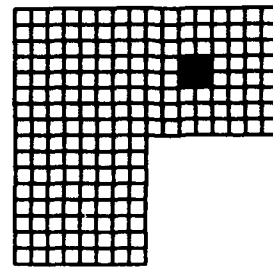


Fig. 25c



**Fig. 25d**

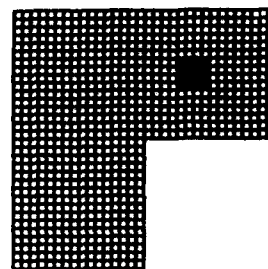
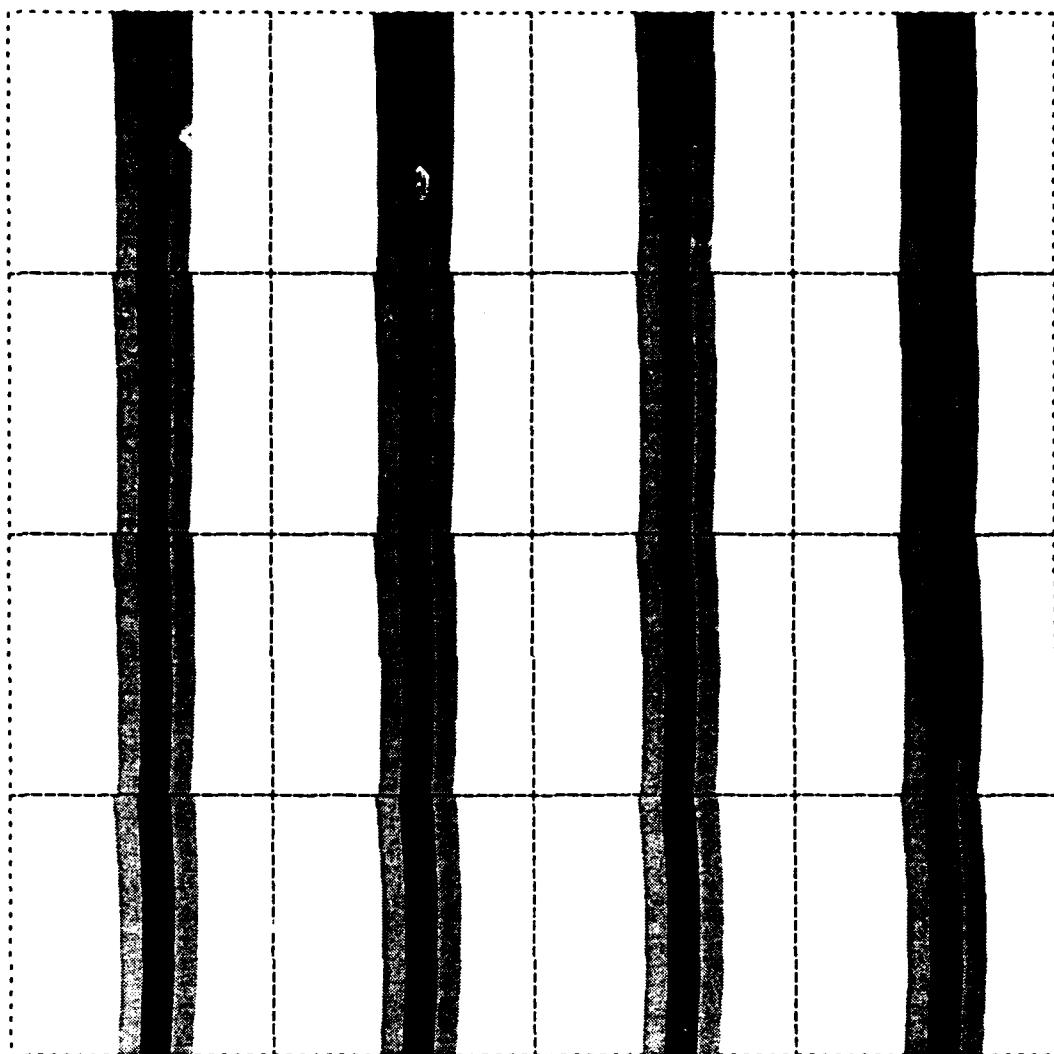
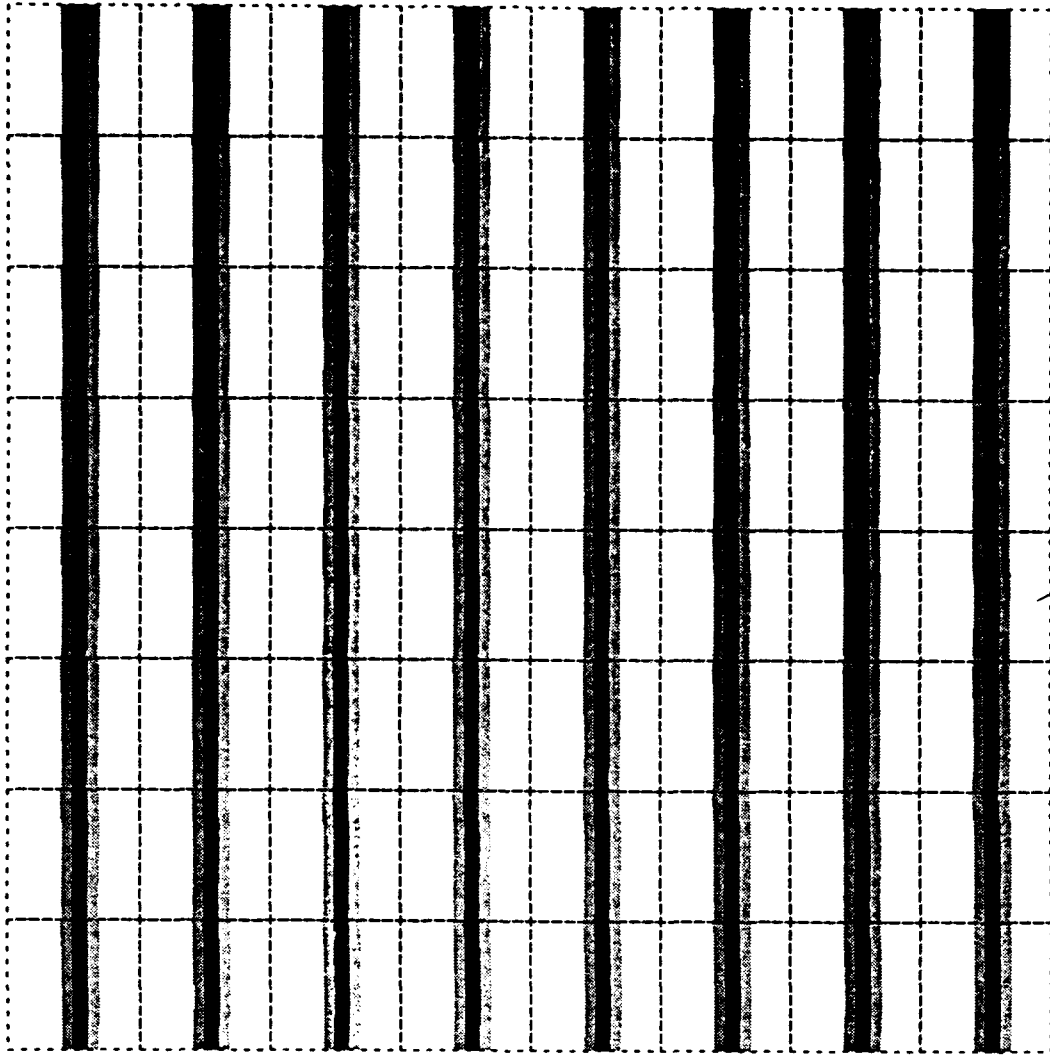
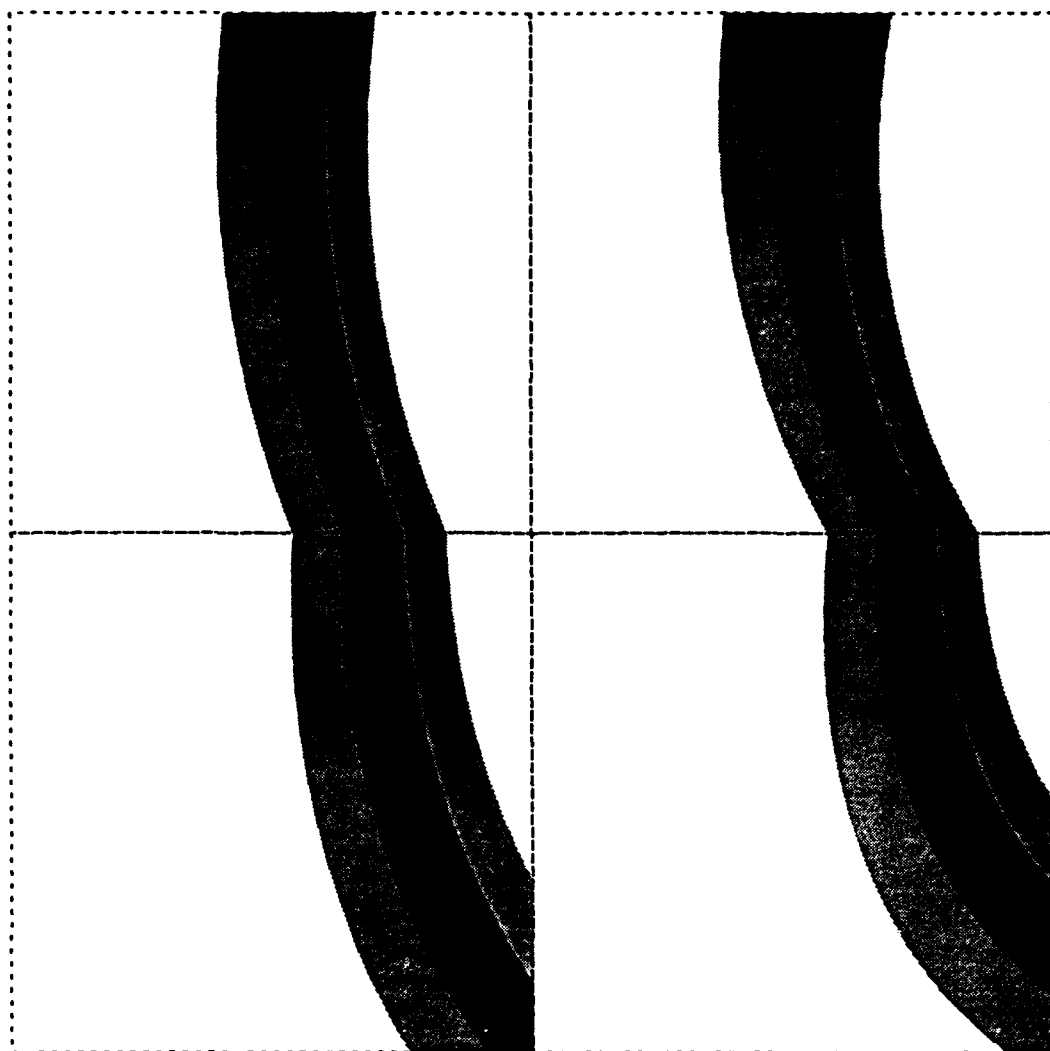


Fig. 25e

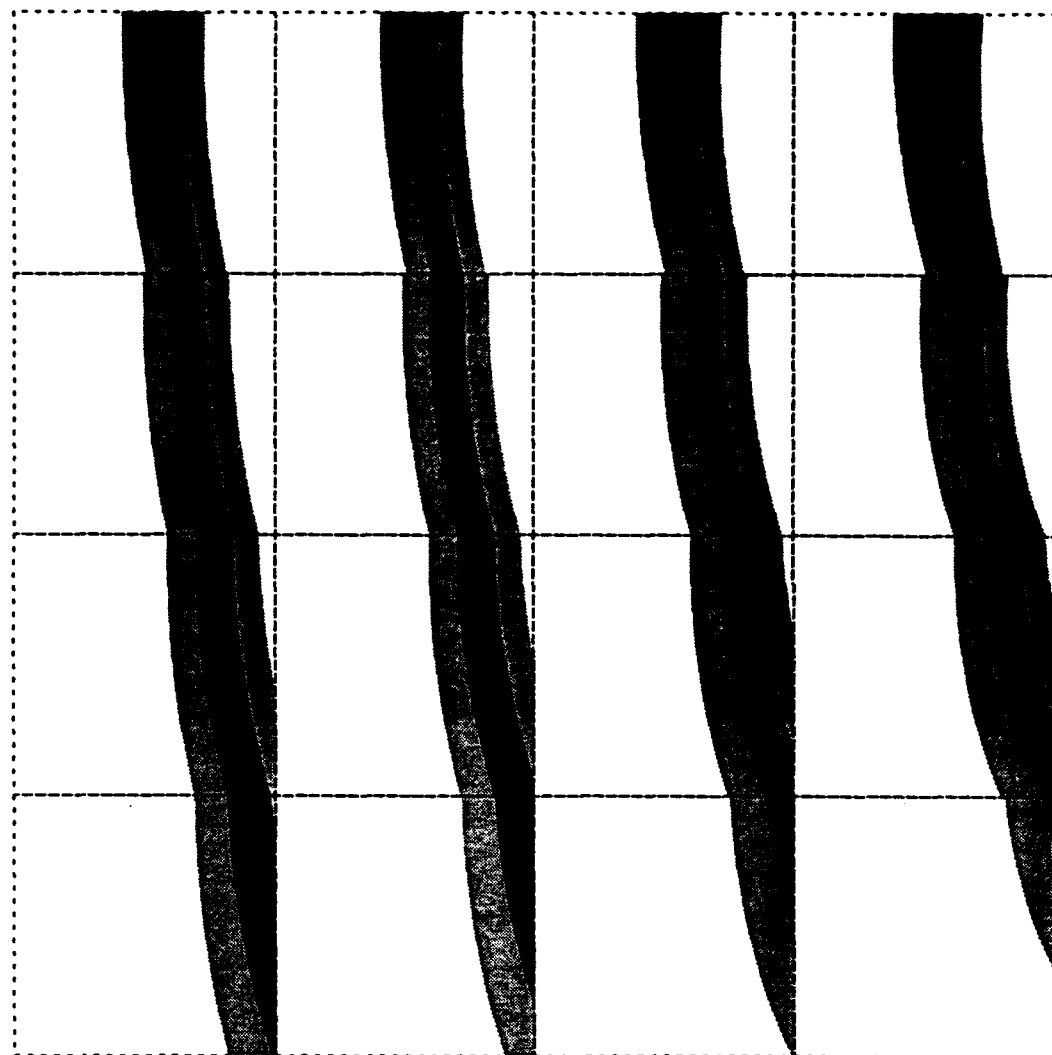
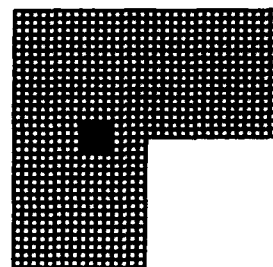


**Fig. 25f**

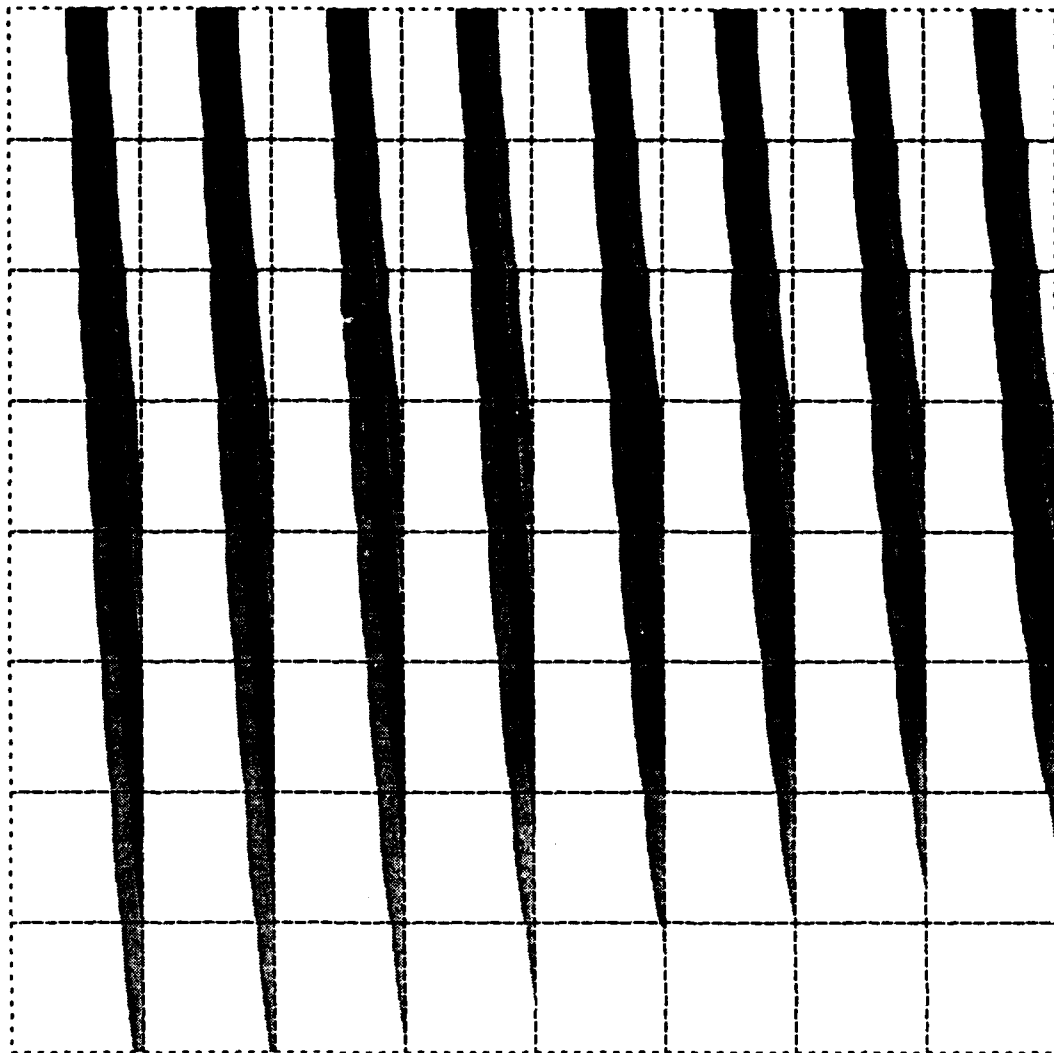


**Fig. 26a**

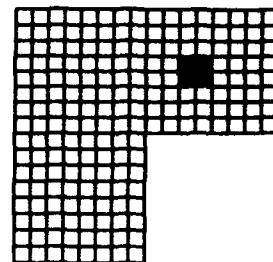
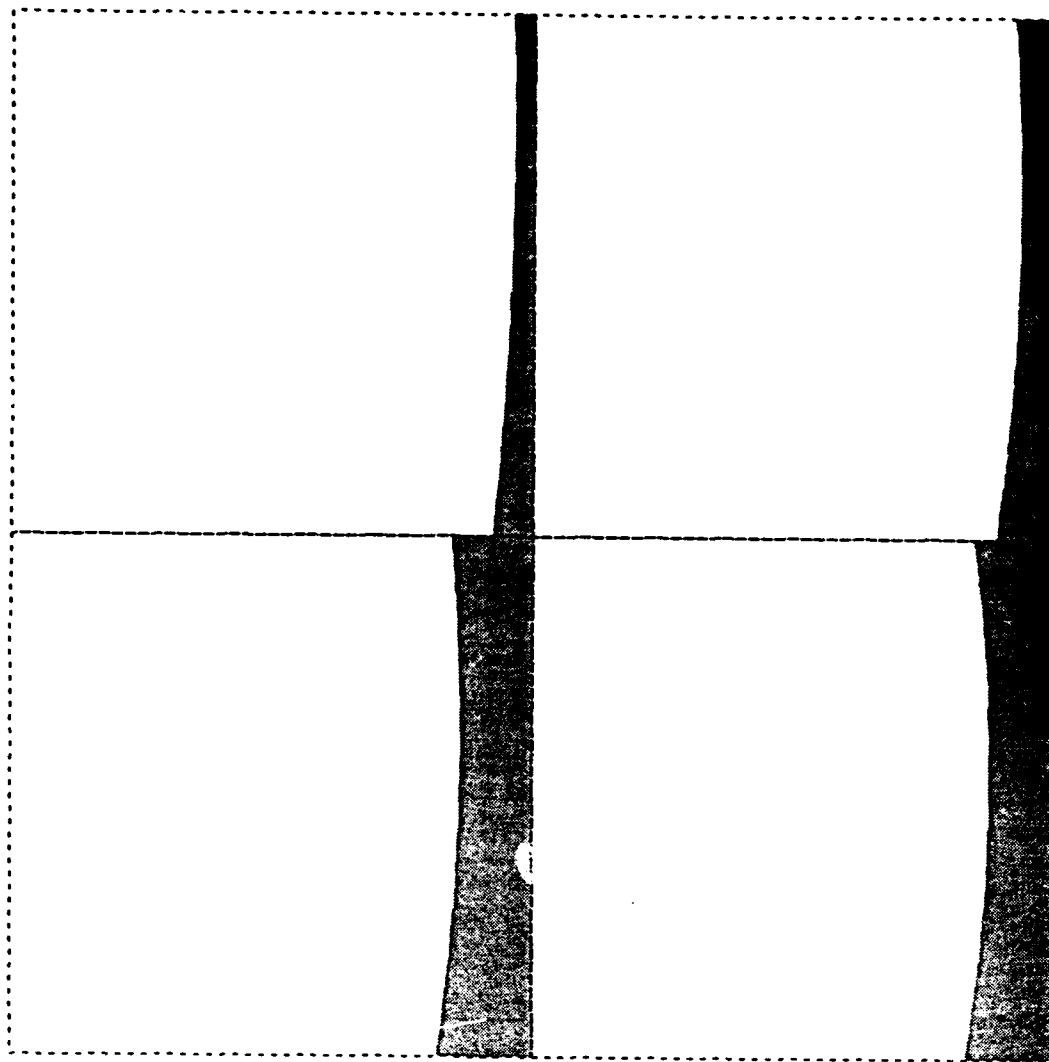




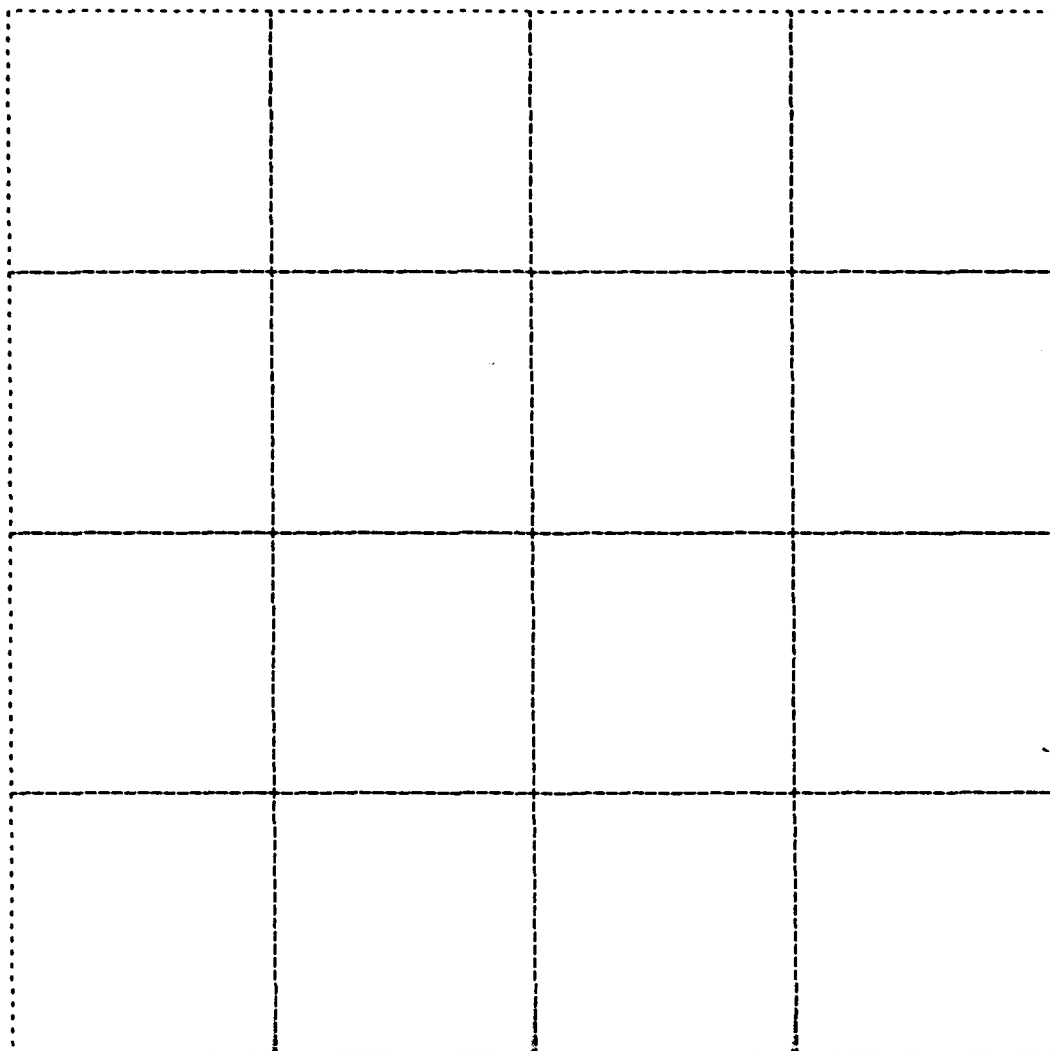
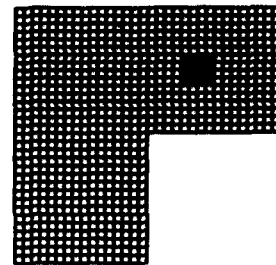
**Fig. 26b**



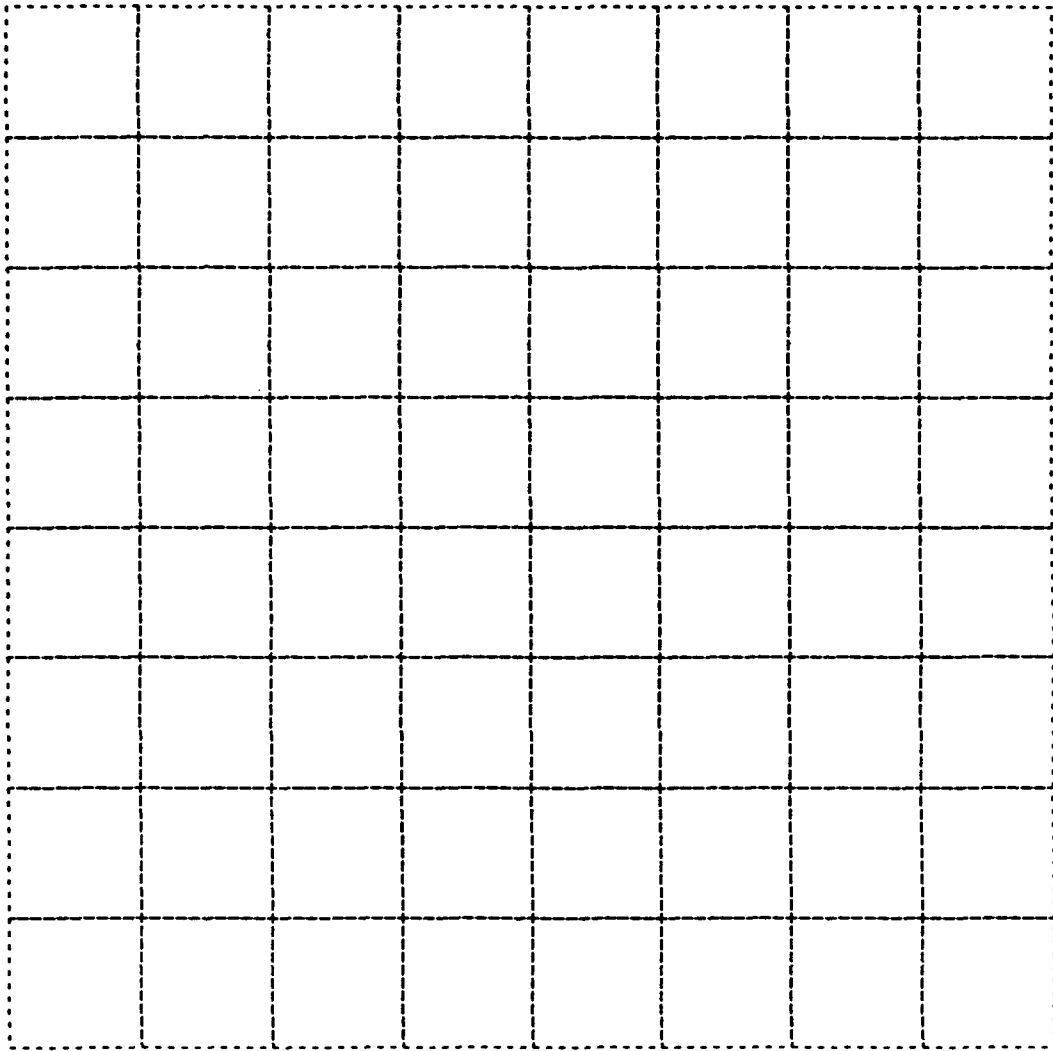
**Fig. 26c**



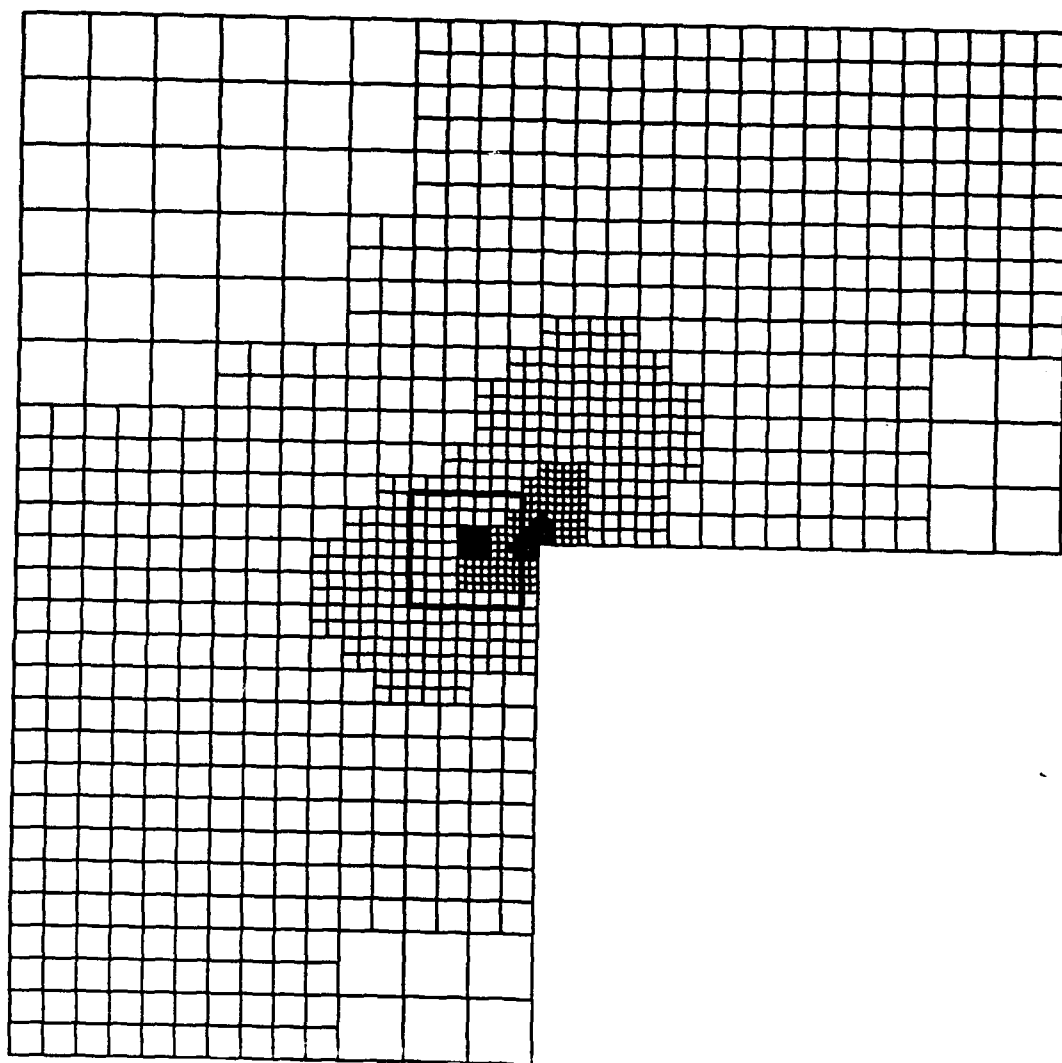
**Fig. 26d**



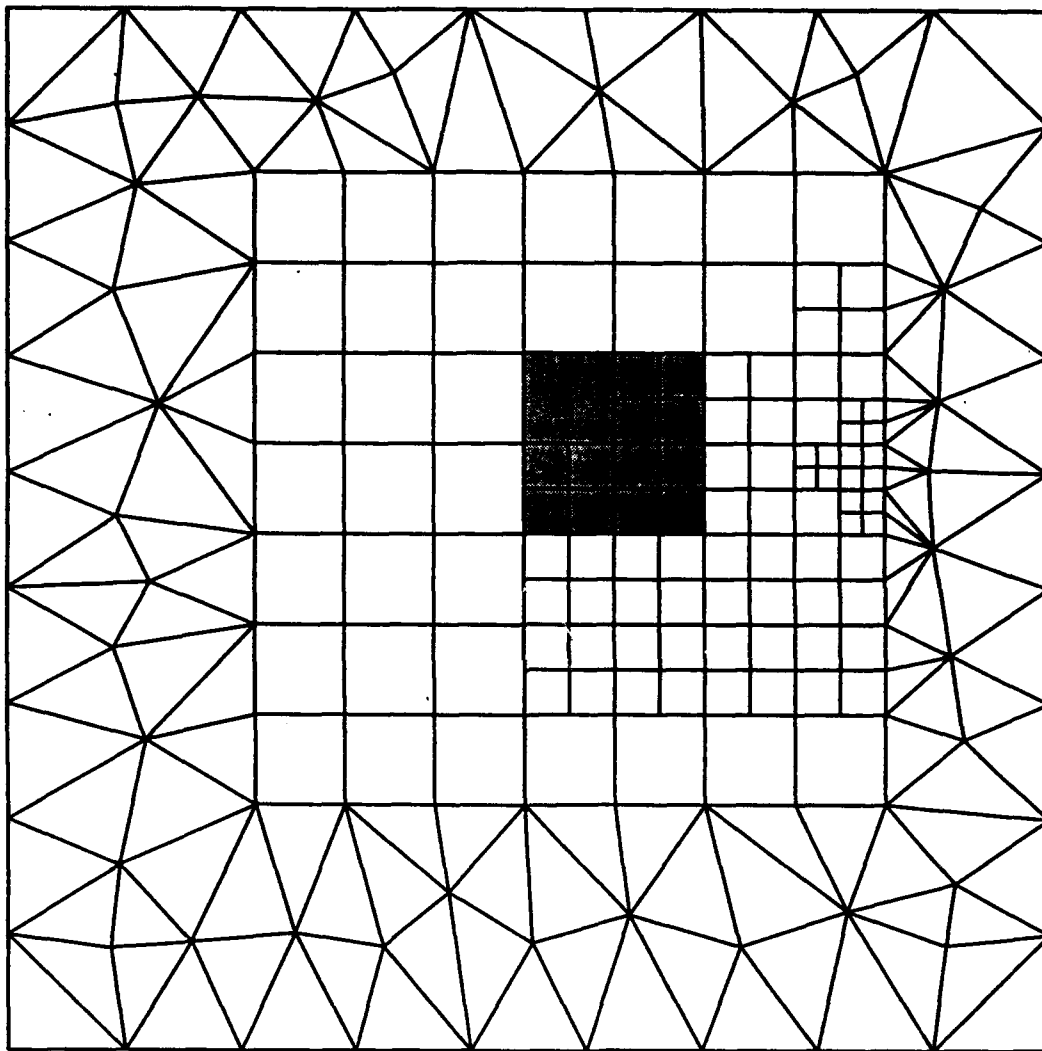
**Fig. 26e**



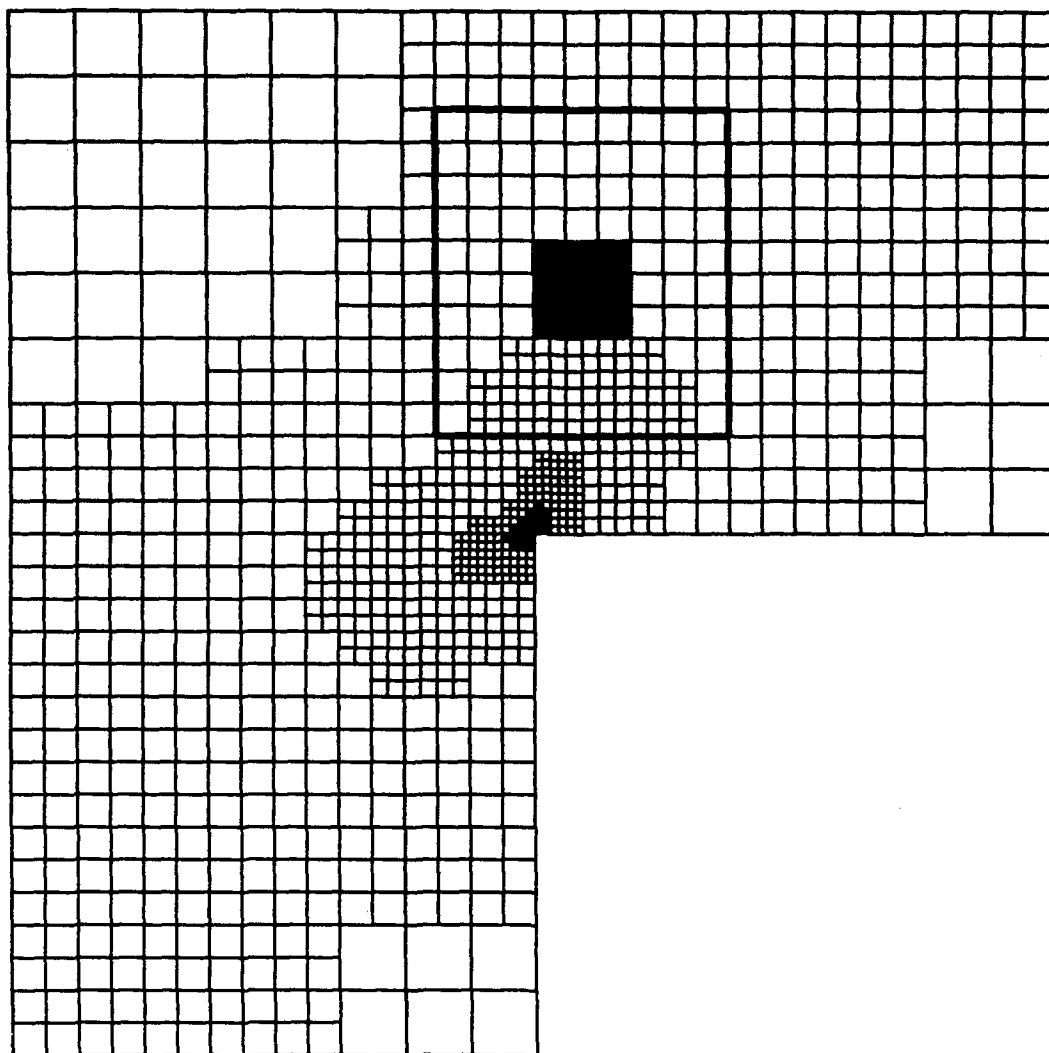
**Fig. 26f**



**Fig. 27a**

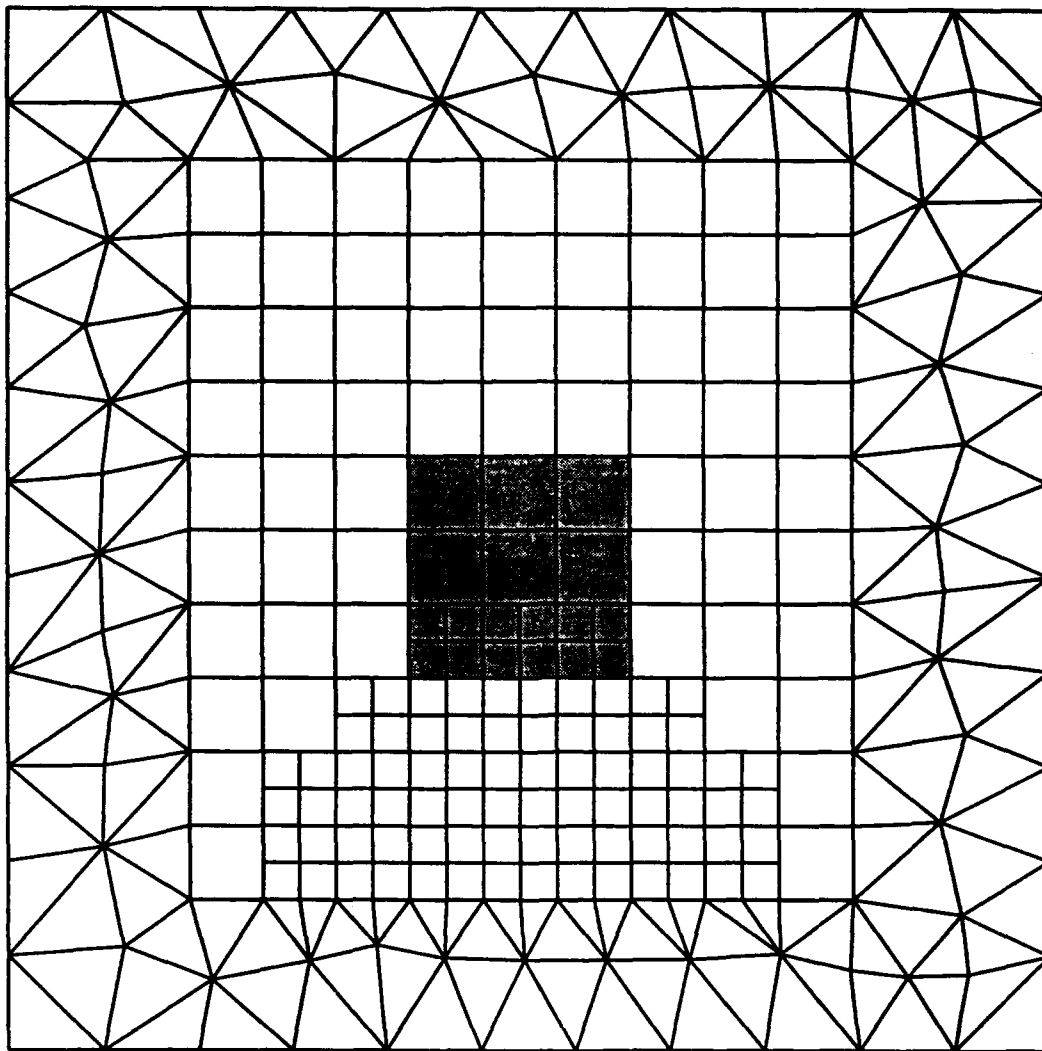


**Fig. 27b**

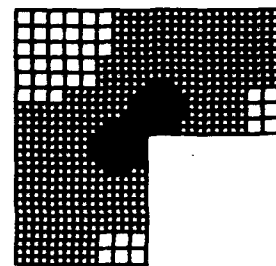
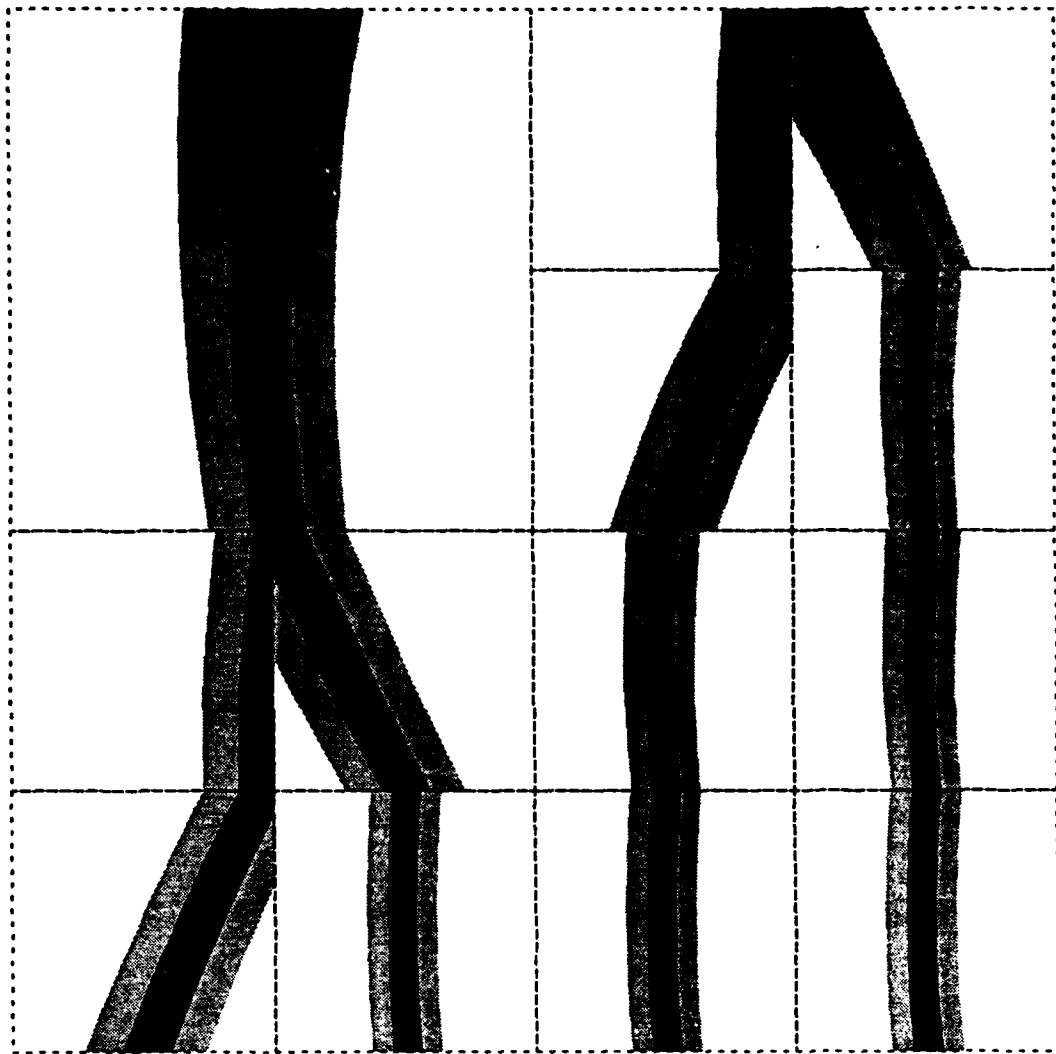


**Fig. 28a**

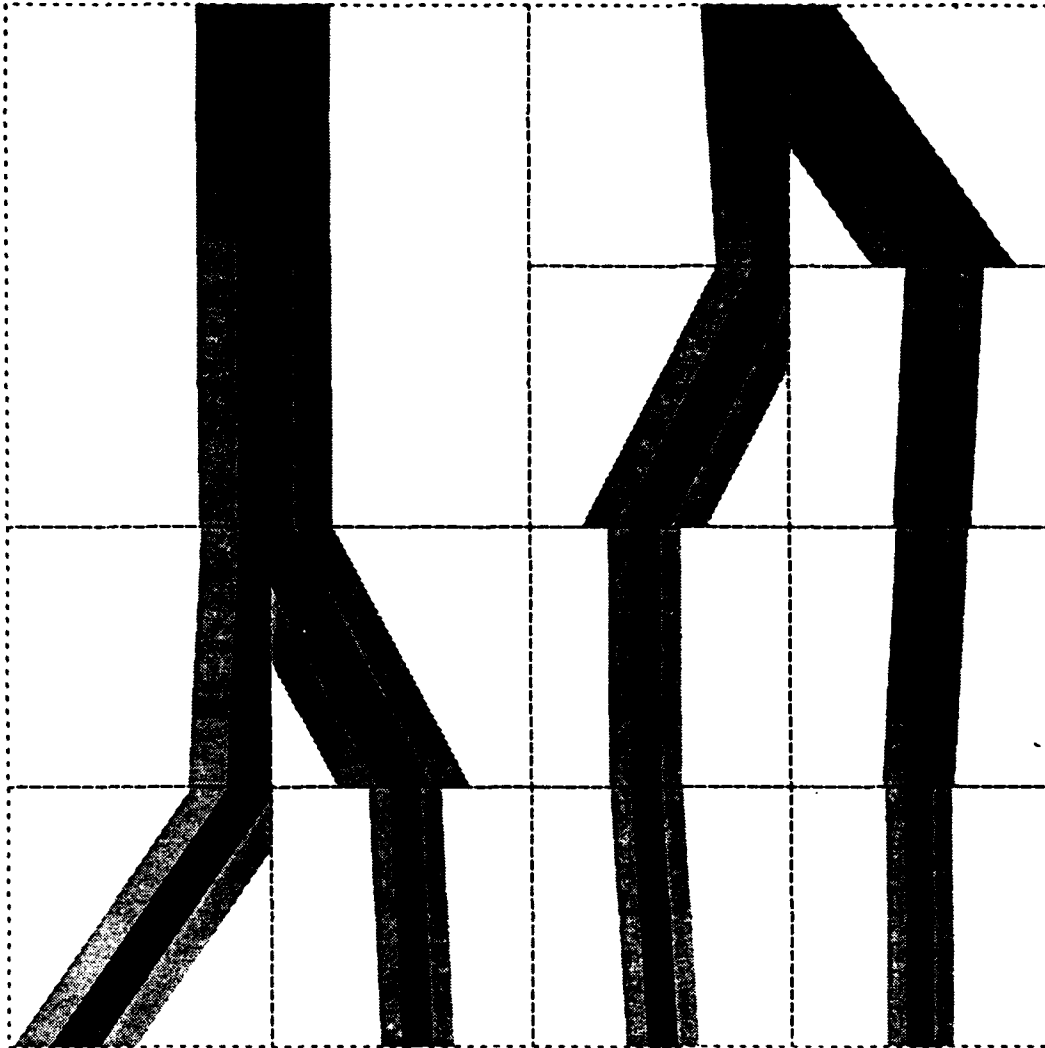
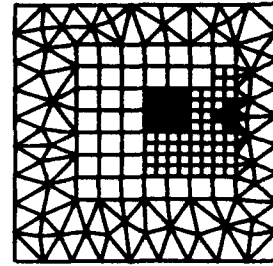




**Fig. 28b**

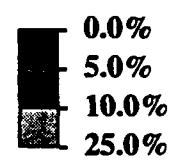


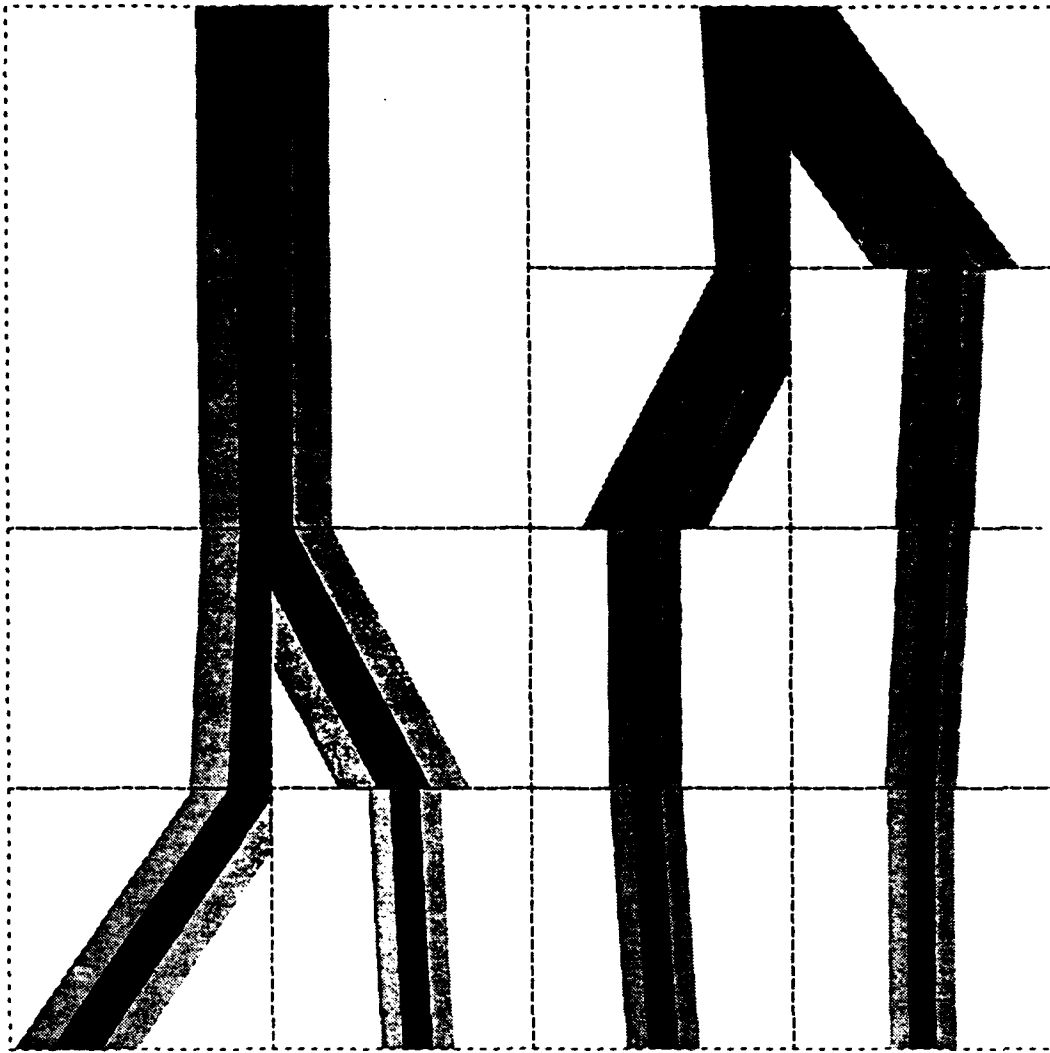
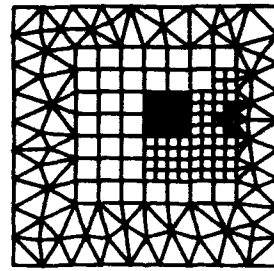
**Fig. 29a**



**Fig. 29b**

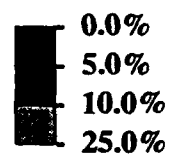
**Simplified approach with L-2 norm**

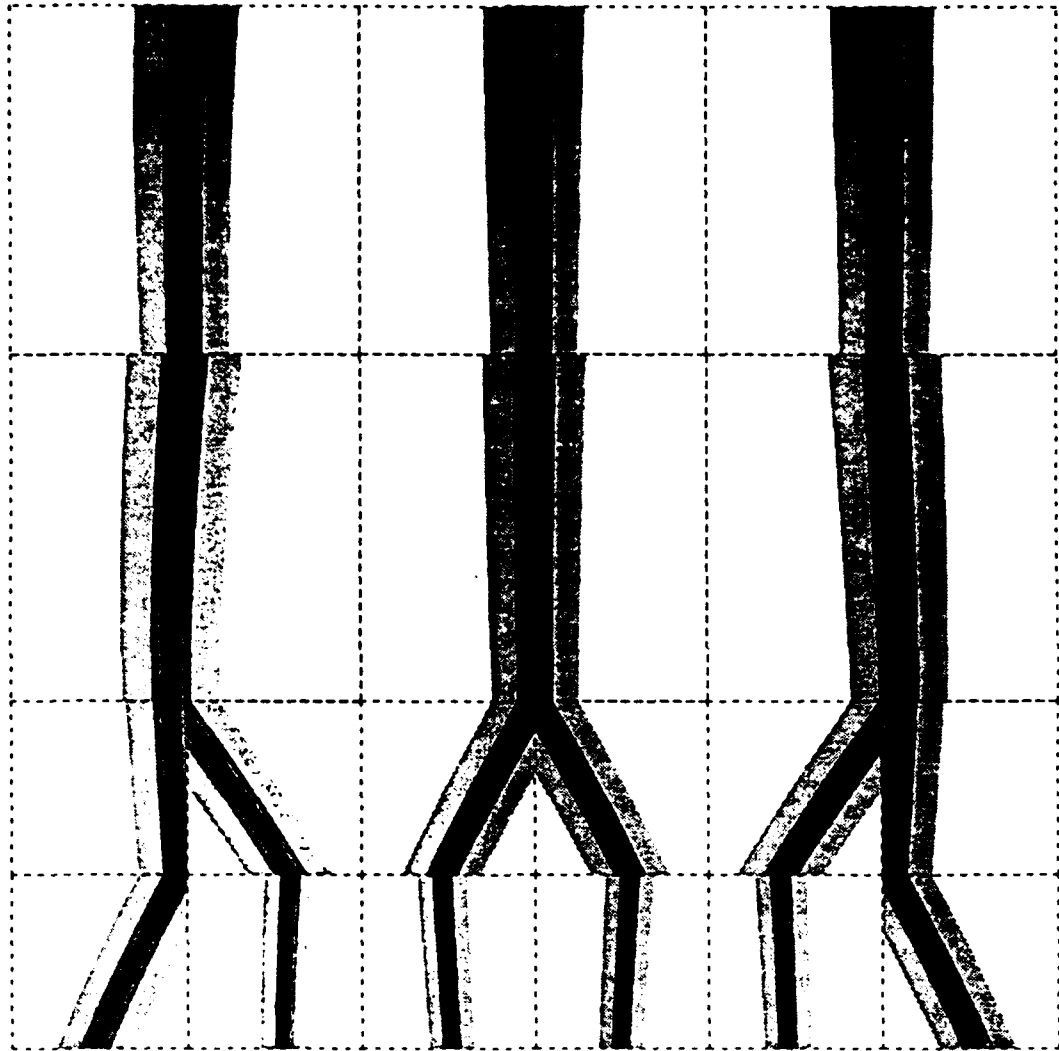
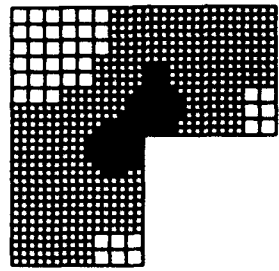




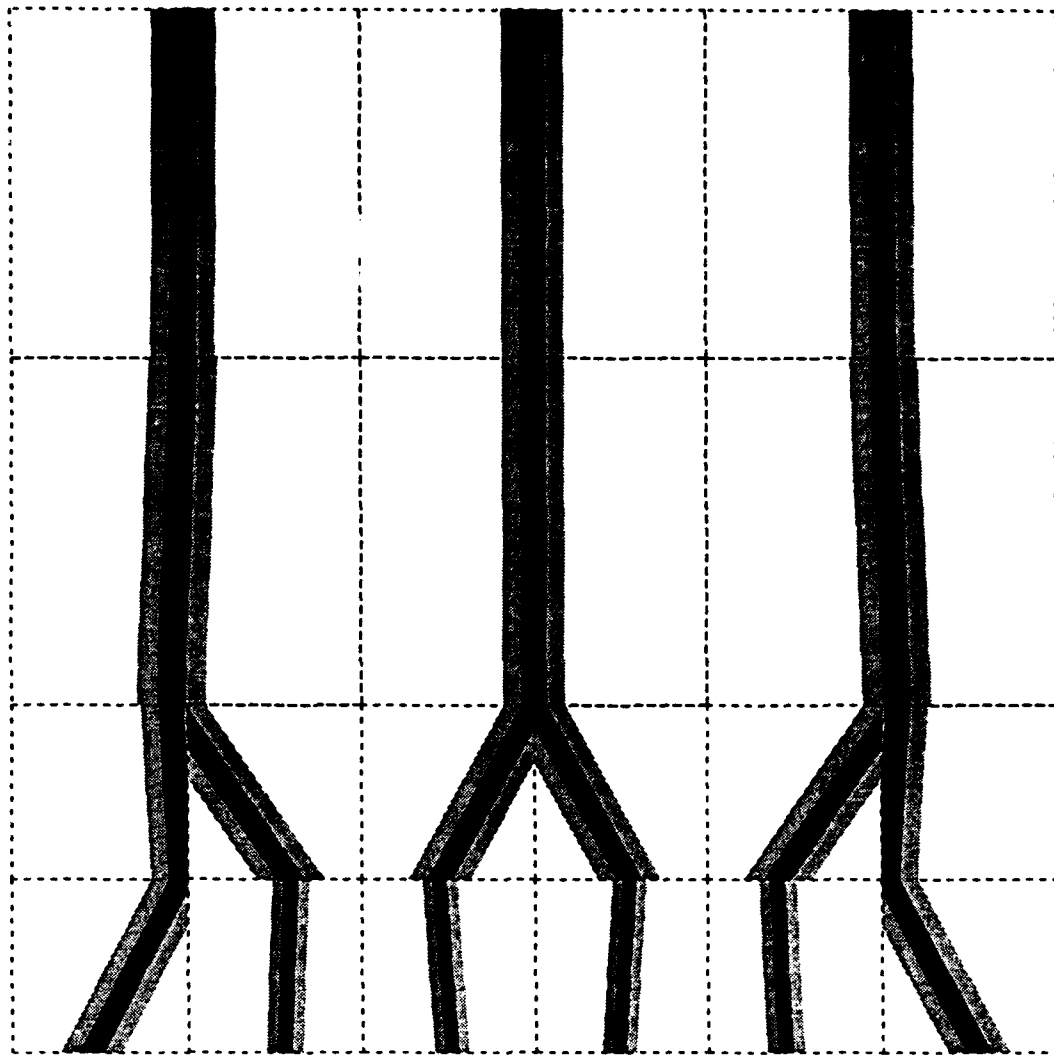
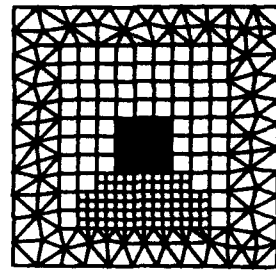
**Fig. 29c**

**Simplified approach with L-2 norm**



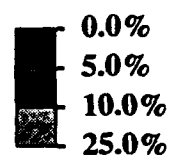


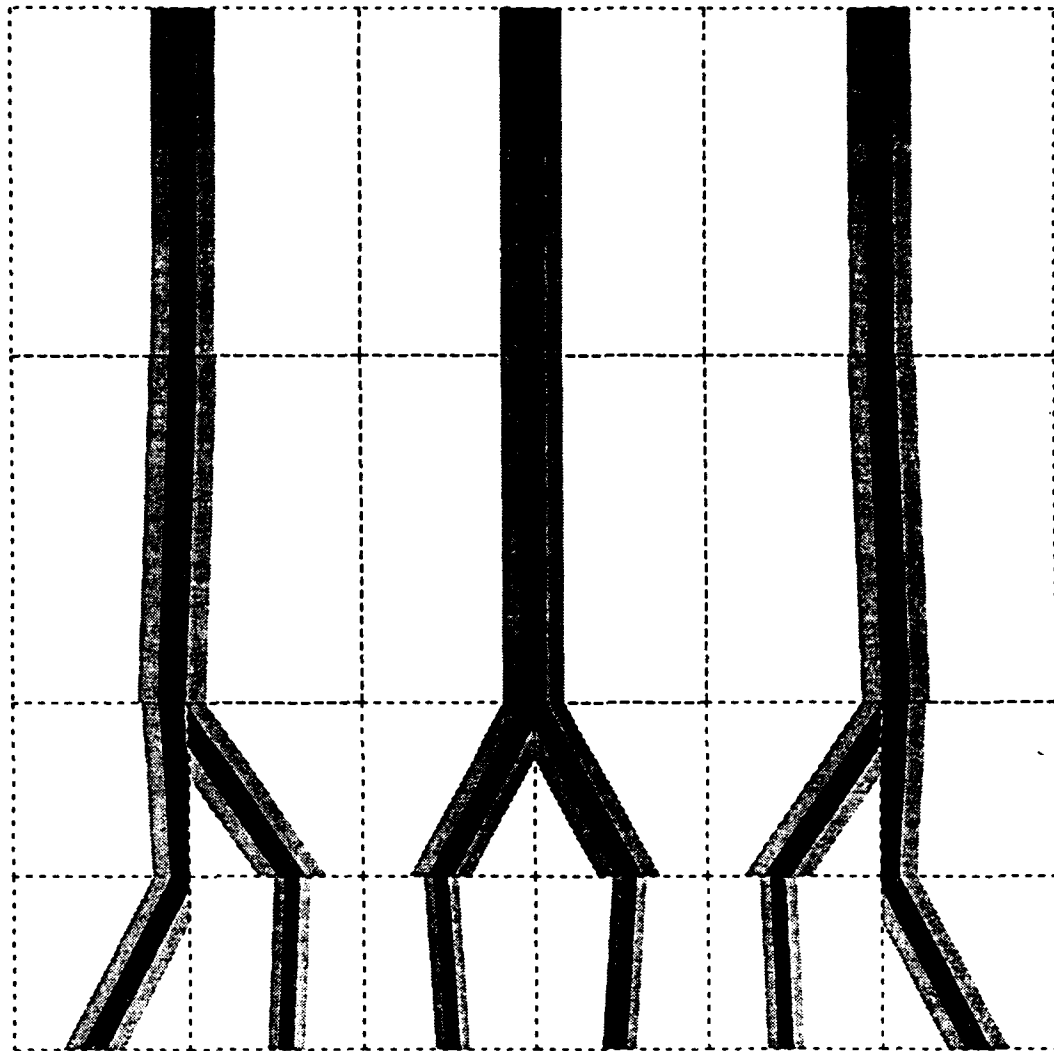
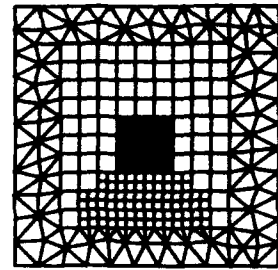
**Fig. 30a**



**Fig. 30c**

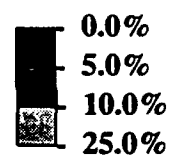
Simplified approach with L-2 norm  
Contours of  $du_x - du_{hx} = \eta$   
 $p = 1$

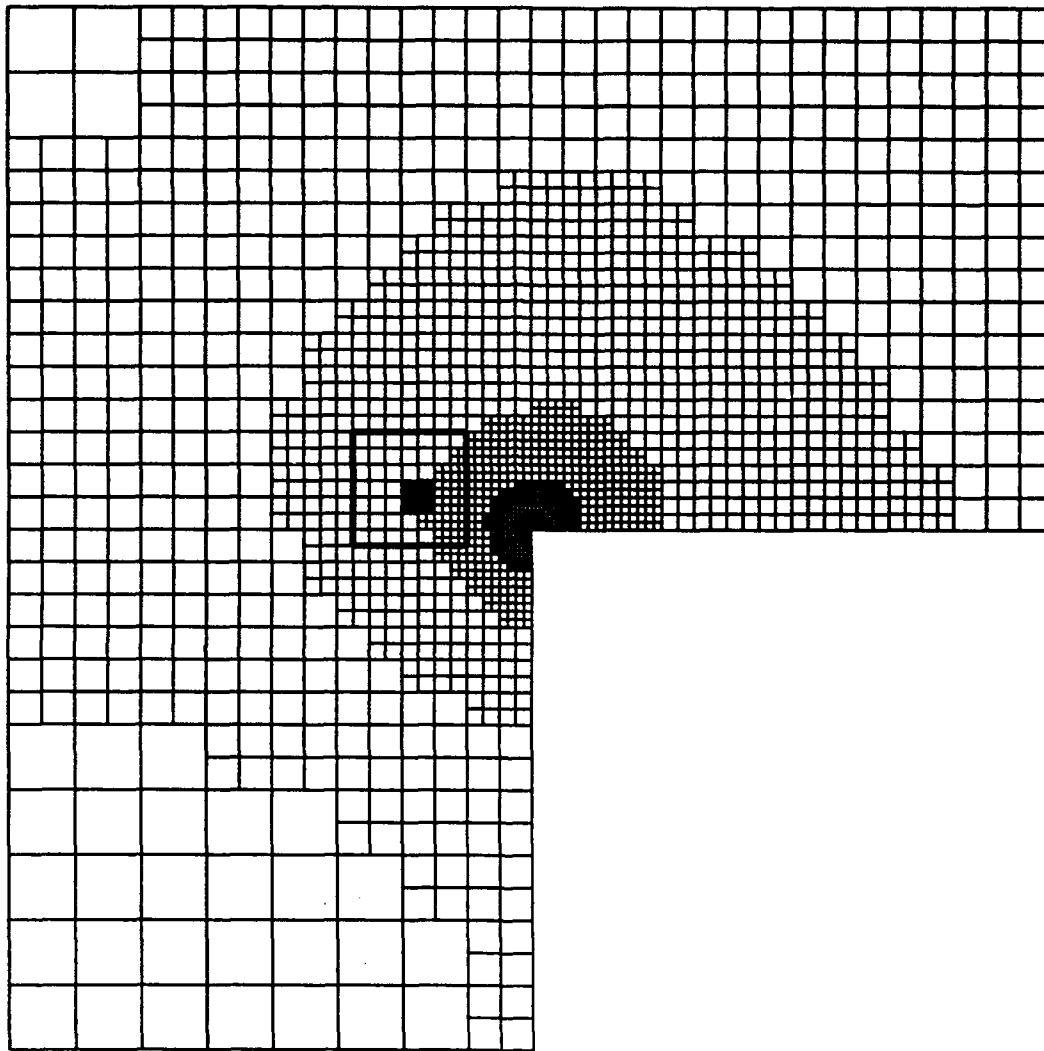




**Fig. 30b**

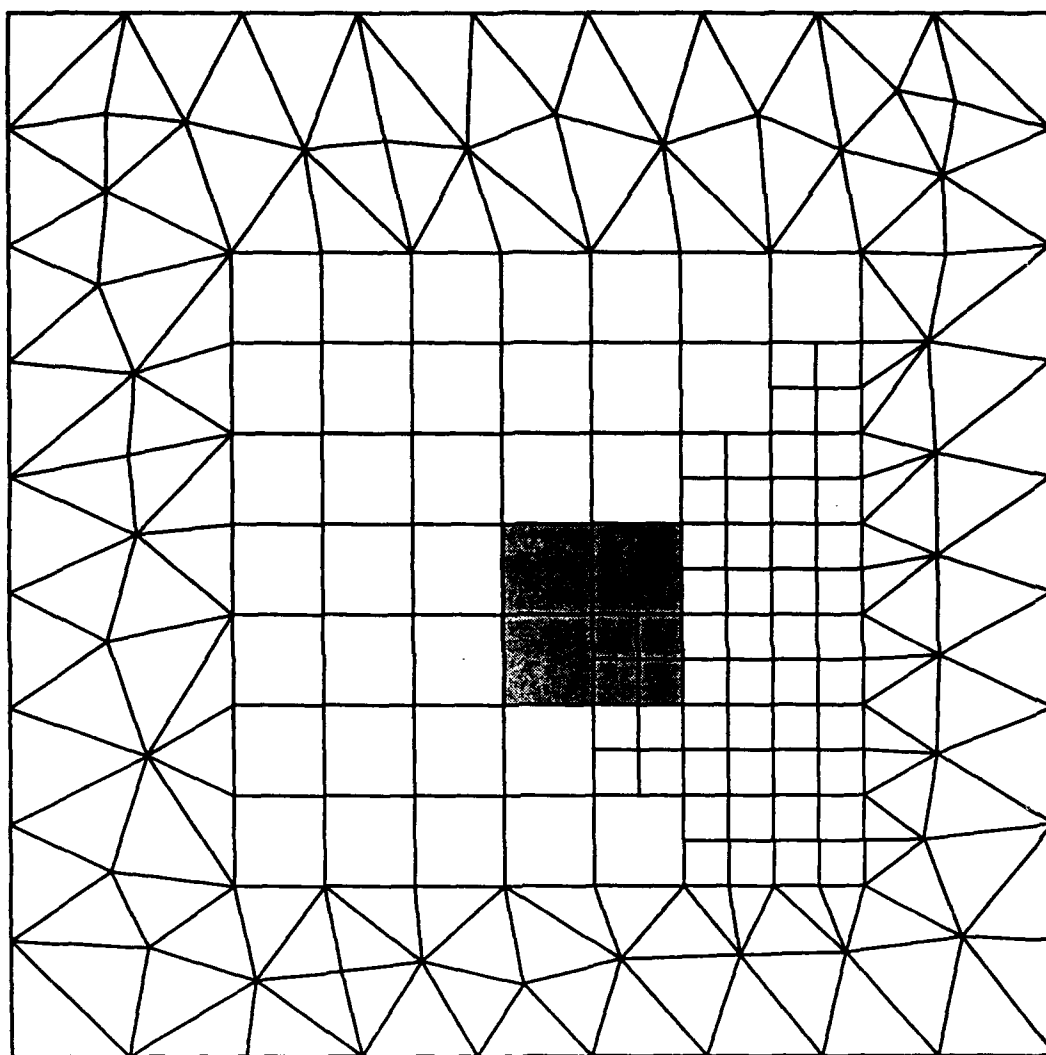
**Simplified approach with L-2 norm**



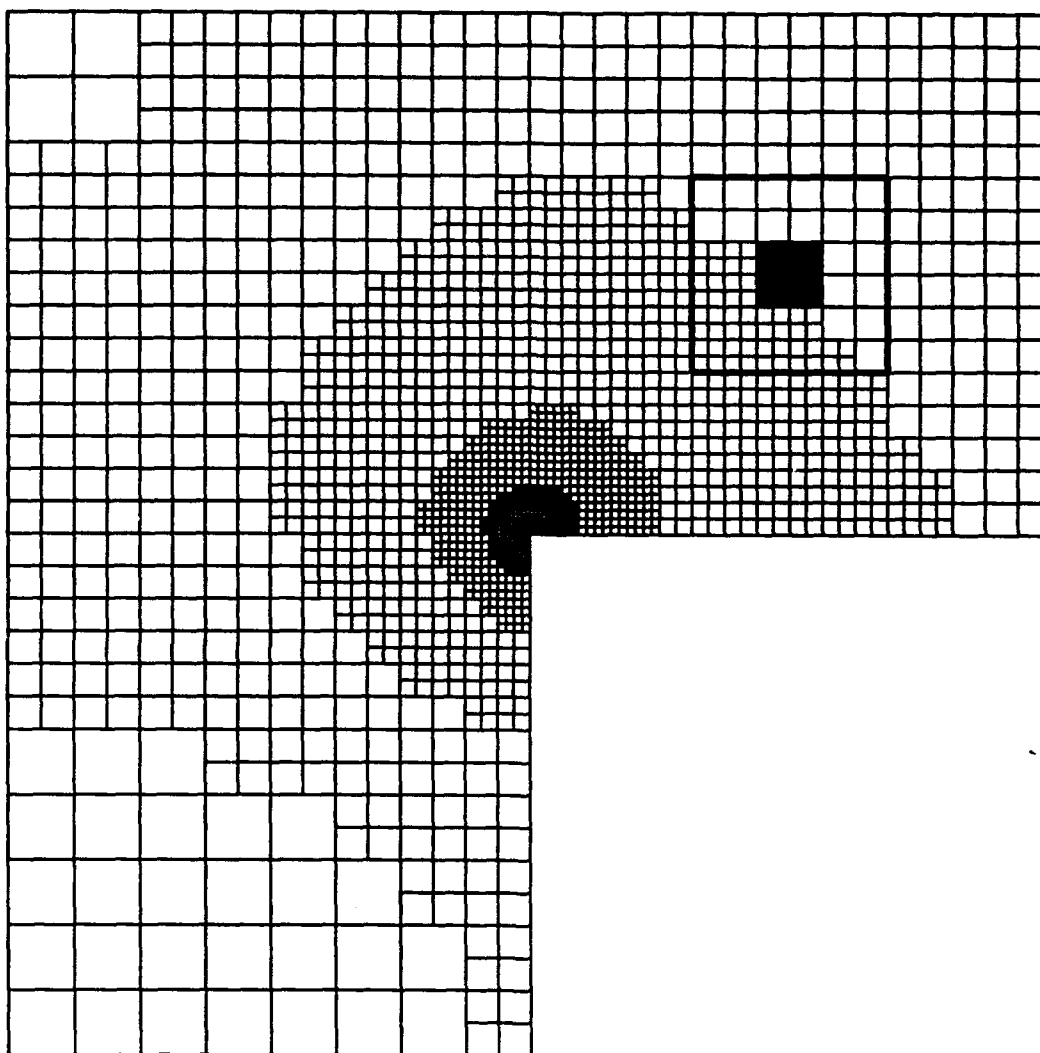


**Fig. 31a**

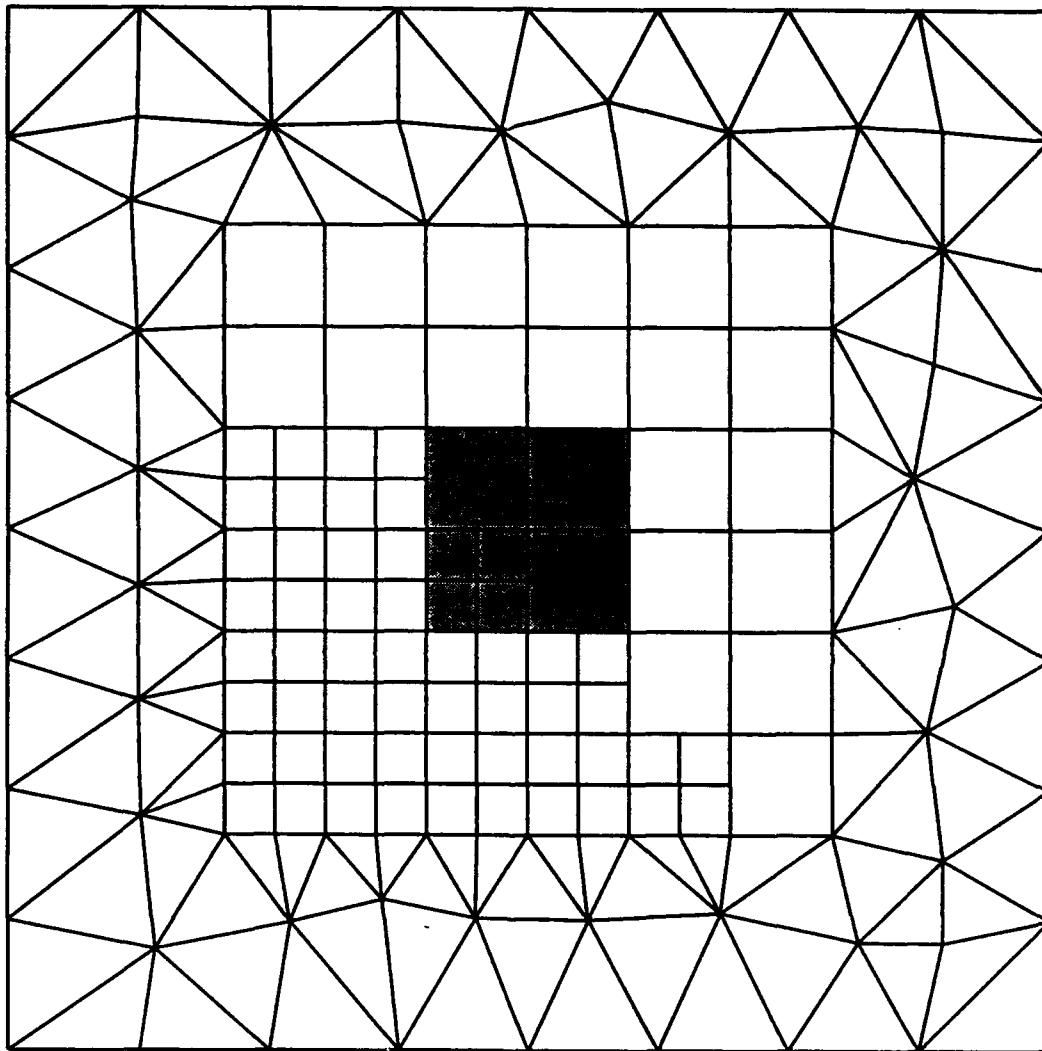




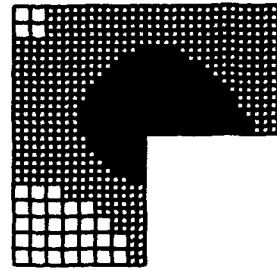
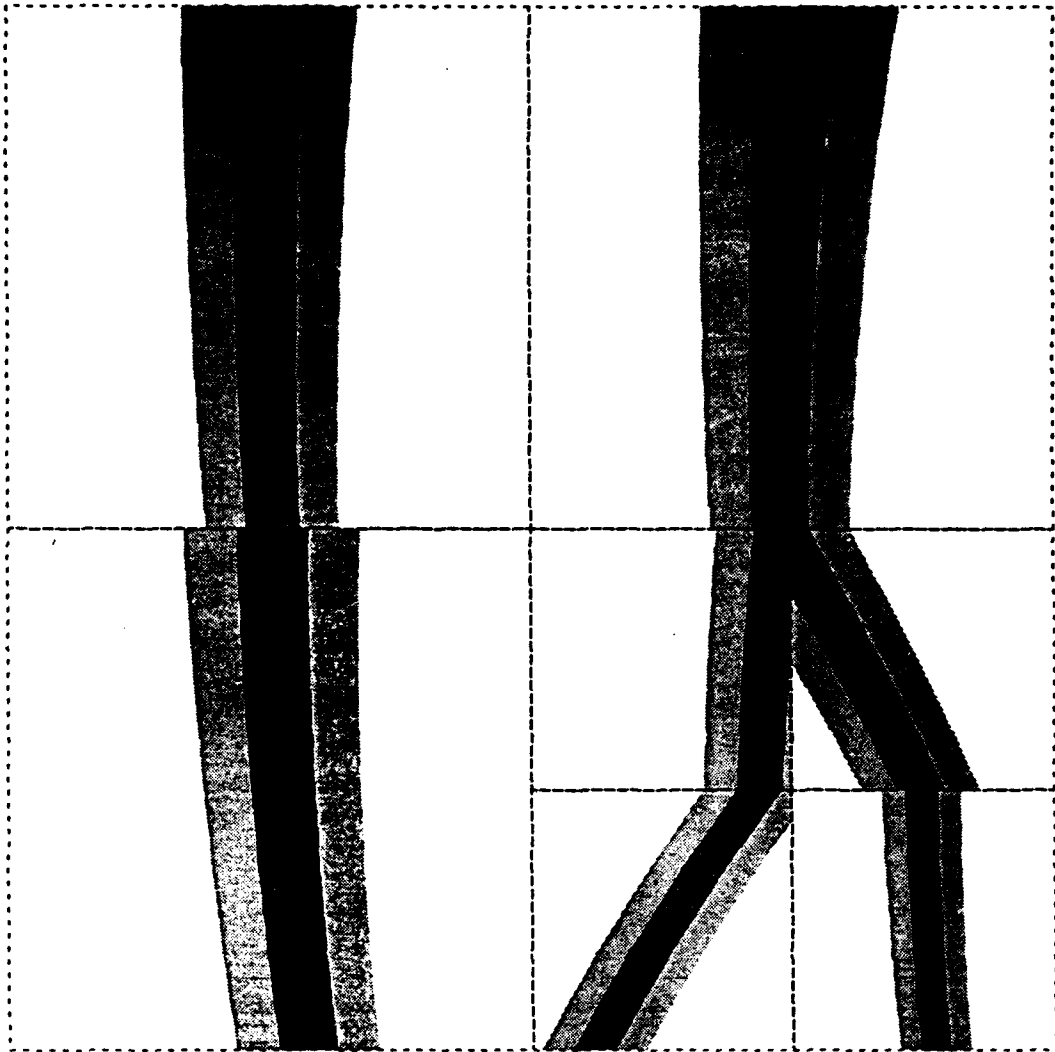
**Fig. 31b**



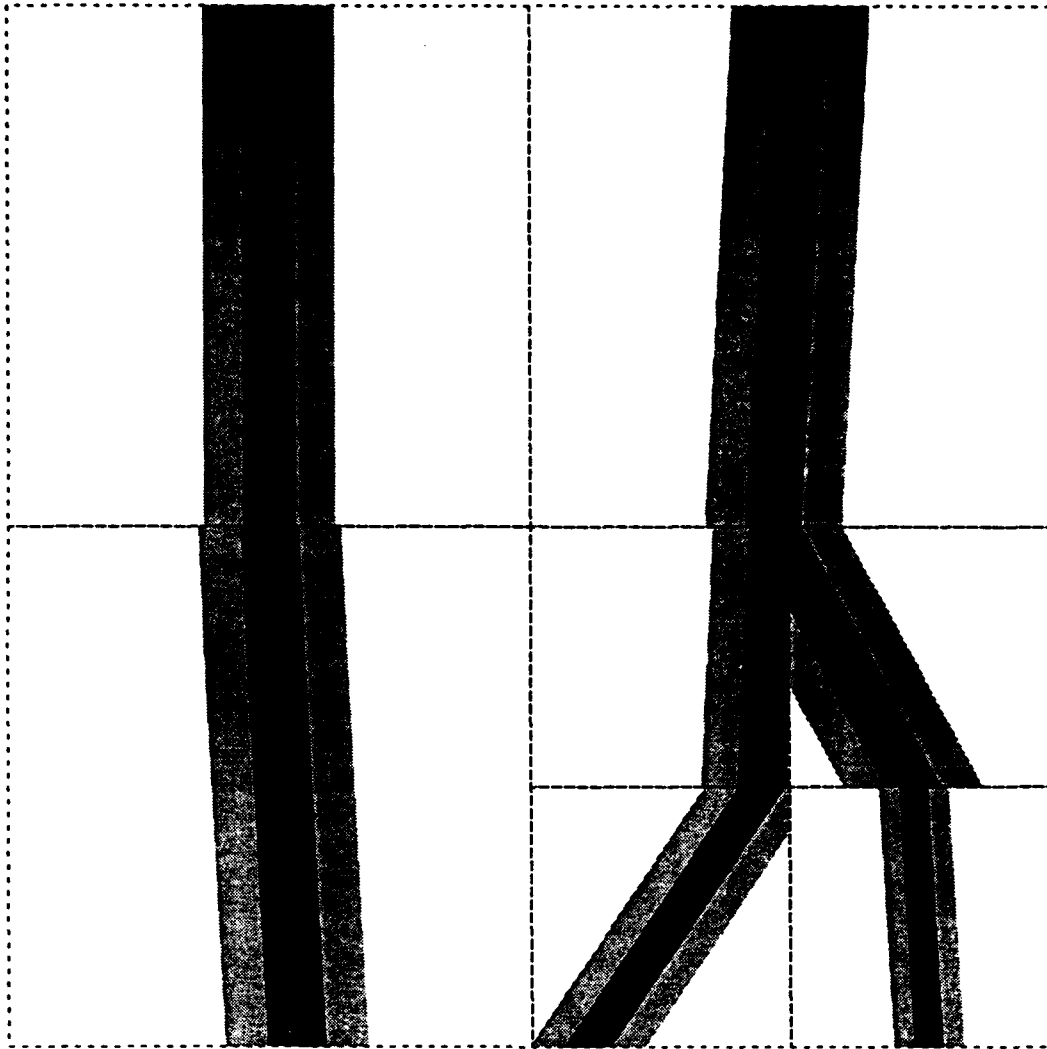
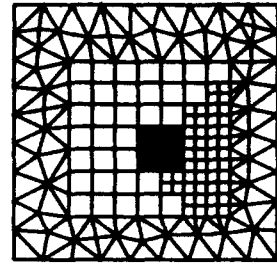
**Fig. 32a**



**Fig. 32b**

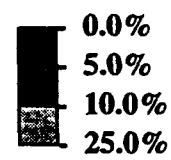


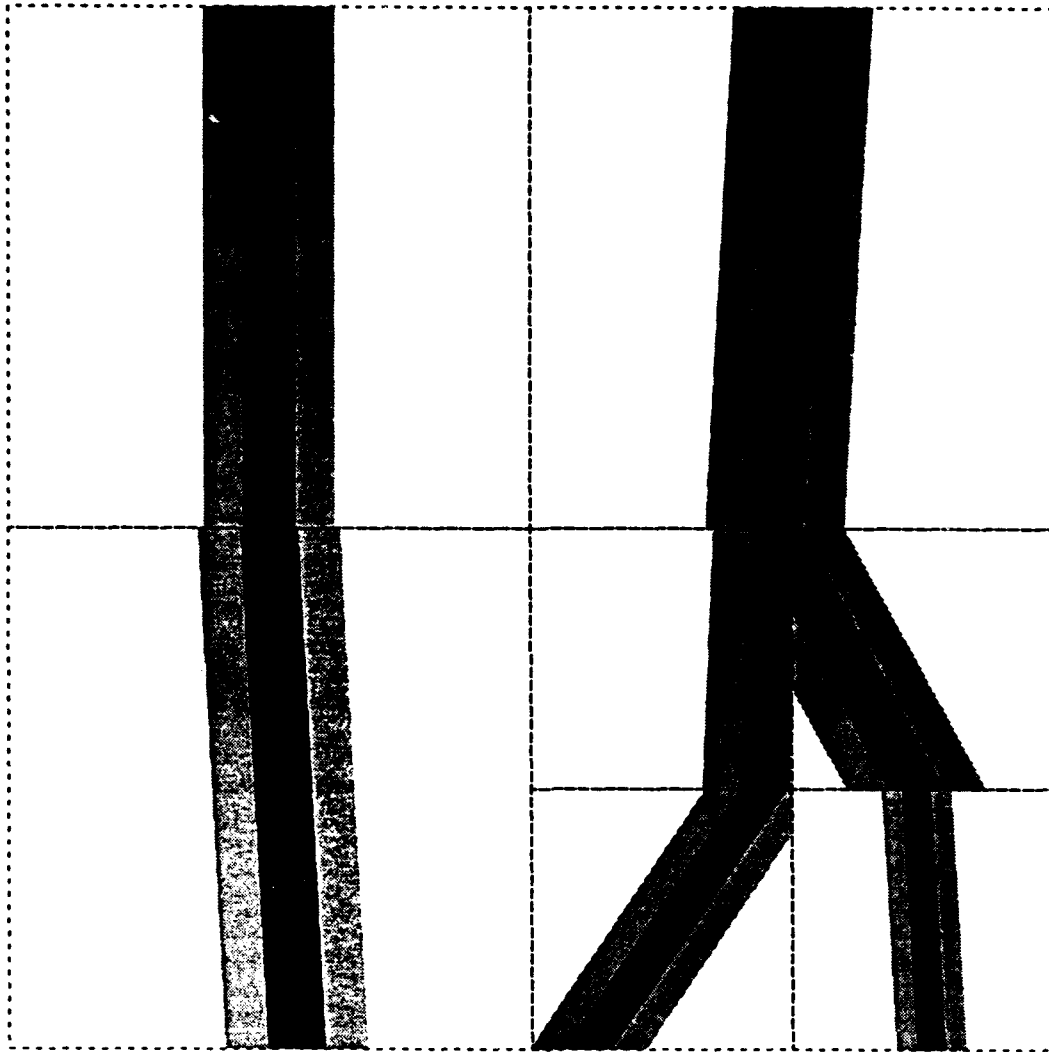
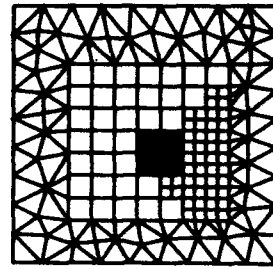
**Fig. 33a**



**Fig. 33b**

**Simplified approach with L-2 norm**

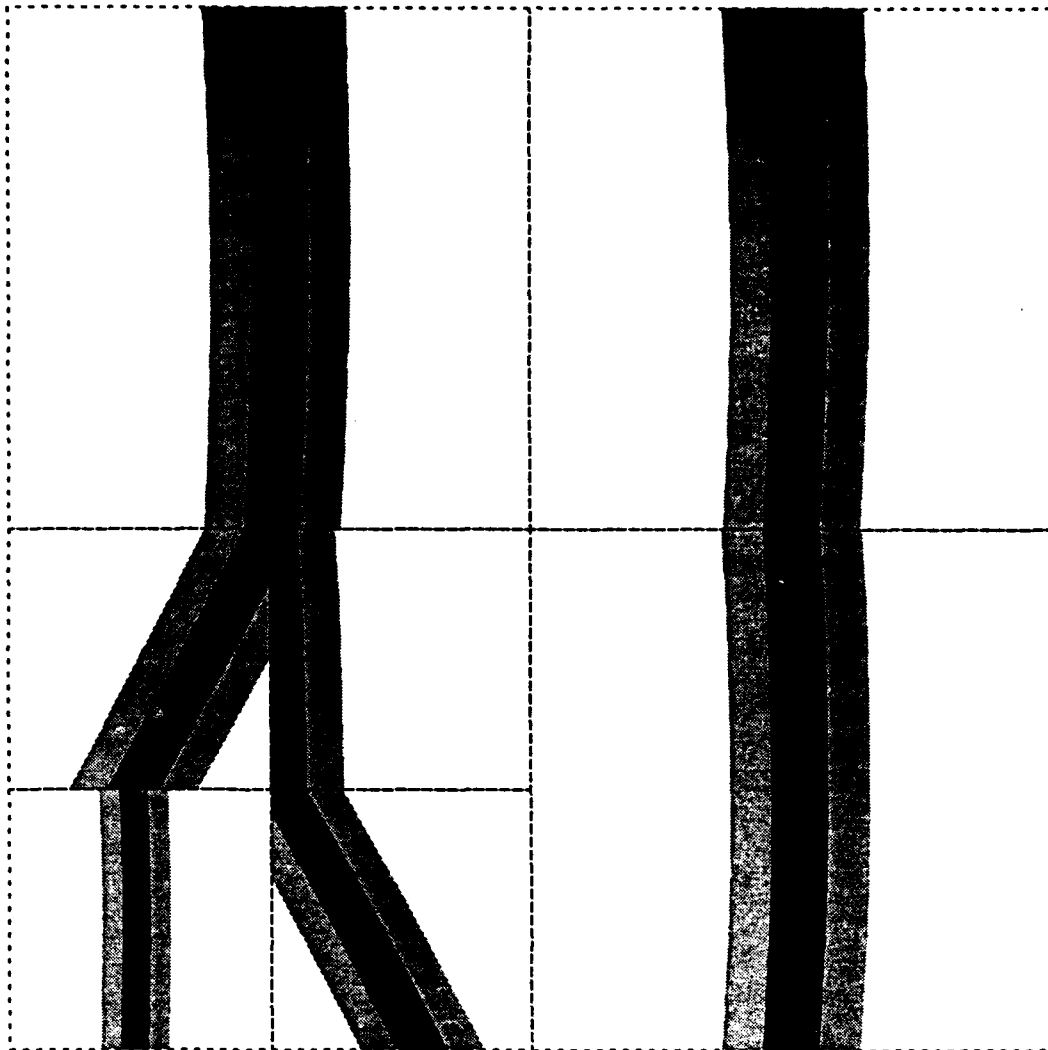
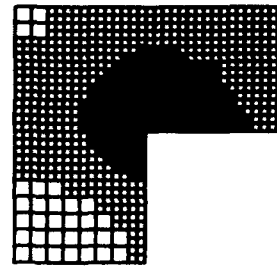




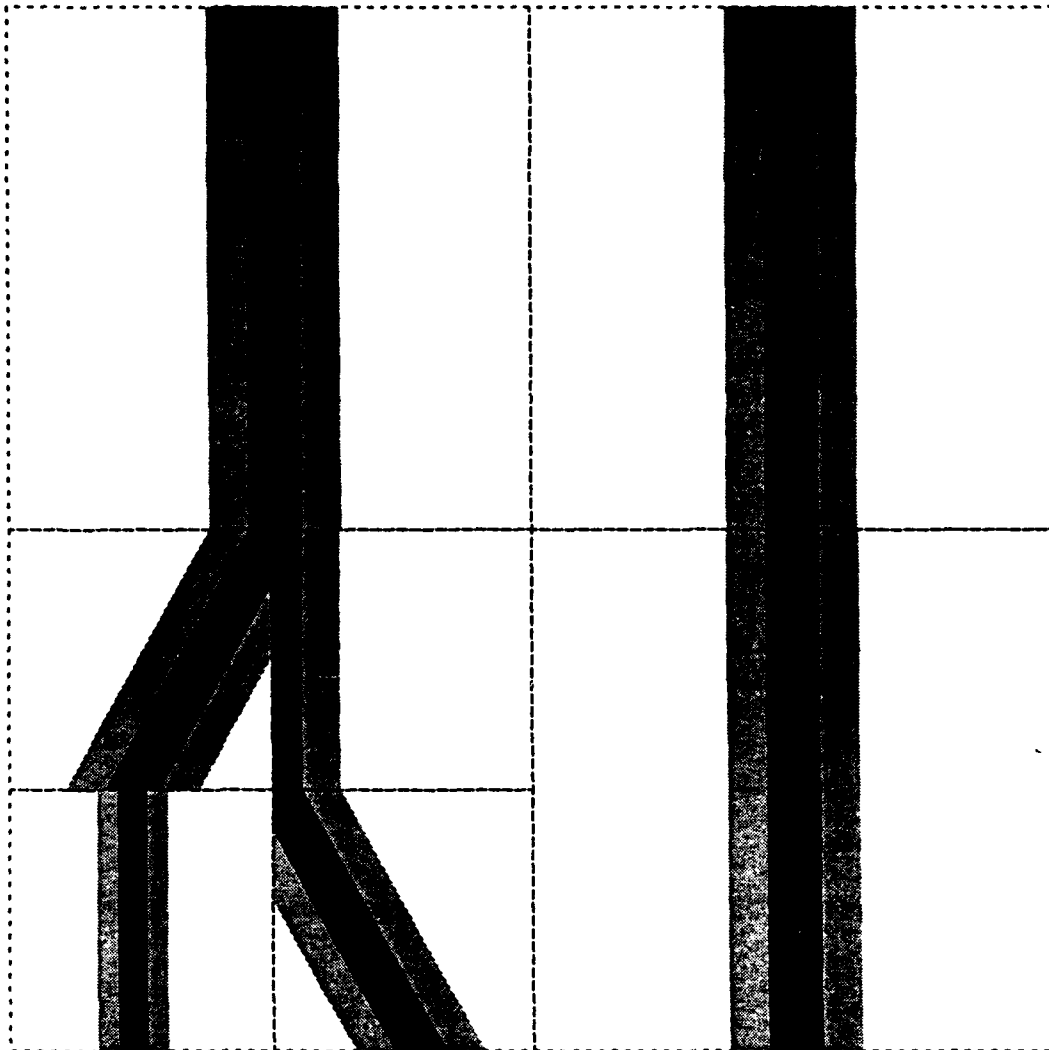
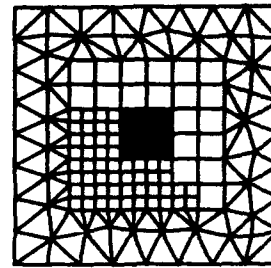
**Fig. 33c**

**Simplified approach with L-2 norm**



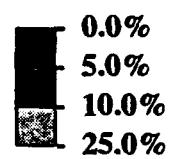


**Fig. 34a**



**Fig. 34b**

Simplified approach with L-2 norm





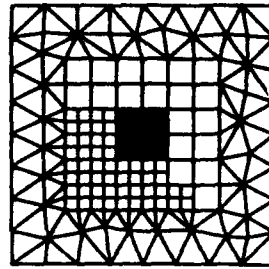
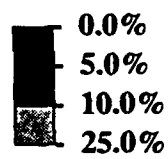


**Fig. 34c**

**Simplified approach with L-2 norm**



**The Laboratory for Numerical Analysis is an integral part of the Institute for Physical Science and Technology of the University of Maryland, under the general administration of the Director, Institute for Physical Science and Technology. It has the following goals:**

**To conduct research in the mathematical theory and computational implementation of numerical analysis and related topics, with emphasis on the numerical treatment of linear and nonlinear differential equations and problems in linear and nonlinear algebra.**

**To help bridge gaps between computational directions in engineering, physics, etc., and those in the mathematical community.**

**To provide a limited consulting service in all areas of numerical mathematics to the University as a whole, and also to government agencies and industries in the State of Maryland and the Washington Metropolitan area.**

**To assist with the education of numerical analysts, especially at the postdoctoral level, in conjunction with the Interdisciplinary Applied Mathematics Program and the programs of the Mathematics and Computer Science Departments. This includes active collaboration with government agencies such as the National Institute of Standards and Technology.**

**To be an international center of study and research for foreign students in numerical mathematics who are supported by foreign governments or exchange agencies (Fulbright, etc.).**

**Further information may be obtained from Professor L. Babuška, Chairman, Laboratory for Numerical Analysis, Institute for Physical Science and Technology, University of Maryland, College Park, Maryland 20742-2431.**